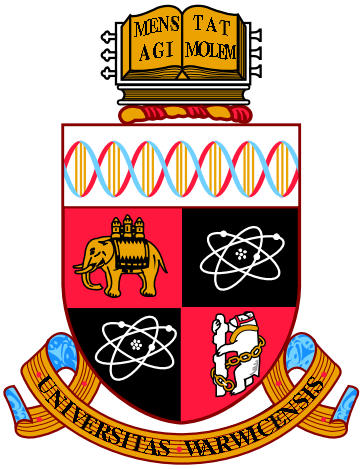

A Numerical Study of Turbulent Drag Reduction Using Streamwise Travelling Waves of Spanwise Wall Velocity

by

Edward Hurst

Thesis

Submitted to the University of Warwick

for the degree of

Doctor of Philosophy

.....

March, 2013

THE UNIVERSITY OF WARWICK

Contents

List of Tables

List of Figures

Acknowledgments

Firstly, I would like to thank my supervisor Dr. Yongmann Chung for his motivation and support. Coming from a non-engineering background meant that his knowledge and advice was invaluable throughout my PhD. I would also like to thank the EPSRC, Airbus and EADS for their financial support through grant EP/GO60215/1 as well as the UK Turbulence Consortium (grant EP/G069581/1), which allowed access to HECToR. Thanks to Ning Li from NAG for his time and guidance during the code parallelisation, and for allowing us to use his decomposition library. I am grateful to the teams at Imperial, Warwick and Cardiff who were also working on the project. A big thanks to all the staff and students in the CSC, especially Chris, for all the help throughout my MSc and PhD. I'd also like to thank Tariq, Dana and Oliver for their technical discussions and help along the way.

I am hugely grateful to my parents for their endless love and support, without which I wouldn't have had this opportunity. Thanks to Becky for leading by example. Most importantly I'd like to thank Fran for being there for me every day. Without you it wouldn't have been possible.

Declarations

This thesis, and the material in it, is my own work. It has not been submitted for a degree at any other university. As part of the work carried out, the work was presented at the following conferences:

E. Hurst and Y. M. Chung. The reynolds number effect of turbulent drag reduction. In *UK Turbulence Consortium*, 2012a

E. Hurst and Y. M. Chung. The reynolds number effect of turbulent drag reduction. In *9th European Fluid Mechanics Conference*, 2012b

Abstract

A parallelisation of the fully-implicit fractional step based in-house DNS code was implemented. Utilising this, DNS of streamwise travelling waves of spanwise wall velocity in a turbulent channel flow were performed at $Re_\tau = 200, 400, 800$ and 1600, scaling the input parameters in wall units. Studying the drag reduction at varying Reynolds number showed that the maximum drag reduction decreased as Re was increased. The scaling with Reynolds number was dependent on the control parameters and therefore the optimal parameters changed with Re. An oscillation in the drag reduction over the forcing period was observed and associated with strong variations in the turbulent statistics, angling of the streaks and coherent structures, and the deterioration of the drag reduction. The conditionally averaged λ_2 structures were found and behaved differently depending on the sign of the vorticity. This included a strong angling of the structure which rotated in agreement with the wall velocity, and this angle reduced over the half- period. The λ_2 structures were moved away from the wall over the period, a feature also visible in the variation of the vorticity fluctuations. The relationship between the drag reduction and the extrema of the turbulent profiles were compared, and showed a good correlation between the maximum of the v rms profile and the DR achieved. This was seen to be independent of Reynolds number when the maximum v rms of the no control flow was subtracted. The variation of the power spent and net power saving with Reynolds number was also studied. The power spent scaled well with $Re_\tau^{-0.16}$, and the net power saving scaled differently depending on the control parameters used. Although the maximum value was reduced as the Reynolds number increased.

Nomenclature

ρ	fluid density
μ	dynamic viscosity
ν	kinematic viscosity
τ_w	wall shear stress
u_τ	wall friction velocity
u_{τ_0}	wall friction velocity from no control case
C_f	skin friction, $\frac{2\tau_w}{\rho U_b^2}$
h	half channel height
U_b	bulk-mean velocity
Re	Reynolds number, $\frac{U_b h}{\nu}$
Re_τ	Reynolds number based on friction velocity, $\frac{u_\tau h}{\nu}$
t	time
x, y, z	streamwise, wall normal and spanwise coordinates
u, v, w	streamwise, wall normal and spanwise velocities
$\omega_x, \omega_y, \omega_z$	streamwise, wall normal and spanwise vorticity
p	pressure
L_x, L_y, L_z	domain size in x,y and z directions
N_x, N_y, N_z	number of grid points in x,y and z directions

W_m	maximum wall velocity of wall forcing
T	time period of wall forcing
ω	temporal frequency of wall forcing, $\frac{2\pi}{T}$
λ_x	spatial wavelength of wall forcing
κ_x	spatial wavenumber of wall forcing, $\frac{2\pi}{\lambda_x}$
ξ	similarity parameter for travelling waves $\xi = \frac{x}{\lambda} - \frac{t}{T}$.
ϕ	phase points for wall oscillation, ωt
S^+	scaling parameter for wall oscillation
u^+	wall units
u^{+_0}	wall units based on the no control flow
$\overline{u}$	mean (in x,z and t)
$\tilde{u}$	phase average
u'	fluctuation (with mean and phase averaged components removed)
DNS	direct numerical simulation
rms	root-mean-squared
DR	percentage drag reduction calculated using $DR = \frac{C_{f,0} - C_f}{C_{f,0}} \times 100$
DI	percentage drag increase (used only for reference, quantitativly this is calculated as a negative DR)
P_{sp}	percentage power spent by wall forcing (does not include actuator efficiancy) $P_{sp} = \frac{\langle w_w \tau_z \rangle_{x,z,t}}{U_b \tau_{x,0}} \times 100$
P_{net}	percentage net power saving of wall forcing, $P_{net} = DR - P_{sp}$

Chapter 1

Introduction

The increasing fuel costs and the evident effect of CO_2 emissions on the atmosphere is an obvious problem affecting the world today. 2-3% of this problem is attributed to the transport industry, especially air travel, which has a considerable environmental impact. One way to alleviate this mounting issue is to use flow control strategies to reduce the skin-friction drag, and thus reduce the energy used by vehicles. Research into Drag Reduction (DR) strategies has therefore been an important area of study over recent years. Computer simulation has become a more commonly used tool due to the ability to perform a high level of analysis and complex flow studies.

This thesis looks into the method of drag reduction by spanwise wall forcing, more precisely streamwise travelling waves of spanwise wall velocity, which has been shown to achieve high levels of DR. Due to the nature of accurate simulation techniques, most simulations are confined to particularly low Reynolds numbers. Although simulation of flight Reynolds numbers are still far off, this study looks to understand the Reynolds number effect and the flow physics to help explain how drag reduction is achieved.

1.1 Basic Concepts

1.1.1 Direct Numerical Simulation

Direct Numerical Simulation (DNS) is a form of computer simulation in which the Navier-Stokes equations are solved directly. This is the most accurate technique available when numerically investigating turbulent flow. The main drawback of this method is the computational expense. However, with the evolution of parallel computing and the use of various solution techniques, simple low Reynolds number flows are easily investigated.

1.1.2 Turbulent Channel Flow

As one of the simplest geometries to study, channel flow is a useful tool to further the understanding of wall turbulence. The simulation comprises a rectangular domain in which the streamwise, wall-normal and spanwise directions are labeled as the x, y and z axes, respectively. No-slip wall boundary conditions are applied at the extremities in y, while the x and z directions can be treated with periodicity. With a flow-rate in x defined by either a fixed mass flow rate or pressure gradient, a shear layer is created. A parabolic laminar flow can be triggered to turbulence which is sustained because of the presence of the wall. With the aid of DNS a highly accurate solution can be achieved given that a sufficiently large domain and a sufficiently fine resolution are employed.

The size of the channel is determined by the dimensionless parameter h, defined as the channel half-height. The domain size is chosen so that independence is achieved between the turbulence separated by half the length and width of the channel. If the width or length of the channel is not large enough the turbulent structures can interact with themselves in an unrealistic manor. For example, if the domain length is too small vortices can stretch the whole length of the channel, causing the simulation of infinitely long vortices. The size of the turbulent struc-

tures diminish as the channel wall is approached, hence a varying grid spacing is necessary in the y dimension to capture the near-wall structures accurately without unnecessary simulation expense. A fixed grid spacing in the streamwise and spanwise direction is used, where the streamwise separation is allowed to be larger due to the elongated nature of near-wall turbulence.

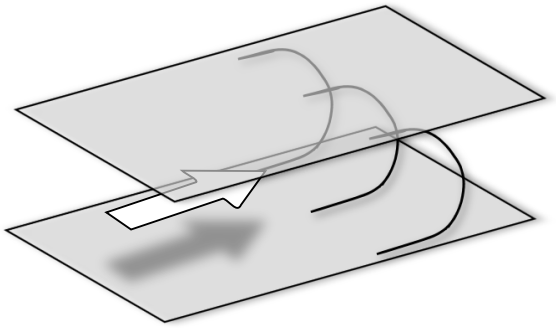

Figure 1.1: Diagram of Channel Flow

1.1.3 Flat-Plate Boundary-Layer Flow

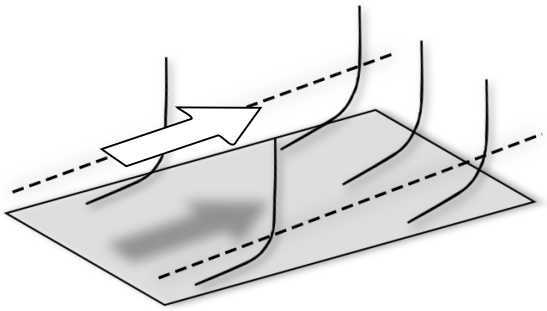

Figure 1.2: Diagram of Boundary Layer Flow

Although channel flow is a useful tool in understanding the flow it is not an accurate physical representation of the turbulence in a large number of real world situations. Because the study of near-wall turbulence is often unbounded away from the wall, a mean wall-normal velocity is established. In order to study this numerically, a freestream velocity U_∞ is applied at the top of the domain and the v

velocity is permitted to exit through this boundary. The consequence of the new flow geometry is that a spatially evolving turbulent boundary layer is produced, where the turbulent activity is confined to a near-wall region, the wall-normal extent of which increases as the location is advanced in the streamwise direction. The drawback of studying the flat-plate boundary layer is that periodic boundary conditions may no longer be used, therefore assorted inflow and outflow techniques must be adopted.

1.1.4 Flow Control

The use of flow control methods to achieve a drag reduction is an important field of study. These control techniques can be divided into two main areas.

Passive control is where no energy is applied to the flow in order to gain a reduction in skin friction. The advantage of this form of control is that any drag reduction obtained is immediately counted as power saved. Also, these methods are usually easier to implement due to the lack of moving parts. The majority of passive control methods use an alteration to the wall geometry in order to modify the flow.

Conversely, active control is where the turbulent activity is reduced by applying energy to the flow. This is often done at, or near, the wall due to the nature of possible forcing methods. This form of control can again be subdivided into two categories.

Feedback control is an intelligent form of control which applies forcing based on measurement from some physical properties from the flow. The main problem with this form of control is related to the practical application, due to the difficulty related to measuring the flow statistics without directly affecting the flow itself.

Open-loop control is a category in which forcing is applied using energy, independent of the flow, so that the drag is reduced sufficiently to achieve a net power saving. This category contains the spanwise wall forcing techniques performed in the current study. The mechanical applicability of the method is not considered, but the physics is studied in order to ascertain its efficacy in real world situations.

1.2 Understanding turbulence

1.2.1 Near-Wall Turbulence

The properties of the fluid can be defined by the dynamic viscosity, μ, and the density, ρ, which are considered constant in the current study. These can be combined to calculate the kinematic viscosity, ν, using:

$$\nu = \frac{\mu}{\rho}. \tag{1.1}$$

For a flow which is homogeneous in the streamwise and spanwise directions, such as channel flow, the shear stress can then be calculated using:

$$\tau = \underbrace{\mu \frac{\partial u}{\partial y}}_{\text{Viscous Stress}} - \underbrace{\rho \overline{u'v'}}_{\text{Reynolds Stress}}. \tag{1.2}$$

At the wall, the velocity is zero, due to no-slip boundary conditions. This means that the Reynolds stresses become zero; hence the wall shear stress is $\tau_w = \mu \left.\frac{\partial u}{\partial y}\right|_{y=0}$. From the wall shear stress, a useful parameter, u_τ, called the wall shear velocity, is defined:

$$u_\tau = \sqrt{\frac{\tau_w}{\rho}}. \tag{1.3}$$

This parameter can be utilised to non-dimensionalise both the velocity and the wall normal displacement in the following manor:

$$u^+ = \frac{u}{u_\tau}, \quad y^+ = \frac{y u_\tau}{\nu}. \tag{1.4}$$

The superscript + notation is used throughout this thesis to denote the wall unit non-dimensionalisation shown above. Other quantities are also defined using these definitions.

Plotting the streamwise, spanwise and time-averaged profile from a turbulent

channel flow using wall units gives the following profile.

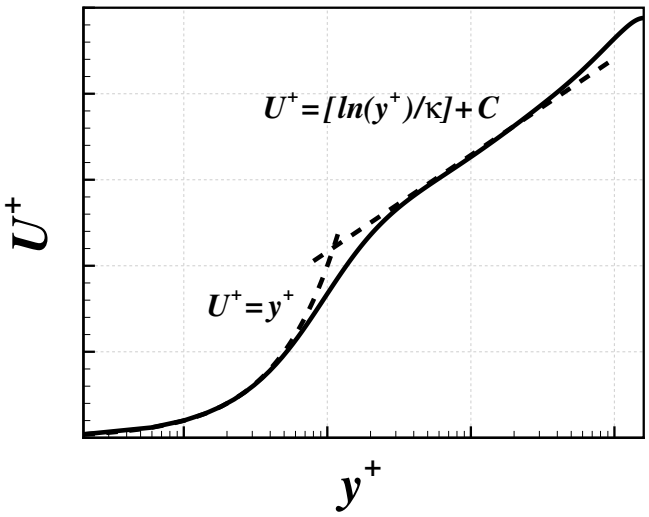

Figure 1.3: Log-law profile

Von Karman 1930 showed that near-wall turbulent boundary layers can be divided into four regions. These are as follows, where the first three can be grouped together as the inner-region:

- Nearest the wall is the viscous sublayer. From the the wall unit definition, $U^+ = y^+$ at the wall, however there is a region near the wall where the stresses are solely viscous.

- Between the viscous sublayer and the log-law region is the buffer layer.

- The log-law region is an area which the mean streamwise velocity satisfies the equation

$$U^+ = \frac{1}{\kappa} \ln(y^+) + C \tag{1.5}$$

  Where $\kappa \approx 0.41$ is the Von Karman constant and is the intercept $C \approx 5.0$.

- The outer region is further from the wall from the previously mentioned layers (combined to be called the inner region) where the mean profile strays from

the logarithmic approximation.

Throughout this thesis two Reynolds numbers will be used to define the channel flow. The friction Reynolds number is defined:

$$Re_\tau = \frac{u_\tau h}{\nu},$$

where u_τ is the wall shear velocity, h is the half-channel height and ν is the kinematic viscosity. The bulk velocity Reynolds number is defined:

$$Re = \frac{U_b h}{\nu},$$

where U_b is the bulk velocity.

1.2.2 Skin Friction Drag

The current study is focused on the application of flow control techniques which target a reduction of skin friction caused by near-wall turbulent flows. The skin friction coefficient is defined as the normalised wall shear stress:

$$C_f = \frac{\tau_w}{\frac{1}{2}\rho U_\infty^2}. \tag{1.6}$$

The drag reduction is the decrease of skin friction drag coefficient from the no control case value. Note that the no control case value is is dependent on the Reynolds number of the baseline flow. Throughout this thesis the term drag reduction will always refer to the percentage drag reduction, which is the reduction in C_f expressed as a percentage of the skin friction of the no control case.

The zero subscript notation, 0, will be used to define quantities from the baseline (no-control) flow. Wall units will be referred to as local units when using the controlled flow values for normaisation and denoted with the subperscript +. The term global wall units refers to normalisation by the no-control flow quantities

and is denoted by the superscript $+_0$.

The drag reduction is calculated by:

$$DR = \frac{C_{f,0} - C_f}{C_{f,0}} \times 100. \tag{1.7}$$

Although the drag reduction is an important parameter to study, because this work investigates active control techniques, it is also useful to understand the net power saving achieved. First, the power required by the flow control strategy must be calculated. As the current body of work is limited to the research of spanwise wall forcing, the spanwise wall shear stress, τ_z, and spanwise wall velocity, w_w, and the bulk velocity, U_b, can be used to calculate the power spent by applying the forcing:

$$P_{sp} = \frac{\langle w_w \tau_z \rangle_{x,z,t}}{U_b \tau_{x,0}} \times 100. \tag{1.8}$$

The notation used here, $\langle \cdot \rangle_{x,z,t}$, defines a plane and time average. To allow for a direct comparison with the drag reduction the power spent is expressed as a percentage of the wall shear stress from the no control case, $\tau_{x,0}$.

1.2.3 Turbulent Kinetic Energy (TKE) Budget

The turbulent kinetic energy, k, is calculated as the average fluctuating energy per unit mass:

$$k = \frac{1}{2}\left(\overline{(u')^2} + \overline{(v')^2} + \overline{(w')^2}\right)$$

In a simple, near-wall flow the turbulent kinetic energy is produced by fluid shear, transferred down the energy cascade and dissipated by viscous forces at the Kolmogorov scale.

The transport of near-wall turbulence can be considered through the understanding of the transport of the Reynolds stresses. This can provide an insight into the underlying physics of turbulence flow. For an incompressible turbulent flow, the

Reynolds stress transport equations are given by

$$\frac{\partial \overline{u_i u_j}}{\partial t} + C_{ij} = P_{ij} + T_{ij} + \Pi_{ij} + \Phi_{ij} + D_{ij} + \epsilon_{ij}. \tag{1.9}$$

Here

$$C_{ij} = U_k \frac{\partial}{\partial x_k} \overline{u_i u_j}$$

$$P_{ij} = -\left(\overline{u_i u_k} \frac{\partial U_j}{\partial x_k} + \overline{u_j u_k} \frac{\partial U_i}{\partial x_k} \right)$$

$$T_{ij} = -\frac{\partial}{\partial x_k} \overline{u_i u_j u_k}$$

$$\Pi_{ij} = -\frac{1}{\rho} \left(\frac{\partial}{\partial x_i} \overline{p u_j} + \frac{\partial}{\partial x_j} \overline{p u_i} \right)$$

$$\Phi_{ij} = \frac{1}{\rho} \overline{p \left(\frac{\partial u_i}{\partial x_j} + \frac{\partial u_j}{\partial x_i} \right)}$$

$$D_{ij} = \nu \frac{\partial^2}{\partial x_k^2} \overline{u_i u_j}$$

$$\epsilon_{ij} = -2\nu \overline{\frac{\partial u_i}{\partial x_k} \frac{\partial u_j}{\partial x_k}}$$

where $C_{ij}, P_{ij}, T_{ij}, \Pi_{ij}, \Phi_{ij}, D_{ij}$ and ϵ_{ij} denote the convection, production, turbulent transport, pressure transport, pressure-strain correlation, viscous diffusion and viscous dissipation, respectively.

1.2.4 Stokes' Second Problem

The wall oscillation control method employed in this thesis consists of turbulent flow over an oscillating wall. It is therefore useful to understand the effect of an oscillating wall with no mass flow. Stokes' second problem consists of an oscillating flat plate in stationary flow. The oscillation is parallel to the plate and there is no pressure gradient, hence the Navier-Stokes equations reduce to:

$$\frac{\partial w}{\partial t} = \nu \frac{\partial^2 w}{\partial y^2}, \tag{1.10}$$

where y is the direction normal to the flat-plate, w is velocity in the direction of oscillation and ν is the kinematic viscosity.

If the plate oscillates sinusoidally in time, then the boundary condition at the wall ($y = 0$) can be written as:

$$w_w = W_m \sin\left(\frac{2\pi}{T} t\right), \tag{1.11}$$

where T is the temporal period of the oscillation and W_m is the maximum wall velocity. This equation can be solved analytically giving the solution:

$$w = W_m \exp\left(-y\sqrt{\frac{\pi}{\nu T}}\right) \sin\left(\frac{2\pi}{T} t - y\sqrt{\frac{\pi}{\nu T}}\right) \tag{1.12}$$

The motion of wall entrains the near-wall fluid which also moves parallel the wall plane. The sinusoidal boundary condition at the wall also causes spanwise temporal oscillation at a giving wall-normal height y. The phase of this oscillation, however, is delayed relative to the wall motion by $-y\sqrt{\frac{\pi}{\nu T}}$ (in equation 1.12). This is therefore a wave of spanwise velocity propagating into the flow. The viscosity of the fluid damps this wave so that the maximum spanwise velocity in a wall-normal plane decays exponentially away from the wall (as $\exp\left(-y\sqrt{\frac{\pi}{\nu T}}\right)$ in equation 1.12). The spanwise velocity profile is shown at various points in the time period in figure 1.4 and gives a visual representation of this viscous wave.

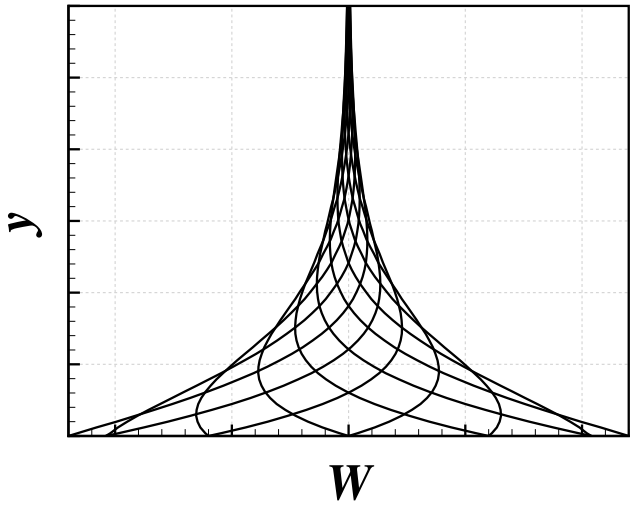

Figure 1.4: The laminar Stokes' Layer

1.3 Thesis Outline

This thesis is structured as follows. Chapters 2-4 present background information and results from preliminary investigations:

- Chapter 2 is the literature review which outlines the influences on the current study. Papers are discussed relating to numerical study of spanwise wall forcing techniques in both channel and boundary layer flows, as well as some experimental results. Work on higher Reynolds number DNS is also summarised. Finally 3d steady boundary layer studies (i.e. crossflow and moving walls of fixed velocity) are discussed along with vortex identification techniques.

- Chapter 3 describes the numerical methods used in the in-house DNS code which is utilised in the current study. The parallelisation strategy is discussed as its implementation was a major part of the current work and allowed for higher Reynolds number simulations to be performed.

- Chapter 4 shows the results from a number of preliminary simulations. These were performed to ensure that the correct domain size, grid resolution and

time-step are employed. Both the no control and wall forcing results are compared to available data in this chapter.

Chapters 5-8 present various results from the wall forcing simulations:

- Chapter 5 discusses the influence of increasing the Reynolds number on the effectivity of the control methods at various values of the forcing parameters. There is an initial description of the effect of increasing the Reynolds number on an unforced channel flow. The chapter concludes with turbulent statistics of the wall oscillation and standing wave cases at the four Reynolds numbers studied.

- Chapter 6 shows how the turbulent statistics vary over the forcing period, using results from fixed Reynolds number of $Re_\tau = 800$. These results are presented for an effective and ineffective case for the wall oscillation, standing wave and travelling wave forcings.

- Chapter 7 shows how the profiles of the turbulent statistics vary with the change in forcing parameters. These are used primarily to investigate the correlations between drag reduction and features of the profiles of the statistics.

- Chapter 8 investigates into the fields of streaks and λ_2 structures within the flow. This includes the eduction of a conditionally-averaged λ_2 structure for the wall oscillation with near-optimal forcing frequency. The angle of these structures is measured and compared to the average streak angle and various flow angles.

Chapter 9 discusses concluding remarks and possible directions of future work.

Chapter 2

Literature Review

2.1 Channel Flow DNS

2.1.1 Wall Oscillation

The first study into spanwise wall oscillation was by Jung et al. [1992], who investigated a turbulent channel flow with $Re_\tau = 200$. The oscillation was applied using the formula:

$$w_w = W_m \sin\left(\frac{2\pi}{T}t\right) \tag{2.1}$$

where the spanwise velocity at the wall w_w is determined by the maximum wall velocity, W_m, the period of oscillation, T, and the time, t. The maximum wall velocity was fixed at $W_m = 0.8$ and a range of parameters were studied; $T^+ = 25, 50, 100, 200$ and 500. The optimal value of T^+ was found to be ≈ 100 where the wall shear stress was shown to reduce by 40%. The rms fluctuations were shown to be reduced by the oscillation and the peaks moved away from the wall. The time evolution of the streamwise wall shear stress showed a large oscillation with greater time periods.

The understanding was furthered by Baron and Quadrio [1996], in which the optimum parameter of $T^+ = 100$ was taken from the previous study and simulations

were performed with amplitudes $W_m = 0, 0.25, 0.5, 0.75, 1$. The drag reduction was shown to increase with increasing velocity amplitude achieving a maximum at just over 40%. The power spent was also calculated and smallest amplitude $W_m = 0.25$ was shown to give net power saving in the order of 10%. A thorough study of the turbulent statistics was performed for the $W_m = 0.75$ case in order to understand the flow physics. It was seen that the velocity and vorticity rms values were reduced by the control method, but for u'^+ (scaled by local units) this reduction was limited to the near-wall region. The turbulent kinetic energy budget showed a decrease in near wall production, hence the location of maximum was increased. A large decrease in the dissipation and viscous diffusion were also seen in the near wall region. Looking at the third and fourth moments it was found that the streamwise skewness was increased near the wall and the maximum location was moved from the wall (in the no-control case) to $y^+ = 5 - 10$. The wall normal component of skewness showed a region of large negative skewness in the region $5 < y^+ < 40$ with a local minima introduced at $y^+ = 15$. It was seen in the flatness that the u and w components exhibited their maximum values at slightly higher y^+, where as v had larger wall values.

The effect of wall oscillation was also studied in pipe flow by Nikitin [2000] at $Re = 4000$ (corresponding to $Re_\tau = 180$). The study agreed that using oscillation frequency $\omega^+ = 0.06$ gave the maximum drag reduction. Using the relationship $\omega = \frac{2\pi}{T}$, this is analogous to a time period of $T^+ \approx 100$. $W^+ = 3, 6$ and 9 were studied and relaminarisation was seen for the larger amplitude. The strong similarity between the results from pipe and channel flow showed that the large wall curvature had little effect on the behaviour of near-wall structures.

Choi et al. [2002] performed DNS of channel flow at $Re_\tau = 100, 200$ and 400 and turbulent pipe flow was simulated with $Re_\tau = 150$. Although a view on the effect of Reynolds number is studied the domain size is quite small and therefore the large scale structures may not be sufficiently independent in space. Also the grid

spacing used is quite large and may not successfully capture the small scales. The paper showed that for $T^+ = 150$, in pipe flow, the mean spanwise velocity profile corresponded well the the laminar stokes solution. The drag reduction was again shown to increase with W_m^+ and plateau at $W_m^+ \approx 10$, while the optimal T^+ is also seen at around 100. Interestingly, these features were seen to be very similar, when the parameters are scaled by wall units, in the higher Reynolds number case, with the overall DR achieved reducing as the value of Re_τ is increased.

The aforementioned paper, Choi et al. [2002], also looks into the physics of wall oscillation flow, plotting conditionally averaged flow-fields based on $Q = \frac{1}{2}\left(\Omega_{ij}^2 - S_{ij}^2\right) > 0$. These fields, shown at different points in an oscillation period, illustrates the idea that when the vorticity is acting in a direction opposed to the wall motion the high speed fluid is moved below the low-speed fluid. Conversely, when the vortex and wall move in the same direction the high-speed fluid is moved away from the vortex and the influence of the low speed fluid is weakened. One of the major contributions of this paper is the introduction of the scaling parameter defined by:

$$S^+ = \frac{a_5^+ y_d^+}{A^+ Re_\tau^{0.2}} = \frac{2}{\sqrt{T^+}} \ln\left(\frac{W_m^+}{W_{th}^+}\right) \exp\left(-\bar{y}^+ \sqrt{\frac{\pi}{T^+}}\right), \tag{2.2}$$

where W_{th}^+ is chosen as 0.5 and $\bar{y}^+ = 5$. Note that a_5 is the acceleration at $y^+ = 5$. It is then suggested that drag reduction scales with this parameter, using the relation $DR = 1000S^{+2} + 50S^+$. This parameter is studied in later work and will be discussed further in section 5.2.7.

The initial response to the wall oscillation at $Re_\tau = 200$ was explored by Quadrio and Ricco [2003] via DNS. A range of forcing parameters were studied with $50 < T^+ < 200$ for fixed $W_m^+ = 18$, and $3 < W_m^+ < 27$ with fixed $T^+ = 125$. A small initial delay in the reduction of drag is noted and attributed to the wall-normal distance of the streak/structure locations. This height causes an offset between in

the spanwise velocity felt at the wall an this y location due to the propagation of the wall motion into the flow. The delay in the reaction of drag to the application of the forcing is lengthened with increasing T^+ or a reduction in W_m^+. For $W_m^+ = 18$ and $T^+ = 125$ a good agreement of the spanwise velocity profile is shown between the laminar solution and DNS results. Studying the initial transient for the same forcing parameters shows an initial decrease in u' followed by an increase, before settling to a steady state. v', $u'v'$ and the production term P_{11} follow quantitatively similar behaviour with a slightly delayed response in the wall normal velocity fluctuation. A large near wall peak is initially generated in w', before a reduction occurs and a fully developed state is established. The production term P_{33} is initially zero, but becomes large in the temporal transient before returning to zero.

Quadrio and Ricco [2004] studied the effects of wall oscillation on a turbulent channel flow at $Re_\tau = 200$. A thorough parametric study was undertaken consisting of 37 simulations spanning the range $T^+ = 0 - 750$ and $W_m^+ = 0 - 27$. A maximum drag reduction was seen at the location $(100, 27)$ in (T^+, W_m^+)-space. For any given W_m the maximum drag reduction was found in the range $T^+ = 100 - 125$, and by increasing W_m the DR is shown to increase at a decreasing rate. One interesting calculation shown here is that of, not only the power saving P_{sav} but also that of the power required for the oscillation P_{req}. These are defined by:

$$P_{sav} = \left\langle \frac{\partial U_0}{\partial y} \right\rangle - \left\langle \frac{\partial U}{\partial y} \right\rangle \tag{2.3}$$

$$P_{req} = \left\langle \frac{\partial W}{\partial y} W \right\rangle \tag{2.4}$$

Here, U_0 represents the space averaged mean of the stream wise velocity from the no-control case, and $\langle \cdot \rangle$ represents the time averaging procedure. The percentage net power saving is then calculated as $\%P_{net} = \%P_{sav} + \%P_{req}$, where $\%P_{req}$ is a percentage of the wall shear stress from the uncontrolled case and $\%P_{sav} = DR$. It was shown that, when $W_m^+ = 4.5$, the maximum net power saving is 7.3% at a time

period of $T^+ = 125$. A net power saving was achieved for $T^+ > 70$ (when $W_m^+ = 45$) and $W_m^+ < 7$ (when $T^+ = 125$).

Using the simulation results the S parameter scaling to DR is revisited, using a linear scaling. The scaling is confined to oscillations with $T^+ \leq 150$, and the best correlation is found when the $\bar{y}^+ = 6.3$ and $W_{th}^+ = 1.2$. This W_{th}^+ value is justified as it is of the order of the turbulent fluctuations. The scaling is then shown to follow the equation $DR = 131S^+ - 2.7$ and will be discussed further in section 5.2.7. The DR prediction is plotted against T^+ showing an over estimation for large T^+. The optimal values, however, are assumed to be predicted correctly and an analytic expression is found to calculate T_{opt}^+.

After performing DNS at $Re_\tau = 173$, Huang and Xu [2004] studied the transport of Reynolds stresses. A single simulation was performed with wall oscillation parameters $W_m^+ = 15$ and $T^+ = 90$, giving a drag reduction of 36%. It is shown analytically that the shear caused by the wall oscillation, $\frac{dW}{dy}$, acts directly on the $\langle u'w' \rangle, \langle v'w' \rangle$ and $\langle w'^2 \rangle$ terms. The results showed that the w'_{rms} and production term P_{33} initially increased slightly and were subsequently decreased, whereas a monotonic in a manor which is dependent on the decrease was seen in the pressure strain term S_{33}. The pressure strain for the wall-normal component is also decreased, reducing the v'_{rms}. This is amplified by $\frac{\partial U}{\partial y}$ to reduce the production of the Reynolds shear stress $P_{12} = -\langle v'^2 \rangle \frac{\partial U}{\partial y}$, diminishing the skin friction.

Ricco and Quadrio [2008] builds upon the previous work in Quadrio and Ricco [2004], using the same domain at $Re_\tau = 200$, though the number of grid points in y was extended to 160. Three further controlled simulations were performed at $Re_\tau = 400$, with $W_m^+ = 12$ and $T^+ = 30, 125, 200$. The plane-averaged, spanwise momentum equation is presented:

$$\frac{\partial \bar{w}^+}{\partial t^+} = \frac{\partial^2 \bar{w}^+}{\partial y^{+2}} - \frac{\partial \overline{v'w'}^+}{\partial y^+},$$

where $\bar{w}^+$ is the average of the spanwise velocity over a wall normal plane. The last term is shown to greatly decrease at $W_m^+ = 18$ and $T^+ = 125$, due to the oscillation. This implies an independence of w to the streamwise flow, justifying the use of the laminar Stokes' solution in the calculation of S^+. The $\%P_{sp}$ is also approximated and an analytic expression for $\%P_{sav}$ is presented. One result of note is that of the $Re_\tau = 400$ simulations. It is shown that, at the higher Reynolds number, a lower level of DR is achieved for the three cases studied. It is also seen that there is a larger decrease in DR of the oscillations with larger time periods, T^+. This is thought to explain the lower level of drag reduction found in experimental data.

Touber and Leschziner [2012] performed DNS at both $Re_\tau = 200$ and 500. At the lower Reynolds number 5 forcing parameters were studied with $W_m^+ = 12$ fixed and, at high values of T^+ an increase in drag was observed. The value of $T^+ = 100$ and 200 were investigated at $Re_\tau = 500$. The correlations of streamwise velocity R_{uu}, in the spanwise direction were shown to indicate an effect of the forcing on the near-wall streaks. The first minimum in the streamwise velocity correlation effectively disappeared when the optimal forcing was applied, corresponding to an increased influence of larger scale structures. The near-wall streaks were visualised and seen to be angled by the oscillation. This streak angle was calculated and its pdf, computed over the oscillation period was considered to be 'close to bimodal'. The phase of the oscillation of the streak angle was close to that of the shear angle at $y^+ = 10$ and the variation of this phase was said to be small in the near-wall region. A conditionally averaged streak was found and the effect of the Stokes' layer was illustrated. This spanwise phase-averaged velocity was compared to that of the laminar solution and as in previous study was shown to have good agreement at $T^+ = 100$. However, for larger periods a substantial difference in this property is observed. LES was also performed at $Re_\tau = 1000$ and the drag reduction of the various Reynolds numbers were compared to the S^+ parameter. This highlighted the Reynolds number effect and the fact that this was not currently incorporated

into the scaling parameter. Other statistical properties of the flow were shown including fluctuations PDFs, TKE budgets, enstrophy variation and the spectral density functions.

Recently, Agostini et al. [2014] have published a study of wall oscillation at $Re_\tau = 1000$. Although results of $T^+ = 100$ were shown, the main focus was around the $T^+ = 200$ case with $W_m^+ = 12$. The results support the previous study of Touber and Leschziner [2012] that points of high skin-friction and streak strength throughout the cycle correspond to high, slowly varying stokes strain. A hysteresis in the drag over the period is attributed to the near-wall velocity skewness. The fluctuations of enstrophy and dissipation show strong similarities over the forcing cycle, and are both shown to have qualitative correlation with the drag.

Cimarelli et al. [2013] looked into the effects of spanwise wall oscillations applying an assortment of different waveforms. It was seen that the sinusoidal forcing remains optimal for $T+ < 100$ and obtains the optimal power saving. The waveforms were broken into different modes whose effects were analysed individually. A waveform was then rebuilt to find a waveform that was approximated it give a greater power saving than the sinusoidal wave. This result was confirmed via DNS.

2.1.2 Standing and Travelling Waves

Viotti et al. [2009] adapted the wall oscillation technique to a temporally constant forcing method by considering the effect on near-wall structures. As the flow has almost constant convection velocity for $y^+ < 15$, the temporal forcing can be translated into a spatial wave, defined as:

$$w_w = W_m \sin(\kappa_x x), \tag{2.5}$$

where $\kappa_x = \frac{2\pi}{\lambda_x}$ is the wavenumber which can be written in terms of the streamwise wavelength, λ_x. While this forcing method is referred to as a standing wave due

to the application of a standing wave of spanwise velocity at the wall, the wave propagates into the flow. This propagation is caused by the mean flow travelling over the wall so that the near-wall fluid feels a spanwise velocity as a sinusoidal wave with a spatial delay from the wall position.

An analytic solution to the laminar case is calculated and is compared to the numerical results. It is seen that the laminar and turbulent profiles of the spanwise mean velocity compare well for both the wall oscillation and standing waves, with $T^+ = 125$ and $\lambda^+ = 1250$ respectively. The drag reduction was calculated for a range of wavelengths and the optimum was found as $\lambda^+_{x,opt} = 1000 - 1250$. A scaling $\lambda_{x,opt} = \mathcal{U}^+_w T^+_{opt}$ is suggested, where $\mathcal{U}^+_w = 10$ is the near-wall convection velocity. The standing wave achieves a higher level of drag reduction than wall oscillation when the value of W^+_m is fixed. In fact, the drag reduction from the standing wave at $W^+_m = 6$ corresponds to similar values to that of the wall oscillation using $W^+_m = 12$. As a function of the maximum wall velocity, the effects of the spatial wave again show a similar trend to that of the temporal case, as it increases monotonically and plateaus out at a higher W^+_m. The power that is required to apply the standing wave forcing (excluding any mechanical losses) is small, and due to the large values of DR achieved it is a much more efficient forcing method. With $W^+_m = 6$, a maximum net power saving of 23% is found. λ_2 visualisation shows the reduction in intensity of the near-wall structures caused by the control method and the u_{rms} shows a reduction of near-wall fluctuations.

The spatial and temporal waves can be combined into a more general forcing method, streamwise travelling waves of spanwise wall velocity, using the equation:

$$w_w = W_m \sin\left(\kappa_x x - \omega t\right), \tag{2.6}$$

where $\kappa_x = 0$ represents wall oscillation and $\omega = 0$ represents the standing wave case. With non-zero forcing parameters the control method can be considered as a

streamwise varying spatial wave with wavenumber κ_x travelling at a speed $c = \frac{\omega}{\kappa_x}$ in the streamwise direction. Simulations were performed by Quadrio et al. [2009] at $Re_\tau = 200$ with parameters range $-3 \leq \omega \leq 3$ and $0 \leq \kappa_x \leq 5$ and fixed $W_m^+ = 12$. A maximum drag reduction of 48% is seen with a forward travelling wave, however, a drag increase is also found in a region with $0.35 \leq c \leq 0.6$ and at small values of ω in the wall oscillation case. The power required to apply the wall motion reaches a minimum value of 23.5%. This occurs when the forcing parameters (ω and κ_x) are the values which achieved the maximum DR. The value of the power spent by the forcing increases rapidly with ω, hence the wall oscillation control method is inefficient as compared to the spatially dependent forcing. A maximum net power saving of 18% at $\omega = 0.15$ and $\kappa_x = 1$, and is heavily affected by the power spent. As W_m is increased the drag reduction increases monotonically and can reach up to 60% with $\omega = 0.16$ and $\kappa_x = 1.66$. The net power saving at this combination of parameters can reach 26% with $W_m = 0.25$. For the maximum drag reduction parameters a simulation at $Re_\tau = 400$ shows a decrease to a value of 42%.

Quadrio and Ricco [2011] extended the previous work on the streamwise travelling waves by performing further simulations with a fixed pressure gradient, as opposed to the fixed mass flow rate used before. The qualitative behaviour of the drag reduction is the same in the two cases, however a difference of up to 12% is seen for certain control parameters. The fixed pressure gradient simulations experience a larger magnitude of drag reduction which is emphasised around the region of drag increase. This study also calculates analytic expressions for the laminar oscillatory flow and therefore the Stokes' layer thickness, δ_l^+, and power required, P_{sp}. The laminar Stokes' layer thickness is seen to compare well to that computed by the simulations only when the 'time period', $\mathcal{T}^+$. The power required compares well between the laminar solution and DNS data, however a slight deviation occurs for large $\mathcal{T}^+$. The drag reduction is also compared to δ_l^+ indicating a minimum Stokes' layer thickness required to achieve a drag reduction. This relates to the S^+

parameter, which requires a threshold velocity to achieve a drag reduction.

A more recent study by Gatti and Quadrio [2013] has made some contribution to the understanding of the Reynolds effect. Due to the high computational cost in full scale DNS studies a minimal channel flow approach was undertaken in which a smaller domain size is used in the homogeneous directions. This study trades simulation accuracy for the ability to study a wide range of control parameters for the streamwise travelling wave forcing up to $Re_\tau = 1000$. A few cases were also performed up to $Re_\tau = 2100$. It was found that the drag reduction decreases with increased Re, and that the rate of decrease is heavily dependent on the control parameters. The steepest decay in DR occurs at regions of either high drag reduction or drag increase from the lower Reynolds number. The slow decay that occurs within the parameter space causes the optimal control parameters to shift towards higher wavenumbers and frequencies. The maximum net power saving seen at higher Re no longer occurs at the same forcing parameters as the minimum required power is observed. Some regions even occur in which the net power saving is found to increase.

Work by Ricco and Hahn [2013] and Wise and Ricco [2014] has investigated the more applicable wall forcing method of having rotating discs which either rotate constantly or oscillate. These studies, performed at $Re_\tau = 180$ finds similar maximum drag reductions of 20% and 23%. These gave maximum net power savings of 5% and 10%.

2.2 Increasing the Reynolds Number

Simulations of channel flow have been compared at various Reynolds numbers, with $Re_\tau < 700$. Moser et al. [1999] performed DNS up to $Re_\tau = 590$, with a fairly small domain. del Alamo and Jiménez [2003] performed channel flow at $Re_\tau = 180$ and 550, with a much larger domain size of $8\pi h \times 2h \times 4\pi h$ at the higher Reynolds

number. By examining the spectra it was concluded that there are two varieties of structures, near wall structures which are streamwise aligned, and larger scales which span the channel height and are more isotropic. A turbulent channel flow, with heat transfer, was studied by Abe et al. [2004], in which four Reynolds numbers were investigated $Re_\tau = 180, 395, 640$ and 1020. Two Prandtl numbers ($Pr = \frac{c_p \mu}{k}$, where c_p is the specific heat, μ is the dynamic viscosity and k is the thermal conductivity) of 0.025 and 0.71 were used. It was shown that the the effect of large scale structures extend to the near-wall, hence the effect of the large scales becomes greater at higher Reynolds numbers.

Tanahashi et al. [2004] performed channel flow simulations using three Reynolds numbers $Re_\tau = 180, 400$ and 800. The rms profiles showed that the peaks become slightly higher and move away from the wall as Re is increased. The turbulent kinetic energy budgets show that the magnitude of the production and dissipation decrease with Reynolds number, however their ratio is independent of Re_τ (as presented by Moser et al. [1999]). The interpretation of the coherent structures showed that the mode of the diameter and maximum azimuthal were independent of Reynolds number. Also observed was a strong directional dependence with y.

del Alamo et al. [2004] extended the range of their previous data by performing a simulation of channel flow at $Re_\tau = 934$ on a larger domain. Simulations on a smaller domain were also studied at $Re_\tau = 550, 964$ and 1901, to both compare with the previous simulations and extend the Reynolds number range further. A study of the uv-cospectra show that the large scale contributions to the Reynolds shear stress take place in the outer region. The structures associated with the streamwise velocity spectra scales, in the spanwise direction, with the square root of their length in the streamwise direction. Also, the largest of these structures in the streamwise velocity spectra are seen to scale with outer scales.

The current highest Reynolds number of channel flow DNS is $Re_\tau = 2003$, performed by Hoyas and Jiménez [2006], where it was compared against their pre-

vious results. Even at the largest value of Re_τ, the inverse 'von Kármán function', $y\frac{\partial U^+}{\partial y^+}$, is not constant in any y^+ region, as seen in experimental results. The logarithmic region is estimated to occur at $100/Re_\tau \leq y/h \leq 0.2$, although the validity of this approximation is questioned. The rms plots of u_i^+ against y/h show that for the v' and w' there is little variation in the profiles at different Reynolds number away from the wall, especially at the channel centreline. With u', however there is an increase in the rms value, even in the centre of the channel. Closer to the wall there is a clear change in all three profiles, with the peak value moving closer to the wall and becoming larger. One interesting feature of the flow is that a clear peak emerges in the w' profile. The 2d spectra for ϕ_{uu}, ϕ_{ww} and $-\phi_{uv}$ are shown at the y location of the maximum kinetic energy. The small scales, when adjusted by wall units, are similar for different Reynolds numbers, whereas the upper right-hand corner extends along $\lambda_z = 0.15\lambda_x$ up to $\lambda_x = 10h$ for ϕ_{uu}.

2.3 Numerical Study of Boundary Layer Flows

The first numerical study of wall forcing control on a boundary layer flow was conducted by Yudhistira and Skote [2011]. The oscillating wall technique was applied in a streamwise region of fully developed turbulent boundary layer. A fringe region was utilised to smooth the interface between the oscillating plate and the stationary wall sections. The Reynolds number in the section in which the wall is in motion varies between 418 and 750, based on the momentum thickness of the no-control case. Two different maximum wall velocities were studied for $W_m^+ = 18$ and 27, with $T^+ = 100$ in both cases. The maximum drag reductions achieved are 40% and 37% for $W_m^+ = 18$ and 27, respectively (slightly lower than the 45% and 39% achieved in the channel flow). The drag reduction increases rapidly downstream of the start of the region of oscillation, reaching its maximum at $\approx 100\delta^*$. The mean streamwise velocity profiles are reduced in the near-wall region and increased in the log-law

region, from the unforced flow. The u and v rms profiles were shown to decrease. The Reynolds shear stress reduced to a greater extent than the rms profiles, due to the quadratic relationship to fluctuation velocity. The turbulent kinetic energy budgets, for uu were shown, and the terms were greatly reduced by the wall forcing. When scaled by local u_τ the maximum of the production term is comparable to the no-control case value and shifted away from the wall, whereas the near-wall dissipation is greatly reduced.

Skote [2011] also numerically investigated the effects of the standing wave of streamwise varying wall velocity on boundary layer flow. The control method was applied using $W_m^+ = 17$ and $\lambda^+ = 1300$ based on $u_{\tau,0}$ at the start of the forcing region. The drag reduction reached a maximum of 46% after $150\delta^*$ (based on the laminar flow). Visualisation showed a tilting of the near-wall streaks by the spanwise velocity. The mean velocity profile indicated a thickening of the viscous sublayer. The maximum of the Reynolds stresses u',v' and w' decrease by 39%, 29% and 52%, respectively. This is a greater decrease than that of the wall oscillation case (with a reduction of 33%, 22% and 40%). A comparison of the DNS to the analytical solution of the mean spanwise velocity component gives good agreement, suggesting that, given the wavelength of the forcing used, the mean spanwise velocity is similar to that of the laminar flow, even in the boundary layer.

Skote [2012] expanded their previous data [Yudhistira and Skote, 2011], performing boundary layer simulations of wall oscillation, retaining the features of the earlier setup. The maximum wall velocities studied were lower with $W_m^+ = 6$ and 12, while the time period was fixed to $T^+ = 132$, these gave maximum DR values of 19% and 29%, respectively. Another simulation of $W_m^+ = 11.3$ and $T^+ = 67$ was performed to compare with available experimental data. A similar spatial development of drag reduction was observed, however slightly higher values were observed in the DNS. Comparing the DR value at different streamwise locations in the boundary layer, some effect of Reynolds number is observed. The drag reduction was slightly

lower in the boundary layer simulation. When compared to the channel flow, the net power saving of the boundary layer DNS is positive and also lower than the channel flow case for $W_m^+ = 6$. For the higher W_m^+ cases a negative net power saving is observed, although these are higher than the channel flow results. The temporal and spatial transients of the streamwise velocity gradients are compared using relationship $t = \frac{x}{U_w}$, giving a reasonable agreement. The variation of maximum $u-$rms value is compared in space and time evolution, showing a non-monotonic development in the temporal transient as compared to the monotonic variation in space. The mean of the spanwise velocity is also seen to compare well with the laminar solution as seen in channel flow.

A comparison between the the temporal and spatial forcings was undertaken by Skote [2013] via a DNS study of boundary layer flows. Two maximum forcing velocities were used of $W_m^+ = 6$ and $W_m^+ = 12$ using control parameters $T^+ = 132$ and $\lambda^+ = 1320$ for the temporal and spatial forcings. This comparison assumes convection velocity of $\mathcal{U}_w^+ = 10$. A larger drag reduction and power saving was found for the standing wave in agreement with channel flow results, and a larger power saving was seen for the lower W_m^+ cases. One interesting result of this study was that the spanwise Reynolds stress is considerably lower for the spatial forcing, whereas the other stresses showed similar magnitudes. Streamwise oscillations in the spanwise fluctuations were seen in the spatial forcing which was attributed to the spanwise Reynolds stress production. This production comes from the positive contribution wall-normal gradient of spanwise velocity term, which is also evident in the temporal forcing, but is reduced by a negative contribution of the streamwise gradient of spanwise velocity term.

Lardeau and Leschziner [2013] studied a boundary layer subjected to spanwise wall oscillations, where the Reynolds number at the onset of the forcing was $Re_\tau = 520$. A range of DNS simulations with forcing periods from $T^+ = 80$ to 200 were performed. The drag reduction was found to be lower than in channel flow by

about 5%-7%, and the largest DR occurred at $T^+ = 80$. The large oscillations in the skin-friction are considerably weaker than in the channel flow. Oscillations in the skin-friction and turbulence statistics are seen in the initial transient and are believed to be caused by the onset of the actuation and are propagated downstream. The maximum drag reduction is reached quickly after the start of the forcing region and recovers quickly after the forcing region. The difference in the drag reduction between channel and boundary layer flows is deemed to be related to the difference in length scales used. Where the channel flow is non-dimensionalised by the half-channel height, the boundary layer utilises the boundary layer thickness. These are physically different quantities, but there may also be a contribution from the differences in the outer scales in the two flow regimes.

2.4 Experimental Work

Laadhari et al. [1994] performed the first experimental investigation of spanwise wall oscillation. The effect of the forcing was studied over a spatially developing boundary layer, by fixing the amplitude and varying the oscillation frequency. The control method reduces the mean streamwise velocity U^+ in the region $y^+ < 30$. The velocity fluctuations showed a reduction from the no-control case for $y^+ < 200$ and a 50% reduction in $-\overline{uv}$ is seen.

A similar study was performed by Choi et al. [1998], in which a boundary layer subjected to various wall oscillation frequencies. In the viscous sublayer there is little variation in the mean velocity, scaled by wall units, whereas the velocity is increased with oscillation frequency in the outer region. Conversely the near-wall gradient is reduced more by greater frequencies when scaled by outer units. The intensity of u' is decreased by the wall motion, however the fluctuations in the outer region are unchanged. The skewness and flatness are increased in the near-wall region due to the increase in thickness of the viscous sublayer. The variation of

skin-friction over the oscillating plate shows that there is a long initial transient which prevents the forced flow from becoming fully developed. The drag reduction is also reduced past the trailing edge of the oscillating region, where a recovery to the uncontrolled case occurs. The streak spacing is increased by the spanwise forcing and flow visualisation shows a tilting of longitudinal vortices.

The length of the moving plate in experiments undertaken by Ricco and Wu [2004] was considerably longer, and hence the oscillatory flow became fully developed. The initial transient is seen over the first 3-4 boundary layer thicknesses of the forced plate. The DR value then plateaus to the end of the moving region, where it decreases to zero over 2δ downstream of the plate. The statistics in the wall normal direction were calculated for two control cases, one with $W_m^+ = 9$ and $T^+ = 83$ and the other with $W_m^+ = 18$ and $T^+ = 42$. Scaling with u_τ showed a reduction of U^+ in the near-wall region with $y^+ < 20$. When scaled by $u_{\tau,0}$ the u' profile is reduced for $y^+ < 20$, above which the profiles appear to collapse onto a single curve. The maximum of the v profile, scaled by u_τ is increased to $y^+ \approx 200$ from the no-control case, which has maximum at $y^+ \approx 150$. This is similar behaviour to that of u', whose maximum increases from $y^+ \approx 15$ to $y^+ \approx 25$. The Reynolds stress, $-\overline{uv}$, is seen to reduce more than the u and v fluctuations individually suggesting a disruption in the dynamical link of the turbulent structures. This idea is supported by the decrease in correlation between u and v, especially in the near-wall region. The effect of the Reynolds number was also explored, with data presented for $Re_\theta = 500, 950$ and 1400. Little variation was seen in the value of DR and any change presented was considered to be within the experimental uncertainty.

The effect of streamwise travelling waves of spanwise velocity was investigated by Auteri et al. [2010]. A pipe flow was studied with discrete rotating sections, which were used to emulate travelling waves with various wavelengths and time periods. Three wave varieties in space were chosen with $\kappa_x^+ = 0.0123, 0.0082$ and 0.0041, testing numerous values of ω^+ for the given spacial waves. Although qualitatively

similar to the numerical results, the maximum drag reduction was smaller (33% as opposed to 48% in DNS) and no drag increase is observed, however a significant drop in DR occurs around $c^+ = 12$. Another notable difference is that there are two peaks of maximum drag reduction for the larger κ_x^+ curve. The discrepancy between the experiment and DNS results is associated with the discretisation of the spatial waveform into a step function. An approximation of the DNS data to a wave of such a form shows the introduction of symmetry between positive and negative ω^+, the reduction in DR and lack of drag increase region.

2.5 Streak Instability

In near-wall turbulent flows long regions of low speed fluid is commonly observed in both experimental and numerical studies [Kline et al., 1967]. These structures, referred to as low-speed streaks are elongated in the direction of the mean flow. Very close to the wall the spanwise spacing of the streaks are measured to have an average distance of 100 wall units [Smith and Metzler, 1983], although the spacing increases as the measurement plane is moved away from the wall. These near-wall streaks have an average length of approximately 1000 wall units.

The existence of the low-speed fluid is attributed to the wall-normal motions within the shear-layer which move the lower speed fluid away from the wall. The streak patterns are seen to be wavy in nature. The assymmetry within streaks is deemed to be an important feature in the evolution of near-wall structures [Johansson et al., 1991]. Schoppa and Hussain [1998] used numerical study to correlate the location of the near-wall streaks to the coherent vortices. This is illustrated in figure 2.1 and shows how the angling of the structures causes the wavy streak patterns.

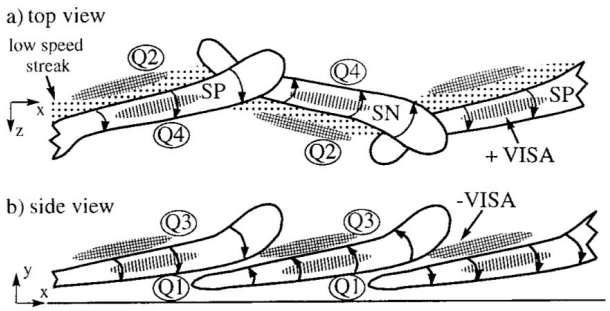

Figure 2.1: Positioning of coherent vortices in relation to the streak pattern [Schoppa and Hussain, 1998]. Q1-Q4 show positions of the quadrant events discussed in section 2.6.

2.6 Quadrant Analysis

The Reynolds shear stress, which is directly linked to the drag reduction, is produced by the near-wall coherent structures [Robinson, 1991]. The near-wall streaks separate some of these events into positive and negative streamwise velocity fluctuations, corresponding to the high and low-speed streaks. These streamwise velocity variations can be subdivided further into positive and negative wall normal variations [Lu and Willmarth, 1973]. The four different quadrants are explained in table 2.1. The second and fourth quadrants have positive contribution to the Reynolds stress and are commonly referred to as ejections and sweeps, respectively.

Quadrant	Velocity Fluctuations	Description
First quadrant ($Q1$)	$u' > 0$ and $v' > 0$	Outward motions of high-speed fluid.
Second quadrant ($Q2$)	$u' < 0$ and $v' > 0$	Outward motions of low-speed fluid.
Third quadrant ($Q3$)	$u' < 0$ and $v' < 0$	Inward motions of low-speed fluid.
Fourth quadrant ($Q4$)	$u' > 0$ and $v' < 0$	Inward motions of high-speed fluid.

Table 2.1: Explanation of quadrant definitions.

2.7 Flow Visualisation

Initial attempts at coherent structure visualisation commonly focussed on simple flow parameters such as pressure minima or vorticity magnitude. Using pressure minima can cause errors from either minima which do not involve vortical motion or the elimination of vorticity based minima from viscous effects. Using $|\omega|$, however, fails in shear flows as the shear contributes to the vorticity measured.

The eigenvalues (σ) of the velocity gradient tensor ∇u satisfies the characteristic equation:

$$\sigma^3 - P\sigma^2 + Q\sigma - R = 0,$$

where $P = u_{i,i}$, $Q = \frac{1}{2}(u_{i,i}^2 - u_{i,j}u_{j,i})$ and $R = \det(u_{i,j})$ are the three invariants of ∇u. Hunt et al. [1988] used a positive second invariant Q to define a vortex core.

Chong et al. [1990] noted that if ∇u has complex eigenvalues at a spatial location then the the velocity distribution is either closed or spiralled around that point, moving with its reference frame. This occurs when:

$$\Delta = \left(\frac{1}{3}Q\right)^3 + \left(\frac{1}{2}R\right)^2 > 0.$$

Let S and Ω denote the symmetric and antisymmetric components of ∇u, respectively, such that:

$$S_{i,j} = \frac{1}{2}(u_{i,j} + u_{j,i}) \text{ and } \Omega_{i,j} = \frac{1}{2}(u_{i,j} - u_{j,i}).$$

Using these definitions Q can be written as $\frac{1}{2}\left(||\Omega||^2 - ||S||^2\right)$, where $||A||^2 = \mathrm{tr}(AA^T)$. Physically, the values of $||S||^2$ and $||\Omega||^2$ correspond to the shear strain rate and vorticity magnitude, respectively. From this notation the $Q > 0$ criterion can be considered as defining a vortex core as a region in which the vorticity magnitude is greater than the shear strain rate.

Similarly, Melander and Hussain [1993] defined a vortex core as a region with

$N_k > 1$, where N_k is defined [Truesdell, 1953] by:

$$N_k = \frac{||\Omega||}{||S||}$$

Note that although this limit of $N_k > 1$ is equivalent to the $Q > 0$ condition, the N_k value is independent of the strength of the vorticity, and can therefore be considered as a measure of the quality of the rotation.

The λ_2 criterion presented by Jeong and Hussain [1995] is derived from the use of pressure minima to visualise vortices. By calculating a matrix equation for the pressure hessian with the unsteady straining and viscous effects removed, a more accurate representation of a vortex core is derived. It is shown that the existence of two negative eigenvalues of the matrix $S^2 + \Omega^2$ constitutes a vortex core. If $\lambda_1 \geq \lambda_2 \geq \lambda_3$ are the eigenvalues of $S^2 + \Omega^2$ then two negative eigenvalues occur if λ_2 is negative.

Following the development of a vortex identification scheme in Jeong and Hussain [1995], Jeong et al. [1997] went on to study coherent structures in uncontrolled channel flow. The profile of $\overline{\lambda_2}$ was calculated, where the average is taken over time and the $x - z$ plane. This showed that there is a balance in the λ_2 values between the region inside and outside of the vortex cores. A strong correlation between $-\lambda_2$ and $|\omega_x|$ in the region $10 < y^+ < 40$ highlights the strong streamwise alignment of near-wall structures. An average near-wall structure was educed for both structures with positive and negative vorticity. It is found that the structures each have an inclination of 9° and a tilting angle of 4° in opposite directions. The spatial relationship between the two structures is found via correlation and ensemble averaging of ω_x. The conditionally averaged velocity fields are also presented and the correlation between the streak and structure location is shown.

2.8 3D Turbulent Boundary Layers

A turbulent boundary layer is considered to be three-dimensional if the mean flow direction varies with the distance from the wall. There are many previous studies of such type, and can either be driven by a spanwise pressure gradient or moving wall in order to create the spanwise shear. In the case of wall motion a stationary or opposing wall is often present to ensure spanwise shear. The spanwise wall forcing techniques which are the focus of the current work are similar, but have a periodicity and constantly varying wall velocity.

Experimental works have been performed using various methods to create the spanwise shear. Anderson and Eaton [1989] hypothesised that the shear caused by the spanwise pressure difference would affect the different vorticity directions in different ways. Asymmetry was found in the conditional averaging around ejection and sweep events by Littel and Eaton [1994]. This suggested that strong sweep events are associated with rotation opposed to the spanwise shear and strong ejections are related to rotation enhanced by the spanwise wall motion. Kang et al. [1998] performed a similar averaging, separating contributions to the local velocity by quadrant analysis. This indicated that the asymmetry was related to the events which produce negative Reynolds shear stress, and that the events which caused positive $\overline{u'v'}$ were symmetric.

Coleman et al. [1996] performed three variations of simulation to understand the effect of using different methods to create the near-wall shear. Two of which use wall motion, either abruptly moving or stopping the wall. The third uses a transverse strain setting $\frac{\partial U}{\partial x} = -\frac{\partial W}{\partial z}$. The greatest drag reduction was seen when the shear was applied in the region $5 < y^+ < 15$. Le et al. [2000] used an impulsive spanwise moving wall with velocity $W_s^+ = -8.5$. The drag is seen to initially decrease before increasing. Two angles are calculated; the mean velocity gradient, γ_s, the turbulent

shear stress, γ_τ, angles. These are defined as:

$$\gamma_s = \arctan\left(\frac{\partial W/\partial y}{\partial U/\partial y}\right) \tag{2.7}$$

$$\gamma_\tau = \arctan\left(\frac{\overline{v'w'}}{\overline{u'v'}}\right) \tag{2.8}$$

The lag angle, quantified by $\lambda = \gamma_s - \gamma_\tau$, is initially large but reduces greatly as the streamwise shear recovers. This compares with calculations in previous experiments [Littel and Eaton, 1994]. Conditional averaging around sweeps and ejections showed that ejections were stronger than sweeps when $\omega_x'^+$ was positive, whereas sweeps were stronger than ejections with ω_x' negative. This was attributed to the near-wall tilting angle of the coherent structures, caused by the spanwise shear.

Jung and Sung [2006] simulated the flow through a concentric annulus via DNS, in which the inner pipe is rotating perpendicular to the mean flow direction. Using the coherent structure eduction method [Jeong et al., 1997] an average λ_2 structure was found for both positive and negative $\omega_x'^+$. The negative vortex, which opposed the wall motion, was lifted up, away from the wall, and therefore had larger inclination angle of 13°, compared to the slightly decreased value of 8° for the positive vortex. The rotation of the inner pipe affected the upstream ends of the structures causing an angling of both in the same direction. The tilting angle was stronger in the positive vortex at $-20°$, whereas the negative vortex had an angle of $-8°$. Studying the field of Reynolds shear stress around the averaged structures shows that the crossflow reduces strong sweeps from the negative vortex and strong ejections from the positive one.

Studying a three-dimensional flow caused by adverse pressure gradient on a Couette flow, Holstad et al. [2010] also looked at equilibrium effects. This work focused on channel flow to remove any implications of the centrifugal force. The angles studied in Coleman et al. [1996] were plotted, as well as the mean velocity angle and the intensity angle. It was seen that the intensity angle is larger than

the mean velocity angle, whereas the turbulent shear stress angle is smaller. The intensity and turbulent shear stress angles are similar toward the channel centre and vary almost linearly. The mean velocity and mean velocity gradient angles are similar in the near wall region, but separate as the velocity gradient tends to zero near the upper wall. Studying the vorticity showed that ω_x is increased in the buffer region from the 2D flow. This was attributed to the mean shear in the spanwise directions which implies an increase in the fluctuations in this direction. For the same reason the spanwise vorticity fluctuation is reduced, and the wall-normal fluctuation unchanged.

2.9 Summary of Spanwise Wall Forcing

Wall oscillation can be determined by two parameters; the maximum wall velocity W_m and the temporal period $T = \frac{2\pi}{\omega}$. For a fixed W_m the the drag reduction has a maximum at around $T^+ = 100 - 125$ [Jung et al., 1992]. At $Re_\tau = 200$ with $W_m = 0.8$ a maximum DR of 40% was found. As T^+ becomes larger than this optimum, the drag reduction decreases [Akhavan et al., 1993]. At $W_m^+ = 12$ there is even drag increase for large T^+ [Quadrio et al., 2009]. Fixing $T^+ = 100$, the drag reduction was seen to increase monotonically with W_m [Baron and Quadrio, 1996]. This increase plateaus at about $W_m^+ = 16$ [Choi et al., 2002]. The drag reduction is commonly found to be lower in experimental studies of wall oscillation [Choi et al., 1998; Ricco and Wu, 2004; Gouder et al., 2013]

Applying a standing wave of spanwise wall forcing at the wall can achieve a greater drag reduction than the wall oscillation method for a fixed W_m^+ [Viotti et al., 2009]. At $W_m^+ = 12$ the optimum standing wavelength forcing uses a wavelength of $\lambda^+ = \frac{2\pi}{\kappa_x}$ of 1000-1250. A drag reduction of 45% is achieved at the optimum. A convection velocity of $\mathcal{U}^+ = 10$ was used to show a qualitative similarity between the standing wave and spanwise wall forcing. If the wave of wall forcing is made to travel

in the streamwise direction, the DR can be increased still (for fixed $W_m^+ = 12$). A drag reduction of 48% is achieved as compared to 38% for the optimal wall oscillation case and 45% for the standing wave case with the same maximum wall velocity [Quadrio et al., 2009]. A studied of various combinations of ω and κ showed that the largest drag reduction is found from forward travelling waves. A large region of drag increase is also found when the forward travelling waves have wave speed $0.35 < c = \frac{\omega}{\kappa_x} < 0.6$. The results from this study are shown in figure 2.2.

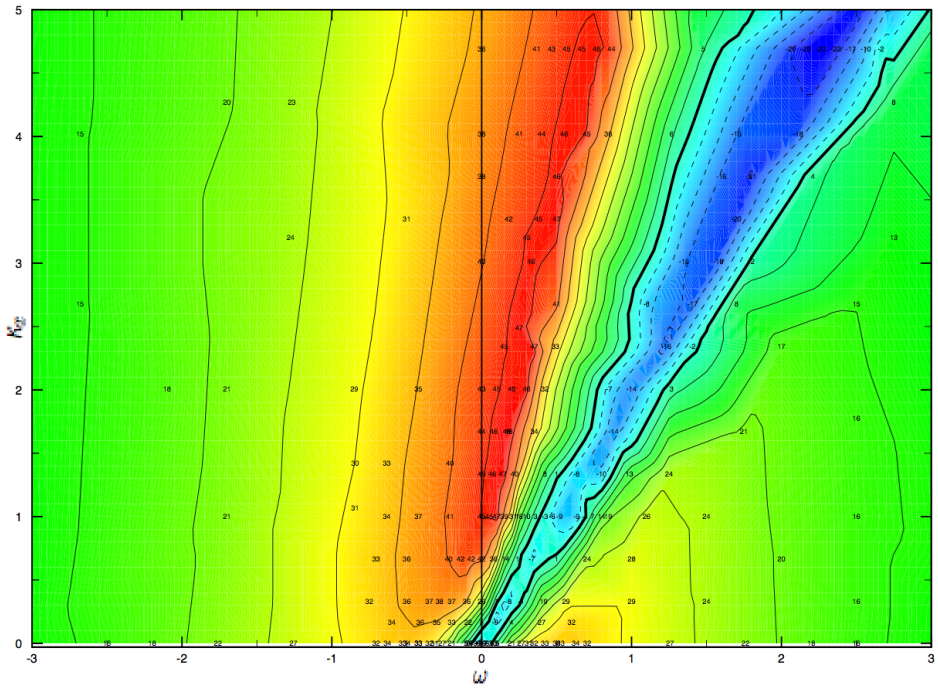

Figure 2.2: Contour plot of DR at $Re_\tau = 200$ from Quadrio et al. [2009].

Other wall forcing techniques such as; spanwise travelling Lorentz forcing [Du and Karniadakis, 2000; Du et al., 2002] and spanwise travelling waves of of a flexible wall [Zhao et al., 2004], have also shown evidence of reasonable drag reduction. However, the current study is restricted to wall forcing embodied by the streamwise travelling wave definition.

As the Reynolds number is increased the drag reduction for the optimal wall oscillation case ($T^+ \approx 100$) decreases [Ricco and Quadrio, 2008]. This effect was

further highlighted by Touber and Leschziner [2012] in which DNS at $Re_\tau = 400, 500$ and LES at $Re_\tau = 1000$ were performed. Agostini et al. [2014] performed DNS at $Re_\tau = 1000$ and suggested that the drag reduction scaled with $Re_\tau^{-0.2}$. This is much faster decay than the $Re_\tau^{-0.04}$ suggested by the high Reynolds number approximations of Belan and Quadrio [2013]. At the time the current work was performed the Reynolds number study was limited to single (or few) forcing parameters and the overall effect on the optimal parameters is not well known. Recently an investigation by Gatti and Quadrio [2013] used minimal channel flow to show that the scaling of the travelling wave forcing was considerably different for different combinations of the forcing parameters ω^+ and κ_x^+.

The S^+ parameter [Choi et al., 2002; Ricco and Quadrio, 2008] relates the input parameters of the wall oscillation forcing to the drag reduction. The S^+ parameter is effective for $T^+ < 150$ but shows an over-prediction of DR above this value. The S^+ parameter is derived from the laminar Stokes' solution. Touber and Leschziner [2012] showed that at $T^+ = 100$ the plane averaged spanwise velocity profile compares well to the Stokes' solution, but at $T^+ = 200$ a large deviation from the laminar solution occurs. This is similar to the turbulent oscillation seen in high Reynolds number oscillatory flows [Jensen et al., 1989; Sarpkaya, 1993]. Touber and Leschziner [2012] also noted that the Reynolds number effect is not accounted for within the S^+ parameter definition.

The application of effective wall oscillation forcing shows a reduction of the Reynolds stresses [Jung et al., 1992]. This agrees with the behaviour of 3D turbulent boundary layers, in which the Reynolds stresses on a swept wing are less than in the 2D boundary layer [Bradshaw and Pontikos, 1985]. There is also an increase in near-wall skewness and kurtosis for both channel flow [Baron and Quadrio, 1996; Choi and Clayton, 2001] and pipe flow [Nikitin, 2000]. When the wall oscillation is initially applied, there is a delay in the response of the Reynolds stresses, most notably in v' [Ricco and Quadrio, 2008]. The production term P_{33} becomes large

within the transient and returns to 0 for low T^+. Ricco et al. [2012] showed that, when the forcing period is such that the skin-friction oscillates over the period, the spanwise production also becomes large at certain points over the phase. Skote [2013] found that, when the temporal and spatial forcings are applied to a turbulent boundary layer, the streamwise gradient of spanwise velocity can have a negative contribution to this production of the spanwise fluctuations. In equilibrium, the production of kinetic energy is reduced [Dhanak and Si, 1999].

The mechanism of turbulence is a much debated topic. Schoppa and Hussain [1998] argued that the turbulence cycle as a generation of low-speed streaks by the near-wall structures, followed by the decay and regeneration through the streak instability. Akhavan et al. [1993] explained the reduction in turbulent activity created by the wall oscillation as a shift of the near-wall vortices relative to the wall layer streaks, thus breaking down the mechanism to sustain turbulence. The angling of near-wall streaks was visualised by Touber and Leschziner [2012]. The orientation of the vorticity field is also modified in the near-wall region by the spanwise vorticity induced by the wall motion [Bandyopadhyay, 2006]. The wall oscillation causes a reduction in the duration and strength of sweep events [Choi, 2002; Dhanak and Si, 1999] and the frequency of the sweeps reduced with the tilting angle. [Choi, 2002] showed that a reduction in streamwise velocity reduces the stretching of vortices and hence limiting the burst events. The drag reduction is also associated with the widening of near-wall streaks [Touber and Leschziner, 2012], a phenomenon also seen in rotating pipe flow [Orlandi and Fatica, 1997].

Through linear modelling of wall oscillations [Jovanović, 2008; Moarref and Jovanović, 2012] and travelling waves [Duque-Daza et al., 2012], a good correlation to the drag reduction was achieved in these forcing methods. The latter showed that the relationship between drag reduction and the forcing parameters of the streamwise travelling wave control technique can be predicted by calculating the magnitude of the transient growth of a disturbance within the flow. This suggests

that a linear mechanism is important in the drag reduction. Blesbois et al. [2013] used general optimum perturbation theory showed that the streak amplification and destruction from the spanwise shear of wall oscillation forcing conform to a time scale of $t^+ \approx 80$. This suggests the reason for a decay in performance above $T^+ \approx 100$. Belan and Quadrio [2013] used a similar model to Moarref and Jovanović [2012] with a RANS approach where the eddy viscosity is calculated from DNS data of the no-control case. A predictor method was employed eliminating the need for high Reynolds number DNS data and was used to calculate the decay in the drag reduction expected over a large Reynolds number range. The decay in drag reduction was shown to scale as $Re_\tau^{-0.04}$ over a range of $100Re_0$.

Chapter 3

Numerical Methods

This chapter describes the numerical procedure which is employed in the simulations throughout this thesis. A two-dimensional parallelisation has been performed and shows a significant improvement in the performance of the DNS code. This allows for the increase in the Reynolds number of simulations performed in this body of work. A brief outline of the statistical averaging for the various forcing waveforms is also outlined in this chapter.

3.1 The Evolution of Fractional Step Methods

To ensure highly accurate numerical solutions, the current work employs direct numerical simulation of incompressible flow. This, therefore, requires a fine grid resolution to ensure that the smallest scales of fluid motion are resolved. The incompressible Navier-Stokes equations (3.1) in three dimensions are solved directly, with a requirement to satisfy the continuity equation (3.2):

$$\frac{\partial u_i}{\partial t} + \frac{\partial}{\partial x_j} u_i u_j = -\frac{\partial p}{\partial x_i} + \frac{1}{Re} \frac{\partial^2}{\partial x_j^2} u_i, \tag{3.1}$$

$$\frac{\partial u_i}{\partial x_i} = 0. \tag{3.2}$$

One early solver, proposed by Harlow and Welch [1965], used explicit finite differences. It was shown that, by taking the divergence of the momentum equations, the pressure can be calculated from the current velocity field such that the continuity equation from the subsequent time step is satisfied. This work also introduced the notion of a staggered grid, in which the velocities are defined at the cell face and the pressure is defined in the cell centre. The advantage of this is that no pressure boundary conditions are required and artificial pressure oscillations are avoided. It is possible to remove the requirement for staggering the grid points by using spectral element methods introduced by Patera [1984], but these will not be discussed here.

The explicit method used in the aforementioned scheme causes heavy limitations on the time step size used. The limit of the numerical stability can be derived in the form of the CourantFriedrichsLewy (CFL) condition, which relates grid resolution, time step size and velocity:

$$\Delta t \sum_{i=1}^{3} \frac{u_i}{\Delta x_i} \leq C_{max}. \tag{3.3}$$

The upper bound, C_{max}, is dependent on the solution procedure and is a useful way to compare the stability of the problem. It is important to note that the accuracy of the solution is not implied from this condition, hence it must be tested using numerical investigation.

Chorin [1967] used artificial compressibility in the continuity equation to allow for the use of implicit discretisation. The drawback of this method is that, although sound for steady-state solutions, certain unsteady problems have a huge effect on stability, as shown by Steger and Kutler [1977]. A semi-implicit fractional step method was presented by Kim and Moin [1985], which uses an explicit Adams-Bashforth method for the convection and implicit Crank-Nicolson for the diffusive terms. An intermediate velocity field, $\hat{u}$, is first calculated from the momentum equation and then pressure is calculated via the Poisson equation. Finally, the

velocity for the next time step is found by updating $\hat{u}$ using the pressure gradient. One useful feature in this procedure is the splitting of a large sparse matrix inversion to three tridiagonal matrix inversions, which is also utilised in later solvers. A further modification to the solver was suggested by Le and Moin [1991], which used a predictor- corrector type scheme as it allows for a higher stability limit (CFL= $\sqrt{3}$), based on the full time step. This applied a Runge-Kutta method, with explicit treatment of the convection and implicit treatment of the diffusion. The procedure divided each time step into three sub-steps, and could be implemented to solve the Poisson equation at only the final sub-step, thus reducing the computational cost.

Dukowicz and Dvinsky [1992] showed that a Crank-Nicolson discretisation removed the requirement for intermediate boundary conditions. An approximate factorisation is used to divide the problem into multiple steps. In a similar study Perot [1993] argued that the fractional step method is a continuous version of a block LU decomposition. By applying this discrete splitting technique a second-order method was developed without the requirement for intermediate velocity or pressure boundary conditions. It was also stated that a poor temporal accuracy found in previous studies was from the method itself, as opposed to the boundary conditions required.

3.2 Implicit Decoupling Procedure

The current in-house code employs the procedure developed by Kim et al. [2002]. The use of an implicit Crank-Nicolson scheme, which is second order in time, for both convection and diffusion reduces the stability dependence on the CFL condition. This allows for reasonably large time steps relative to the explicit and semi-implicit methods that came before. The splitting is based on block LU decomposition and hence there is no need for intermediate velocity or pressure boundary conditions. The code is tested by Talha [2012] and a comparison of the efficiency is performed

against the previously implemented procedure of Le and Moin [1991]. It is found that, due to the single solution per time step and the increase in time step, that the new implementation is less computationally expensive.

The procedure begins by discretising the Navier-Stokes equations:

$$\frac{u^{n+1}-u^n}{\Delta t}+\frac{1}{2}\left(Hu^{n+1}+Hu^n\right)=-Gp^{n+\frac{1}{2}}+\frac{1}{2Re}\left(Lu^{n+1}+Lu^n\right)+mbc, \quad (3.4)$$

$$Du^{n+1}=0+cbc, \quad (3.5)$$

where L, H, G and D are the discrete Laplacian, convective, gradient and divergence operators, respectively. The operators are defined only on the interior points and the boundary conditions are stored in the arrays mbc and cbc. The convective terms are non-linear as the velocities for the $(n+1)^{th}$ step are unknown. These are linearised using Beam and Warming [1978] so that the second order accuracy in time is maintained:

$$u_i^{n+1}u_j^{n+1}=u_i^{n+1}u_j^n+u_i^nu_j^{n+1}-u_i^nu_j^n+O\left(\Delta t^2\right). \quad (3.6)$$

This can be rewritten in terms of the convective operator:

$$\frac{1}{2}\left(Hu^{n+1}+Hu^n\right)=\frac{1}{2}\left(\frac{\partial}{\partial x_j}u_i^{n+1}u_j^{n+1}+\frac{\partial}{\partial x_j}u_i^nu_j^n\right) \quad (3.7)$$

$$=\frac{1}{2}\left(\frac{\partial}{\partial x_j}u_i^{n+1}u_j^n+\frac{\partial}{\partial x_j}u_i^nu_j^{n+1}\right)+O\left(\Delta t^2\right) \quad (3.8)$$

$$=Nu^{n+1}+O\left(\Delta t^2\right). \quad (3.9)$$

Here, N is a new linear operator representing the convective discretisation and contains only the information from the n^{th} time step. The Navier-Stokes and continuity equations can be combined into a single matrix equation, using $\delta p^{n+\frac{1}{2}}=p^{n+\frac{1}{2}}-p^{n-\frac{1}{2}}$

and $M = N - \frac{1}{2Re}L$:

$$\begin{pmatrix} A & G \\ D & 0 \end{pmatrix} \begin{pmatrix} u^{n+1} \\ \delta p \end{pmatrix} = \begin{pmatrix} r \\ 0 \end{pmatrix} + \begin{pmatrix} mbc \\ cbc \end{pmatrix}, \tag{3.10}$$

$$A = \frac{1}{\Delta t}\left(I + \Delta t M\right), \tag{3.11}$$

$$r = \frac{1}{\Delta t}u^n - Gp^{n-\frac{1}{2}} + \frac{1}{2Re}Lu^n. \tag{3.12}$$

The matrices A, G and D as well as the vector r all contain known information from the previous time step. Hence an inversion of the matrix equation yields the velocity and pressure for the next step. This is a large sparse matrix problem and must be adapted in order to improve the efficiency of the method. Equation (3.10) is approximately factorised using an LU decomposition, and can then be divided into two equations:

$$\begin{pmatrix} A & 0 \\ D & -\Delta t DG \end{pmatrix} \begin{pmatrix} u^* \\ \delta p \end{pmatrix} = \begin{pmatrix} r \\ 0 \end{pmatrix} + \begin{pmatrix} mbc \\ cbc \end{pmatrix}, \tag{3.13}$$

$$\begin{pmatrix} I & \Delta t DG \\ 0 & I \end{pmatrix} \begin{pmatrix} u^{n+1} \\ \delta p \end{pmatrix} = \begin{pmatrix} u^* \\ \delta p \end{pmatrix}. \tag{3.14}$$

The error from the decomposition is in the form $\Delta t MG\delta p$. This is second order in time due to the fact that the change in pressure is used, and is multiplied by Δt. Using the terminology $\delta u^* = u^* - u^n$, the first line of equation (3.13) can be rewritten as:

$$A\delta u^* = -Au^n + r + mbc = R. \tag{3.15}$$

This can be written as a matrix expression which represents the individual velocity

components:

$$\frac{1}{\Delta t}\begin{pmatrix} I+\Delta tM_{11} & \Delta tM_{12} & \Delta tM_{13} \\ \Delta tM_{21} & I+\Delta tM_{22} & \Delta tM_{23} \\ \Delta tM_{31} & \Delta tM_{32} & I+\Delta tM_{33} \end{pmatrix}\begin{pmatrix} \delta u^* \\ \delta v^* \\ \delta w^* \end{pmatrix} = \begin{pmatrix} R_1 \\ R_2 \\ R_3 \end{pmatrix}. \tag{3.16}$$

A further LU decomposition, is shown to be second order in time, giving an approximate factorisation of the left hand side of equation (3.16):

$$\frac{1}{\Delta t}\begin{pmatrix} I+\Delta tM_{11} & 0 & 0 \\ \Delta tM_{21} & I+\Delta tM_{22} & 0 \\ \Delta tM_{31} & \Delta tM_{32} & I+\Delta tM_{33} \end{pmatrix}\begin{pmatrix} I & \Delta tM_{12} & \Delta tM_{13} \\ 0 & I & \Delta tM_{23} \\ 0 & 0 & I \end{pmatrix}. \tag{3.17}$$

This means that a series of three equations must be solved in the form $\frac{1}{\Delta t}(I + \Delta tM_{ii})\delta u_i^* = f_i$, where f is some function of previously calculated quantities. M_{ii} contains the derivatives with respect to x,y and z and can therefore be subdivided into blocks of three tridiagonal matrices M_{ii}^1, M_{ii}^2 and M_{ii}^3, respectively. Beam and Warming [1978] showed that an error, which is also second-order in time, is found when the three vector equations are written in the form:

$$\frac{1}{\Delta t}(I + \Delta tM_{ii}^3)(I + \Delta tM_{ii}^2)(I + \Delta tM_{ii}^1)\delta u_i^* = f_i. \tag{3.18}$$

The procedure, therefore, consists of 9 tridiagonal matrix inversions and the solution calculation of the Poisson equation.

3.3 Poisson Solver

The calculation of change in pressure, δp, appears in equation (3.13) in the form:

$$DG\delta p = \frac{1}{\Delta t}(Du^* - cbc) \tag{3.19}$$

This can be expanded, and expressed as the Poisson equation:

$$\frac{\partial^2(\delta p)}{\partial x^2} + \frac{\partial^2(\delta p)}{\partial y^2} + \frac{\partial^2(\delta p)}{\partial z^2} = \frac{1}{\Delta t}\left(\frac{\partial u^*}{\partial x} + \frac{\partial v^*}{\partial y} + \frac{\partial w^*}{\partial z} - cbc\right) = f, \tag{3.20}$$

where f is the right-hand side of the Poisson equation which can be calculated from the known intermediate velocity information. Given that, for channel flow, there is a uniform mesh in the x and z directions, and that we have periodic boundary conditions in these directions it is possible to take a two dimensional Fourier transform. A fast Fourier transform (FFT) is used which expresses the pressure variable as $\delta p = \sum_{x,z} \widehat{\delta p} \cdot e^{ik_x x} e^{ik_z z}$. When using central differences for the discretisation of the second-order derivative, the modified wavenumbers (which are found in the same way for x and z) are calculated as:

$$k_x(i) = \frac{\cos\left(\frac{2\pi i}{N_x}\right) - 2}{\Delta x^2}. \tag{3.21}$$

Equation (3.20), after applying an FFT, can be written:

$$-k_x^2 \widehat{\delta p} + \frac{\partial^2(\widehat{\delta p})}{\partial y^2} - k_z^2 \widehat{\delta p} = \hat{f}(k_x, y, k_z). \tag{3.22}$$

As $\widehat{\delta p}$ is dependent on y, and a central difference discretisation in y gives a simple tridiagonal matrix equation, with the influence of the wavenumbers in the diagonal. This can be solved with a 1D inversion algorithm in the wall-normal direction. The inverse transform is performed on the resulting vector, $\widehat{\delta p}$, in order to evaluate the change in pressure.

3.4 Parallelisation

The aim of the current work was to create an efficient parallel code to perform DNS of channel flow at increased Reynolds numbers. The method presented by Kim et al.

[2002], although an efficient algorithm, is slow and there is a limit of simulation size set by the memory requirements. The main drawback of this method, when considering parallelisation, is the need for one-dimensional banded matrix inversions which prevent division of the domain in the direction of the algorithm. This means that the domain must be split onto the individual processors in a 2D fashion. This is performed using the library developed by Li and Laizet [2010], which contains some useful subroutines for an MPI parallelisation strategy. It adopts the pencil structure shown in figure 3.1.

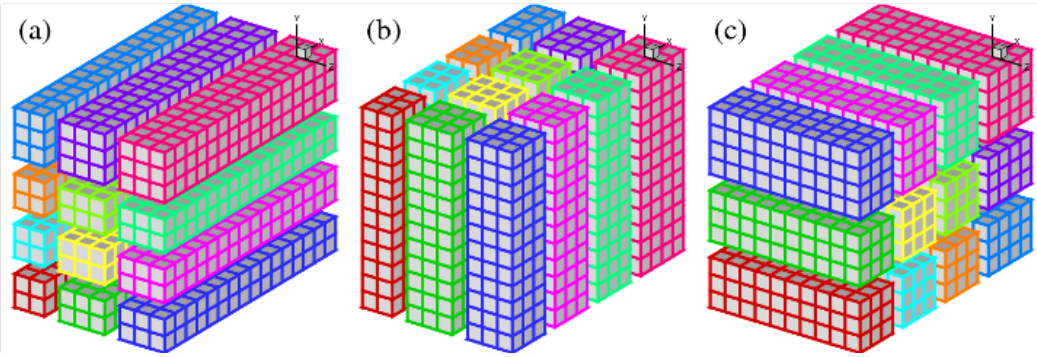

Figure 3.1: Pencil structure for parallelisation, the notation used is (a) x pencil (b) y pencil (c) z pencil.

The advantage of this structure is that, for transpositions between the x and y pencils, data is shared between groups of processors, so the communication can be performed in parallel between processors in the z direction. A similar situation occurs for transpositions between the y and z pencils. This is not the same when transferring from the z pencil to the x pencil or vice versa, however the most efficient transpositions of the data between these formats requires an intermediate step into the y pencil. The local data is also required in directions, other than that of the one dimensional algorithms, as the gradients must be calculated based on the currently known information. To avoid the requirements for unnecessary transpositions, the local data around the edge of the blocks in all three directions must be kept. Thus, two layers of halo cells are used and updated before its use, only when the interior

information is modified. An illustration of this is shown in figure 3.2.

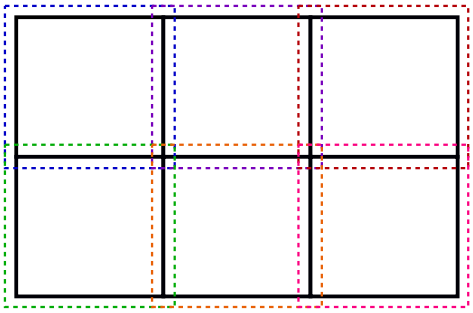

Figure 3.2: Halo cells for parallelisation

To solve the Poisson equation a two dimensional Fourier transform is required. This is performed by using FFTW in the x direction, then transposing through the y pencil into the z pencil, and applying FFTW in the z direction. This must in turn be transferred to the y pencil structure in order to perform a tridiagonal matrix inversion. The application of this set of transpositions must be treated carefully as there is a change from real to complex variables and hence a reduction in length of the data set. This applies after the first use of FFTW and reduces that dimension of the arrays in x from N_x to $\frac{N_x}{2} + 1$. The consequence of this is that transpositions after this must be performed using smaller arrays of complex type. After the calculation in y is performed a set of transposition steps in reverse to those performed initially, along with inverse Fourier transforms are necessary to return the correct change in pressure.

Reading and writing the data in serial is time consuming, especially in a parallel system, which requires a copious amount of data transfer before the information is written to file. When writing output, namely turbulent statistics or data fields, the frequency of this action causes heavy load in I/O. To reduce this effect, MPI I/O is used, which writes the data from each processor to file, simultaneously. The method to implement this is to calculate the blocks of continuous data contained on each processor, and the locations which each of those blocks fit into the

file to create an ordered data file which is independent of the number of processors or decomposition geometry used.

3.5 Algorithm

The following parallel algorithm is performed at each time step.

- Solve for u velocity:
  - Calculate $\Delta t R_1$ in the x pencil.
  - Transpose $x \rightarrow y$
  - Transpose $y \rightarrow z$
  - Calculate $\left(I + \Delta t M_{11}^3\right)^{-1} \Delta t R_1$
  - Transpose $z \rightarrow y$
  - Calculate $\left(I + \Delta t M_{11}^2\right)^{-1} \left(I + \Delta t M_{11}^3\right)^{-1} \Delta t R_1$
  - Transpose $y \rightarrow x$
  - Calculate $\delta u_1^{**} = \left(I + \Delta t M_{11}^1\right)^{-1} \left(I + \Delta t M_{11}^2\right)^{-1} \left(I + \Delta t M_{11}^3\right)^{-1} \Delta t R_1$
- Solve for v velocity:
  - Calculate $\Delta t R_2^{**} = \Delta t (R_2 - M_{21} \delta u_1^{**})$ in the x pencil.
  - Transpose $x \rightarrow y$
  - Transpose $y \rightarrow z$
  - Calculate $\left(I + \Delta t M_{22}^3\right)^{-1} \Delta t R_2^{**}$
  - Transpose $z \rightarrow y$
  - Calculate $\left(I + \Delta t M_{22}^2\right)^{-1} \left(I + \Delta t M_{22}^3\right)^{-1} \Delta t R_2^{**}$
  - Transpose $y \rightarrow x$
  - Calculate $\delta u_2^{**} = \left(I + \Delta t M_{22}^1\right)^{-1} \left(I + \Delta t M_{22}^2\right)^{-1} \left(I + \Delta t M_{22}^3\right)^{-1} \Delta t R_2^{**}$

- Solve for w velocity:
  - Calculate $\Delta t R_3^{**} = \Delta t(R_3 - M_{31}\delta u_1^{**} - M_{32}\delta u_2^{**})$ in the x pencil.
  - Transpose $x \to y$
  - Transpose $y \to z$
  - Calculate $\left(I + \Delta t M_{33}^3\right)^{-1} \Delta t R_3^{**}$
  - Transpose $z \to y$
  - Calculate $\left(I + \Delta t M_{33}^2\right)^{-1} \left(I + \Delta t M_{33}^3\right)^{-1} \Delta t R_3^{**}$
  - Transpose $y \to x$
  - Calculate $\delta u_3^* = \left(I + \Delta t M_{33}^1\right)^{-1} \left(I + \Delta t M_{33}^2\right)^{-1} \left(I + \Delta t M_{33}^3\right)^{-1} \Delta t R_3^{**}$
- Find intermediate velocities:
  - Calculate $\delta u_2^* = \delta u_2^{**} - \Delta t M_{23}\delta u_3^*$
  - Calculate $\delta u_1^* = \delta u_1^{**} - \Delta t M_{12}\delta u_2^* - \Delta t M_{13}\delta u_3^*$
  - Calculate $u_i^* = u_i^n + \delta u_i^*$ for $i = 1, 2, 3$
- Solve Poisson equation for pressure:
  - Calculate $f = \frac{1}{\Delta t}(Du^* - cbc)$ in the x pencil.
  - Perform Fourier transform of f in the x direction.
  - Transpose $x \to y$
  - Transpose $y \to z$
  - Perform Fourier transform of f in the z direction.
  - Transpose $z \to y$
  - Calculate $\widehat{\delta p} = \left(-k_x^2 + \frac{\partial^2}{\partial y^2} - k_z^2\right)^{-1} \hat{f}$
  - Transpose $y \to z$
  - Perform inverse Fourier transform of $\widehat{\delta p}$ in the z direction.

- Transpose $z \rightarrow y$
- Transpose $y \rightarrow x$
- Perform inverse Fourier transform of $\widehat{\delta p}$ in the x direction to find δp.

- Update new velocities and pressure:
  - Calculate $u_i^{n+1} = u_i^* - \Delta t \frac{\partial}{\partial x_i} \delta p$ for $i = 1, 2, 3$ in the x pencil.
  - Calculate $p^{n+\frac{1}{2}} = p^{n-\frac{1}{2}} + \delta p$
  - Calculate turbulent statistics.
  - Write statistical data.

In the above we calculate the right-hand side of the velocity equations as:

$$R_i = \frac{1}{Re} L u_i^n - N u_i^n - \frac{\partial}{\partial x_i} p^{n-\frac{1}{2}} + mbc_i. \tag{3.23}$$

Also, the matrix M is defined by:

$$M_{ij} = N_{ij} - \frac{1}{2Re} L_{ij}, \tag{3.24}$$

where N_{ij} and L_{ij} are discretisations of the velocity u_i in direction x_j.

3.6 Scaling

The parallel code was tested on HECToR using two different grid sizes in order to understand the scaling. Figure 3.3 plots the time taken per iterations compared to the number of cores used to parallelise the simulation. The scaling is close to the ideal scaling, and only deviates slightly as the number of processors becomes large.

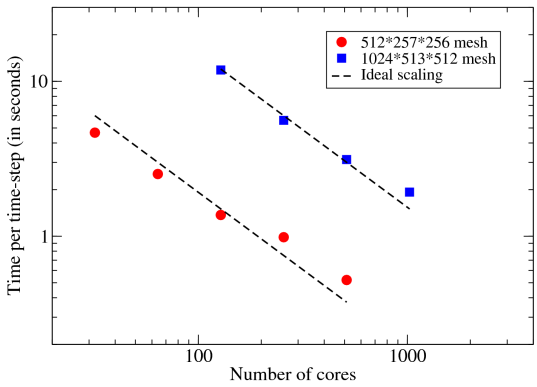

Figure 3.3: Scaling up to 1000 cores using two grid sizes.

3.7 Statistical Analysis

3.7.1 Triple Decomposition

When performing simulations on large data sets, multiple simulations are required in order to achieve a long time average of the turbulent statistics. The length of simulations is currently limited on both the local machine and on HECToR, hence the requirement to perform different simulations in which the output velocity and pressure fields are used as an input for the next. It was therefore necessary to develop a post-processing code in which the long time average from various continuous simulations is combined to calculate the turbulent statistics. This code requires various different averaging techniques to analyse the three waveforms involved in the streamwise travelling wave.

When calculating turbulent statistics for non-periodic channel flow, namely the no control case, it is common to adopt a double decomposition in the form $u = U + u'$, where U is the mean velocity averaged both temporally and spatially in x and z and u' is the fluctuation from the mean. With a periodic element, it is necessary to use a triple decomposition. This can be expressed as:

$$u = U + \tilde{u} + u'. \tag{3.25}$$

In this form U is the mean in space and time, as before, whereas $\tilde{u}$ is the purely periodic component of the mean (phase-averaged in time) and u' is the fluctuation from the periodic mean. It is important to note here that, although the periodic mean is removed from the fluctuation, the intensity of the fluctuation can vary over the period and hence the variation of the root-mean-square over the period can be of interest. An example of the format of presentation of this data is shown in figure 3.4.

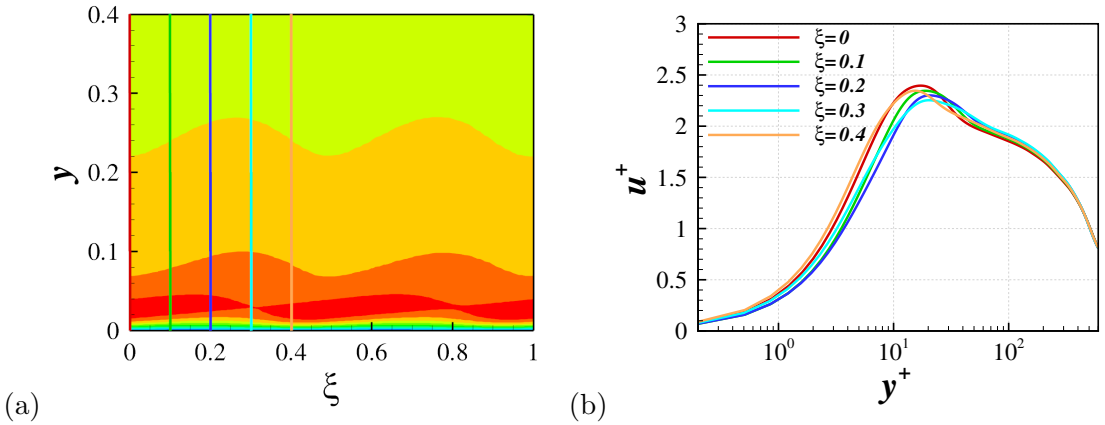

(a) (b)

Figure 3.4: Variation of u' over the period in 2D format (a) and 1D format (b) (plotted at the locations of coloured lines in (a)).

Figure 3.4a shows the rms fluctuation u' over a period, with the periodic and time-averaged mean removed. The x-variable is the normalised period, ξ, and depends on the form of control used. For the oscillating wall $\xi = t/T$ where t is the time and T is the period of oscillation. For the standing and travelling waves this is set to $\xi = \frac{x}{\lambda} - \frac{t}{T}$ (therefore $\xi = \frac{x}{\lambda}$ for the standing wave) as in Quadrio et al. [2009]. The coloured lines show the locations of the 1D plots presented in figure 3.4b, which shows the same data at five points in a half-period. This is due to the symmetry of the oscillation and independence of the direction of motion. Hence the variation loops twice over each period. A time-averaged and space-averaged 1D profile can also be obtained by taking the average over ξ. This, notably, is different from performing a double decomposition as the periodic component is also removed.

This is not always appropriate, given large oscillations in the statistics, but can give a useful insight into the general trend throughout the oscillation.

3.7.2 Data Output

To express the turbulent statistics in the above form the data must be saved in various different ways. As writing 3d velocity data is expensive in terms of memory, it is useful to calculate the statistics at each time-step and perform any necessary averaging to save the data. For the wall-oscillation cases, spatial averaging may be performed in both the streamwise and spanwise directions. Due to the dependency in time this 1D data must be written out for every (or possibly every k^{th}) time step. For the standing wave, the statistical information cannot be averaged in the streamwise direction, however time-averaging can be performed. Therefore xy-dependent 2D data can be written at the end of each simulation. For the streamwise travelling wave, spanwise-averaging can again be performed, however a simple time-average is not possible. Due to the similarity in the parameter:

$$\xi = \frac{x}{\lambda} - \frac{t}{T},$$

a spatial shift can be performed based on the time, and then a time average can be taken. Hence $(\xi - y)$-dependent 2D data can be written at the end of each simulation.

The post-processing code can then be used to gather the data from sequential simulations and either take the time average (in the standing or travelling wave cases) or concatenate the time dependent information (for the wall oscillation). The phase averaging can then be performed by first interpolating onto a grid (in either t,x or ξ) which has a number of grid points which is a multiple of the number of periods of the forcing. Then the phase average can be taken simply. This data (now in the same format independent of control method) can be written in 2D or 1D

format, as in figure 3.4.

Chapter 4

Preliminary Simulations

To carry out DNS correctly the simulations must be performed such that the solution is independent of domain size and resolution used. This means that the large scale and small scale structures must be captured correctly. In order to ascertain the necessary simulation parameters, the accuracy must be tested by checking that an increase in length or number of grid points does not affect the result. Any drag reduction or drag increase will affect the size of the near wall streaks, hence the comparison must also be performed with the application of control method.

4.1 Previous Study

	Domain Size	Grid Size	$\Delta x^+, \Delta y^+, \Delta z^+$
Jung et al. [1992]	$1.6\pi h \times 2h \times 1.6\pi h$	$64 \times 129 \times 128$	$15.7, -, 7.9$
Baron and Quadrio [1996]	$4.05h \times 2h \times 2.5h$	$54 \times 120 \times 60$	$15, -, 8.3$
Choi et al. [2002]	$4\pi h \times 2h \times \frac{4\pi}{3}h$	$128 \times 129 \times 128$	$19.6, -, 6.5$
Quadrio and Ricco [2004]	$21h \times 2h \times 4.2h$	$321 \times 129 \times 129$	$13, 0.8 - 5.4, 6.5$
Quadrio et al. [2009]	$6\pi h \times 2h \times 3\pi h$	$320 \times 160 \times 320$	$11.8, 0.7 - 4.1, 5.9$
Touber and Leschziner [2012]	$2\pi h \times 2h \times \pi h$	$128 \times 128 \times 128$	$9.7, 0.7 - 5.6, 4.8$

Table 4.1: Domain sizes and grid sizes of previous research.

An idea of the simulation parameters can be achieved from a brief literature review. The majority of previous work is confined to the Reynolds number $Re_\tau =$

200. Table 4.1 shows the domain sizes and resolutions used in the study of flow control by wall oscillation and streamwise travelling waves. The domain size is affected by large DR values as a lower skin friction would imply large structures and could affect independence of the periodic boundary conditions. This suggests that the use of large domain sizes in the x and z directions are an advantage. Due to the parallelisation, simulations of this size are reasonably easy to achieve. Another advantage of a large simulation size is that the length of time required for averaging can be reduced. To simulate streamwise varying waves, an integer number of waves must fit in to the domain length. A large streamwise length will therefore allow the study of the effect of larger wavelengths.

The effect of wall oscillation, especially in the z direction, would imply the requirement of fine resolution. This is because the large spanwise velocity must be captured correctly. Any angling of flow structures would also suggest a fine resolution in the x direction, as the smaller scale fluctuations, normal to the flow direction would have a component in the x direction.

As a base flow to investigate the mesh, domain and time step sensitivity at $Re_\tau = 200$, the domain length is chosen as $16h \times 2h \times 6h$ and the resolution is chosen as $320 \times 140 \times 240$. This gives grid spacings $\Delta x^+ = 10, \Delta y^+ = 0.4 - 6, \Delta z^+ = 5$. The effect of variation from the chosen simulation parameters is studied to obtain information on the accuracy. Three different combinations of the forcing parameters are used to analyse the propriety of the given domains and resolutions. These are chosen as the no control case (abbreviated to NC), the travelling wave with $\omega^+ = 0.02$ and $\kappa_x^+ = 0.008$, achieving a large drag reduction (abbreviated to DR) and the travelling wave with $\omega^+ = 0.18$ and $\kappa_x^+ = 0.016$, achieving a large drag increase (abbreviated to DI).

4.2 Domain Size Test

The domain size of the simulations must be large enough to capture the large scale structures so that independence is achieved over the direction of the periodic boundary conditions. Three cases are studied at fixed $Re_\tau = 200$ in order to understand the accuracy of the chosen domain size in the x and z direction. Table 4.2 shows the domain and grid sizes used and the values C_f found for the different forcing parameters studied. Note that the grid size is also doubled as the domain is extended to ensure that the same resolution is maintained. The values of C_f shows that there is very little effect of the change in size of the domain, suggesting that the dimensions from Case 0 are sufficient in resolving the large scale structures, even when the oscillation is applied. For all simulations C_f is maintained to within 0.5%, suggesting a highly accurate solution to the forced flow.

	Domain Size	Grid Size	$10^3 C_f$ (NC)	$10^3 C_f$ (DR)	$10^3 C_f$ (DI)
Case 0	$16h \times 2h \times 6h$	$320 \times 140 \times 240$	7.93	3.98	9.90
Case 1	$32h \times 2h \times 6h$	$640 \times 140 \times 240$	7.90	4.03	9.86
Case 2	$16h \times 2h \times 12h$	$320 \times 140 \times 480$	7.91	3.94	9.87

Table 4.2: Domain size tests performed at $Re_\tau = 200$.

Figure 4.1a shows that the mean velocity profiles are very similar for all three domains. For the no control and maximum drag increase cases there is almost no variation between any of the shear stress or rms profiles shown in figures 4.1, 4.2 or 4.3. The expected cases of interest are for the maximum DR as the value of u_τ is decreased. As the forcing reduces the drag, the Reynolds number is also decreased. This would normally be associated with an increase in the scale of the structures, in outer units, and would therefore require a larger domain to capture these structures correctly. The Reynolds shear stress is slightly different for the maximum drag reduction cases, shown in figure 4.1b, but this is an acceptable level of error. The u-rms profiles also show a small variation for the DR cases, figure 4.2a, whereas the

rms values for v and w are seen to be almost identical in figures 4.2b and 4.3a. The values of p-rms for the DR case with doubled domain length is slightly higher than the other two, but again has a reasonably small variation.

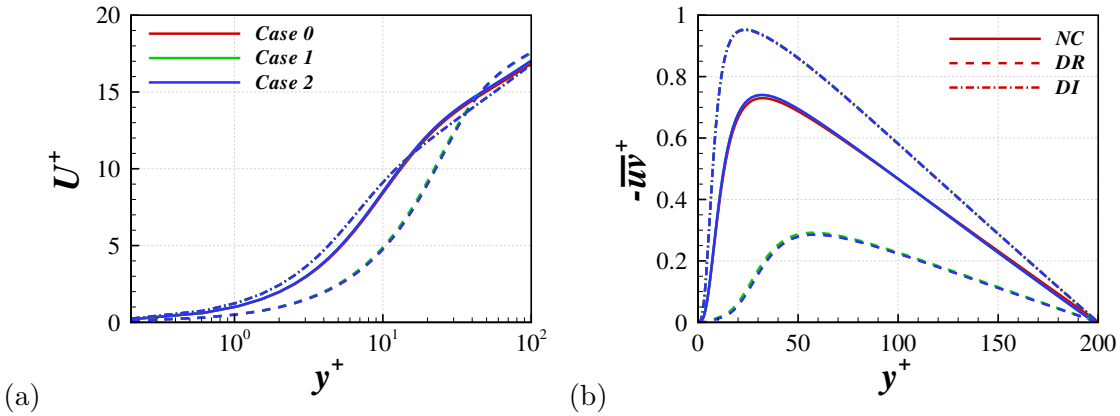

(a) (b)

Figure 4.1: Comparison of the mean velocity (a) and Reynolds stress (b) for the cases with different domain sizes (colours), using the no control case, maximum DR and maximum DI forcing (line types).

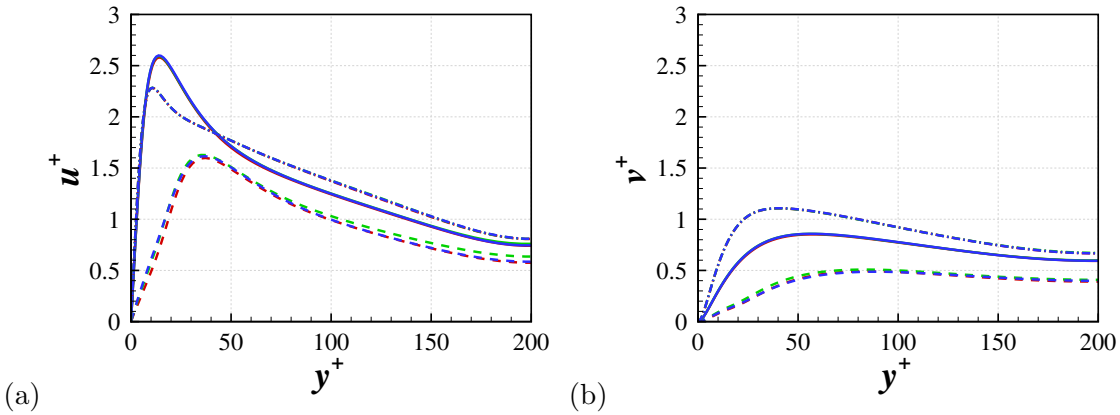

(a) (b)

Figure 4.2: Comparison of the root-mean-squared of u (a) and v (b) for the cases with different domain sizes, using the no control case, maximum DR and maximum DI forcing. Legend as in figure 4.1.

Overall, the base domain size of $16h \times 2h \times 6h$ appears to be reasonably good. The variation of DR achieved in all domain sizes studied is very small and the profiles of turbulent statistics do not vary significantly. Hence this domain size is concluded to be sufficiently accurate.

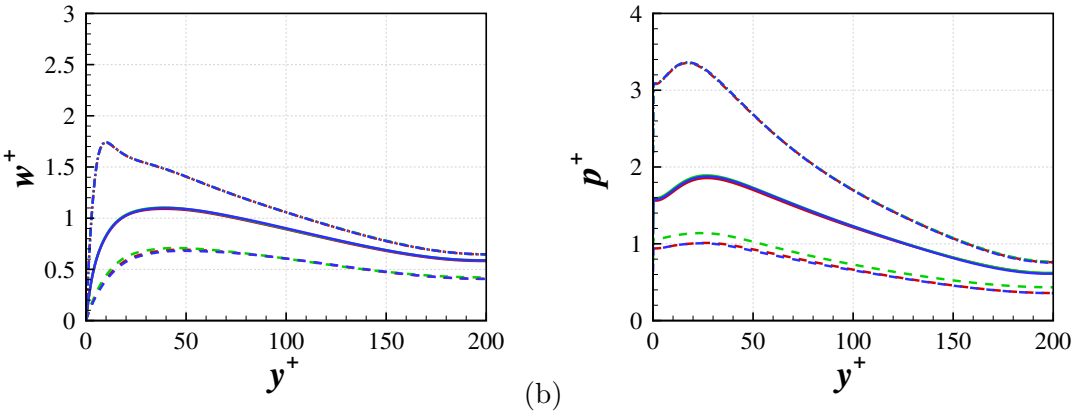

Figure 4.3: Comparison of the root-mean-squared of w (a) and p (b) for the cases with different domain sizes, using the no control case, maximum DR and maximum DI forcing. Legend as in figure 4.1.

4.3 Grid Resolution Test

The grid resolution which is chosen to perform DNS must be sufficiently small to resolve all the small scale structures. This means that it is also necessary to test that the number of grid points in each direction is sufficiently large. Table 4.3 shows the tests performed at $Re_\tau = 200$ to validate the resolution of the simulation. The number of grid points is doubled in the x, y and z directions and the skin-friction is again shown. It is clear that the C_f value is very similar between all four resolutions of the DI case. However, there is slight difference in the skin friction value of the no-control cases and the maximum drag-increase cases between the Case 0 and 1 resolutions. Although this difference appears large when studying the C_f values reported, this corresponds to an error in the drag-increase of only 1%. Considering that these resolutions are to be maintained at higher Reynolds number, computation time will be saved by using the coarser resolution, and an error in the DI of this level is acceptable.

Figure 4.4a shows that the mean profiles are similar when the resolution is increased in all three cases. The Reynolds shear stress, figure 4.4b, shows little variation for the no control and DR cases. There is a small difference in $-\overline{uv}$ for the

	Domain Size	Grid Size	$10^3 C_f$ (NC)	$10^3 C_f$ (DR)	$10^3 C_f$ (DI)
Case 0	$16h \times 2h \times 6h$	$320 \times 140 \times 240$	7.93	3.98	9.90
Case 1	$16h \times 2h \times 6h$	$640 \times 140 \times 240$	7.77	3.98	9.62
Case 2	$16h \times 2h \times 6h$	$320 \times 280 \times 240$	7.91	4.00	9.92
Case 3	$16h \times 2h \times 6h$	$320 \times 140 \times 480$	7.92	3.94	9.69

Table 4.3: Resolution tests performed at $Re_\tau = 200$.

maximum drag increase simulation. This is the forcing expected to be most reliant on fine resolution as there is an increase in u_τ. As the friction Reynolds number is increased by the wall forcing, the size of the structures is decreased in outer units as compared to the no-control flow. This suggests that a finer grid resolution would be required to accurately capture these structures. The u rms profiles are shown in figure 4.5a. It can be seen that there is a slight difference in the profiles of the no control flow for case 1. This suggests that the resolution is slightly coarse in the x direction. The u rms profile for the drag increase flow is also slightly different for the double streamwise resolution, with a lower peak value than that of the other cases. The v rms profiles are similar for all cases, figure 4.5b. The drag reduction and no control cases are also similar for the w rms in figure 4.6a, but the peak of the maximum DI case is slightly lower for the increased x resolution case, when compared to the other three cases. Figure 4.6a shows that the p rms also varies slightly for the case 1 resolution in the drag increase case, but otherwise are almost equivalent.

From the grid-resolution test the base resolution of $320 \times 140 \times 240$ appears to be fairly reasonable. The variation of DR is small and the profiles of the turbulent statistics are very similar when increasing the resolution in the y and z directions. When varying the resolution in the x direction, there is a visible change, which is strongest in u rms and $-\overline{uv}$ of the no control and drag increase simulations. Although this change occurs, the effect on the DR is believed to be no more than 2%, which is an acceptable level of error in the cases which achieve a drag increase.

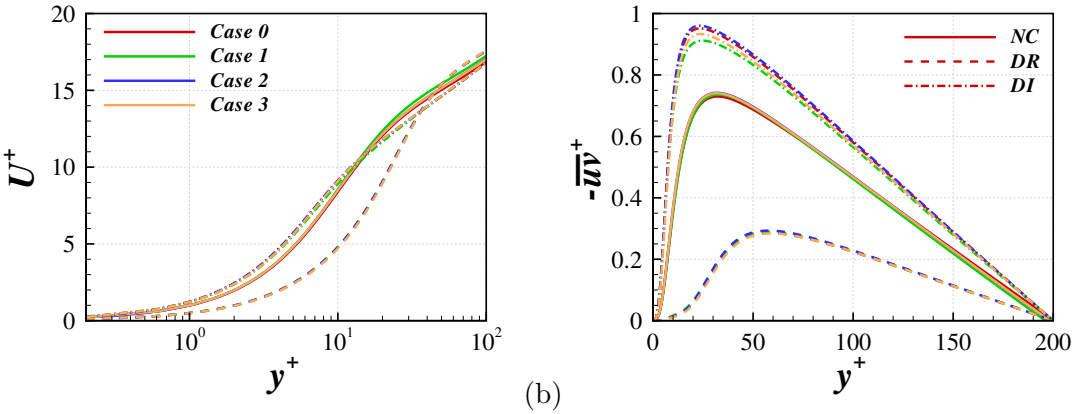

(a) (b)

Figure 4.4: Comparison of the mean velocity (a) and Reynolds stress (b) for the cases with different resolutions (colours), using the no control case, maximum DR and maximum DI forcing (line types).

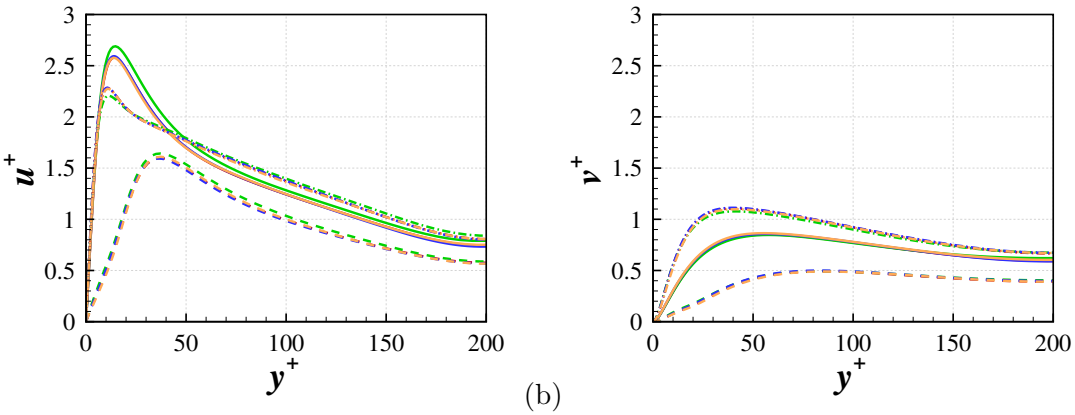

(a) (b)

Figure 4.5: Comparison of the root-mean-squared of u (a) and v (b) for the cases with different resolutions, using the no control case, maximum DR and maximum DI forcing. Legend as in figure 4.4.

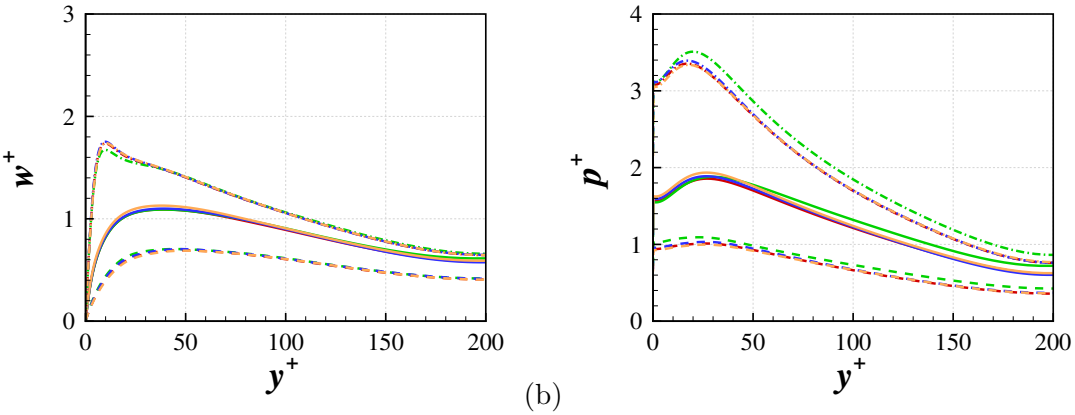

Figure 4.6: Comparison of the root-mean-squared of w (a) and p (b) for the cases with different resolutions, using the no control case, maximum DR and maximum DI forcing. Legend as in figure 4.1.

4.4 Time Step Size Test

The time step size can also affect the accuracy of the simulation. The value used is heavily reliant on the numerical algorithm, and therefore an algorithm can be deemed more efficient if the time step can be increased. The time step can be limited by both the numerical stability and accuracy of the algorithm. It can also be reliant on the grid spacing used and the velocity of the flow field, as discussed previously, the CFL condition relates the time step to the velocity and grid spacing, as in equation (3.3). Due to the implicit treatment of the convection, this condition does not hold in the current code. The accuracy of the time step used must be understood with spanwise forcing applied. The rapid changes in spanwise velocity may create a requirement for a small time step as well as the increase or decrease in turbulent activity. Table 4.4 shows the four different time steps investigated at $Re_\tau = 200$. Again, the maximum drag reduction and maximum drag increase cases are also studied. Note that at $\Delta t = 0.05$ the numerical stability is lost for the no control case, limiting the maximum time step tested.

	Δt	$10^3 C_f$ (NC)	$10^3 C_f$ (DR)	$10^3 C_f$ (DI)
Case 0	0.01	7.93	3.98	9.90
Case 1	0.001	7.93	3.97	9.89
Case 2	0.005	7.93	3.98	9.89
Case 3	0.02	7.94	4.03	9.91

Table 4.4: Time step size tests performed at $Re_\tau = 200$.

Figure 4.7a shows the mean profiles from the four different time steps studied. All four cases show very similar results for each of the no control, maximum drag reduction and drag increase cases. For the Reynolds shear stress, figure 4.7b, the plots are again almost exactly overlaid. There is some evidence that the profile of the largest time step is very slightly high in the drag increase case. For the u rms profile in the no control case the $\Delta t = 0.02$ case is slightly lower than the cases with other time step sizes, shown in figure 4.8a. For the DI cases the higher time step

size profile is slightly high. All cases from the v rms profiles in figure 4.8b show a strong similarity. Figure 4.9a shows the w rms profiles, giving good agreement, except for a slightly higher curve in the drag increase case with $\Delta t = 0.02$. The p rms profiles also show a strong similarity, figure 4.9b.

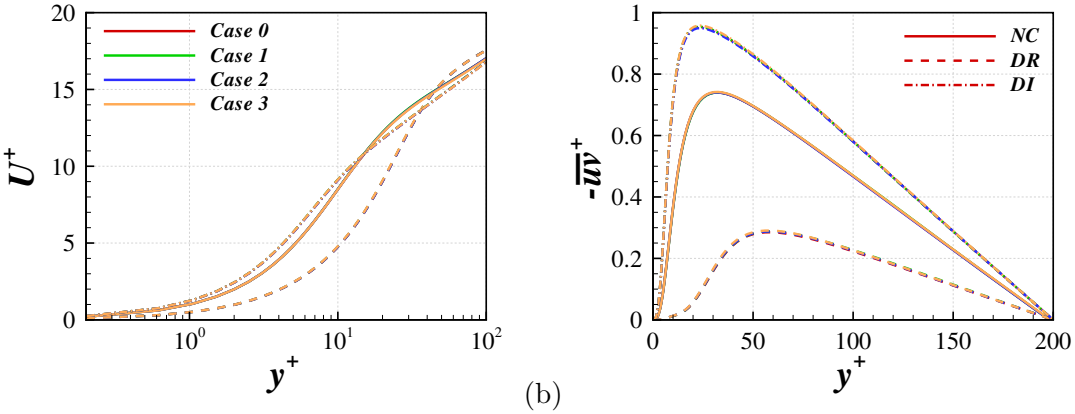

(a) (b)

Figure 4.7: Comparison of the mean velocity (a) and Reynolds stress (b) for the cases with different time step sizes (colours), using the no control case, maximum DR and maximum DI forcing (line types).

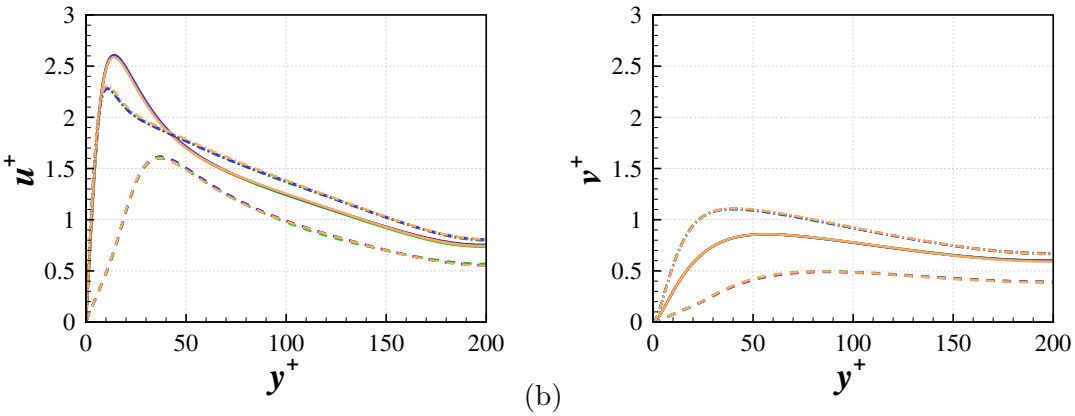

(a) (b)

Figure 4.8: Comparison of the root-mean-squared of u (a) and v (b) for the cases with different time step sizes, using the no control case, maximum DR and maximum DI forcing. Legend as in figure 4.4.

From the different time step sizes tested there is actually very little variation in both the DR values achieved and the profiles shown in figures 4.7-4.9. Accuracy is mostly maintained up to $\Delta t = 0.02$ and the numerical stability is lost by $\Delta t = 0.05$.

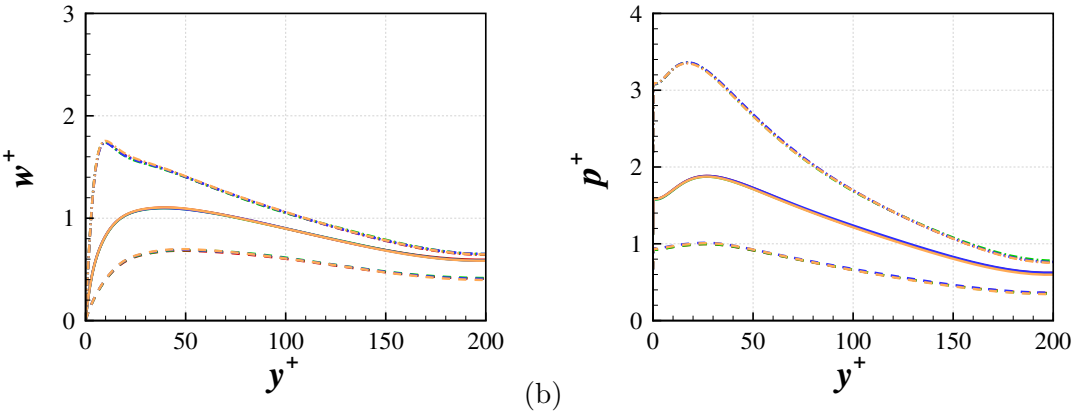

(a) (b)

Figure 4.9: Comparison of the root-mean-squared of w (a) and p (b) for the cases with different time step sizes, using the no control case, maximum DR and maximum DI forcing. Legend as in figure 4.1.

More time step sizes must be performed to check if the accuracy is maintained up to the point where stability is lost, however this is a reasonably large time step to use. Although not studied in detail in the current work the initial transient, after the forcing is applied, may be an important area of study. This would require a finer temporal resolution in order to capture transient effects accurately. With this concept in mind the time step is chosen to be $\Delta t = 0.01$, so that the data may be reserved for further investigation.

4.5 Higher Reynolds Number

4.5.1 Simulation Parameters

Performing the same detail of tests at higher Reynolds number is extremely computationally expensive, however it is possible to obtain an idea of the accuracy of the chosen simulation set-up. Due to the requirement to capture the fine scales of turbulence it is adequate to scale the grid by wall units so that the fine resolution is maintained. The domain size must be kept of similar size, but a slightly smaller size is used at the higher Reynolds numbers in order to increase the computational efficiency. With such ideas in mind the four sets of simulation parameter are shown

in Table 4.5.

Re_τ	200	400	800	1600
Re_b	3150	7000	15700	34500
$L_x \times L_y \times L_z$	$16h \times 2h \times 6h$	$16h \times 2h \times 6h$	$12h \times 2h \times 4h$	$12h \times 2h \times 4h$
$N_x \times N_y \times N_z$	$320 \times 140 \times 240$	$640 \times 240 \times 480$	$960 \times 384 \times 640$	$1920 \times 800 \times 1280$
$\Delta_x^+, \Delta_y^+, \Delta_z^+$	$10, 0.4 - 6, 5$	$10, 0.4 - 7.2, 5$	$10, 0.4 - 9.7, 5$	$10, 0.4 - 9.2, 5$

Table 4.5: Simulation parameters for the four Reynolds numbers studied.

Table 4.6 shows the time step sizes used in the various simulations. The time step size is calculated in wall units for the $Re_\tau = 200$ case is found via $\Delta t^+ = \frac{u_\tau^2}{\nu}\Delta t$. The time step size is maintained to be $\Delta t^+ = 0.12$ at the higher Reynolds numbers so that the accuracy in time is roughly maintained in the near wall region.

Re_τ	200	400	800	1600
Δt	0.01	0.005	0.003	0.0015
Δt^+	0.13	0.11	0.12	0.11

Table 4.6: Time step sizes for the four Reynolds numbers studied.

4.5.2 No Control Case

Comparison to Literature

Many previous studies of a turbulent channel flow have been performed at various Reynolds numbers. In order to further understand the accuracy of the current study, the results of cases without flow control are compared to profiles from available DNS databases. The simulation parameters of the past study is shown in Table 4.7.

Figure 4.10 compares results from the no control case at $Re_\tau = 200$ of the current study to available data at $Re_\tau = 180$ [Moser et al., 1999; del Alamo and Jiménez, 2003]. Figure 4.10a shows a good comparison between the mean streamwise velocity profiles. The rms fluctuations are shown in figure 4.10b. A very good comparison is seen for the v and w profiles. For the u fluctuations the values from

	Re_τ	Domain Size	Grid Size	$\Delta x^+, \Delta y^+_{max}, \Delta z^+$
Moser et al. [1999]	178	$4\pi h \times 2h \times \frac{4}{3}\pi h$	$128 \times 129 \times 128$	$17.7, 4.4, 5.9$
del Alamo and Jiménez [2003]	180	$12\pi h \times 2h \times 4\pi h$	-	$8.9, 6.1, 4.5$
Moser et al. [1999]	392	$2\pi h \times 2h \times \pi h$	$256 \times 192 \times 192$	$10, 6.5, 6.5$
Iwamoto et al. [2002]	395	$2.5\pi h \times 2h \times \pi h$	$192 \times 257 \times 192$	$16.4, 4.91, 6.5$
del Alamo and Jiménez [2003]	547	$8\pi h \times 2h \times 4\pi h$	-	$8.9, 6.7, 4.5$
Hoyas and Jiménez [2006]	934	$8\pi h \times 2h \times 3\pi h$	-	$9.2, 7.6, 3.8$

Table 4.7: Reynolds numbers, domain sizes and grid sizes of previous research of channel flow with no control applied.

the current study are slightly low in the buffer region. This is unusual as the maximum value of u' is seen to increase with Reynolds number [Townsend, 1976], and the current value of Re_τ is actually slightly higher. This slight discrepancy is likely to be an attribute of the small error seen when increasing the streamwise grid resolution in section 4.3, which only affects the drag reduction minimally.

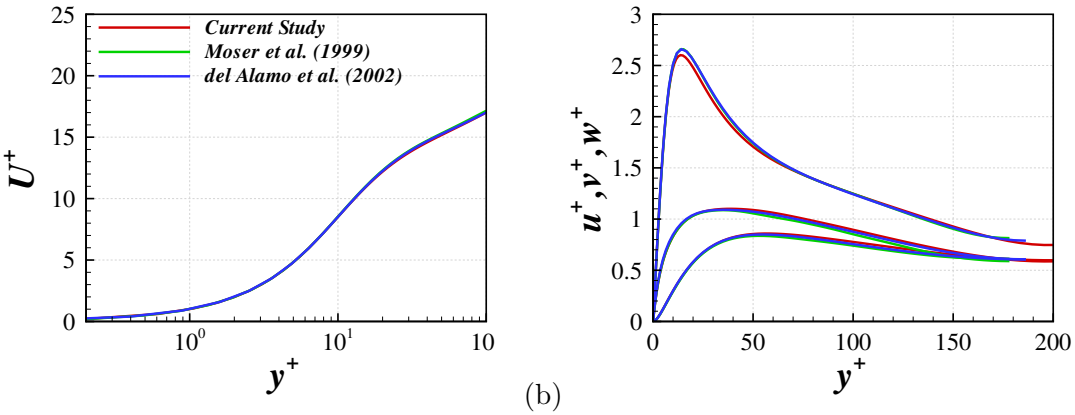

(a) (b)

Figure 4.10: Comparison of 2d channel flow at $Re_\tau = 200$. The results from the literature use cases with $Re_\tau \approx 180$ [Moser et al., 1999; del Alamo and Jiménez, 2003].

Figure 4.11 compares the current data to that of previous studies [Moser et al., 1999; Iwamoto et al., 2002] at $Re_\tau = 400$. The mean u profiles, presented in figure 4.11a, show a very good agreement. The v and w profiles are again similar, seen in figure 4.11b, and the u-rms profile is reasonable, but slightly low in the buffer region.

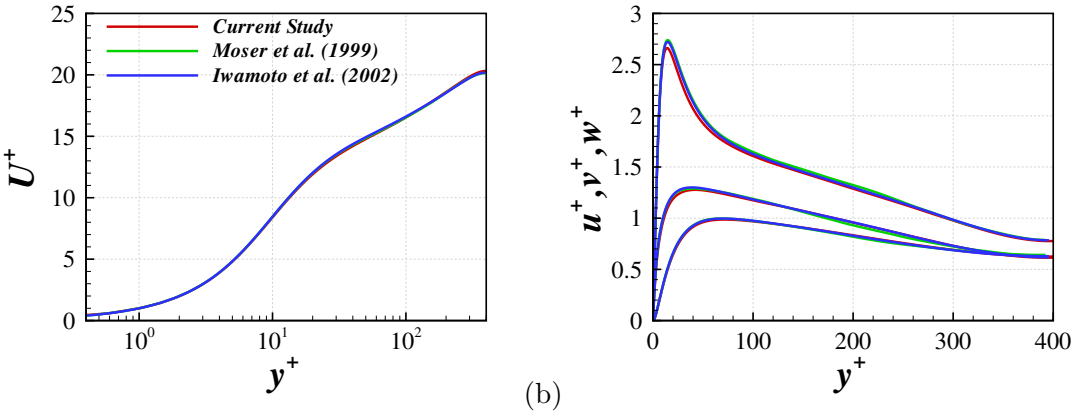

(a) (b)

Figure 4.11: Comparison of 2d channel flow at $Re_\tau = 400$. The results from the literature use cases with $Re_\tau \approx 400$ [Moser et al., 1999; Iwamoto et al., 2002].

Figure 4.12a shows the comparison of the $Re_\tau = 800$ case from the current simulations to the higher Reynolds number simulation data [del Alamo and Jiménez, 2003; Hoyas and Jiménez, 2006]. The Reynolds number of the current study lies between the two Reynolds numbers of the literature. The mean streamwise velocity profile shows good agreement with the mean profiles at the straddling Reynolds numbers. The rms profiles from the $Re_\tau = 800$ case fit between the profiles from the literature as expected, 4.12b.

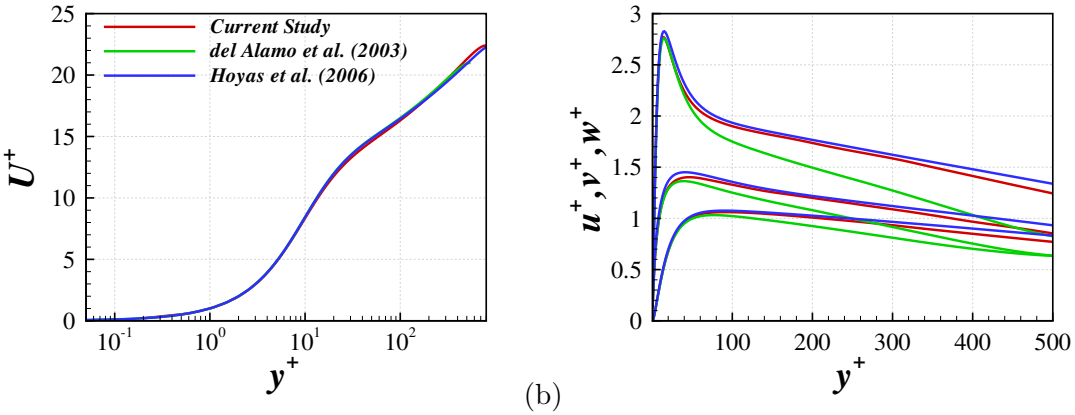

(a) (b)

Figure 4.12: Comparison of 2d channel flow at $Re_\tau = 800$. The results are compared to simulations with del Alamo and Jiménez [2003] and Hoyas and Jiménez [2006]

Correlations and Spectra

One way to test the independence of the domain size is by looking at the correlations [Kim et al., 1987] . The influence of large scale structures is most dominant in the centre of the channel, hence the correlations are shown at $y = h$. Figures 4.13, 4.14 and 4.15 show the correlations for the no-control cases at $Re_\tau = 200$, 400 and 800 respectively. For each of the Reynolds numbers, the correlations decay to 0 over a half channel length. The decay is slowest in the streamwise velocity. This indicates that the domain lengths in both the x and z directions are sufficiently large.

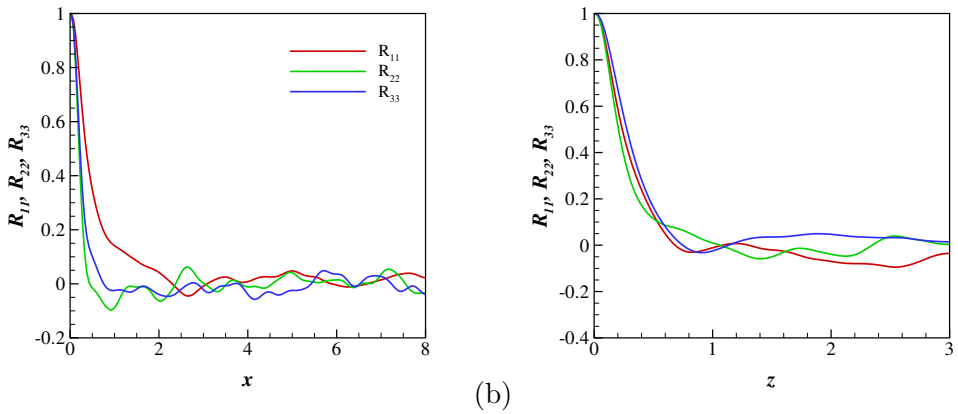

(a) (b)

Figure 4.13: Correlations at $y = h$ with $Re_\tau = 200$ in the x direction (a) and z direction (b).

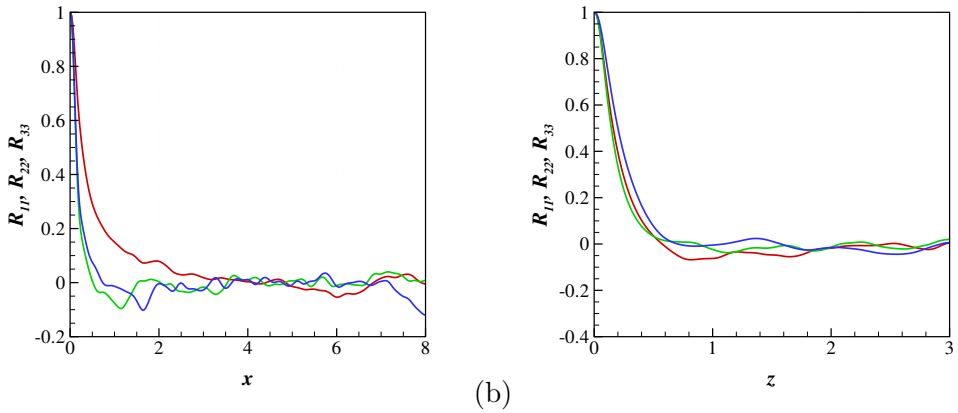

(a) (b)

Figure 4.14: Correlations at $y = h$ with $Re_\tau = 400$ in the x direction (a) and z direction (b).

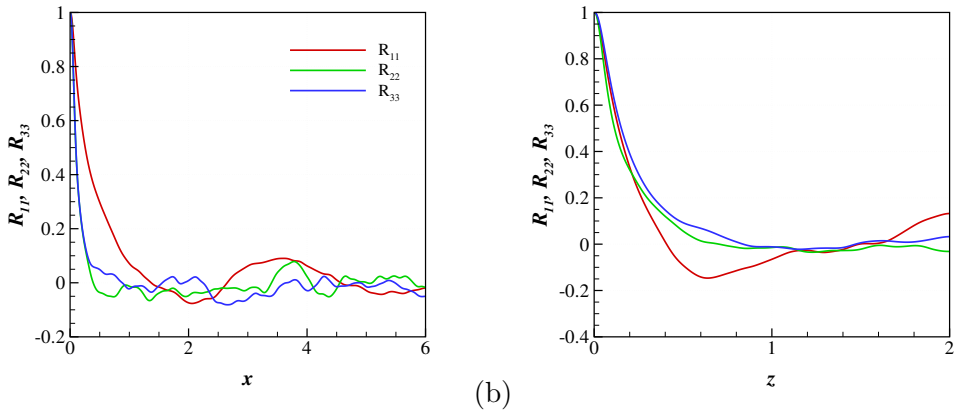

(a) (b)

Figure 4.15: Correlations at $y = h$ with $Re_\tau = 800$ in the x direction (a) and z direction (b).

To check the grid resolution, the energy spectra are calculated. When a coarse grid resolution is used there is evidence of 'pile up' of energy in the small scales. Figures 4.16, 4.17 and 4.18 show the energy spectra for the no-control cases at $Re_\tau = 200$, 400 and 800 respectively. The small scales are most dominant in the near-wall region, and their y location scales with wall units. The spectra are therefore shown at $y^+ = 5$. The spectra in the x direction decay well. In the z direction the w spectrum shows a good decay to the small scales. The u and v velocities show very small increase in the spectrum at the smallest scales, however this is only a small.

The Kolmogorov length scale is defined as:

$$\eta = \left(\frac{\nu^3}{\epsilon}\right)^{\frac{1}{4}},$$

where ν is the kinematic viscosity and ϵ is the average dissipation rate of turbulent kinetic energy per unit mass. At the Kolmogorov scale the viscosity dominates and the turbulent kinetic energy is dissipated. The dissipation rate can be approximated using:

$$\epsilon \approx \frac{u_\tau^4}{\nu}.$$

Then:

$$\eta \approx \frac{\nu}{u_\tau}.$$

Using this approximation, the streamwise grid spacing can be written as:

$$\Delta x = \Delta x^+ \frac{\nu}{u_\tau} \approx 10\eta$$

This corresponds to the peak in the dissipation spectrum at 10η, signifying that the streamwise resolution is correctly capturing the small scales.

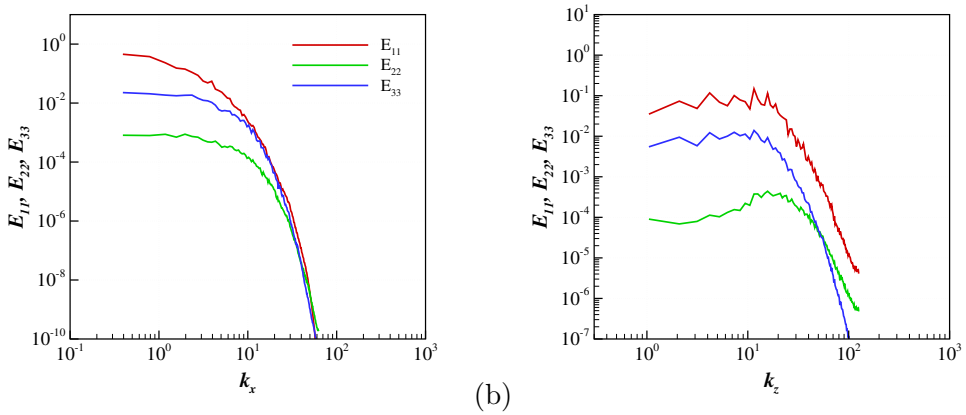

(a) (b)

Figure 4.16: Energy spectra at $y^+ = 5$ with $Re_\tau = 200$ in the x direction (a) and z direction (b).

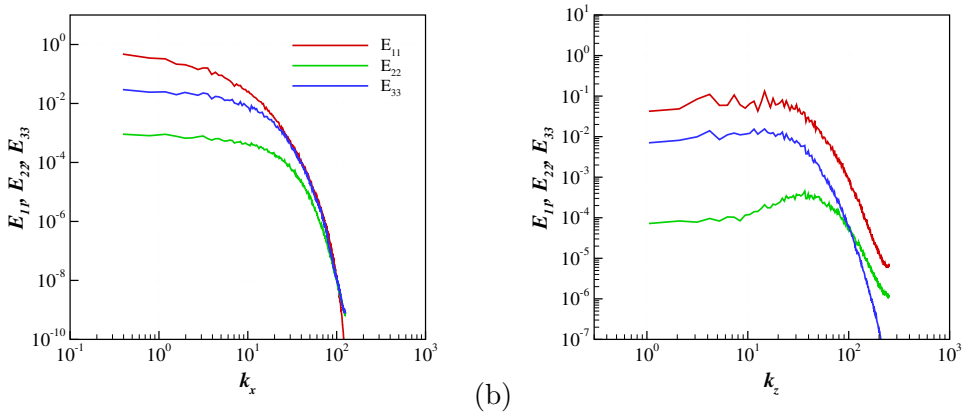

(a) (b)

Figure 4.17: Energy spectra at $y^+ = 5$ with $Re_\tau = 400$ in the x direction (a) and z direction (b).

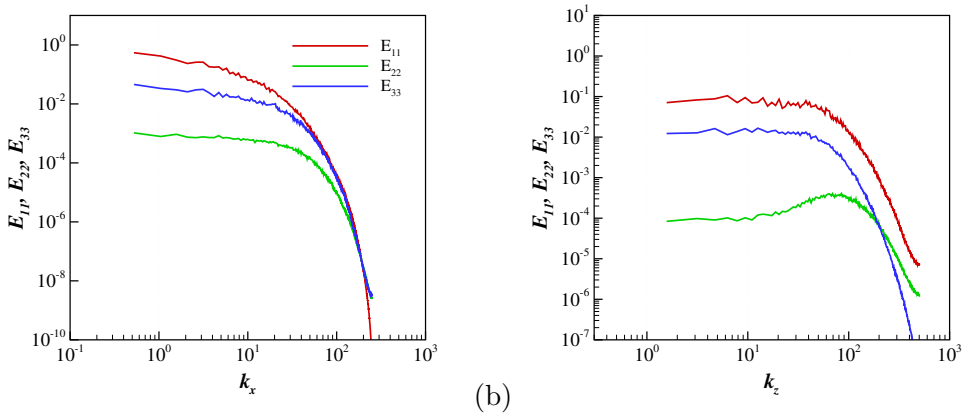

(a) (b)

Figure 4.18: Energy spectra at $y^+ = 5$ with $Re_\tau = 800$ in the x direction (a) and z direction (b).

4.6 Wall Forcing

4.6.1 Control Parameters

Due to the computational expense of running higher Reynolds number simulations, the forcing parameters studied must be considered. A few reasonable parameters are chosen in order to help understand the general effect of the control strategy at higher Reynolds numbers. The drag reduction map of Quadrio et al. [2009] is shown here in figure 4.19. In the region in which the waves of spanwise velocity travel forwards in the domain ($\omega > 0$) both the maximum drag reduction and the region of large drag increases are found. Because both of these interesting phenomena are found in this region the current study will be limited to forward travelling waves.

Figure 4.19 overlays the DR map with filled circles representing the cases studied in the current research. Table 4.8 shows the values of the forcing parameters in wall units and in global units, calculated from the $Re_\tau = 200$ case. The temporal frequencies, Table 4.8a, are simply chosen so that a reasonable region of the DR map is covered. There is a finer region when $0 < \omega^+ < 0.03$ so that the area around the maximum DR for the travelling waves is captured accurately and can be investigated at higher Re values. The global value of temporal frequency is

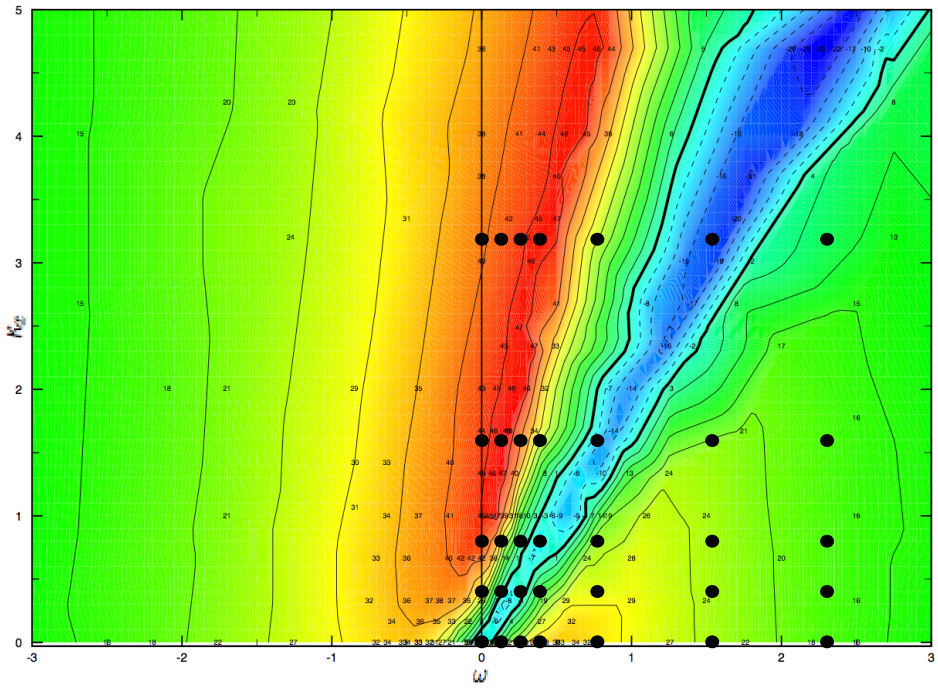

Figure 4.19: Contour plot of DR at $Re_\tau = 200$ from Quadrio et al. [2009], filled circles represent the cases undertaken in the current study.

calculated using $\omega = \frac{u_\tau^2}{\nu}\omega^+$, with period $T = \frac{2\pi}{\omega}$. The spatial wavenumber cannot be calculated so easily, as there is a requirement to have an integer number of waves within the domain length as periodic boundary conditions are applied in this direction. Table 4.8b therefore shows the approximate values of κ_x^+, however the values of λ^+ are exact. The value of wavenumber in global units $\kappa_x = \frac{u_\tau}{\nu}\kappa_x^+$, with wavelength $\lambda = \frac{2\pi}{\kappa_x}$. Note that if the domain length (in wall units) is divisible by 3200 then it is also divisible by $1600, 800$ and 400. The domain lengths in wall units for $Re_\tau = 200, 400, 800$ and 1600 can be calculated as $L_x^+ = 3200, 6400, 9600$ and 19200, respectively (corresponding to $1, 2, 3$ and 6 waves for $\kappa_x^+ = 0.002$). This means that the chosen values of κ_x^+ may be performed at all four Reynolds numbers.

(a)

ω^+	ω	T^+
0.0	0.0	∞
0.01	0.127	628
0.02	0.254	314
0.03	0.381	209
0.06	0.762	105
0.12	1.524	52
0.18	2.286	35

(b)

κ_x^+	κ_x	λ^+
0.0	0.0	∞
0.002	0.4	3200
0.004	0.8	1600
0.008	1.6	800
0.016	3.2	400

Table 4.8: Forcing parameters in wall units and global units (from the $Re_\tau = 200$ case).

4.6.2 Comparison to Existing Results

The results from the current study were compared to those of Quadrio et al. [2009]. Figure 4.20a shows a drag reduction achieved at $Re_\tau = 200$ for wall oscillation control. The discussion also includes the DR values from Touber and Leschziner [2012]. The maximum value achieved in the current study is 36.5% at $T^+ = 104$, which lies between the 33% and 38.5% found at $T^+ = 100$ in the literature. As ω^+ becomes small, reasonably small changes in frequency correspond to large changes in the time period of oscillation and hence larger deviation in the DR occurs. This means that small differences in the numerical scheme and simulation parameters can magnify in the drag reduction. This effect is more visible in figure 4.20b which shows the comparison to the standing wave case. This comparison is good showing maximum drag reduction of 47%, which is similar to the 45% seen in Quadrio et al. [2009]. The maximum value is found in the region $\lambda^+ = 1000 - 1250$ [Viotti et al., 2009], which corresponds to the maximum found at $\lambda^+ = 1000$ ($\kappa_x^+ = 0.006$).

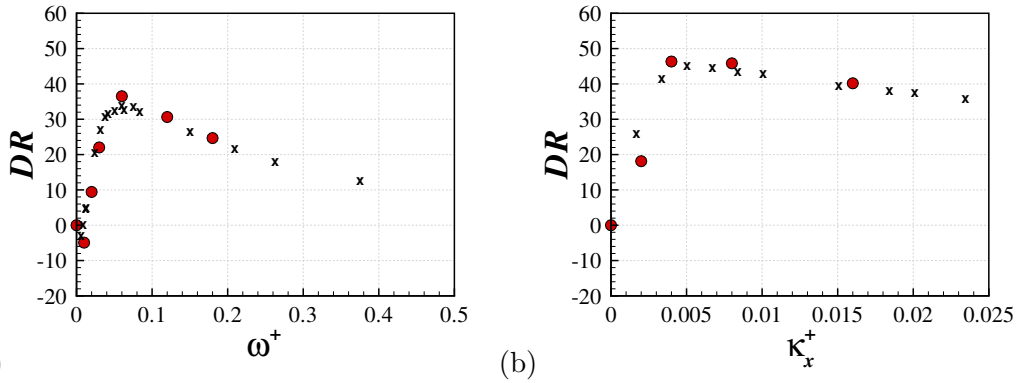

(a) (b)

Figure 4.20: Drag reduction at $Re_\tau = 200$ from the current study (circles) and Quadrio et al. [2009] (crosses) for (a) the wall oscillation case, $\kappa_x^+ = 0$, and (b) the standing wave case, $\omega^+ = 0$.

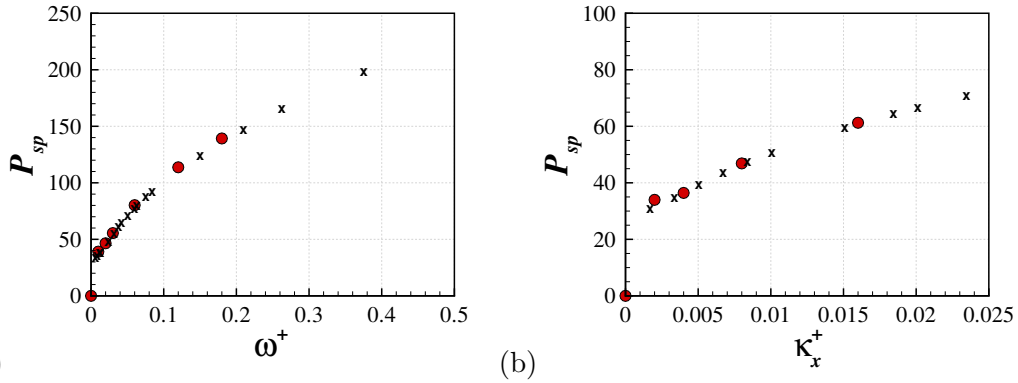

(a) (b)

Figure 4.21: Power spent at $Re_\tau = 200$ from the current study (circles) and Quadrio et al. [2009] (crosses) for (a) the wall oscillation case, $\kappa_x^+ = 0$, and (b) the standing wave case, $\omega^+ = 0$.

Chapter 5

Reynolds number effects

An understanding of the effect of Reynolds number on any flow control method is of huge importance. Any practical application of a drag reduction mechanism is likely to be at high Reynolds numbers, for example in transport and aircraft situations. Currently, the use of DNS at a value of Re required for aviation is a long way off, however the study of control at a range of Reynolds numbers can give a valuable insight into how the flow physics changes. This leads to the investigation of how the DR scales with Reynolds number and whether the optimal control parameters scale with wall units. In the canonical flow an increase in the Reynolds number causes a decrease in the size of the near-wall structures, in outer units. The outer scales, however, are limited by the channel height. This means that the largest scales in the simulation increase in wall units (with $Re_\tau = h^+$) when the Reynolds number is increased. A decrease in the drag reduction as the Reynolds number is increased has been seen in previous studies of wall oscillation [Ricco and Quadrio, 2008; Touber and Leschziner, 2012]. These were either limited to a reasonably small change in Reynolds number, or focused on a few (or a single) forcing parameters. While the current work was being presented at the EFMC9 [Hurst and Chung, 2012b], a similar investigation was brought to the authors attention. This work was recently published [Gatti and Quadrio, 2013] and although there is great similarity to the

current work, a minimal channel flow approach is undertaken. The current study aims to expand the current knowledge by performing a parametric study over four Reynolds numbers using a full sized computational domain ensuring full confidence in the results.

5.1 Scaling of no-control case

Before studying the effect of applying the control, the consequence of changing the Reynolds number on the base flow must first be understood. It is common understanding that the size and spacing of streaks decrease as the Reynolds number is increased, an idea highlighted in various high fidelity computational studies [Moser et al., 1999; del Alamo and Jiménez, 2003; Abe et al., 2004; Hoyas and Jiménez, 2006]. This decrease in the fluctuations comes from a decrease in the size of the streamwise vortical structure, a concept illustrated by Figures 5.1 and 5.2, in which isosurfaces of λ_2^+ are shown at $Re_\tau = 200, 400$ and 800. These isosurfaces indicate the locations of vortex cores [Jeong and Hussain, 1995]. When the value of λ_2 is scaled by wall units, the size of the near-wall structures is seen to decrease with increasing Re.

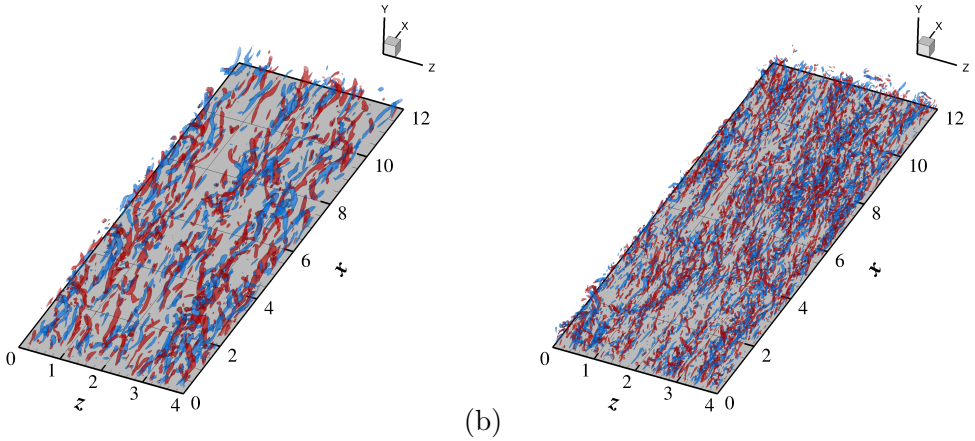

Figure 5.1: Isosurfaces of $\lambda_2^+ = -0.01$ for (a) $Re_\tau = 200$ and (b) $Re_\tau = 400$. The colouring displays the direction of streamwise vorticity, red structures have $\omega_x^+ > 0$ and blue have $\omega_x^+ < 0$.

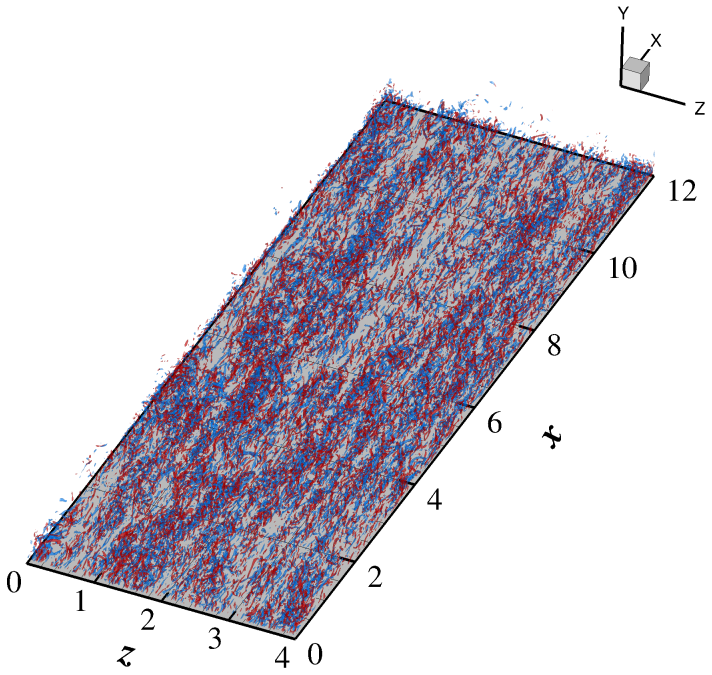

Figure 5.2: Isosurfaces of $\lambda_2^+ = -0.01$ for $Re_\tau = 800$. The colouring displays the direction of streamwise vorticity, red structures have $\omega_x^+ > 0$ and blue have $\omega_x^+ < 0$.

Figure 5.3 shows the streak visualisation at the highest Reynolds number case studied of $Re_\tau = 1600$. This consists of a field of streaks, which have much larger length than the vortical structures seen previously. As the visualisation plane is moved away from the wall the larger scale variations are visible with regions of high and low speed fluid. This fluctuation in the velocity field comes from the wall normal movement of high speed fluid towards the wall (sweeps) and the movement of low speed fluid away from the wall (ejections) as discussed by Lu and Willmarth [1973].

Figure 5.4a shows the mean streamwise velocity profiles from all four Reynolds numbers. The dashed lines show both the linear near-wall behaviour, $U^+ = y^+$ and the log-law relation $U^+ = \frac{1}{\kappa}\ln(y^+) + C^+$, where $\kappa = 0.41$ is the von Kármán constant and $C^+ = 5$ [Townsend, 1976]. The linear wall relation is satisfied for all the Reynolds numbers. The $Re_\tau = 200$ case is slightly high in the logarithmic region,

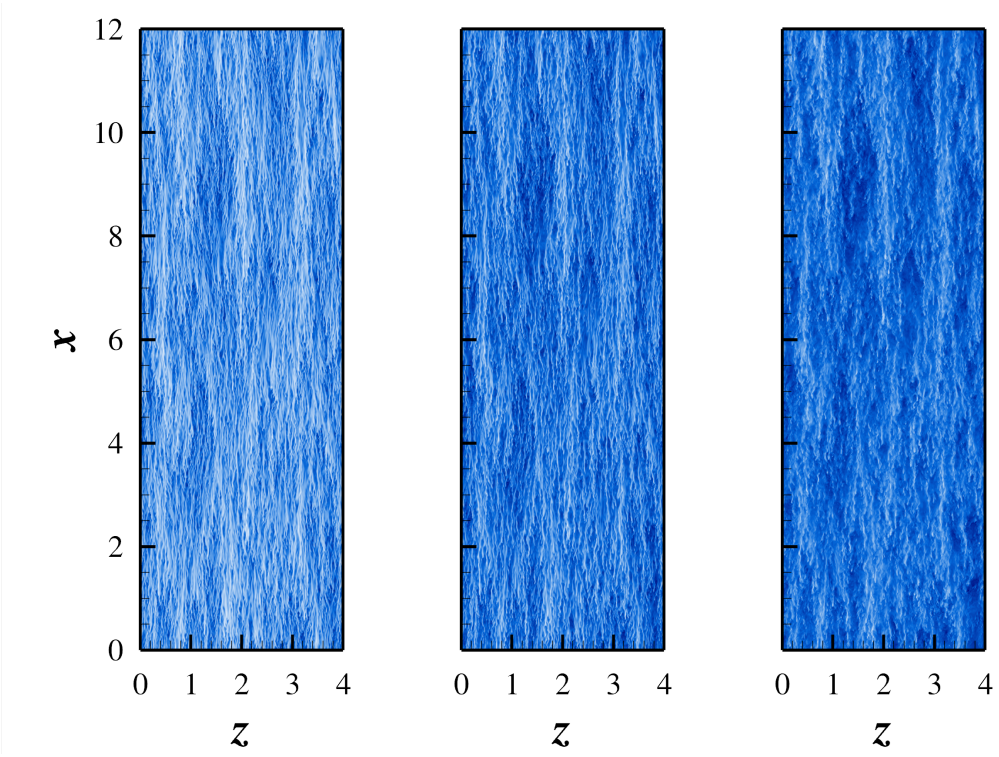

Figure 5.3: Visualisation of the streaks for $Re_\tau = 1600$ at $y^+ = 10, 20$ and 50.

but as the Reynolds number increases the mean profiles converge to the log-law. At $Re_\tau = 1600$ there appears to be a substantial region at which the log-law is satisfied. Despite this, Hoyas and Jiménez [2006] showed that the inverse von Kármán function is nowhere constant, even up to $Re_\tau = 2003$.

Figure 5.4b show the streamwise velocity rms profiles. As the Reynolds number increases the location of the near-wall maximum remains in the same position, when scaled in wall units. The intensity of the fluctuations, however, increases with Reynolds number. At $Re_\tau = 1600$ there is evidence of an emerging outer peak, a phenomenon seen in many higher Re studies [Reviewed in Smits et al. [2011]; Jiménez [2012]]. This outer peak is an increase in turbulent activity associated with large scale structures. Townsend [1976] divides near-wall turbulence into momentum transporting active motion and inactive motion, which is an outer scale phenomenon. The large scales contribute to the Reynolds stresses so that a

simple wall-unit scaling does not hold. This is because the wall-parallel and wall-normal components adhere to different boundary conditions at the wall. While the wall-parallel velocities are subject to a no-slip condition, there is a requirement for non-permeability from the v velocity. This means that when large scale motions are within proximity to the wall, the wall normal motion is converted into wall-parallel velocity. As the Reynolds number is increased, and the size of the outer scale structures increases in wall units, then there is a greater large scale fluctuation to convert to wall-parallel motions. Morrison [2007] argued that the interaction between inner and outer scales is non-linear and that the large-eddies contribute significantly to the Reynolds stresses. This means that the Reynolds stresses do not scale with the wall friction velocity.

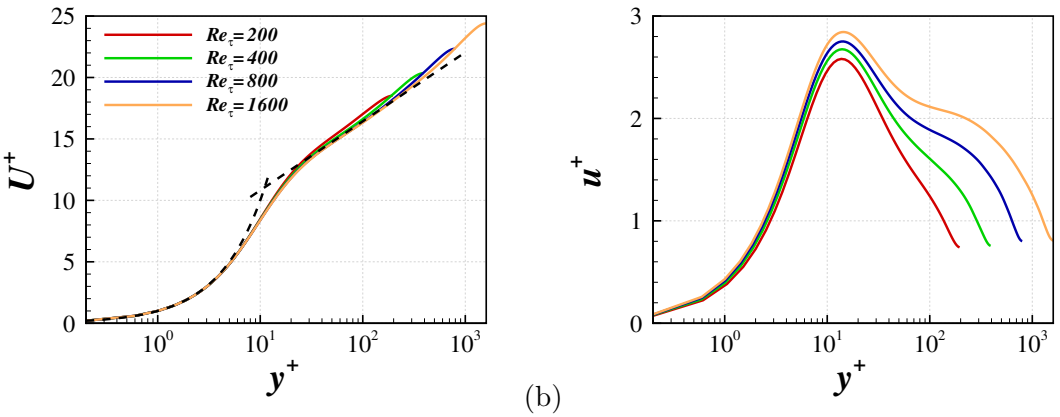

Figure 5.4: Log-law profiles (a) and streamwise velocity rms profiles (b) for the no-control case at all four Reynolds numbers.

A similar behaviour occurs in the wall-normal and spanwise velocity fluctuations, figure 5.5. From $Re_\tau = 200$ to 1600 the profiles increase, although the rate of increase in the peak values appear to reduce slightly for larger Re_τ values. A prominent near-wall peak is seen to emerge in the w-profile, and is a consequence of inactive motion causing an increase in the wall-parallel velocity fluctuation.

The streamwise vorticity rms profile also increases as the Reynolds number is increased, figure 5.6a. This rate of increase reduces at higher Reynolds numbers,

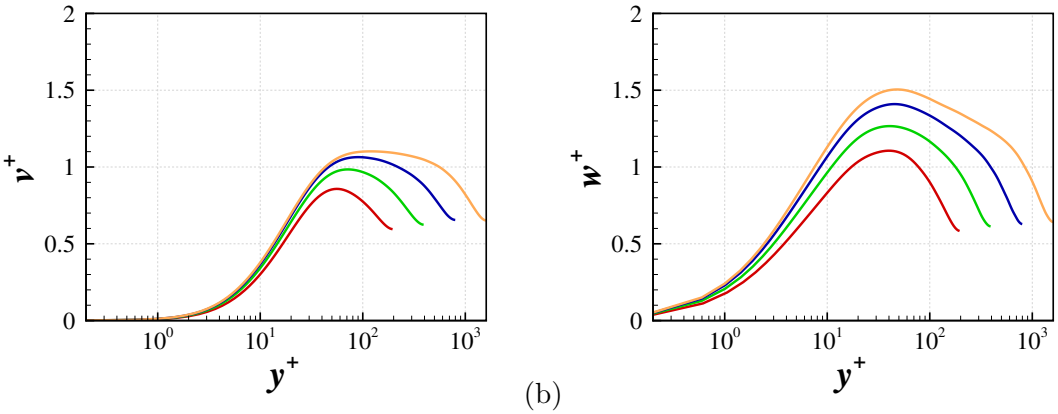

(a) (b)

Figure 5.5: Wall normal velocity rms profiles (a) and spanwise velocity rms profiles (b) for the no-control case at all four Reynolds numbers.

with the profiles at $Re_\tau = 800$ and 1600 being very similar in the log-law region. The local minima are in the same wall normal location, when scaled by wall units. The local maximum appears to move very slightly towards the wall as Re increases, and the ω_x^+ value at the centre of the channel decreases.

The wall normal vorticity rms profiles almost collapse over each other at the various Reynolds numbers studied, figure 5.6b. The peak value is seen to be almost exactly the same, although it moves towards the wall by a very small amount as Re increases. This is combined with a very slight increase in the near-wall fluctuations.

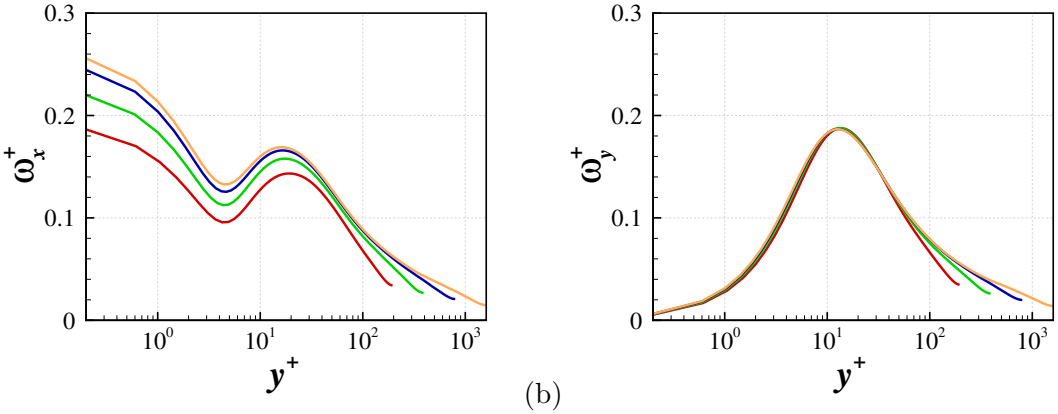

(a) (b)

Figure 5.6: Streamwise vorticity rms profiles (a) and wall normal vorticity rms profiles (b) for the no-control case at all four Reynolds numbers.

Figure 5.7a shows the spanwise vorticity fluctuations at all four Reynolds numbers. The wall value increases at a constant rate (which means logarithmically with Re_τ). As the Reynolds number increases, the point of inflexion at $y^+ = 10$ becomes less apparent. This relates to the overlapping of the profiles for all Reynolds numbers at around $15 < y^+ < 30$.

The Reynolds shear stress is scaled in wall units and plotted against y/h in figure 5.7b. The maximum is increased (in wall units) and moves towards the wall (in global units).

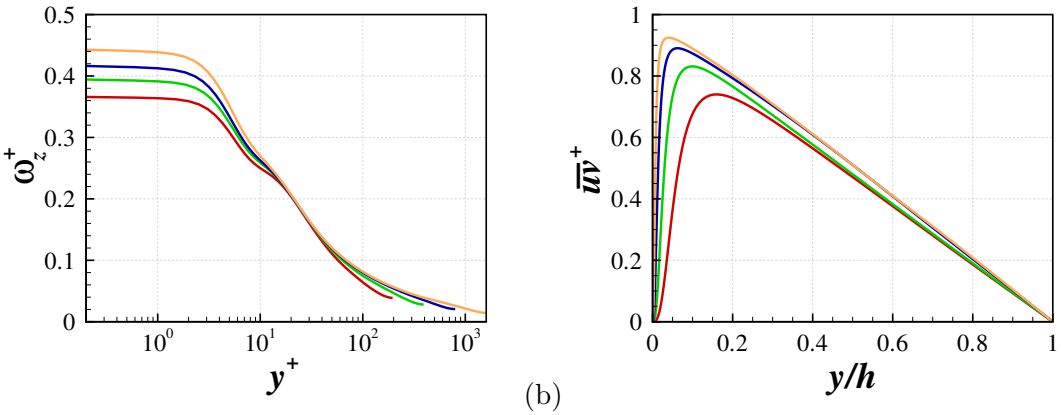

(a) (b)

Figure 5.7: Spanwise vorticity rms profiles (a) and Reynolds shear stress profiles (b) for the no-control case at all four Reynolds numbers.

5.2 Power Scaling

This section investigates the consequences of the applying the wall forcing. The drag reduction, power spent and net power saving is computed for the various control parameter combinations. This is discussed with the aim to understand the effect of Reynolds number on the efficiency of the control method.

5.2.1 Drag Reduction

Figures 5.8 and 5.9 show contour plots of the drag reduction calculated from simulations of the spanwise wall forcing at $Re_\tau = 200$, 400 and 800. The maximum wall

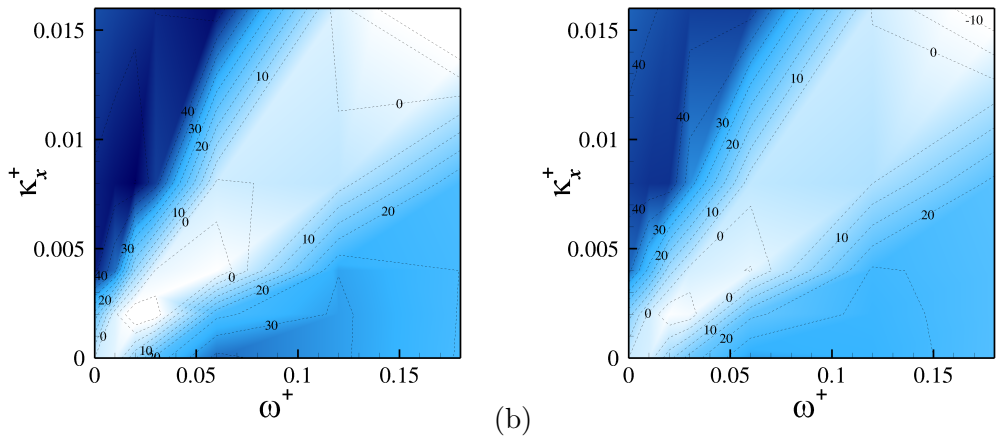

Figure 5.8: Drag reduction map for the forward travelling waves at (a) $Re_\tau = 200$ and (b) $Re_\tau = 400$. Contour levels are drawn at 5% intervals. The bright (white) colour indicates a drag increase, and the dark (blue) indicates a drag reduction.

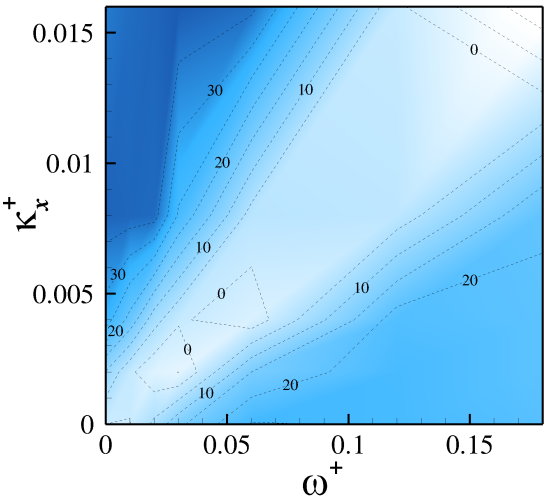

Figure 5.9: Drag reduction map for the forward travelling waves at $Re_\tau = 800$. Contour levels are drawn at 5% intervals. The bright (white) colour indicates a drag increase, and the dark (blue) indicates a drag reduction.

velocity is fixed at $W_m^+ = 12$ and the temporal and spatial frequencies are varied to generate a 35 point map. The lower Reynolds number case is quantitatively similar to the map presented by Quadrio et al. [2009] and the two cases with increased Re_τ show qualitative similarities. The region studied (with positive ω^+) corresponds to only waves which travel forwards through the domain, with the mass flow. The

region of drag increase corresponds to waves travelling at specific speed c (or within a certain range of speeds).

Figure 5.8 shows contours of the drag reduction values achieved in both the $Re_\tau = 200$ and 400 cases. The maximum drag reduction for the $Re_\tau = 200$ case is found as 50% with forcing parameters $\omega^+ = 0.02$ and $\kappa_x^+ = 0.008$. The figure shows that, at $Re_\tau = 400$, the drag reduction achieved is reduced universally, and the drag increase is also lower at the higher Reynolds number. At $Re_\tau = 800$ the drag reduction is reduced further still, figure 5.9. This can be considered as the idea that the overall change in the drag is reduced when the Reynolds number is increased. At $Re_\tau = 400$ the maximum value of DR drops to 44%, which is seen with the same control parameters as for $Re_\tau = 200$, based on the parameters studied. By $Re_\tau = 800$ the maximum drag reduction of 39% is found at $\omega^+ = 0.03$ and $\kappa_x^+ = 0.016$. The reduction in DR with Reynolds number is consistent with studies of wall oscillation in which the drag reduction was seen to decrease at the optimal forcing of $T^+ = 100$ [Ricco and Quadrio, 2008; Touber and Leschziner, 2012].

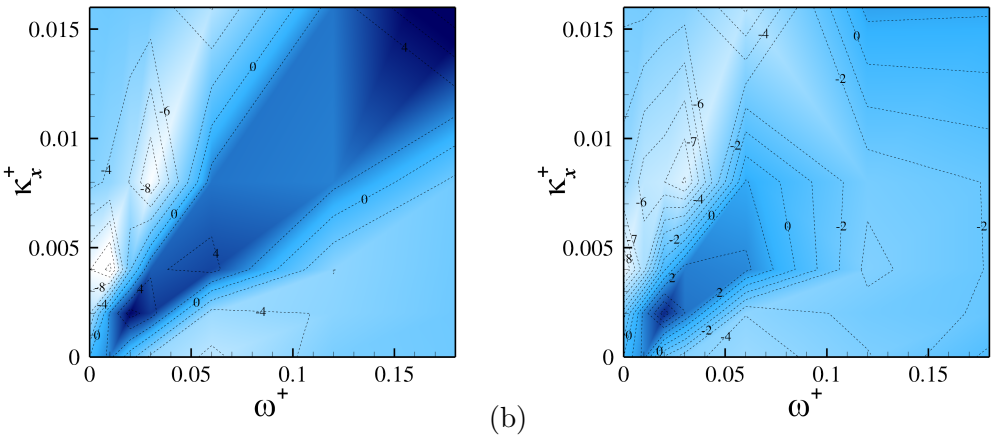

Figure 5.10: Change in drag reduction from $Re_\tau = 200$ to 400 (a) and from $Re_\tau = 400$ to 800 (b). The bright (white) colour indicates an increase in DR, and the dark (blue) indicates a decrease in DR.

Figure 5.10a illustrates the effect of increasing the value of Re_τ from 200 to 400. The parameter plotted is denoted ΔDR, the difference in drag reduction

between two Reynolds numbers, given the forcing parameters ω^+ and κ_x^+. From $Re_\tau = 200$ to $Re_\tau = 400$ this is defined as:

$$\Delta DR = DR(Re_\tau = 400, \omega^+, \kappa_x^+) - DR(Re_\tau = 200, \omega^+, \kappa_x^+).$$

In the region of drag increase, the magnitude of the increase is smaller at the higher Reynolds number corresponding to positive values of ΔDR. With forcing parameters close to that of maximum drag reduction the change is large and negative with a reduction of up to 12%, which relates to a reduction in the maximum DR achieved. Using parameters away from the optimal gives a relatively small ΔDR suggesting that, for example, in the wall oscillation case the larger values of ω^+ may give a more favourable scaling as the Reynolds number is increased. The change in drag reduction when increasing the Reynolds number from $Re_\tau = 200$ to 400 is shown in figure 5.10b. The magnitude of the ΔDR is similar to the lower Re change and the reduction and increase regions are comparable.

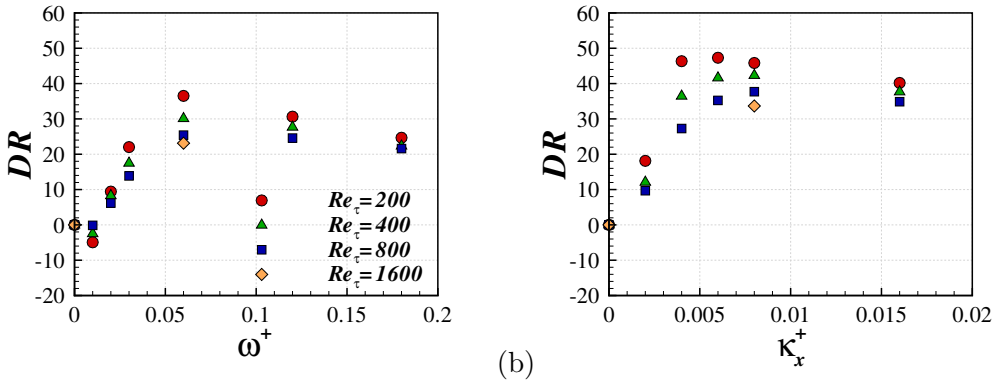

Figure 5.11: Drag reduction at the four Reynolds numbers studied for (a) the wall oscillation case, $\kappa_x^+ = 0$, and (b) the standing wave case, $\omega^+ = 0$.

The drag reduction for all the Reynolds numbers studied are shown in figure 5.11. The results for the wall oscillation case show the reduction in the value of DR as the Reynolds number is increased. As presented in Ricco and Quadrio [2008], using results from $Re_\tau = 400$, there appears to be less of an effect of Re at larger

values of ω^+ (corresponding to small T^+) in the drag reduction region. Although it is clear that the change in DR at the optimal value is greater, this optimum remains at $\omega^+ = 0.06$ from $Re_\tau = 200$ to 800. For the the wall oscillation the drag reduction is calculated at $\omega^+ = 0.06$ up to $Re_\tau = 1600$. At this Reynolds number the value of DR has reduced to 22%, a 15% reduction from the $Re_\tau = 200$ case. In figure 5.11b, the results from the standing wave cases ($\omega^+ = 0$) are presented. One interesting feature of the standing wave is that, based on the parameters studied, the location of the optimal parameter moves from $\kappa_x^+ = 0.006$ at $Re_\tau = 200$, to $\kappa_x^+ = 0.008$ by $Re_\tau = 400$ and $Re_\tau = 800$. When considering the optimal value from the cases studied at $Re_\tau = 200$, increasing the frictional Reynolds number to 800 causes the drag reduction to decrease from 47% to 35%. However, if the wavenumber at $Re_\tau = 800$ is changed to $\kappa_x^+ = 0.008$, a DR of 38% can still be achieved. This means that choosing the optimal parameters from a low Reynolds number flow, and scaling the parameters in wall units will not guarantee the optimal drag reduction at the higher Reynolds number.

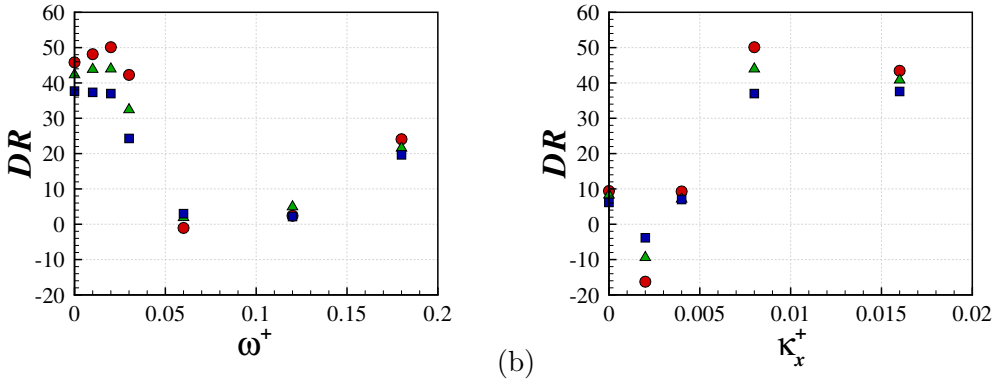

(a) (b)

Figure 5.12: Drag reduction at the four Reynolds numbers studied for the travelling wave cases at (a) a horizontal line through the map with $\kappa_x^+ = 0.008$ and (b) a vertical line through the map with $\omega^+ = 0.02$.

Figure 5.12 shows the drag reduction at the Reynolds numbers up to $Re_\tau = 800$ for the travelling wave case. Again, the change in value of DR appears to be larger at the optimal location. Looking at a horizontal line through the parameter

space with $\kappa_x^+ = 0.008$, figure 5.12a, the optimal frequency is found at $\omega^+ = 0.02$ with $Re_\tau = 200$, giving a maximum drag reduction of 50%, slightly higher than that of the standing wave. By $Re_\tau = 800$ this reduced to 37% with the same frequency parameter, whereas at $\omega^+ = 0.01$ a DR of 38% is achieved. This suggests that, for the travelling wave, the the optimal frequency decreases as Re_τ increases. With fixed $\omega^+ = 0.02$, figure 5.12b, the optimal location is also changing. Comparing $\kappa_x^+ = 0.008$ and $\kappa_x^+ = 0.016$ at $Re_\tau = 200$, there is a difference in the measured DR levels of 7%. At $Re_\tau = 800$, these two points achieve a similar drag reduction at $\approx 37\%$, showing the larger reduction in DR at smaller κ_x^+.

In general the increase in the Reynolds number causes the optimal DR parameters to move towards higher forcing frequencies (both temporal and spatial) for the wall oscillation and travelling wave cases. The optimal travelling wave case, however moves to larger κ_x^+ and smaller ω^+. These findings agree with a similar study recently published [Gatti and Quadrio, 2013]. The accuracy of the results of this study is relatively unknown due to the use of minimal channel flow, although the fact that the two studies agree help validate the results. As the current work uses full size channel flow, these results are considered to be highly accurate. The fact that minimal channel flow results do give a strong indication of the changing DR with Reynolds number, suggests that the drag reduction is not heavily dependent on the large scale structures which are not correctly captured by this form of simulation. This is understandable as the spanwise motions tend to be limited to a very thin layer near the wall, and targets near-wall turbulence.

Decay of Drag Reduction

In order to have an impression of the drag reductions that can be achieved at high Reynolds numbers it is useful to quantify the decay in the drag reduction. As discussed previously, this study has found that the optimal parameters change as the Reynolds number increases. This is linked to the notion that there are differing

rates of decay when different values of the control parameters are used. A scaling of the form $Re_\tau^{-\alpha}$ is calculated at the points straddling the optimal control parameters, to quantify the effect of the Reynolds number. For the wall oscillation Choi et al. [2002] suggested a general scaling of $\alpha = 0.2$, which was originally used to scale the S^+ parameter. This scaling has been recently supported by DNS study of the optimal wall forcing case up to $Re_\tau = 1000$ [Agostini et al., 2014].A large value of α corresponds to a large reduction in DR as the Reynolds number increases and can therefore be interpreted as an unfavourable scaling (ie. the drag reduction decays rapidly with increased Reynolds number).

(a)	ω^+	0.03	0.06	0.12	(b)	κ_x^+	0.004	0.006	0.008
	$DR \sim$	$Re_\tau^{-0.31}$	$Re_\tau^{-0.26}$	$Re_\tau^{-0.14}$		$DR \sim$	$Re_\tau^{-0.38}$	$Re_\tau^{-0.18}$	$Re_\tau^{-0.13}$

Table 5.1: DR scalings for (a) wall oscillation and (b) the standing wave.

(a)	ω^+	0.01	0.02	0.03	(b)	κ_x^+	0.004	0.008	0.016
	$DR \sim$	$Re_\tau^{-0.17}$	$Re_\tau^{-0.22}$	$Re_\tau^{-0.38}$		$DR \sim$	$Re_\tau^{-0.38}$	$Re_\tau^{-0.22}$	$Re_\tau^{-0.11}$

Table 5.2: DR scalings for (a) the horizontal line through the map with $\kappa_x^+ = 0.008$ and (b) the vertical line with $\omega^+ = 0.02$.

The calculated scalings for wall oscillation control are shown in table 5.1a, and emphasise the fact that the scaling is much worse at lower values of ω^+. These results agree that the scaling is approximately $\alpha = 0.2$ for the near-optimal travelling wave case [Choi et al., 2002; Agostini et al., 2014]. Belan and Quadrio [2013] used a RANS-predictor model to show that, although a scaling of $\alpha = 0.2$ is seen at low Reynolds number (up to $5Re_0$), when considering a higher Reynolds number range of $100Re_0$ the scaling reduces to $\alpha = 0.04$. Table 5.1b shows the possible Reynolds number scalings for the standing wave at different κ_x^+ values. Similarly to the wall oscillation case, the DR for the standing wave case is also seen to be affected more by the Reynolds number at lower values of κ_x, where there are large values of α in the

scaling. This illustrates how the optimal value of κ_x^+ is increasing with increased Re. The scaling around the region of optimal DR for the standing wave is better than for the wall oscillation, hinting that, at higher Reynolds number, the standing wave may remain a more advantageous control method. However, this may be an artefact of the parameters studied. Table 5.2 shows the values of the scalings calculated for the travelling wave, emphasising the variation of the scaling dependent on the oscillation parameters. The scaling is better for smaller ω^+ and larger κ_x^+. The main impact of this is that, although the DR is reducing as the Reynolds number is increased, and the scaling is strong at the optimal control parameters, by adjusting the control parameters correctly, the scaling with Reynolds number is improved. This means that, at a higher value of Re_τ, using the parameters which were not optimal at low Reynolds number gives a more favourable drag reduction. In the wall oscillation and standing wave case, lower values of ω^+ and κ_x^+ have higher α values, hence the drag reduction deteriorates more rapidly as the Reynolds number is increased. This in fact means that the magnitude of the drag increase achieved, when using small values of the forcing parameters, is reducing at a faster rate than the drag reduction. This implies that the region of the parameter space in which the drag increase is found diminishes as the Reynolds number is increased, and is confirmed in figures 5.11 and 5.12.

The drag reduction is scaled by the $Re_\tau = 200$ case and plotted against Reynolds number in figure 5.13. Figure 5.13a shows results from the wall oscillation, with a large difference of scaling for this case alone. It was suggested by Ricco and Quadrio [2008] that a stronger effect of Reynolds number occurs for smaller ω^+ (large T^+). Due to the fact that a reduction in the drag increase also occurs, there is a location in which there is no Reynolds number effect between the values of ω^+ with maximum drag reduction and increase. This implies that the scaling does not simply get stronger with reduced ω^+ in the whole domain. Looking at the $\omega^+ = 0.06$ case in figure 5.13a, there is a slight decrease in the rate of the decay, even with this

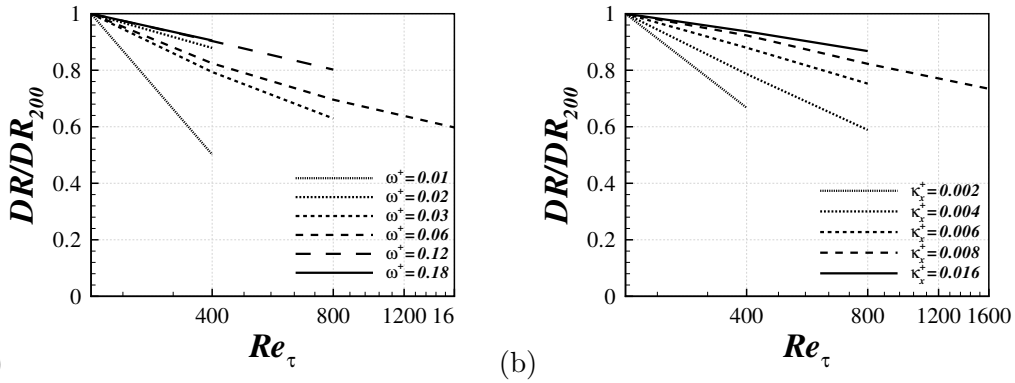

Figure 5.13: Change in drag reduction with Re_τ scaled by the results from the $Re_\tau = 200$ case. Results are shown for wall oscillation (a) and the standing wave (b). A longer dash length corresponds to a larger forcing parameter; ω^+ for wall oscillation and κ_x^+ for the standing wave.

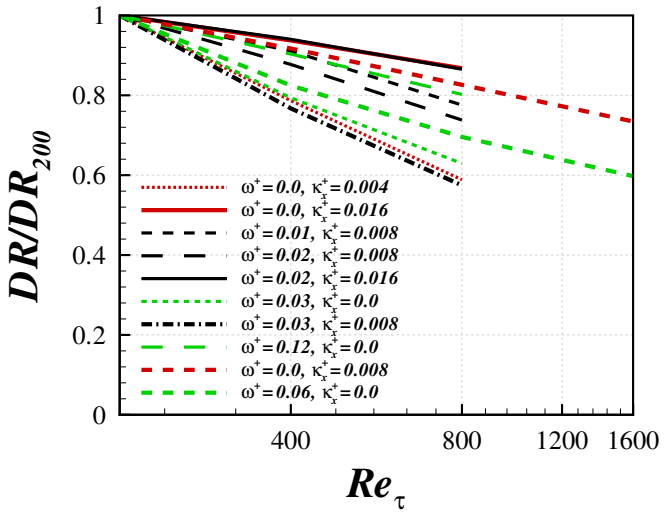

Figure 5.14: Change in drag reduction with Re_τ scaled by the results from the $Re_\tau = 200$ case, for all cases taken to $Re_\tau = 800$ and above.

logarithmic representation. This suggests that this power scaling may not be correct and agrees with the model of Belan and Quadrio [2013] that the decay reduces at higher Reynolds number. [Iwamoto et al., 2005] studied the effect of diminishing the near-wall velocity fluctuations by active feedback control and found that the decay in drag reduction was a low Reynolds number effect. This also agrees with the suggestion of Laadhari et al. [1994] that at higher Re the near-wall turbulence

cycle has less effect on the overall flow due to the influence of outer scales.

The results from the standing wave simulations are also shown, figure 5.13b, showing an increase in Reynolds scaling as κ_x^+ becomes smaller. This is likely due to the limit on the minimum value of κ_x^+ studied, and is expected to behave similarly to that of wall oscillation.

Figure 5.14 shows the values of the drag reduction at the four Reynolds numbers studied. The data is normalised by the drag reduction achieved in the $Re_\tau = 200$ case. This highlights the difference in scalings dependent on the forcing parameters chosen. The scaling is not necessarily limited to the range shown in this figure as this only shows the cases studied to $Re_\tau = 800$ and higher. It is possible that there is a larger range in the scalings than presented.

5.2.2 Oscillation in Drag Reduction

In order to better understand Reynolds-number effects, the flow physics must be considered. The wall oscillation case is used here as an example, with the premise that the ideas can be extended to the general travelling wave. It has been shown that, when the oscillation is applied for large time periods (corresponding to small ω^+), substantial oscillations occur in the skin-friction [Jung et al., 1992]. This is due to the turbulence responding to the wall motion, and an increase of turbulent intensity in the new shear direction. At certain points throughout the oscillation drag is increased, and can lead to an overall drag increase when ω^+ is sufficiently small (figure 5.11a). Figure 5.15a shows the initial response of the skin-friction to the wall oscillation, normalised by $C_{f,0}$, the skin friction from the no-control case. The level of oscillation in this parameter is seen to increase as the Reynolds number is increased. This suggests that the oscillation in the drag reduction does not scale with wall units, and therefore the drag achieved rapidly deteriorates as Re increases, at the optimal parameters. Another interesting point from this figure is that the rate of the initial decay in C_f is very similar at all Reynolds numbers. However this

decay is sustained for longer at the lower values of Re.

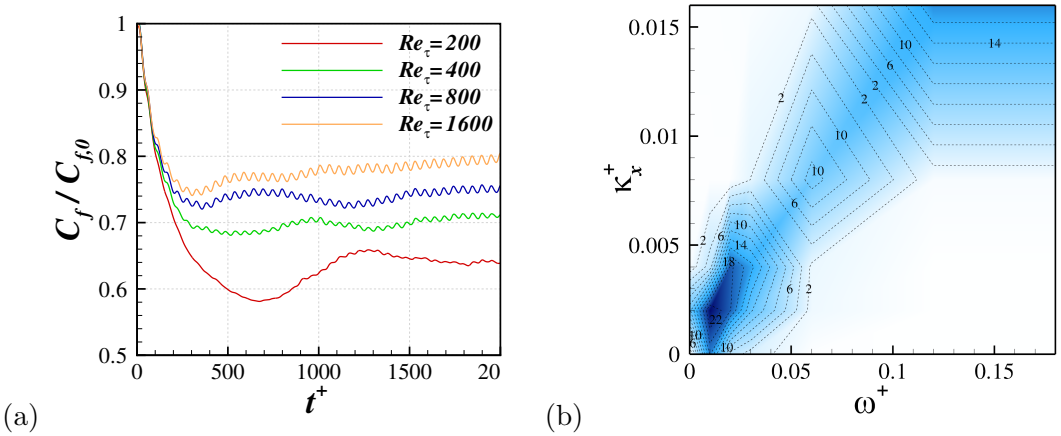

Figure 5.15: Initial response of skin-friction (normalised by the no-control case) at the four Reynolds numbers (a). The forcing used is the near-optimal wall oscillation case from $Re_\tau = 200$, with $\omega^+ = 0.06$. Amplitude of the oscillation in the percentage drag reduction, δ_{DR} $Re_\tau = 200$ (b).

The amplitude of the oscillation in the percentage drag reduction, δ_{DR}, is quantified by taking the difference between the maximum and minimum value of the DR found within an oscillation period. This can be defined as:

$$\delta_{DR} = \overline{DR}_{max} - \overline{DR}_{min},$$

where $\overline{DR}$ is the phase-averaged drag reduction, taken over the oscillation period (Note that this also defines an oscillation in a drag increase as DI is considered as -DR). This is temporal in the wall oscillation cases, but is the spatial maxima and minima in the standing and travelling wave cases. Figure 5.15b shows the amplitude of this oscillation in DR parameter at different forcing parameters. This is fairly discontinuous due to the large range and coarse mapping over the parameter space. The general trend is that there is a high level of oscillation in DR in a certain range of wave-speeds c. The amplitude of the oscillation in DR is large in a similar region to where the drag increase is seen.

Figure 5.16a shows the amplitude of the oscillation in the drag reduction for

the wall oscillation cases. For large ω^+, the oscillation is almost zero. As the forcing frequency decreases there is a greater oscillation in the drag reduction, a growth which appears exponential. As the Reynolds number is increased the amplitude of DR increases when $0.02 \leq \omega^+$. This has been seen up to $Re_\tau = 1600$ in the initial response of the $\omega^+ = 0.06$ case, figure 5.15a. At $\omega^+ = 0.01$ the amplitude in the drag is seen to decrease with an increase of Re. The amplitude in drag reduction for the standing wave cases are shown in figure 5.16b. The behaviour is similar to the wall oscillation cases, in that the oscillation of DR increases as the wavenumber decreases. As the Reynolds number is increased the value of δ_{DR} increases for all the cases studied here. At $\kappa_x^+ = 0.002$ the increased oscillation from $Re_\tau = 200$ to 400 is larger than from $Re_\tau = 400$ to 800, suggesting a behaviour similar to the low ω^+ wall oscillation cases at small κ_x^+. This hints that there may be values at which the oscillation also decreases with Reynolds number.

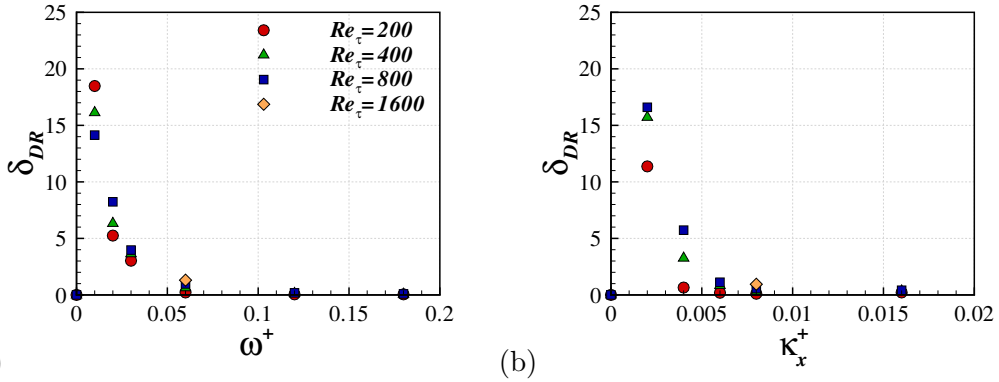

(a) (b)

Figure 5.16: Drag reduction oscillation at the four Reynolds numbers studied for (a) the wall oscillation case, $\kappa_x^+ = 0$, and (b) the standing wave case, $\omega^+ = 0$.

The amplitude of the oscillation in the drag reduction is shown for the travelling wave cases in figure 5.17a, with fixed $\kappa_x^+ = 0.008$ and varying temporal frequency. The standing wave case with this wavenumber (when $\omega^+ = 0$) has very small oscillation in the drag. This δ_{DR} value increases with increased ω^+ reaching a maximum of 11% when $\omega^+ = 0.06$ at $Re_\tau = 200$. As the temporal frequency increases further the oscillation of DR decreases to zero. The amplitude increases

with Reynolds for $\omega^+ < 0.06$, but actually decreases at $\omega^+ \geq 0.06$. This means that either the maximum oscillation decreases and the region in which the amplitude is large increases, or the maximum value moves to smaller ω^+. When studying the effect of changing κ_x^+ and fixing $\omega^+ = 0.02$, figure 5.17b, similar behaviour occurs. The wall oscillation case has moderate level of variation (5% at $Re_\tau = 200$), this increases with κ_x^+ reaching a maximum at $\kappa_x^+ = 0.004$. When the spatial wavenumber becomes larger still, the δ_{DR} decreases to zero. As the Reynolds number increases the amplitude of the DR oscillation at the $\kappa_x^+ = 0.002$ case increases, whereas at $\kappa_x^+ = 0.004$ it initially increases as Re_τ becomes 400, and then reduces again as Re_τ becomes 800. This change in δ_{DR} gives the impression that the maximum amplitude is increasing in κ_x^+ as the Reynolds number is increased.

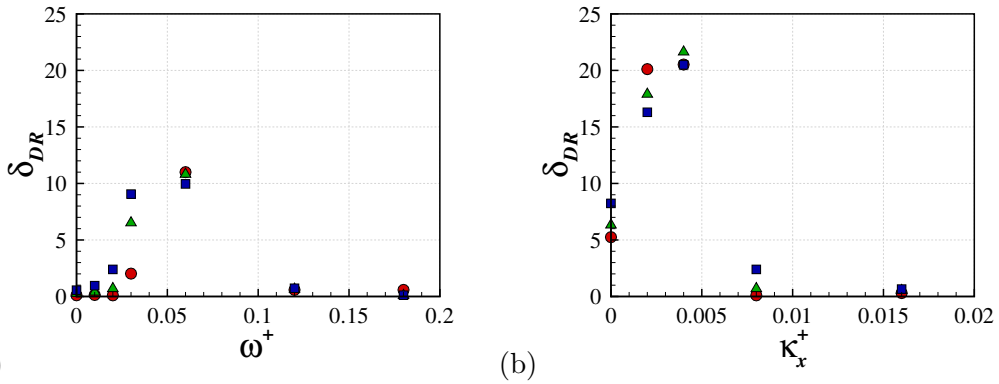

Figure 5.17: Drag reduction oscillation at the four Reynolds numbers studied for the travelling wave cases at (a) a horizontal line through the map with $\kappa_x^+ = 0.008$ and (b) a vertical line through the map with $\omega^+ = 0.02$.

The interesting feature about this amplitude in DR oscillation is that it becomes large in the region in which the drag increase occurs. At these combinations of the forcing parameters the oscillations in the DR may be linked to the mechanism which causes this reduction in the DR (or which causes the drag increase). This hints at the idea that there are two features within the flow. A drag reducing mechanism (which may be related to the laminar solution and S^+ parameter) and a drag increasing mechanism linked to this oscillation in skin-friction.

As the Reynolds number is increased the control parameters with large δ_{DR} vary. A greater oscillation in DR occurs at higher ω^+ and κ_x^+ for the wall oscillation and standing wave cases respectively. The movement of this amplitude is similar to the Reynolds number effect on the DR implying a possible relationship between the movement of the maxima and this change in δ_{DR} with Re.

5.2.3 Relationship Between Spatial and Temporal Forcing

The main reason for using standing waves is that, when the flow moves over the wall with a fixed wave of spanwise velocity, the near-wall structures effectively feel a spanwise velocity similar to the wall oscillation case. With this idea at the heart of the development of flow control using standing waves, Viotti et al. [2009] proposed a velocity $\mathcal{U}$ which could be used to relate the temporal and spatial forcing techniques in the form $\omega^+ = \mathcal{U}^+\kappa_x^+$. Although unknown whether a wall unit scaling is best suited, a scaling of $\mathcal{U}^+ = 10$ was applied to show that, although the drag reduction of the standing wave is considerably larger, the optimal values could be related in this manner.

Figure 5.18a shows the results from the current study at $Re_\tau = 200$. The κ_x^+ values from the standing wave cases are scaled by $\mathcal{U}^+ = 10$ and the drag reduction is scaled by 0.77. This DR scaling was chosen so that the $\kappa_x^+ = 0.006$ and $\omega^+ = 0.06$ cases agree. Although the scaling equates the maximum drag reduction levels, the values still differ for both $\omega^+ < 0.06$ and $\omega^+ > 0.06$. This gives the impression that the two types of forcing do not behave in the same way, even though the DR changes in a similar fashion. At $Re_\tau = 400$ and 800, figures 5.18b and 5.18c, the two forcing strategies appear to relate in a similar way. Although the optimal values vary, it looks possible (though not conclusive due to the available data), that the $\mathcal{U}^+ = 10$ scaling does relate the maxima. Interestingly, the 0.77 scaling of DR also gives a reasonable relationship between the optimal values. A $\mathcal{U}^+$ scaling of this form suggests that the mechanism for the drag reduction, and also the Reynolds number

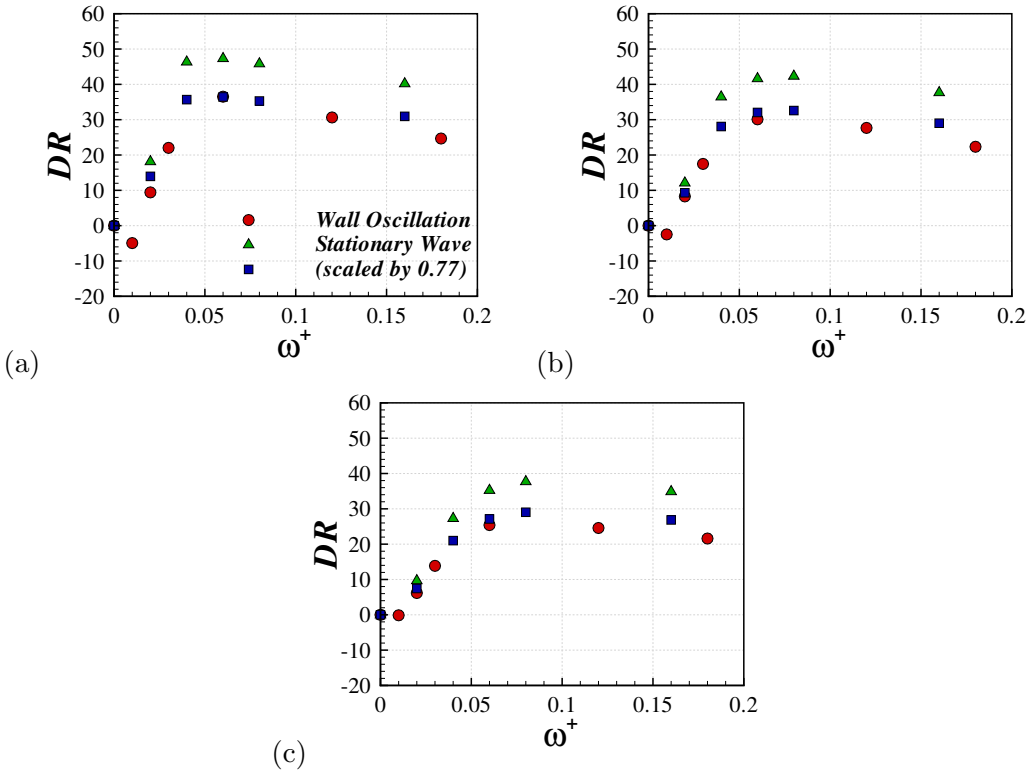

Figure 5.18: The drag reduction for the wall oscillation is compared to the standing wave using $\mathcal{U}^+ = 10$. To aid the comparison, the drag reduction from the standing wave is multiplied by 0.77. Cases are shown with $Re_\tau = 200$ (a), $Re_\tau = 400$ (b) and $Re_\tau = 800$ (c).

scaling, is dependent on wall units and therefore based on near-wall phenomena.

5.2.4 Power Spent

The percentage power spent for the flow control technique can be calculated using the following equation

$$P_{sp} = \frac{\langle w_w \tau_z \rangle_{x,z,t}}{U_b \tau_{x,0}} \times 100\%,$$

where w_w is the wall velocity, U_b is the bulk velocity, τ_z is the spanwise wall shear stress and $\tau_{x,0}$ is the streamwise wall shear stress from the base flow. The average, $\langle \cdot \rangle_{x,z,t}$, is taken over space and time. Figures 5.19 and 5.20 shows the power spent for the wall forcing at $Re_\tau = 200, 400$ and 800. At the lower Reynolds number, the

minimum is found to be 31% at the forcing parameters which achieved the optimum drag reduction. The value of P_{sp} is reduced universally both at $Re_\tau = 400$ and 800, agreeing with results from the wall oscillation case presented by Ricco and Quadrio [2008].

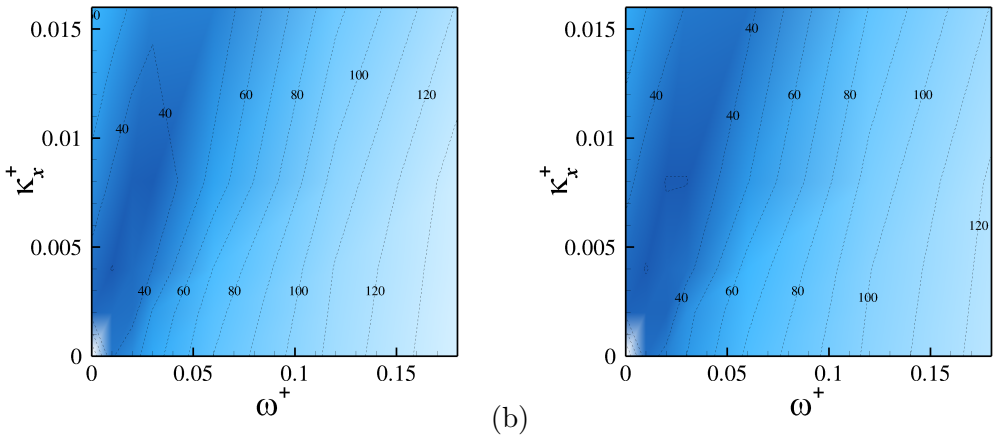

(a) (b)

Figure 5.19: Map of power spent for the forward travelling waves at (a) $Re_\tau = 200$ and (b) $Re_\tau = 400$. Contour levels are drawn at 10% intervals.

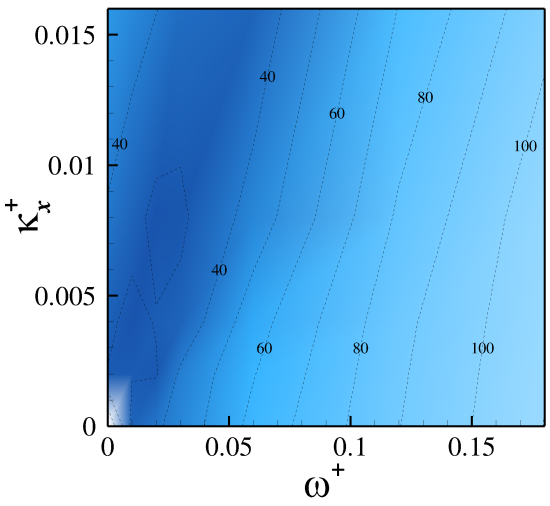

(a)

Figure 5.20: Map of power spent for the forward travelling waves at $Re_\tau = 800$. Contour levels are drawn at 10% intervals.

Figure 5.21a shows the power spent by the wall oscillation case, with varying Reynolds number. A monotonic increase of P_{sp} is seen with increasing w^+. As the

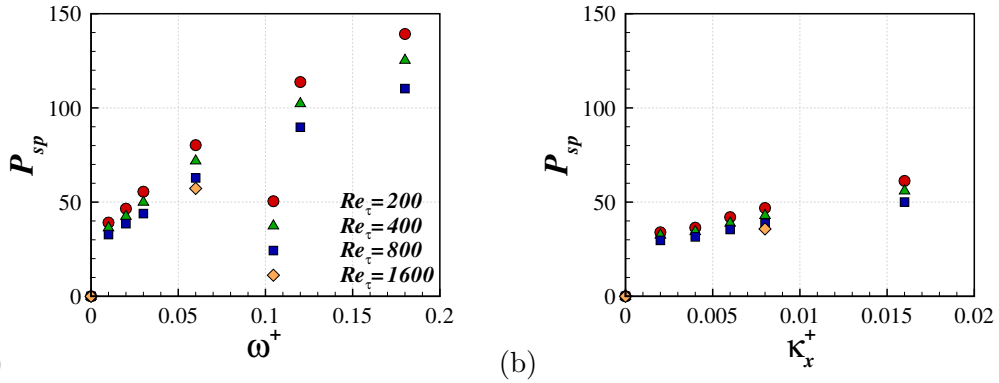

Figure 5.21: Power spent at the four Reynolds numbers studied for (a) the wall oscillation case, $\kappa_x^+ = 0$, and (b) the standing wave case, $\omega^+ = 0$.

Reynolds number increases the percentage power spent reduces. Figure 5.21b shows results for the standing wave case. It is clear that the power spent is much smaller than for the wall oscillation in the region studied, as shown by Viotti et al. [2009], and given that a larger drag reduction is achieved, is therefore a much more efficient waveform. Similarly to the wall oscillation, the power spent for the standing wave increases with κ_x^+, albeit a small increase. Figure 5.22 shows the power spent for the travelling wave cases. In both the horizontal and vertical directions in the map, a minimum is found at $\omega^+ = 0.02$ and $\kappa_x^+ = 0.008$. This minimum is achieved by using the same control parameters for all of the Reynolds numbers simulated.

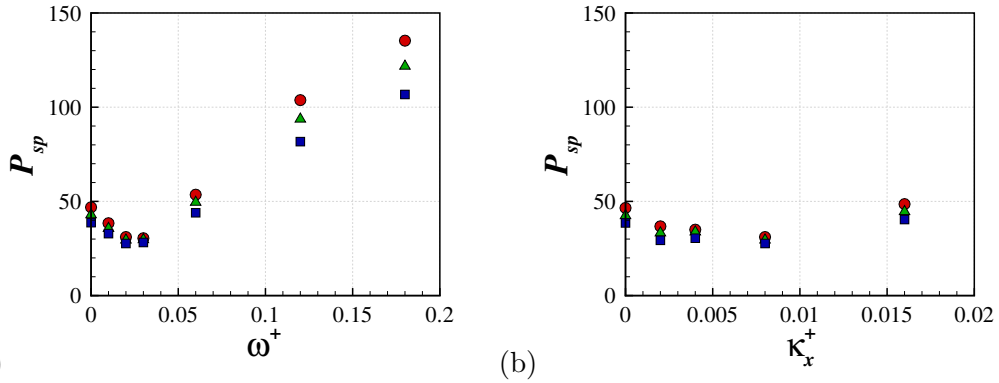

Figure 5.22: Power spent at the four Reynolds numbers studied for the travelling wave cases at (a) a horizontal line through the map with $\kappa_x^+ = 0.008$ and (b) a vertical line through the map with $\omega^+ = 0.02$.

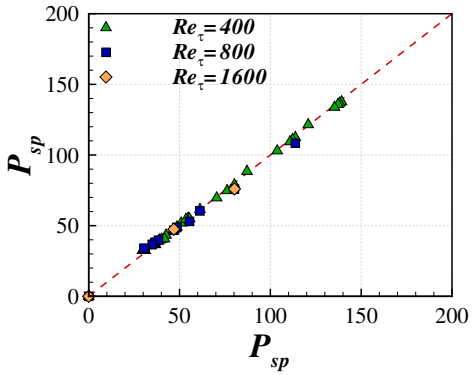

Figure 5.23: Power spent from the $Re_\tau = 200$ simulations plotted against the required power from the higher Reynolds number simulations, scaled using $Re_\tau^{-0.16}$

From the power spent calculated at each Reynolds number it appears as if there could be a simple scaling which could explain the reduction in P_{sp} as the Reynolds number increases. Figure 5.23 compares the values found at the lower Reynolds number to those at $Re_\tau = 200$ and 400, scaled by $Re_\tau^{-0.16}$. The scaling is applied from a best fit approximation of the DNS results. This scaling shows that, for each parameter studied, the same value can be used to equate the results from each Reynolds number.

5.2.5 Net Power Saving

The percentage net power saving is calculated using

$$P_{net} = DR - P_{sp}.$$

As the power spent was shown to scale with $Re_\tau^{-0.16}$, and the drag reduction scaled dependent on the parameter in a minimum range of $Re_\tau^{-0.10}$ to $Re_\tau^{-0.38}$, it is clear that the net power saving may be dependent on the location in the map. Due to the values found for some of the forcing parameters P_{net} will be improved. From figure 5.24 an overall reduction in intensity of the net power saving is seen as the frictional Reynolds number changes from 200 to 400. In the region where a net power saving

is achieved at $Re_\tau = 200$, a lower value of P_{net} is found at $Re_\tau = 400$. Similarly for the region of large net power loss, the loss is reduced as the Reynolds number increases.

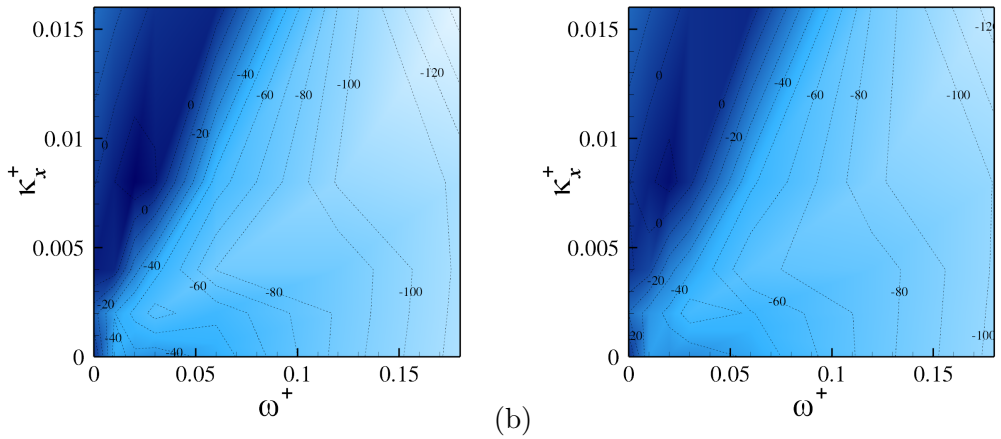

Figure 5.24: Power saving map for the forward travelling waves at (a) $Re_\tau = 200$ and (b) $Re_\tau = 400$. Contour levels are drawn at 10% intervals.

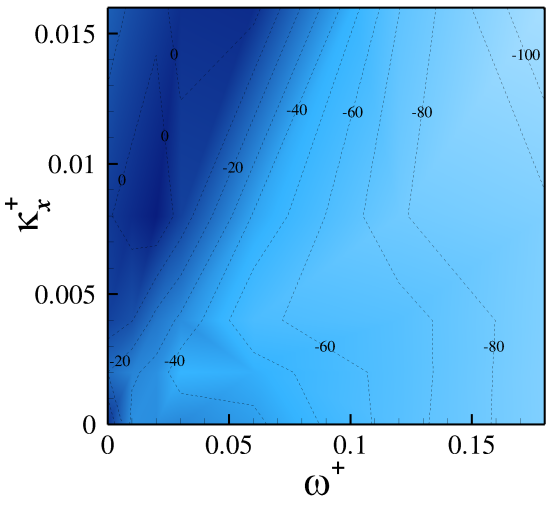

Figure 5.25: Power saving map for the forward travelling waves at $Re_\tau = 800$. Contour levels are drawn at 10% intervals.

The net power saving for the wall oscillation is presented in figure 5.26a. Although a net loss is achieved for all values of ω^+, using $W_m^+ = 12$, a peak is seen at $\omega^+ = 0.03$. As Re is increased the net loss is reduced, for each ω^+, as shown

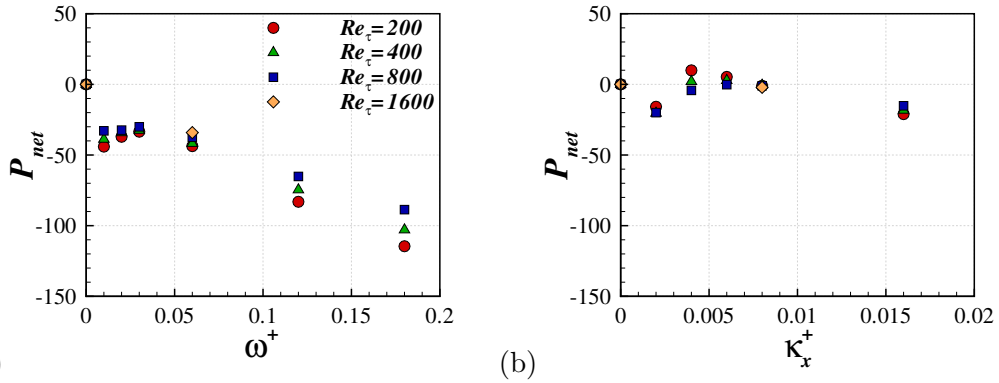

Figure 5.26: Net power saving at the four Reynolds numbers studied for (a) the wall oscillation case, $\kappa_x^+ = 0$, and (b) the standing wave case, $\omega^+ = 0$.

by Ricco and Quadrio [2008]. At $Re_\tau = 200$ the standing wave case achieves a net power saving of 9%, shown in figure 5.26b. This reduces rapidly and at $Re_\tau = 400$ and 800 a gain of 1% and loss of 2% are calculated, respectively. At $\kappa_x^+ = 0.008$ a loss of $\approx 2\%$ is sustained for all three Reynolds numbers, with an increase in P_{net} for $\kappa_x^+ = 0.016$.

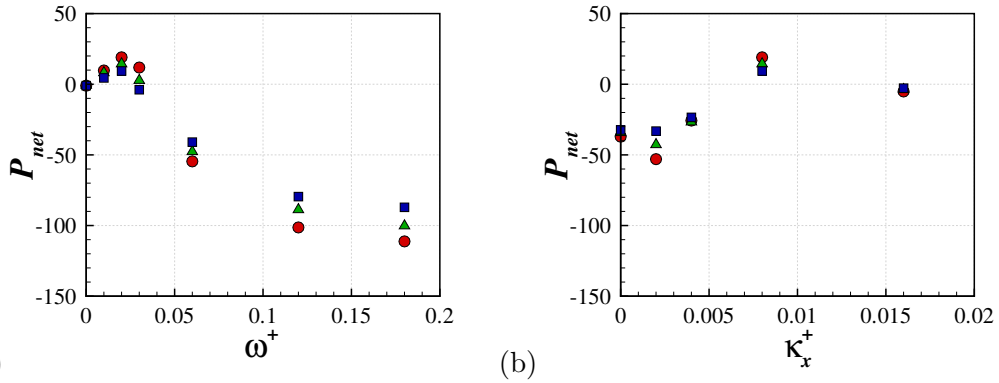

Figure 5.27: Net power saving at the four Reynolds numbers studied for the travelling wave cases at (a) a horizontal line through the map with $\kappa_x^+ = 0.008$ and (b) a vertical line through the map with $\omega^+ = 0.02$.

Figure 5.27 show the results for the travelling wave. At the location of optimal DR a large net power saving of 19% is found at at $Re_\tau = 200$. By $Re_\tau = 400$ this gain has reduced to 14%, and by $Re_\tau = 800$ has reduced further to 9%. Looking at the horizontal line through the parameter space, figure 5.27a, the value of P_{net} is

seen to increase for large ω^+. In the vertical line with $\omega^+ = 0.02$, the power saving increases at larger Re, for small κ^+ values.

5.2.6 Effect of Maximum Wall Velocity

The effect of varying W_m^+ has been studied since Baron and Quadrio [1996]. The drag reduction is increased monotonically with increasing maximum wall velocity. Figure 5.28a shows the change in the drag reduction with W_m^+ at $Re_\tau = 200$. The drag reduction initially increases slowly, but the rate of increase is larger as $W_m^+ > 1$, this then reduces again as W_m^+ becomes large. The main aim of this study is because the drag reduction is decreased as the Reynolds number is increased. The W_m^+ value, when investigating the Reynolds number effect is currently fixed. As the maxima of the velocity fluctuations of the no-control case increase with Reynolds number, even in wall units, it is possible that the maximum wall velocity of the control method does not simply scale in wall units. To test if a different W_m scaling is required, the maximum wall velocity is varied with $\omega^+ = 0.06$ until a drag reduction value is found at $Re_\tau = 200$ similar to the $Re_\tau = 400$ value, forced at the same frequency with $W_m^+ = 12$. For $W_m^+ = 8.5$ and $Re_\tau = 200$ a drag reduction of 30.5% is found, which related well to the 30.1% when $W_m^+ = 12$ and $Re_\tau = 400$.

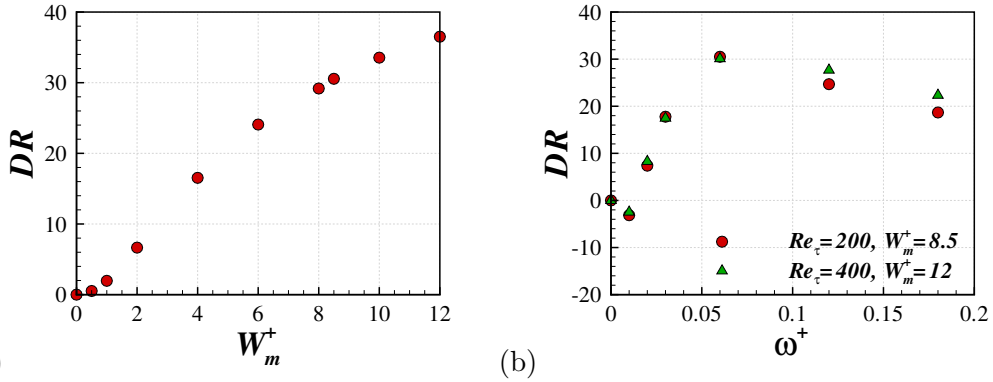

(a) (b)

Figure 5.28: Effect of varying W_m^+ for wall oscillation case with $\omega^+ = 0.06$ at $Re_\tau = 200$ (a), and the comparison of ω^+ variation at $Re_\tau = 200$ with $W_m^+ = 8.5$ and $Re_\tau = 400$ with $W_m^+ = 12$ (b).

Figure 5.28b shows the DR as ω^+ is varied for $W_m^+ = 8.5$ at $Re_\tau = 200$ and $W_m^+ = 12$ at $Re_\tau = 400$. Although, the two curves are similar, the drag reduction in the $Re_\tau = 400$ cases are slightly higher both above and below $\omega^+ = 0.06$. The difference between the cases also appears larger for $\omega^+ > 0.06$, implying that there is some physical difference between the two cases.

5.2.7 Scaling Parameter and Laminar Stokes Solution

The laminar solution to the second Stokes problem is a well known function [Batchelor, 1967] to define the motion of the fluid above a flat oscillating plate, and can be written:

$$w = W_m^+ \exp\left(-y^+\sqrt{\frac{\omega^+}{2}}\right)\sin\left(\omega^+ t^+ - y^+\sqrt{\frac{\omega^+}{2}}\right) \tag{5.1}$$

Using this laminar solution, a parameter was developed by Choi et al. [2002] which was seen to scale well with the drag reduction. This was calculated using a combination the maximum acceleration at a given y^+ location, the distance at which the velocity is above some threshold value, and the maximum wall velocity. This incarnation of the S^+ parameter also included a Reynolds scaling of $Re_\tau^{0.2}$.

$$S^+ = \frac{a_m^+ y_d^+}{W_m^+ Re_\tau^{0.2}} \tag{5.2}$$

The parameter was also adopted by Quadrio and Ricco [2004], where the Reynolds scaling was ignored and the variable parameters were chosen to give the best fit to their drag reduction data, choosing $W_{th}^+ = 1.2$ and $y_d^+ = 6.3$. The justification for this threshold value was that it was similar to the maximum in the spanwise velocity rms profile from the no-control flow. A linear fit of $DR = 131S^+ - 2.7$ was used to relate the input parameters to the drag reduction, with the condition that $T^+ < 150$.

Figure 5.29a shows the S^+ parameter plotted against the drag reduction for

the four Reynolds number studied. The plotted points are shown only for points which satisfy $T^+ < 150$. At $Re_\tau = 200$ the cases are from $W_m^+ = 8.5$ and 12 with varying $\omega^+ = 0.06, 0.12$ and 0.18, as well as the effect of changing W_m^+ with fixed $\omega^+ = 0.06$. At the higher Reynolds numbers the available frequencies are plotted with $W_m^+ = 12$. The dashed line represents the linear scaling found by Quadrio and Ricco [2004]. This agrees reasonably well with the results from the $Re_\tau = 200$ cases, although the DR values are slightly high when S^+ is large (also seen by Touber and Leschziner [2012]). Although the relationship is known to break down for large time periods, the effect of small W_m^+ is not commonly discussed. It is seen here that, in the $Re_\tau = 200$, the $S^+ - DR$ correlation is certainly not linear for small W_m^+, which is also clear from the requirement to pass through the origin (due to the no control case). This suggests that the scaling of this parameter with small maximum wall velocity is incorrect, although well approximated at reasonable W_m^+ values. The effect of the increase in Reynolds number also causes concern with the propriety of the S^+ parameter. When this does not include any scaling, and as the DR is seen to decrease with increasing Re, the correlation diminishes at higher Reynolds numbers [Touber and Leschziner, 2012].

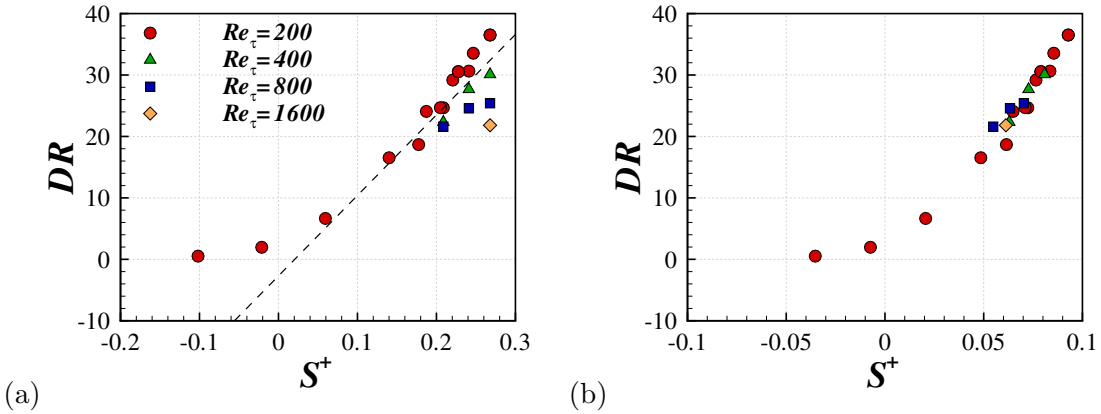

Figure 5.29: S^+ parameter from the four Reynolds numbers (a) and the $Re_\tau^{-0.2}$ scaled S^+ parameter (b).

When the scaling included by Choi et al. [2002] is used, there is definitely an

improvement in the relationship, based on the available data, figure 5.29b. This kind of scaling is not believed to be effective because of the clear difference in Reynolds number scalings found in the current study, depending on the forcing parameter used. Evidence for this is that, for the $\omega^+ = 0.18$ case at $Re_\tau = 800$, the data point lies slightly out of the correlation line. The reason for this possible fit for the majority of the frequencies studied is that, the scaling is appropriate around $\omega^+ = 0.06$.

Touber and Leschziner [2012] also showed that for large T^+ the mean spanwise velocity profile deviates from the laminar Stokes solution. This is a reason why the S^+ scaling does not work at these forcing parameters, as it is derived from the laminar flow. Figure 5.30a shows the laminar solution to the mean spanwise velocity profiles of the turbulent flow at all four Reynolds number when $\omega^+ = 0.06$. At $Re_\tau = 200$ the turbulent and laminar profiles are very similar and, although the change is very slight, the profiles differ more from the Stokes solution as the Reynolds number is increased. This effect is more visible in the $\omega^+ = 0.03$ case, figure 5.30b. The turbulent effects are evident when $Re_\tau = 200$, but the profiles become further from the laminar profiles as Re increases. This change causes there to be smaller gradient in the profile and the turbulent stokes layer thickens.

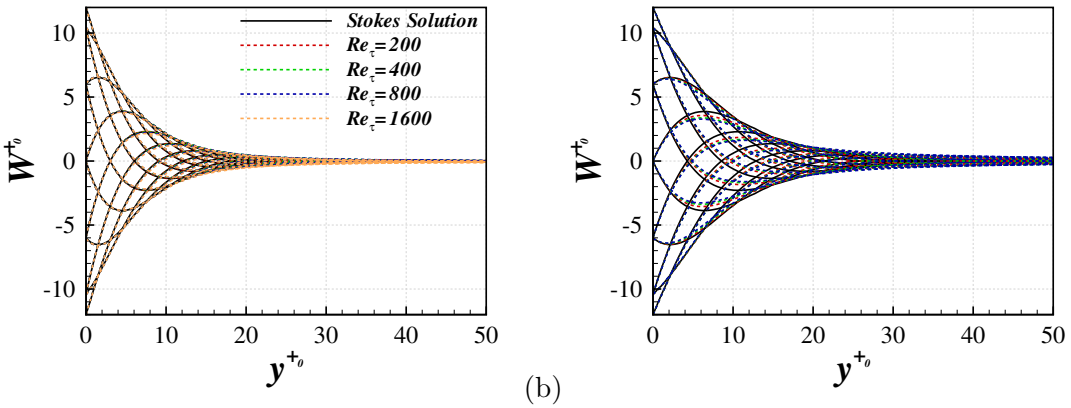

(a) (b)

Figure 5.30: Laminar Stokes solution compared to the turbulent counterparts at various Reynolds numbers for wall oscillation with $\omega^+ = 0.06$ (a) and $\omega^+ = 0.03$ (b).

5.3 Turbulent Statistics

In order to investigate the effect of Reynolds number on the turbulent statistics, various profiles are plotted from simulations with fixed forcing parameters (scaled in wall units). This is limited to the wall oscillation and standing wave cases as these include the highest studied Re data. The results are presented, plotted against y^{+_0}, with the phase averaged mean component removed, and the variables are scaled by the no-control wall units. The results from the no-control cases at each of the Reynolds numbers are also shown, for comparison, and are indicated by the dashed lines where the colour specifies the value of Re_τ.

5.3.1 Wall-Oscillation Case

The wall oscillation case presented here applies forcing at a frequency $\omega^+ = 0.06$. This is approximately the optimum parameter from $Re_\tau = 200$, and remains the optimum at $Re_\tau = 400$ and 800, based on the parameters studied. The drag reductions achieved are $37\%, 30\%, 25\%$ and 22% at the increasing Reynolds numbers, respectively.

Figure 5.31a shows the mean profiles from the four Reynolds numbers. As Re increases the decrease from the control cases reduces near the wall, corresponding to the decay in drag reduction. In the log-law region the higher Reynolds number profiles are increased further from the no-control case.

The streamwise velocity fluctuations are presented in figure 5.31b. The profiles at all Re values are reduced from the no-control case. The difference in the peak values from the control case is larger than the difference in the no-control flow. This corresponds to a stronger decrease in the fluctuations at the lower Reynolds numbers. The peaks are all in similar locations in y^{+_0}, although the lower Re cases are slightly further from the wall.

The v and w fluctuations show similar behaviour, figure 5.32. The amount

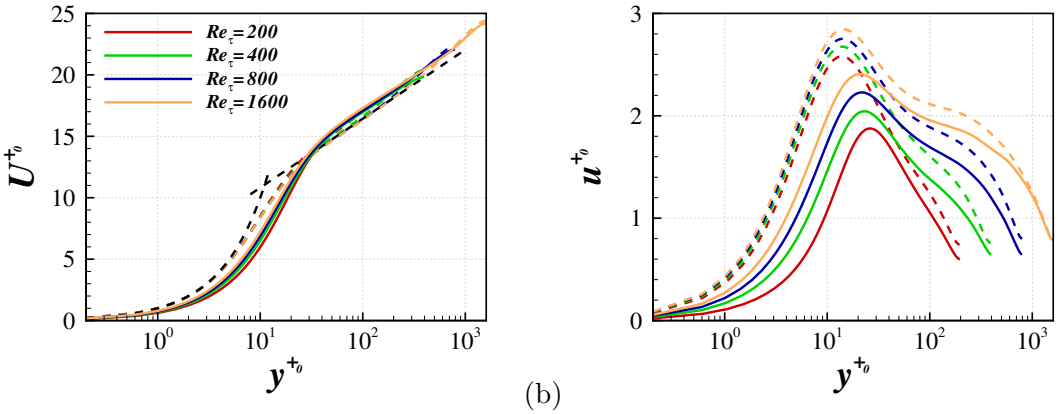

(a) (b)

Figure 5.31: Log-law profiles (a) and streamwise velocity rms profiles (b) for the wall oscillation cases at all four Reynolds numbers. The dashed lines depict the results from the no-control cases, whereas the solid lines show the wall oscillation results.

of reduction from the no-control case decreases at higher Reynolds numbers. The maxima of the spanwise velocity profile, although reduced, move towards the wall and is in a similar y^{+0} location for all four Reynolds numbers.

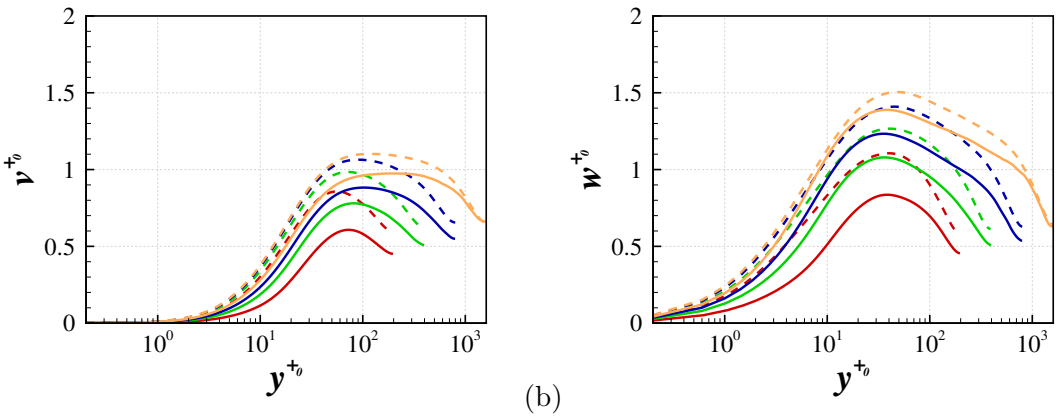

(a) (b)

Figure 5.32: Wall normal velocity rms profiles (a) and spanwise velocity rms profiles (b) for the wall oscillation cases at all four Reynolds numbers. The dashed lines depict the results from the no-control cases, whereas the solid lines show the wall oscillation results.

The streamwise vorticity profiles are shown in figure 5.33a. At $Re_\tau = 200$ and 400 the fluctuations are reduced universally from the no-control case. For $Re_\tau = 800$, although reduced from the no-control profile at the wall, the fluctuations are slightly

increased between the local maximum and minimum. At $Re_\tau = 1600$ this effect is stronger with an increase from the no-control case for $5 < y_0^+ < 15$.

The wall-normal vorticity fluctuations are reduced from the no-control flow for all the Reynolds numbers, figure 5.33b. Although the peaks are at approximately the same value and location for the no-control cases, they vary for the control flow. The $Re_\tau = 200$ case is strongly reduced from the no-control profile near the wall, hence the peak is reduced and moved away from the wall. As the Reynolds number increases the maximum value is reduced to a lesser extent from the no-control flow and is not moved so far from the wall.

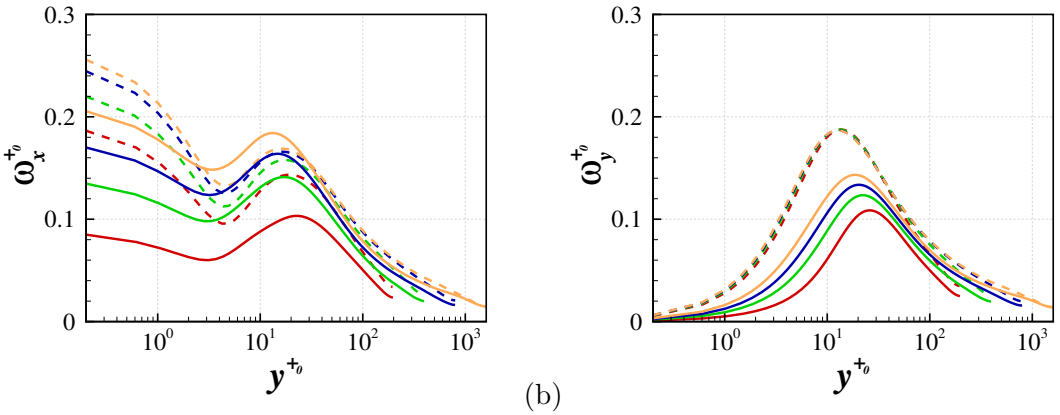

Figure 5.33: Streamwise vorticity rms profiles (a) and wall normal vorticity rms profiles (b) for the wall oscillation cases at all four Reynolds numbers. The dashed lines depict the results from the no-control cases, whereas the solid lines show the wall oscillation results.

Figure 5.34a shows the spanwise vorticity rms profiles from the four Re values. For all the Reynolds numbers the wall value is reduced from the no-control flow. The difference between the wall values in the control flow is much larger than in the no-control cases. This corresponds to a smaller reduction in the fluctuations at higher Reynolds numbers. The $Re_\tau = 200$ case is strongly reduced at the wall, causing the emergence of a peak at $y^{+_0} = 15$. As the Reynolds number increases the peak becomes less prominent and moves towards the wall.

The effect of the change in Re on the Reynolds shear stress for the wall os-

cillation cases is shown in figure 5.34b. The profiles are reduced from the no-control profiles, as expected from the drag reduction. For the $Re_\tau = 1600$ case the profile is curved, following the no-control profile in the outer region. This suggests that the control case is not fully converged, although the skin friction was settled to a steady state. This simulation is ongoing and heavily limited by available computational resources.

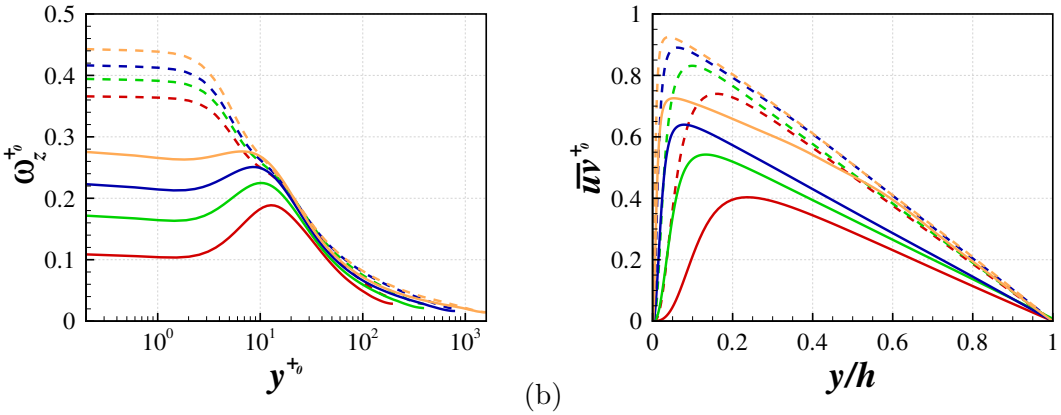

(a) (b)

Figure 5.34: Spanwise vorticity rms profiles (a) and Reynolds shear stress profiles (b) for the wall oscillation cases at all four Reynolds numbers. The dashed lines depict the results from the no-control cases, whereas the solid lines show the wall oscillation results.

5.3.2 Standing-Wave Case

The standing wave case with $\kappa_x^+ = 0.008$ is studied at all four Reynolds numbers. Although not optimal at $Re_\tau = 200$, this parameter gives the maximum drag reduction at $Re_\tau = 400$ and 800. The drag reductions achieved are $46\%, 42\%, 38\%$ and 34% as the Reynolds number increases, respectively.

Figure 5.35a shows the mean streamwise velocity profiles from the standing wave forcing at all four Reynolds numbers. As in the wall oscillation, the profile is reduced further from the no-control flow in the near-wall region at lower Reynolds numbers. The profiles are also increased by a greater amount at the higher Re in the log-law region.

The u rms profiles at the four Reynolds numbers are strongly reduced from the no-control profiles, figure 5.35b. This reduction is stronger at low Reynolds numbers, where the peak is also further from the wall.

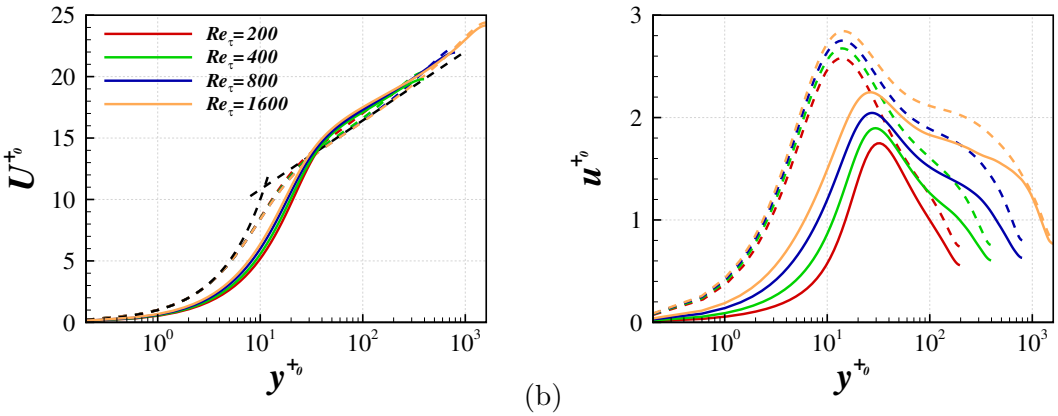

(a) (b)

Figure 5.35: Log-law profiles (a) and streamwise velocity rms profiles (b) for the standing wave cases at all four Reynolds numbers. The dashed lines depict the results from the no-control cases, whereas the solid lines show the results from the standing wave forcing cases.

The wall normal and spanwise velocity fluctuations are also decreased from the no-control case at all four Reynolds numbers, figure 5.36. This decrease is again found to be smaller at the higher Re values.

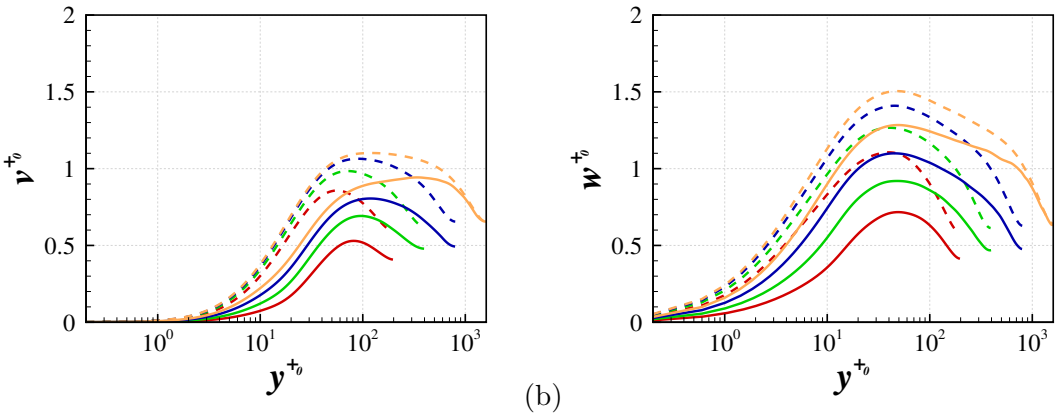

(a) (b)

Figure 5.36: Wall normal velocity rms profiles (a) and spanwise velocity rms profiles (b) for the standing wave cases at all four Reynolds numbers. The dashed lines depict the results from the no-control cases, whereas the solid lines show the results from the standing wave forcing cases.

Figure 5.37a shows the streamwise vorticity profiles of the standing wave cases. At $Re_\tau = 200$ the wall value is greatly reduced from the no-control case causing the local minimum the be less pronounced, and the local maximum is moved away from the wall. As the Reynolds number is increased the reduction of the profiles from the no-control flow decreases. At $Re_\tau = 800$ the profile is reduced universally, but by $Re_\tau = 1600$ the fluctuations are increased for $2 < y^{+0} < 15$, flattening the near-wall profile.

The response of the wall normal vorticity fluctuations are shown in figure 5.37b. As in the wall oscillation study the profiles are decreased and the peaks moved away from the wall. This change is stronger at the lower Reynolds numbers.

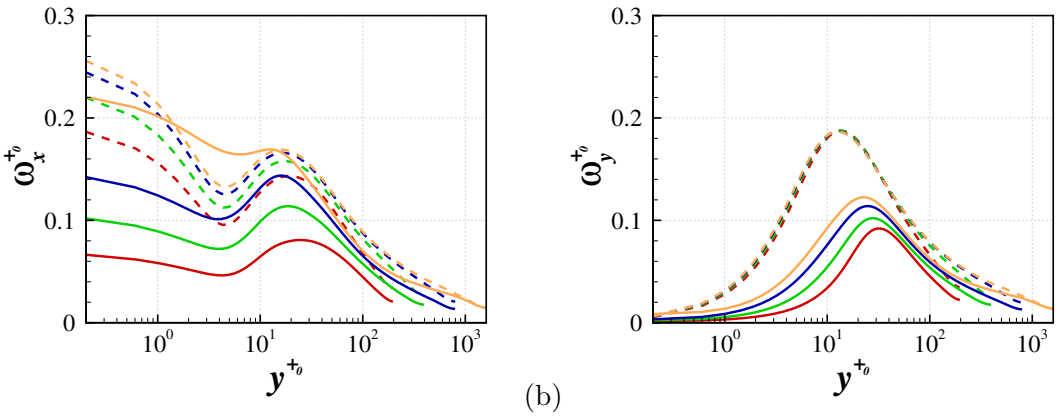

(a) (b)

Figure 5.37: Streamwise vorticity rms profiles (a) and wall normal vorticity rms profiles (b) for the standing wave cases at all four Reynolds numbers. The dashed lines depict the results from the no-control cases, whereas the solid lines show the results from the standing wave forcing cases.

The spanwise vorticity profile for the $Re_\tau = 200$ case is strongly reduced from the no-control profile, especially in the near-wall region, figure 5.38a. This causes a peak at $y^{+0} = 15$. As the Reynolds number is increased the reduction from the no-control decreases. At $Re_\tau = 1600$ a peak in the profile is still evident.

Figure 5.38b shows the Reynolds shear stress profiles from the standing wave forcing. The profiles are again reduced from the no-control flow. The $Re_\tau =$ 1600case is clearly not converged, hence the similarity to the no-control flow in

the outer region. This simulation is also ongoing.

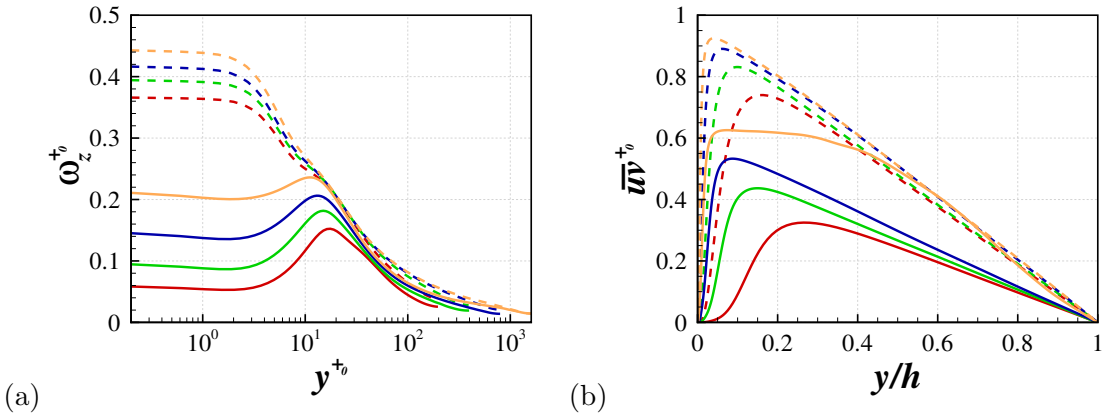

(a) (b)

Figure 5.38: Spanwise vorticity rms profiles (a) and Reynolds shear stress profiles (b) for the standing wave cases at all four Reynolds numbers. The dashed lines depict the results from the no-control cases, whereas the solid lines show the results from the standing wave forcing cases.

5.4 Conclusions

The effect of Reynolds number on the drag reduction, power spent and net power saving were investigated. Although the drag reduction was commonly seen to decay exponentially, the decrease in the DR achieved with increased Reynolds number is not uniform. In the wall oscillation cases the drag reduction around the maximum from $Re_\tau = 200$ reduces more rapidly than at higher ω^+. Despite this, the maximum DR was achieved at $\omega^+ = 0.06$ for $Re_\tau = 200, 400$ and 800. A similar behaviour occurred in the standing wave cases, with the maximum drag reduction actually moving from $\kappa_x^+ = 0.006$ at $Re_\tau = 200$ to $\kappa_x^+ = 0.008$ at $Re_\tau = 400$ and 800. This change in the drag reduction was also seen in the travelling wave cases, where the region of drag increase varied slightly with Reynolds number, causing a change in the optimal values of the forcing parameters. The scaling of the maximum wall velocity was discussed and the incorrect scaling of this parameter was dismissed.

The region of drag increase in the parameter space was also correlated to

an oscillation in the drag reduction over the forcing period. The oscillation in drag reduction over the forcing period, δ_{DR}, was large where the drag increase occurred. The level of oscillation also changed with Reynolds number, becoming greater at large ω^+ and κ_x^+ in the wall oscillation and standing wave forcing, respectively. This oscillation was linked to the deviation of the mean spanwise velocity profile from the laminar flow.

By studying the turbulent statistics, the reduction in the velocity fluctuations from the no-control case was seen to diminish as the Reynolds number was increased. A similar situation occurred in the vorticity profiles, and at the higher Reynolds numbers the streamwise vorticity fluctuations were even increased in a specific wall normal region. This effect was stronger in application of the standing wave forcing.

Chapter 6

Phase-Averaged Turbulent Statistics of Different Types of Wall Forcing at $Re_\tau = 800$

This chapter investigates the in-phase variation of statistical data, comparing the effect of the three different control methods on the turbulent statistics. The time- and space- averaged (1d) profiles have been presented in previous work [Jung et al., 1992; Choi et al., 2002], but this study looks into the change in the statistics over the forcing period. The 2d representation used in this study was presented by Quadrio et al. [2009] and Agostini et al. [2014] to show the difference between two traveling wave cases, one which achieved a drag reduction and one which found a drag increase at $Re_\tau = 200$. The current study is similar but presents results of higher Reynolds number $Re_\tau = 800$, allowing for comparison with the lower Reynolds number results and looking in the differences between the different wall-forcing methods. One of the aims of this investigation is to understand reasons for the oscillation in drag reduction at certain forcing parameter combinations. The Reynolds number is fixed at $Re_\tau = 800$ and the effect of varying the control parameters is investigated. In order

to display the information in its simplest form three subsections are used, separating the study of the wall oscillation, standing wave and travelling wave. These statistics are presented in the representation discussed in section 3.7.1, showing profiles at six points over the first half-period. Because of the nature of this presentation, two cases are compared from each variety of forcing, the optimum drag reduction case and a further case in which the drag reduction begins to deteriorate (i.e. the control parameters are closer to the values which achieve a drag increase than the optimal case). The maximum wall velocity is fixed at $W_m^+ = 12$.

6.1 Wall Oscillation

To understand the effect of the wall oscillation, a comparison is made between the two cases with $\omega^+ = 0.06$ and $\omega^+ = 0.03$. These frequencies correspond to time periods of $T^+ \approx 100$ and $T^+ \approx 200$ respectively. Similar cases have been studied previously at $Re_\tau = 200$, with $T^+ = 100$ widely considered to be the optimal forcing period for wall oscillation [Jung et al., 1992; Choi et al., 2002; Quadrio and Ricco, 2003]. There is an indication that the optimal wall oscillation period is subtly changing as the Reynolds number increases, however based on the forcing parameters studied this remains the optimum (as discussed in section 5.2.1). The wall oscillation with $T^+ = 200$ has also been investigated previously at $Re_\tau = 200$, and at $T^+ \geq 200$ a clear oscillation occurs in the time history of the skin friction [Jung et al., 1992]. As the Reynolds number increases, this oscillation is seen to increase at the two parameter values studied in the current section (discussed in section 5.2.2).

To illustrate the oscillation, the drag reduction is plotted over the time period in figure 6.1. The time averaged drag reduction achieved is 25.4% for $\omega^+ = 0.06$, which drops to 13.9% for $\omega^+ = 0.03$. It is clear that the variation in DR is much larger for the case with lower frequency (higher period) of oscillation. The oscillation

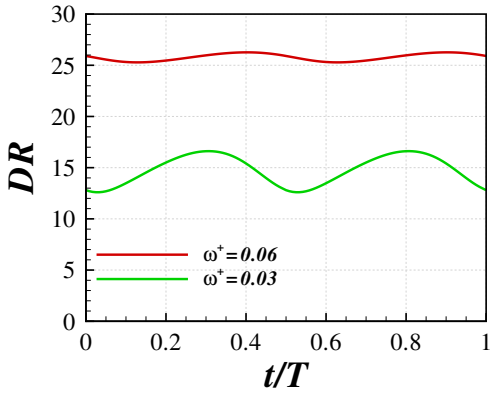

Figure 6.1: Variation of DR over the time period for the frequencies $\omega^+ = 0.06$ and $\omega^+ = 0.03$.

in the drag reduction has a wavelength of half of the oscillation period. This is because the drag reduction is independent of the direction of wall motion and is only related to the change in velocity at the wall. It is also important to note that, between the two forcing frequencies, there is a shift in the maximum and minimum values of DR throughout the period. The $\omega^+ = 0.06$ case takes its minima at $t/T \approx 0.125/0.625$ whereas the $\omega^+ = 0.03$ case takes its minima at $t/T \approx 0.025/0.525$. The fact that the drag reduction is not directly aligned with the phase of the oscillation, suggests that it related to properties within the flow, as opposed to at the wall. The propagation of the wave of spanwise motion into the flow means that at some y height away from the wall there is a delay of the spanwise forcing felt. A hysteresis is also seen in the profile in agreement with the results of Skote [2012], in which the drag reduction phase exists over a longer portion of the period than the drag increase phase. Agostini et al. [2014] attributed this hysteresis to the asymmetric flow skewness.

6.1.1 Mean Profiles

The mean streamwise velocity profile for the $\omega^+ = 0.06$ case is presented in figure 6.2, scaled by the no-control friction velocity. The reduction of drag is visible as

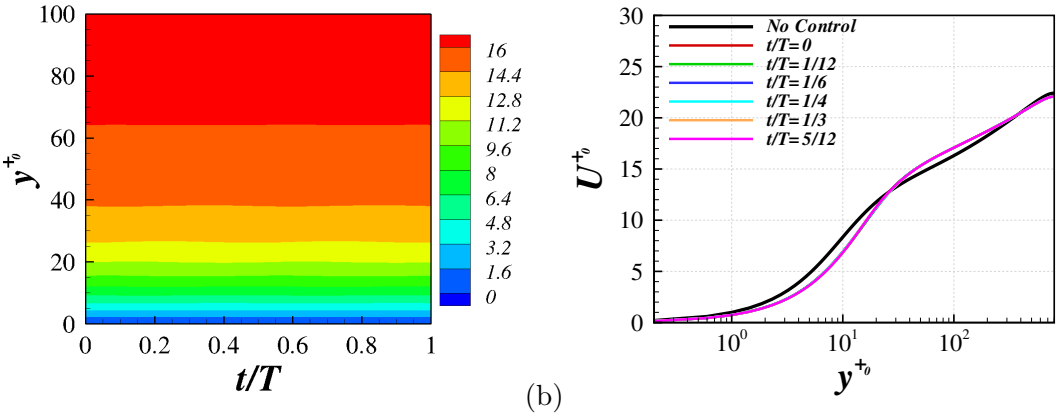

(a) (b)

Figure 6.2: Variation of U^+ over the period for oscillation frequency $\omega^+ = 0.06$ in 2d format (a) and 1d format (b).

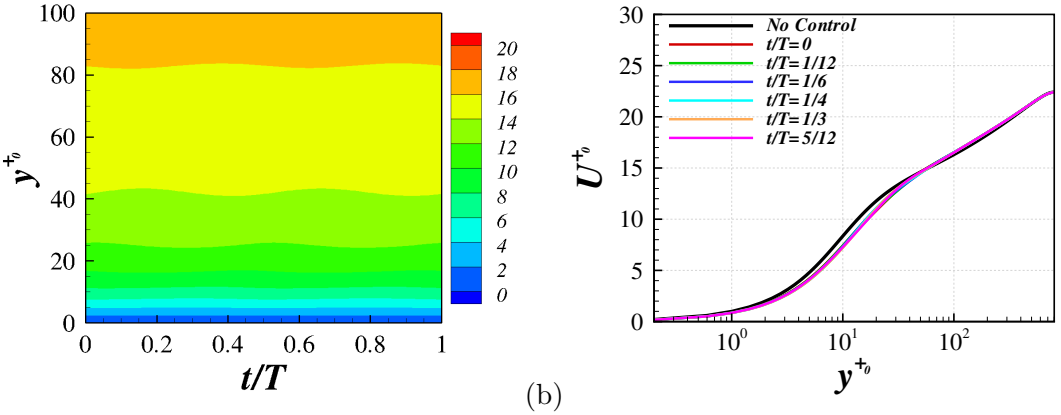

(a) (b)

Figure 6.3: Variation of U^+ over the period for oscillation frequency $\omega^+ = 0.03$ in 2d format (a) and 1d format (b).

a strong decrease in U^+ in the near-wall region from the no-control flow. This is accompanied by an increase in U^+ for $50 < y^+ < 350$, which arises from the fixed mass flow rate, and a slight decrease is observed in the centre of the channel. Figure 6.2 shows that the mean streamwise velocity profile from $\omega^+ = 0.03$ behaves similarly to the near-optimal case. There is a weaker decrease of U^+ near the wall, hence the weaker DR achieved. The increase in U^+ from the no-control data also occurs for $50 < y^+$. This reduction in the near-wall region is commonly seen in the near-optimal case ($T^+ \approx 100$) at lower Reynolds number ($Re_\tau = 200$) [Jung et al., 1992; Baron and Quadrio, 1996] and at $Re_\tau = 500$ [Touber and Leschziner, 2012].

The current scaling is essentially an outer scaling as the normalisation is performed relative to the no-control friction velocity. Baron and Quadrio [1996] and later Ricco et al. [2012] showed that when scaled by the local u_τ, the mean streamwise velocity profile increases away from the wall and is therefore consistent with profiles shown in experimental studies [Choi et al., 1998; Ricco and Wu, 2004]

There is little obvious oscillation in the mean profiles of both forcing frequencies in the 1d plots, whereas the 2d plot for the $\omega^+ = 0.03$ does show some sign of a stronger oscillation in the near-wall region.

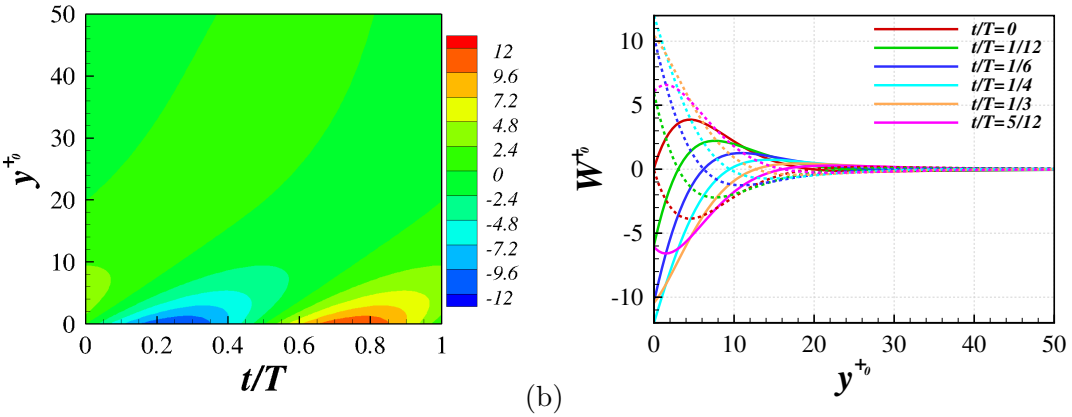

Figure 6.4: Variation of W^+ over the period for oscillation frequency $\omega^+ = 0.06$ in 2d format (a) and 1d format (b). The solid lines represent the time points over the first half period and the dashed lines are from the second half-period.

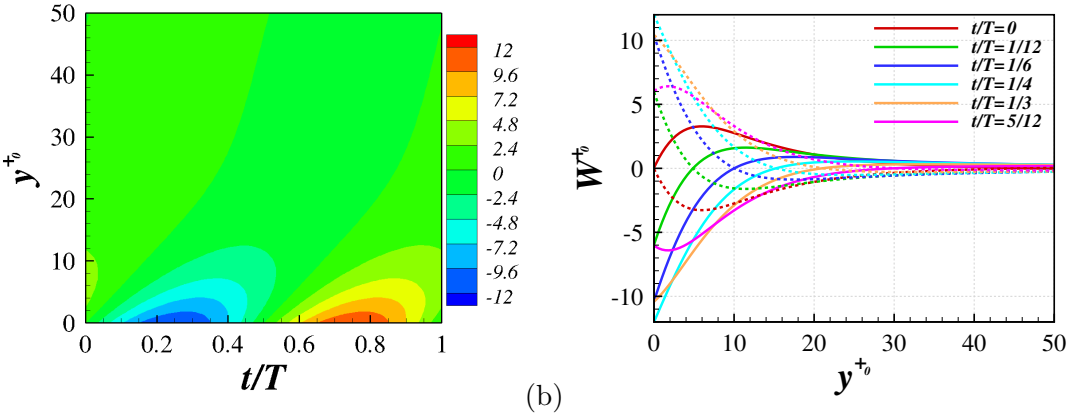

Figure 6.5: Variation of W^+ over the period for oscillation frequency $\omega^+ = 0.03$ in 2d format (a) and 1d format (b). The solid lines represent the time points over the first half period and the dashed lines are from the second half-period.

Figure 6.4 shows the mean spanwise velocity profile from the wall oscillation case with $\omega^+ = 0.06$. Due to the fact that the mean velocity switches between positive and negative wall values over the period, both half-periods are plotted in the 1d plot, but the two line types are therefore symmetric around $W^{+0} = 0$. The initial velocity direction is negative due to the implementation of the travelling wave [Quadrio et al., 2009] (shown in present work in equation 2.6). With $k_x^+ = 0$ this reduces to $w_w^+ = W_m^+ \sin(-\omega^+ t^+)$. The maximum wall velocity $W_m^+ = \pm 12$ is achieved at $t/T = 0.25$ and $t/T = 0.75$. The mean spanwise velocity from the $\omega^+ = 0.03$ case in figure 6.5 shows that the smaller the oscillation frequency, the further the Stokes' layer extends into the domain in y.

The 2d representation of the turbulent statistics in the current section on wall oscillation all show *sloped* contour levels. This is clearest in the mean spanwise profiles (figures 6.4 and 6.5). Due to the temporally changing velocity of fluid at the wall, the near wall fluid is entrained. This entrainment of fluid is strongest near the wall and follows the wall with a temporal decay. The time (x) axis in the 2d plots therefore show that this delay occurs in the turbulent statistics. I similar behaviour is seen in the results at $Re_\tau = 1000$ presented by Agostini et al. [2014].

6.1.2 Velocity Fluctuations

The root-mean-square profile of the streamwise velocity for the $\omega^+ = 0.06$ case is presented in figure 6.6. The u fluctuations are reduced universally from the no-control case and the peak value is moved away from the wall. This reduction in the fluctuations is mainly related to the drag reduction and scaling by the no-control u_τ (essentially an outer scaling). Baron and Quadrio [1996] showed that, at $Re_\tau = 200$, although a reduction in the streamwise fluctuations is seen when this scaling is used, by using a local scaling (based on the time-averaged u_τ of the forced case) the profile is substantially unchanged. Studying the variation over the half-period shows little oscillation in the u-rms profile, although some variation is

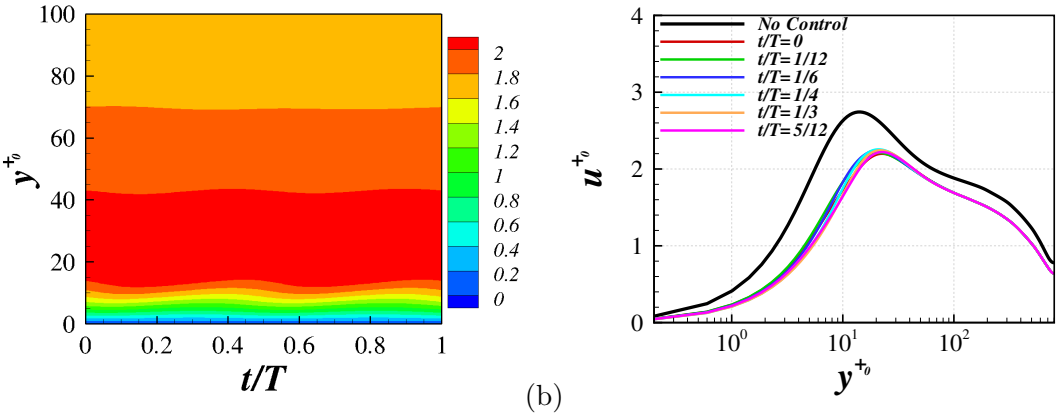

(a) (b)

Figure 6.6: Variation of u^+-rms over the period for oscillation frequency $\omega^+ = 0.06$ in 2d format (a) and 1d format (b).

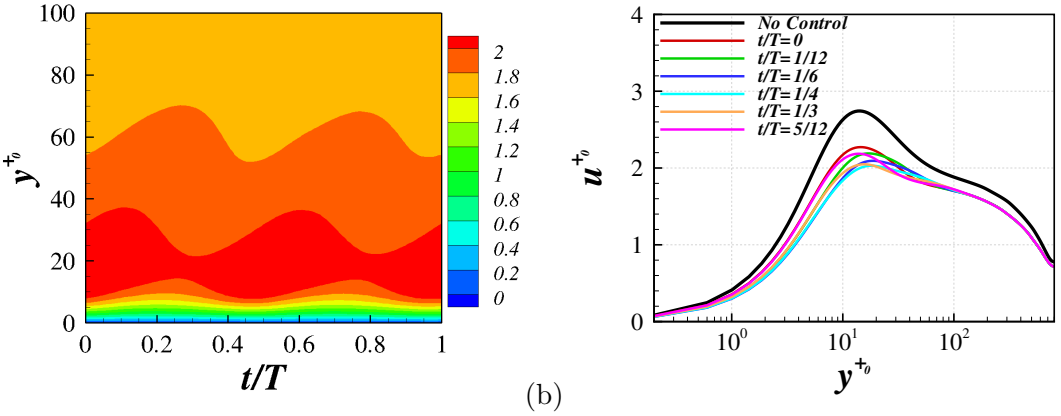

(a) (b)

Figure 6.7: Variation of u^+-rms over the period for oscillation frequency $\omega^+ = 0.03$ in 2d format (a) and 1d format (b).

present in the near-wall region. This oscillation is very small at the y location of the peak value and barely visible above this value. The level of oscillation in the u-rms profile for the $\omega^+ = 0.03$ case is much larger, shown in figure 6.7. This oscillation extends up to $y^+ = 100$, above which the oscillation becomes negligible. This lack of oscillation in the centre of the channel, combined with the idea that there is a large change in the drag reduction over the period, suggests that the turbulence is not changing in time away from the wall and that the oscillation in skin-friction over the period is a near-wall effect.

In turbulent flow streaks of high speed and low speed fluid are visible when

the streamwise velocity is visualised at a fixed wall-normal height. The fluctuations of u are an indication of the strength of the streaks. The near-wall oscillation in the u-rms profile seen in figure 6.7 therefore corresponds to a change in the streak strength over the forcing period. The temporal oscillation of the wall, especially when there is a large time period, has been previously seen to angle the near-wall streaks, shown for the $T^+ = 200$ case at $Re_\tau = 500$ by [Touber and Leschziner, 2012] (discussed in present work in chapter 8). In the steady flow with spanwise pressure gradient applied [Coleman et al., 1996; Holstad et al., 2010] the mean flow direction varies with y location causing a three-dimensional turbulent boundary layer. Using the wall oscillation forcing at larger time periods creates similar three-dimensionality. Because of this wall-normal change in the spanwise velocity, the effective flow direction changes with distance from the wall, with additional shearing being created in this new flow direction. Figure 6.7 shows that the peak value is largest at $t/T = 0$, coinciding with the point in the period when the minimum drag reduction is achieved (see figure 6.1). This peak decreases and moves away from the wall as t/T increases, and takes the minimum value at approximately $t/T = \frac{1}{4}$, when the maximum drag reduction is seen.

The v^+-rms profile for the $\omega^+ = 0.06$ case is plotted over the temporal period, shown in figure 6.8. There is very little change in the profile over the time period and the fluctuations are reduced due to the drag reduction. Ricco et al. [2012] show that this profile is largely unchanged when plotted using local units at $Re_\tau = 200$. There is still a relatively small change in the v-rms plot over the wall oscillation period for the $\omega^+ = 0.03$ case, as seen in figure 6.9. There is no mean flow in the wall-normal direction over the whole of the forcing period for the wall oscillation cases. This suggest that there is no production of turbulent kinetic energy of the wall normal fluctuations and are solely generated from transport.

The w^+-rms fluctuations over the period of wall oscillation for the $\omega^+ = 0.06$ case is presented in figure 6.10. There appears to be more oscillation in the w

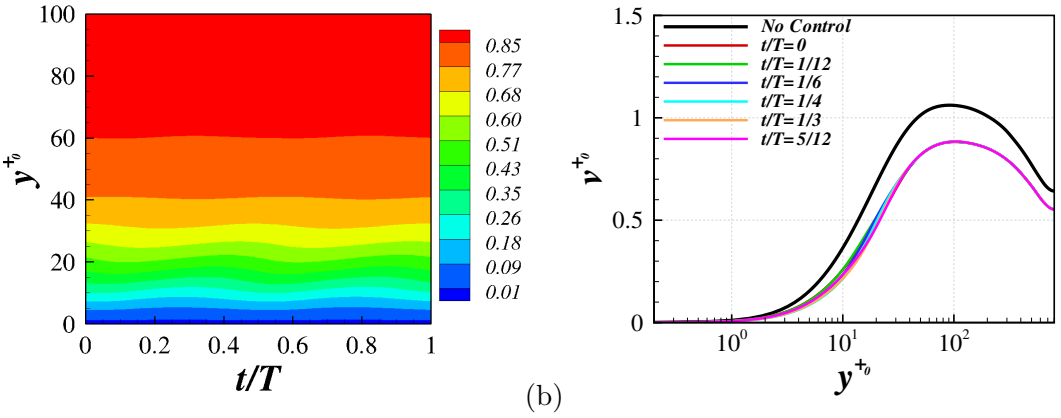

(a) (b)

Figure 6.8: Variation of v^+-rms over the period for oscillation frequency $\omega^+ = 0.06$ in 2d format (a) and 1d format (b).

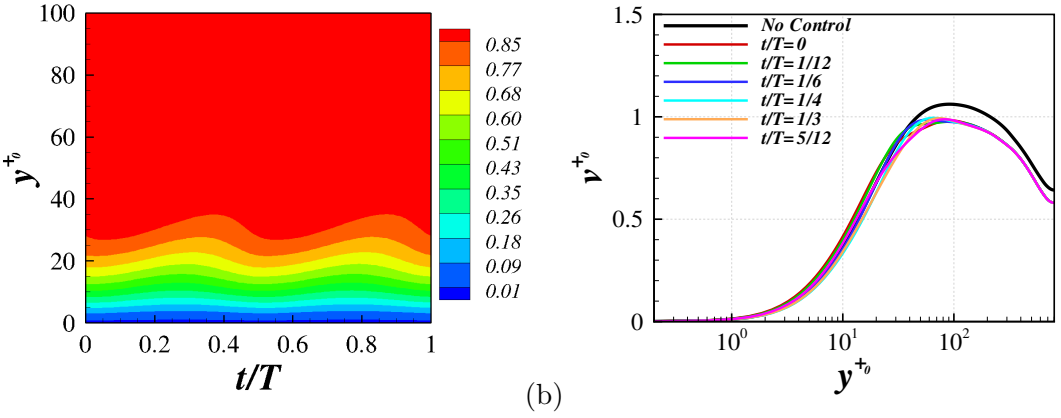

(a) (b)

Figure 6.9: Variation of v^+-rms over the period for oscillation frequency $\omega^+ = 0.03$ in 2d format (a) and 1d format (b).

component than either the u or v profiles seen previously. In this profile a peak appears at $y^+ = 10$ and increases up to $y^+ = 40$. The overall profile is again reduced from the no-control case because of the reduction in drag, with a steady profile in the centre of the channel. A similar behaviour occurs for the $\omega^+ = 0.03$ case in the centre of the channel, with a reduction in the profile, shown in figure 6.11. In the near-wall region the w-rms profile is actually larger than the no-control case, even though the drag is reduced. This peak takes it maximum when $t/T = 0$ and decreases and moves away from the wall over a half-period. Is the peak moves away from the wall, a new peak is seen to emerge close the wall. Interestingly the peak location appears

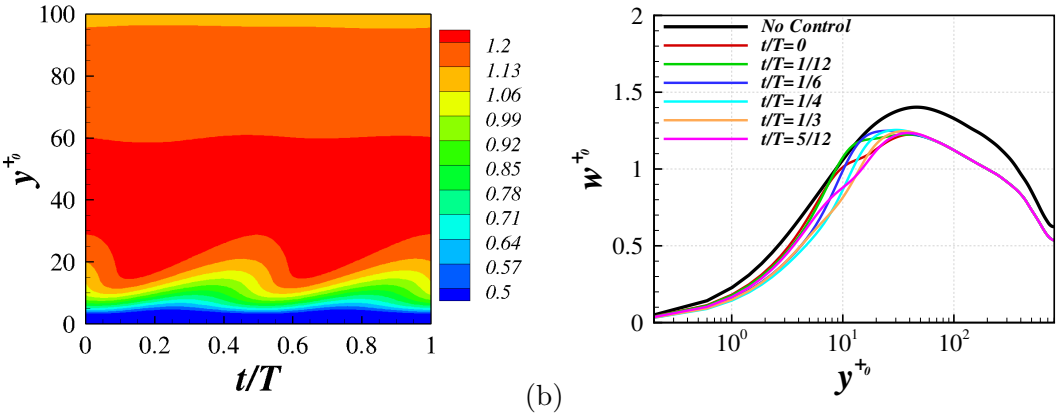

(a) (b)

Figure 6.10: Variation of w^+-rms over the period for oscillation frequency $\omega^+ = 0.06$ in 2d format (a) and 1d format (b).

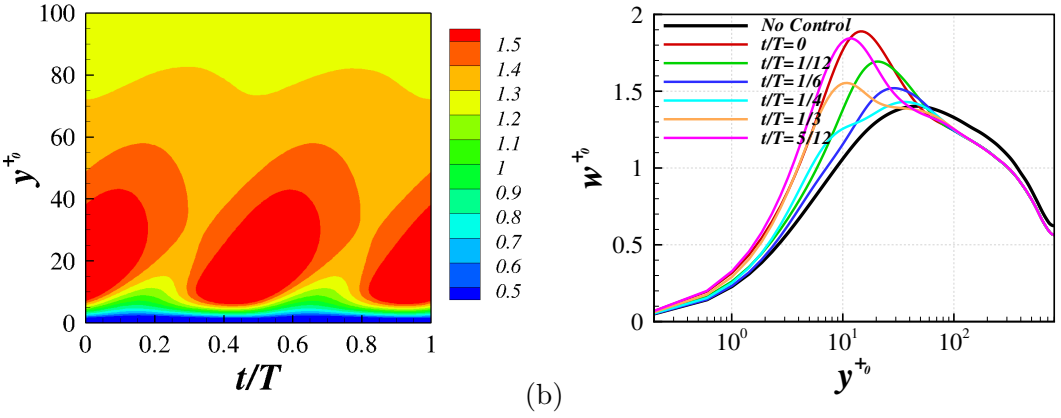

(a) (b)

Figure 6.11: Variation of w^+-rms over the period for oscillation frequency $\omega^+ = 0.03$ in 2d format (a) and 1d format (b).

to be constantly increasing, emerging from the profile at $y^+ \approx 10$ and increases up to $y^+ = 30$. This is also seen by Agostini et al. [2014] who find that the peak spanwise stress becomes 50% of the peak streamwise stress at points throughout the cycle. This large increase in the w^{+0} may be understood by investigating the production of this term. With no streamwise or spanwise dependency of the averaged statistics this term reduces to:

$$P_{33} = -2\overline{vw}\frac{\partial W}{\partial y}$$

Due to the spanwise oscillation $\frac{\partial W}{\partial y}$ is generated in the near-wall region. Because of the no slip condition $\overline{vw}$ is zero at the wall, and hence is small in the near-wall region.

If the spanwise oscillation in the flow is confined to the near-wall region (large ω^+) then production of w^{+0} is small. As the stokes layer (small ω^+) extends into the flow the gradient of spanwise velocity is large as is $\overline{vw}$, causing large production values in w^{+0}, hence a large peak is observed in this parameter. The non-zero value of $\overline{vw}$ is shown at $Re_\tau = 200$ by Ricco et al. [2012], and was seen to oscillate over the period. The production of w' was also shown to be positive (and non zero) with a peak forming and increasing over the half-period. Agostini et al. [2014] also showed large oscillations in the production of spanwise fluctuations.

6.1.3 Vorticity Fluctuations

Figure 6.12 shows the streamwise vorticity fluctuations. Note that due to the oscillation there is a mean component of ω_x which stems from the mean spanwise variation in the wall-normal direction, $\frac{\partial W}{\partial y}$. The fluctuation shows that the minimum and maximum ω_x' values are being moved away from the wall. The wall value oscillates in a range $0.15 < \omega_x^+ < 0.2$ which is lower than that of the no-control case. Due to the movement of the peak value the profile does become larger than the no-control value. In the centre of the channel there is little change in the profile over the period and the value is lower due to the drag reduction. In the centre of the channel there is also little oscillation in the streamwise vorticity for the higher frequency oscillation, figure 6.13. Below $y^+ \approx 300$ the profile is always larger than the profile of the no-control case. The wall value varies between $0.25 < \omega_x^+ < 0.35$, with the minima and maxima also moving away from the wall. The peak in the streamwise vorticity fluctuation is an indication of the location of near-wall wall coherent structures. The behaviour of the profile in both wall oscillation flows presented, suggest the movement in y location of the coherent structures over the phase. From the 2d visualisation the peak location is seen to move away from the wall over the first half period. It is currently unclear as to whether this is the cause or an effect of the oscillation in skin-friction over the period. This concept is studied in further

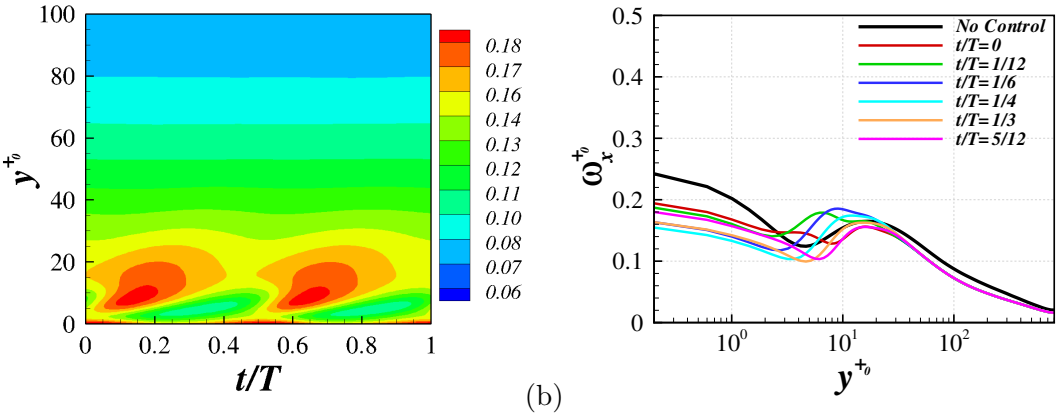

(a) (b)

Figure 6.12: Variation of ω_x^+-rms over the period for oscillation frequency $\omega^+ = 0.06$ in 2d format (a) and 1d format (b).

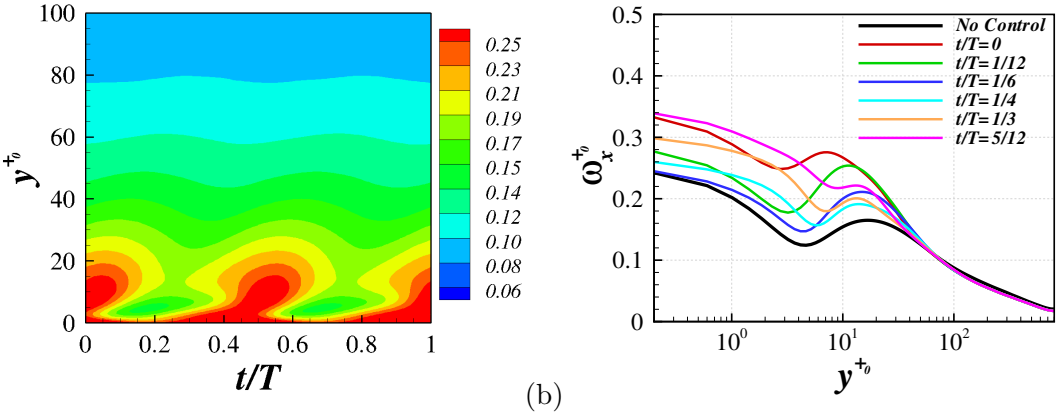

(a) (b)

Figure 6.13: Variation of ω_x^+-rms over the period for oscillation frequency $\omega^+ = 0.03$ in 2d format (a) and 1d format (b).

detail in chapter 8. The results here show qualitative similarity with the enstrophy study of Touber and Leschziner [2012] despite the Reynolds number difference.

The wall-normal vorticity fluctuations are also reduced in the $\omega^+ = 0.06$ case, figure 6.14. There a a clear oscillation in the near-wall region which only extends up to the peak location. The peak value is rising as the location increases before reducing again. A cycle which, again, lasts the half-period. The $\omega^+ = 0.03$ case shows a higher level of oscillation in figure 6.15. The peak of ω_y increases to value which surpasses that of the no-control case, even though the drag reduction never reduces below zero. The profile at $t/T = \frac{1}{4}$ becomes very flat and may be evidence

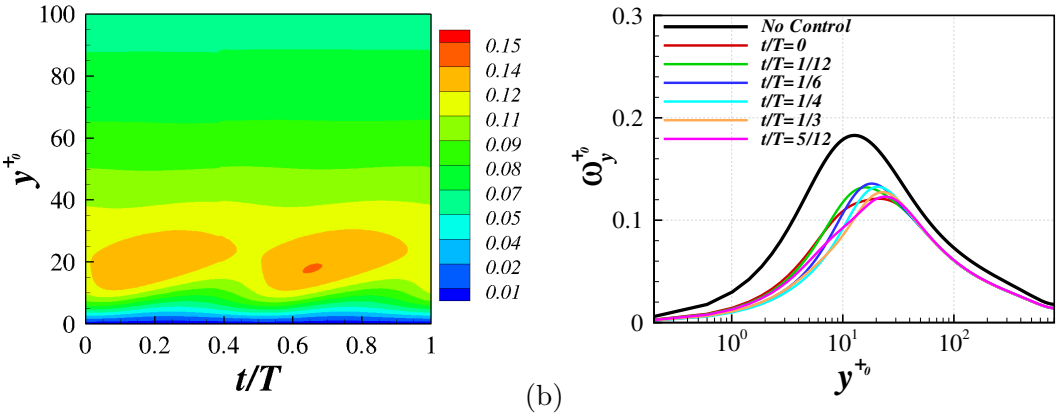

(a) (b)

Figure 6.14: Variation of ω_y^+-rms over the period for oscillation frequency $\omega^+ = 0.06$ in 2d format (a) and 1d format (b).

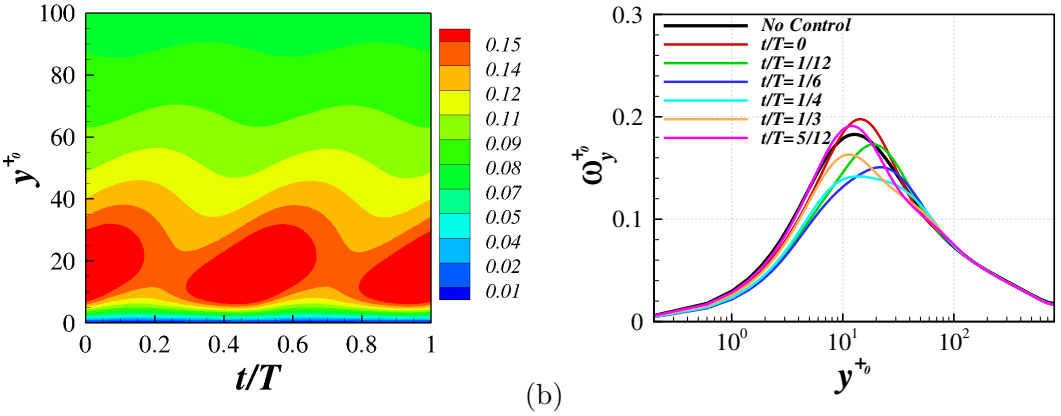

(a) (b)

Figure 6.15: Variation of ω_y^+-rms over the period for oscillation frequency $\omega^+ = 0.03$ in 2d format (a) and 1d format (b).

of two local maxima occurring simultaneously.

Figure 6.16 shows that the near-wall spanwise vorticity fluctuations are greatly reduced by the wall oscillation [Baron and Quadrio, 1996; Touber and Leschziner, 2012]. In the current simulation the wall value is almost halved from the no-control case. This reduction causes a peak in the value of ω_z^+-rms at $y^+ \approx 10$ which is also moved away from the wall periodically by the oscillation. For the case with $\omega^+ = 0.03$ there is still a decrease in the wall value of the spanwise vorticity fluctuations, however this reduction is less than that of the larger frequency case. It is also noticeable that the fluctuation is larger in the wall value figure 6.17 which

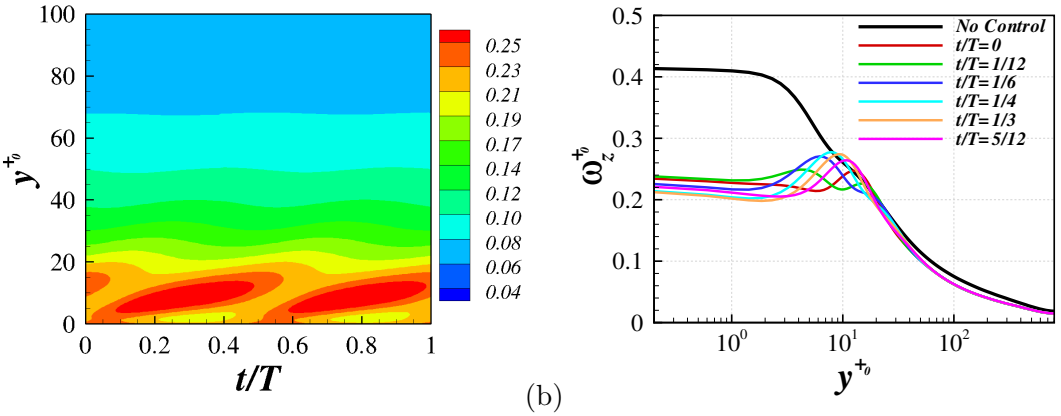

(a) (b)

Figure 6.16: Variation of ω_z^+-rms over the period for oscillation frequency $\omega^+ = 0.06$ in 2d format (a) and 1d format (b).

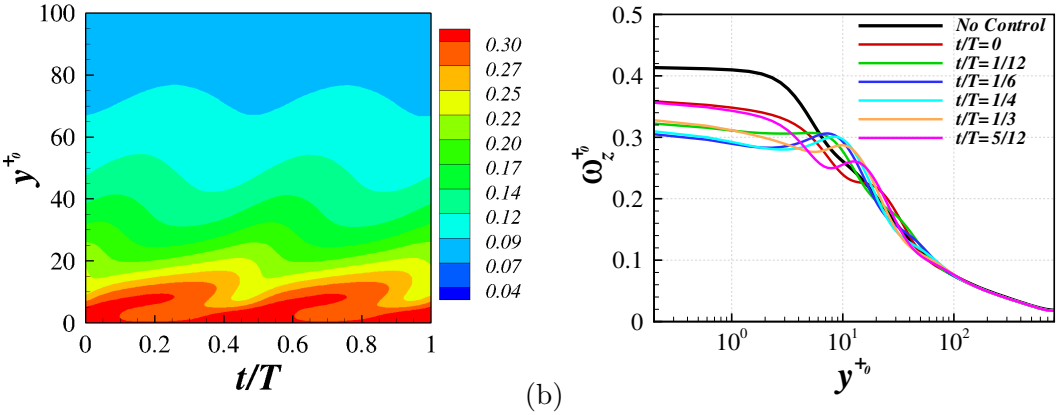

(a) (b)

Figure 6.17: Variation of ω_z^+-rms over the period for oscillation frequency $\omega^+ = 0.03$ in 2d format (a) and 1d format (b).

shows qualitatively similar behaviour to the drag reduction. A peak also occurs at $y^+ \approx 10$, the location of which oscillates over the period.

6.2 Standing Wave

The following is a statistical comparison for two cases in which the standing wave wall forcing is applied. As for the wall oscillation, these two cases are chosen at the near-optimal case and when the DR value begins to deteriorate. For the standing wave at $Re_\tau = 200$ the maximum drag reduction is achieved in the range $\lambda^+ = 1000 - 1250$ [Viotti et al., 2009]. As the Reynolds number is increased the λ^+ value which achieves this maximum is seen to decrease, with the maximum wavenumber from the current study increasing from $\kappa_x^+ = 0.006$ to $\kappa_x^+ = 0.008$. A large oscillation in skin-friction over the spatial period is seen to occur with $\kappa_x^+ \leq 0.006$, hence this is large at $\kappa_x^+ = 0.004$. The two cases compared are therefore $\kappa_x^+ = 0.008$ and $\kappa_x^+ = 0.004$, which correspond to $\lambda^+ = 1600$ and $\lambda^+ = 800$ respectively. Figure 6.18 shows the how the drag reduction changes over the spatial period. The average drag reduction for the $\kappa_x^+ = 0.008$ case is 38%, and is only 27% for the $\kappa_x^+ = 0.004$ simulation.

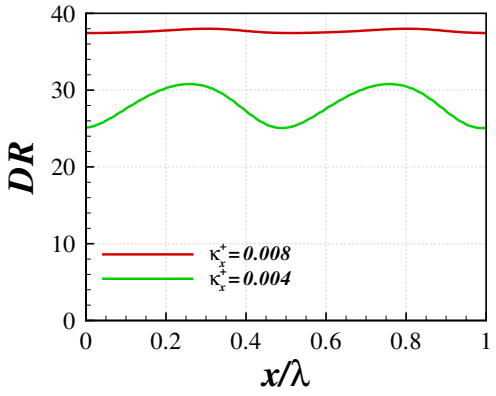

Figure 6.18: Variation of DR over the spatial period for the wavenumber $\kappa_x^+ = 0.008$ and $\kappa_x^+ = 0.004$.

There is again a large oscillation in the drag reduction of the less efficient forcing case ($\kappa_x^+ = 0.004$). This oscillation in the drag reduction was shown by Skote [2011] to occur in a boundary layer simulation. As in the wall oscillation the period of this oscillation is half that of the forcing wavelength, which is again because the

drag reduction is independent of the sign of the wall velocity. The slight phase-shift in the oscillation in the drag when compared to the period of the wall forcing is likely related to the dependence of the skin-friction on properties within the flow (such as coherent structure or streak locations). This shift is therefore related to the propagation of the wall velocity wave into the flow as shown in the analytic Stokes' profile [Viotti et al., 2009].

6.2.1 Mean Profiles

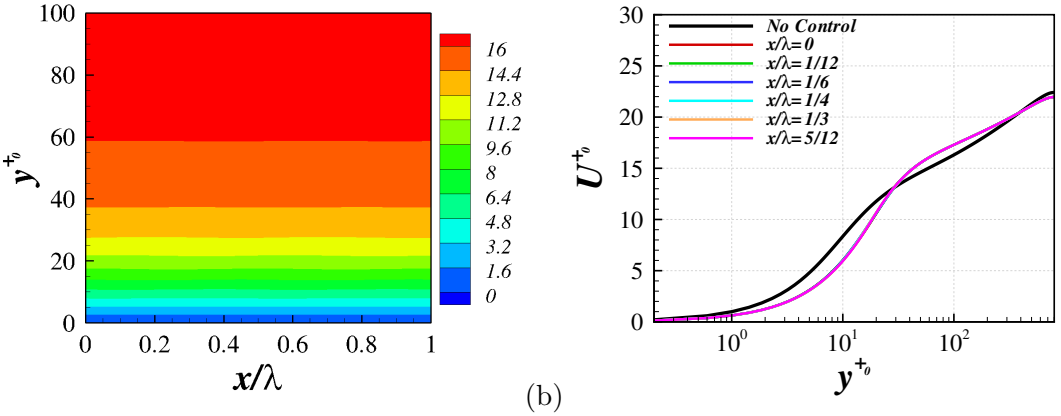

(a) (b)

Figure 6.19: Variation of U^+ over the period for wavenumber $\kappa_x^+ = 0.008$ in 2d format (a) and 1d format (b).

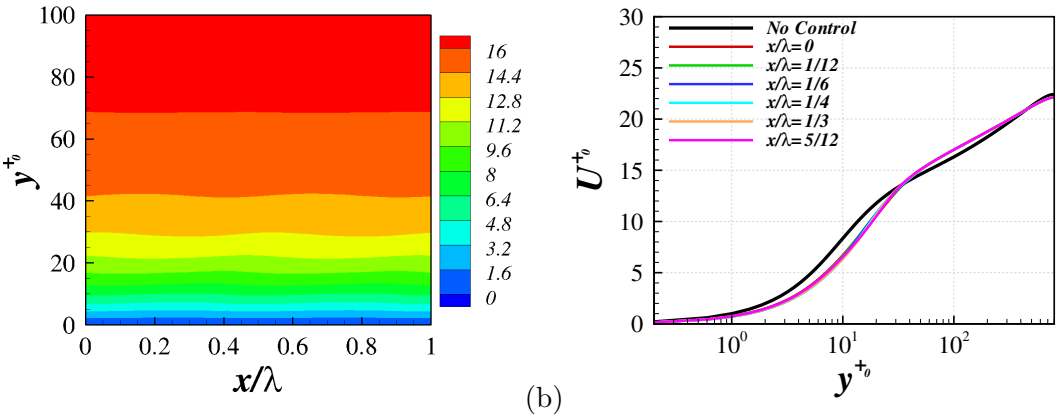

(a) (b)

Figure 6.20: Variation of U^+ over the period for wavenumber $\kappa_x^+ = 0.004$ in 2d format (a) and 1d format (b).

The effect of the standing wave forcing with $\kappa_x^+ = 0.008$ on the mean stream-

wise velocity profile is shown in figure 6.19. The velocity profile is greatly reduced from the no-control case in the near-wall region and increased in the log-law region. This is similar behaviour to that of the wall oscillation case. Similarly, for the $\kappa_x^+ = 0.004$, shown in figure 6.20 the value of mean streamwise velocity is reduced near the wall and increased in the log-law region. When scaled by local units the normal upward shift in the logarithmic part of the profile associated with a drag reduction is observed (in agreement with Viotti et al. [2009]). The 2d plot, figure 6.20a, shows evidence of an oscillation in the profile in the near-wall region which relates to the oscillation in the drag reduction seen in figure 6.18.

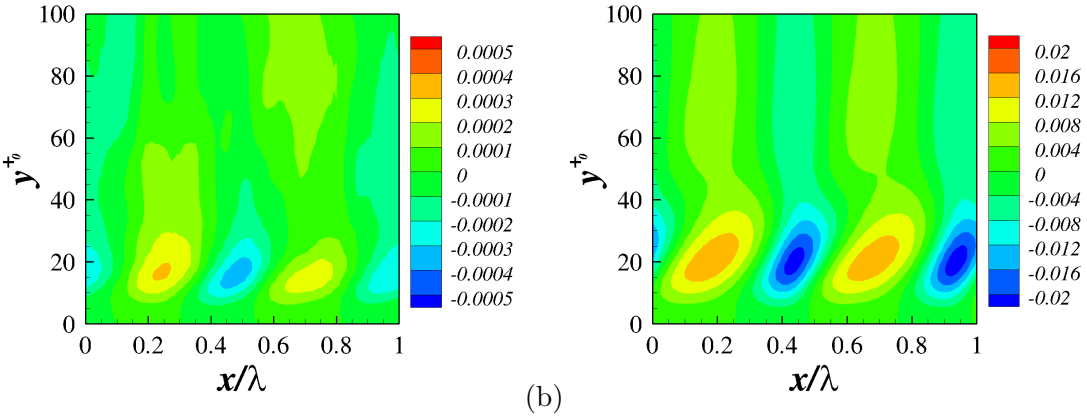

(a) (b)

Figure 6.21: Variation of V^+ over the period for wavenumber $\kappa_x^+ = 0.008$ in 2d format (a) and $\kappa_x^+ = 0.004$ in 2d format (b).

Figure 6.21 shows the mean wall-normal velocity profiles over the spatial phase. The value of this mean is considerably smaller than that of both the spanwise and streamwise means. As $\frac{\partial W}{\partial z} = 0$ due to the homogeneity in the spanwise direction, the phase averaged continuity equation in incompressible flow reduces to:

$$\frac{\partial U}{\partial x} + \frac{\partial V}{\partial y} = 0.$$

As there is a streamwise oscillation in U, seen in figures 6.19 and 6.20, then there must be an opposing $\frac{\partial V}{\partial y}$. The mean wall-normal velocity is strongest in the $\kappa_x^+ = 0.004$ case when there is a stronger oscillation in the mean streamwise flow (and

hence the DR).

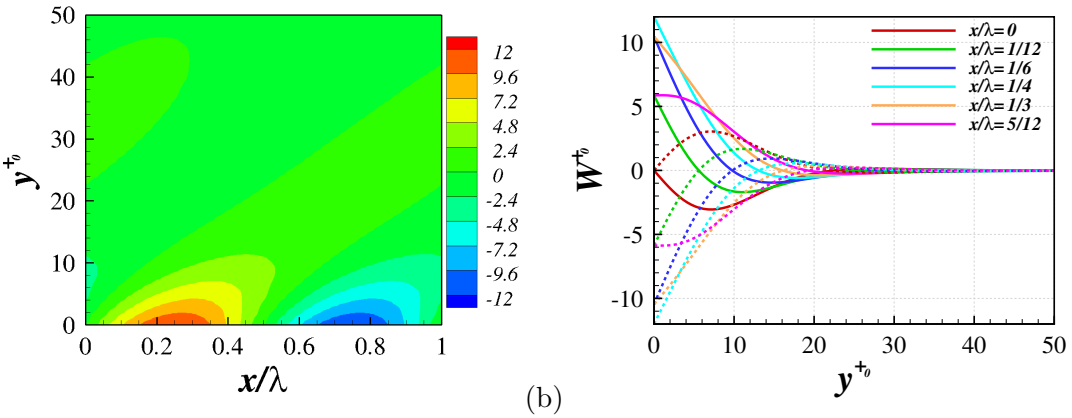

(a) (b)

Figure 6.22: Variation of W^+ over the period for wavenumber $\kappa_x^+ = 0.008$ in 2d format (a) and 1d format (b). The solid lines represent the time points over the first half period and the dashed lines are from the second half-period.

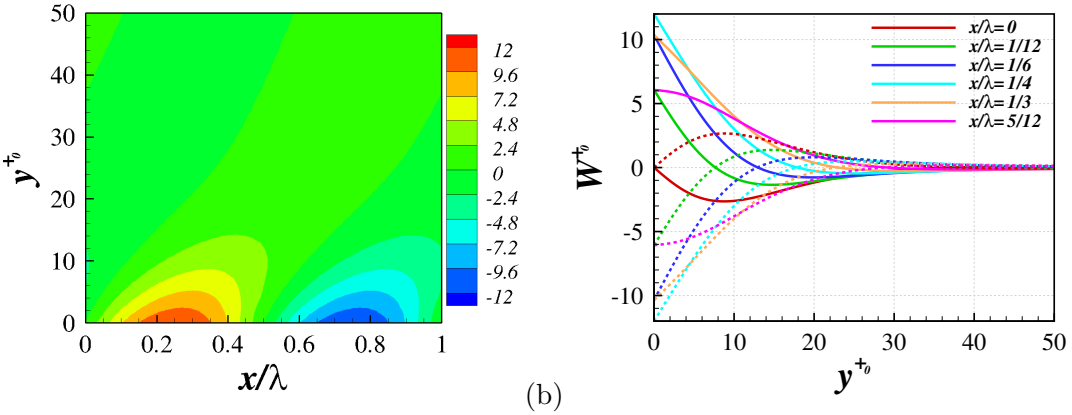

(a) (b)

Figure 6.23: Variation of W^+ over the period for wavenumber $\kappa_x^+ = 0.004$ in 2d format (a) and 1d format (b). The solid lines represent the time points over the first half period and the dashed lines are from the second half-period.

Figure 6.22 shows the mean spanwise wall velocity from the $\kappa_x^+ = 0.008$ standing wave case. The velocity profile is shown over the spatial period in the streamwise direction. The wall velocity varies sinusoidally with $k_x x$ (which is initially positive, unlike the wall oscillation). This oscillation is between the maximum and minimum wall velocities $W_m^+ = \pm 12$, moving the fluid in the spatial Stokes' layer which extends into the flow. For the $\kappa_x^+ = 0.004$ case, the Stokes' layer is seen to be thicker, figure 6.23, as the spanwise velocity extends further into the domain.

Because of this, the oscillation of mean spanwise velocity in y, $\frac{\partial W^{+0}}{\partial y^{+0}}$, is smaller in the $\kappa_x^+ = 0.004$ case. A strong similarity between the mean profiles of the spatial and temporal Stokes' layers is shown by Viotti et al. [2009] over the diffence forcing periods. The way that the temporal wave propagates into the flow over time is seen to be comparable to the way that the spatial wave propagates into the flow in the streamwise direction.

Sloped contours also appear in the 2d plots from the turbulent statistics and mean profiles of the standing wave control method [Viotti et al., 2009]. This is similar behaviour to that seen in the wall oscillation. However there is a propagation of the spatial wave of wall velocity in space, caused by the streamwise flow. The spatially varying wave entrains the near wall fluid, and as the flow travels over the sinusoidal wall velocity feels the effects of the wall with a delay dependent on the wall normal height. As the propagation of the wave is dependent on the streamwise velocity of the flow, and the velocity is lower near the wall due to the shear, the contours become more sloped further from the wall.

6.2.2 Velocity Fluctuations

The streamwise fluctuations for the standing wave forcing with $\kappa_x^+ = 0.008$ are presented in figure 6.24. The overall profile is greatly reduced from the no-control case and the location of the maximum is moved away from the wall as seen by Viotti et al. [2009]. There is a very small level of oscillation in the profile and this is confined to the near-wall region. For the $\kappa_x^+ = 0.004$ case, the u-rms profile is shown in figure 6.25. The fluctuations are again reduced from the no-control case, but the peak value oscillates over the spatial period, and the region in which the oscillation takes place extends further into the flow. The location of the peak is also moved away from the wall at points within the period. As in the wall oscillation flow, the reduction in the streamwise fluctuations are strongest when the drag reduction is largest. Similarly, the maximum peak value in the profile coincides with the point

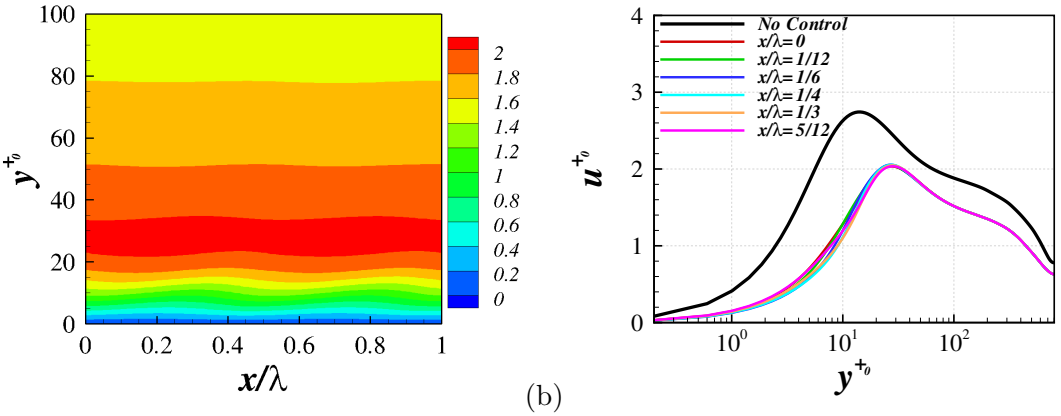

(a) (b)

Figure 6.24: Variation of u^+-rms over the period for wavenumber $\kappa_x^+ = 0.008$ in 2d format (a) and 1d format (b).

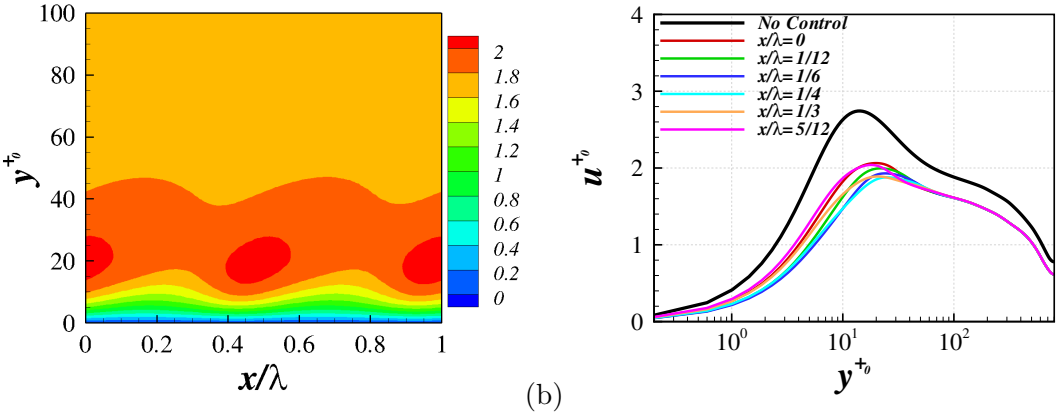

(a) (b)

Figure 6.25: Variation of u^+-rms over the period for wavenumber $\kappa_x^+ = 0.004$ in 2d format (a) and 1d format (b).

in the period in which the lowest drag reduction is achieved.

The streamwise fluctuations can be considered physically as streaks. Skote [2011] showed that in a boundary layer flow the spatial forcing both weakens and angles the near-wall streaks. This is also shown in the current work for the $\kappa_x^+ = 0.008$ cases at all four Reynolds numbers studied in figures 8.20 and 8.21.

For the v rms fluctuations in the $\kappa_x^+ = 0.008$ case, figure 6.26, there is a little oscillation, which again is confined to the near-wall region, but this oscillation is minimal. The profile is again reduced. The reduction in v rms is not as large in the $\kappa_x^+ = 0.004$ case, as shown in figure 6.27. The oscillation in the v rms

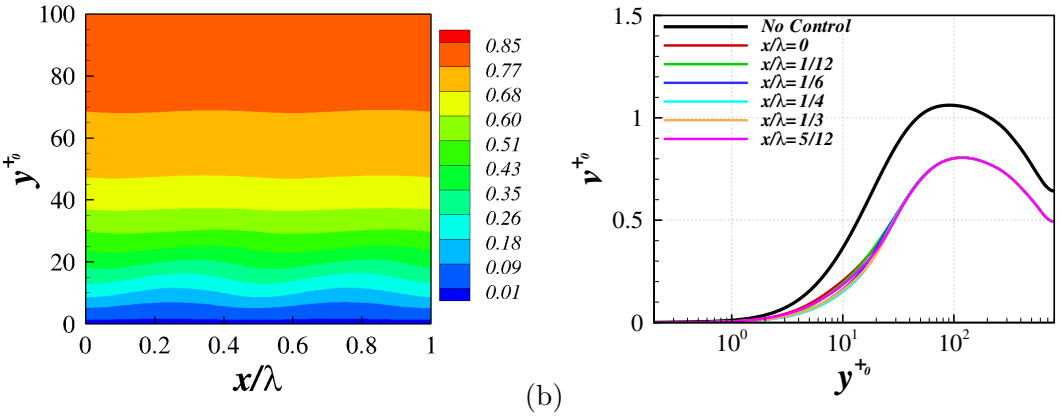

(a) (b)

Figure 6.26: Variation of v^+-rms over the period for wavenumber $\kappa_x^+ = 0.008$ in 2d format (a) and 1d format (b).

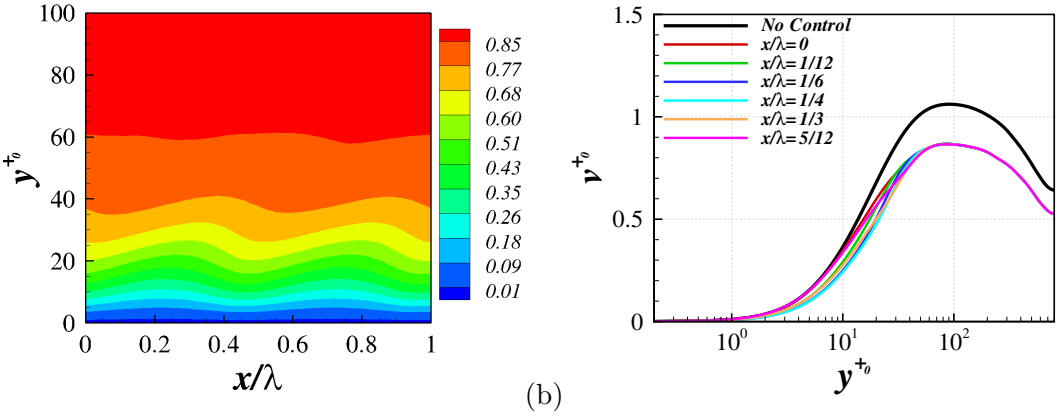

(a) (b)

Figure 6.27: Variation of v^+-rms over the period for wavenumber $\kappa_x^+ = 0.004$ in 2d format (a) and 1d format (b).

profile extends further into the domain, and the level of oscillation is larger than the higher κ_x^+ value case. It is important to note that, similarly to the wall oscillation control, the oscillation in the v fluctuations are considerably smaller than the u and w fluctuations.

The w rms profile at different points throughout the spatial half-period, with $\kappa_x^+ = 0.008$ is shown in figure 6.28. There appears to be a noticeable oscillation in the near-wall region, in which a peak appears and moves away from the wall as the streamwise location moves through the period, a phenomenon also seen in the spatial evolution of boundary layer flows [Skote, 2013]. This oscillation is much

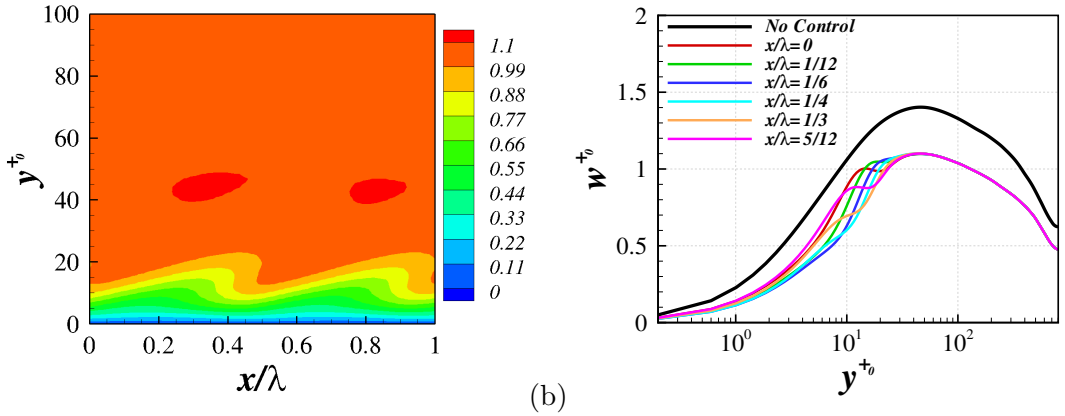

(a) (b)

Figure 6.28: Variation of w^+-rms over the period for wavenumber $\kappa_x^+ = 0.008$ in 2d format (a) and 1d format (b).

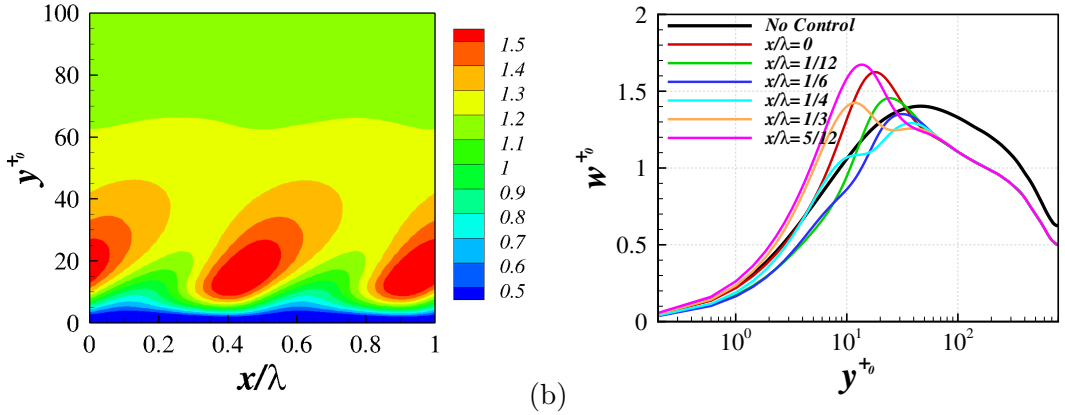

(a) (b)

Figure 6.29: Variation of w^+-rms over the period for wavenumber $\kappa_x^+ = 0.004$ in 2d format (a) and 1d format (b).

stronger in the $\kappa_x^+ = 0.004$ case, figure 6.29, in which the peak value is increased so much that it surpasses that of the no-control case (despite the drag reduction). The w rms values are reduced from the no-control case in the outer region, where the profile does not vary in x. Due to the extra streamwise dependency from the wall oscillation case the production term for w^{+0} is:

$$P_{33} = p_{uw} + p_{vw} = -2\overline{uw}\frac{\partial W}{\partial x} - 2\overline{vw}\frac{\partial W}{\partial y}.$$

Due to the large spanwise shear from the standing wave forcing the production of w^{+0} is increased. This extra term in the production, p_{uw}, may give an explanation

to the higher drag reductions achieved by the standing wave forcing and is an interesting area of possible further investigation. The large production of spanwise fluctuations has been seen in the wall oscillation case [Ricco et al., 2012; Agostini et al., 2014], where this term is zero. If the values of $\frac{\partial W}{\partial x}$ and $\overline{uw}$ are aligned as to give negative contribution to the production, then greater spanwise shear may be possible without this production term being increased. This effect has been recently shown in boundary layer simulations by Skote [2013]. Where the spanwise wall oscillation forcing is compared to the streamwise standing wave control (both near optimal cases), the p_{vw} terms are very similar in magnitude, a negative profile of p_{uw} contributes to a reduction in the production of w' in the standing wave case.

6.2.3 Vorticity Fluctuations

The behaviour of the streamwise vorticity fluctuations for the $\kappa_x^+ = 0.008$ is shown in figure 6.30. Interestingly, there is almost no change in the ω_x^+ rms wall value over the period, which is reduced significantly from the no-control case. The maximum and minimum values are moved away from the wall and the peak re-emerges at $\frac{x}{\lambda} = \frac{5}{12}$. For the $\kappa_x^+ = 0.004$ case, figure 6.31, there is a high level of oscillation in the wall value of ω_x^+ rms. This may be related to the strong oscillation in DR. The wall value also becomes larger than that of the no-control case for $\frac{1}{3} < \frac{x}{\lambda} < \frac{1}{2}$. The peak value becomes very large at $\frac{x}{\lambda} = 0$ and is reduced as it moves away from the wall.

The wall-normal component of the vorticity fluctuation is greatly reduced from the no-control case when a standing wave of $\kappa_x^+ = 0.008$ is applied, figure 6.32. The peak value stays fairly constant over the period, although it is moved away from the wall. The peak re-emerges at $\frac{x}{\lambda} = \frac{5}{12}$ where there is evidence of two local maxima occurring at one x location. Figure 6.33 shows the ω_y^+ rms profile from the $\kappa_x^+ = 0.004$ case. The maximum values of the profile range between 0.12 and 0.17, with a value almost as large, at $\frac{x}{\lambda} = \frac{5}{12}$, as the no-control peak value.

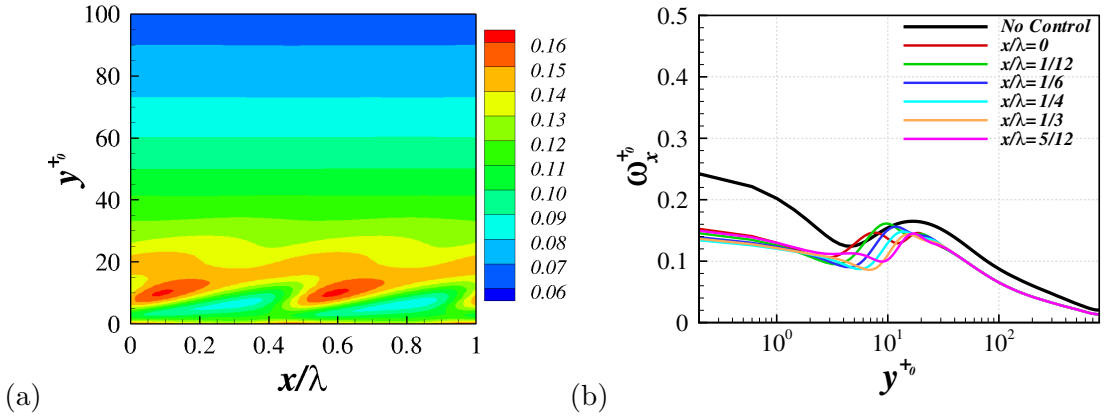

(a) (b)

Figure 6.30: Variation of ω_x^+-rms over the period for wavenumber $\kappa_x^+ = 0.008$ in 2d format (a) and 1d format (b).

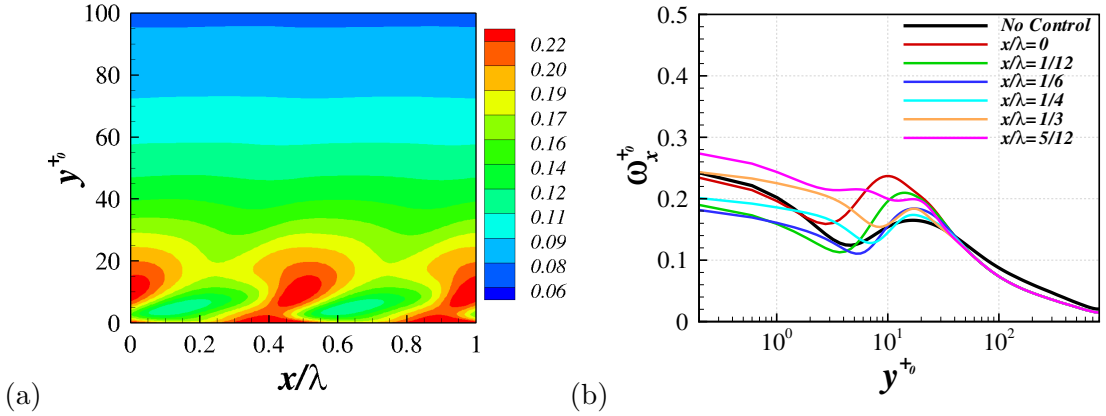

(a) (b)

Figure 6.31: Variation of ω_x^+-rms over the period for wavenumber $\kappa_x^+ = 0.004$ in 2d format (a) and 1d format (b).

The spanwise vorticity fluctuations for the $\kappa_x^+ = 0.008$ case are presented in figure 6.34. The wall value is greatly reduced in the near-wall region and a local maximum appears at $y^+ \approx 10$. This peak value increases and moves away from the wall before another emerges. For the $\kappa_x^+ = 0.004$ case, figure 6.35, there is greater oscillation in the wall value. The reduction of this wall value from the no-control case is smaller than when $\kappa_x^+ = 0.008$. A peak is evident, even with the lower wavenumber, the location of which also varies over the period.

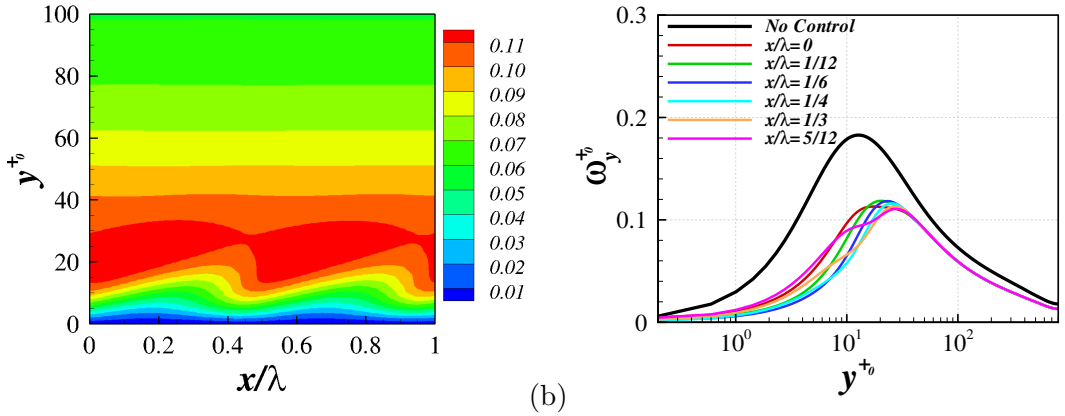

(a) (b)

Figure 6.32: Variation of ω_y^+-rms over the period for wavenumber $\kappa_x^+ = 0.008$ in 2d format (a) and 1d format (b).

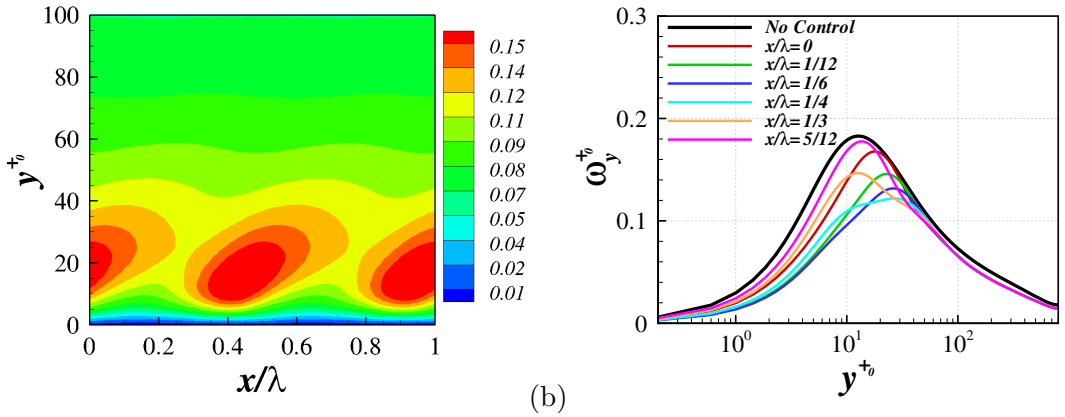

(a) (b)

Figure 6.33: Variation of ω_y^+-rms over the period for wavenumber $\kappa_x^+ = 0.004$ in 2d format (a) and 1d format (b).

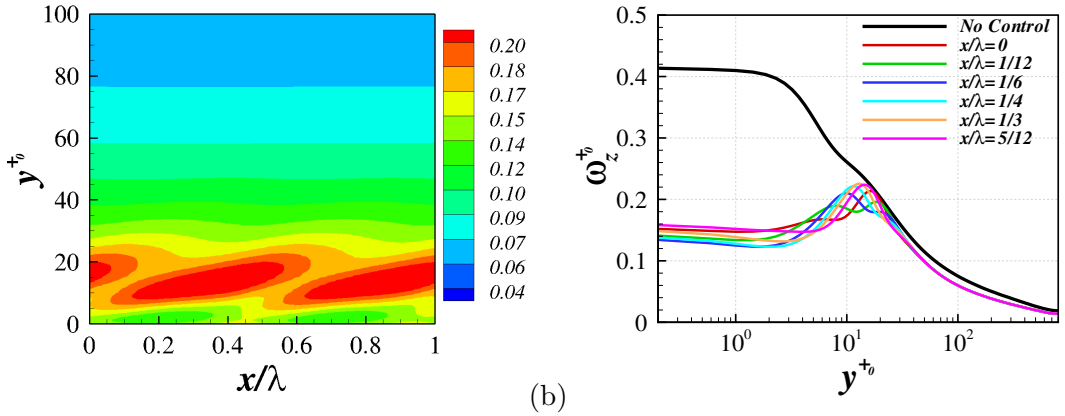

(a) (b)

Figure 6.34: Variation of ω_z^+-rms over the period for wavenumber $\kappa_x^+ = 0.008$ in 2d format (a) and 1d format (b).

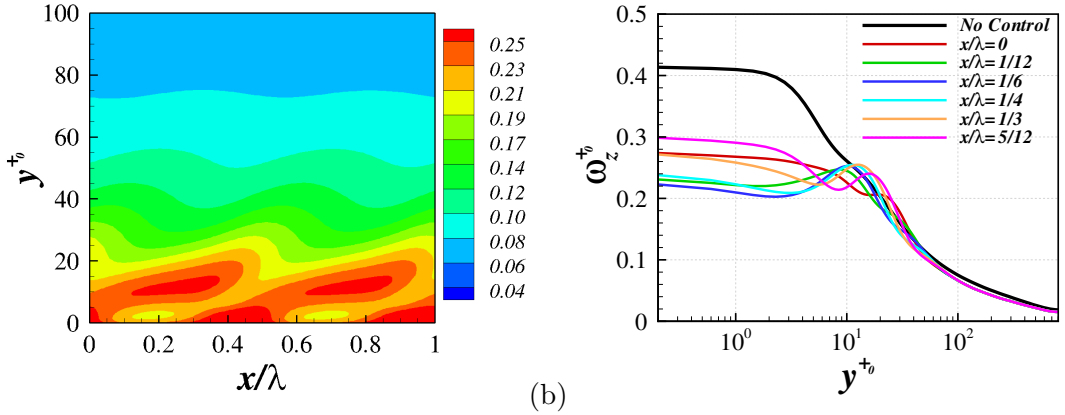

(a) (b)

Figure 6.35: Variation of ω_z^+-rms over the period for wavenumber $\kappa_x^+ = 0.004$ in 2d format (a) and 1d format (b).

6.3 Travelling Wave

The turbulent statistics over the spatially varying, temporally shifted average, ξ (discussed in section 3.7.1), is investigated for two travelling wave cases. This shifted average is defined by:

$$\xi = \frac{x}{\lambda} - \frac{t}{T}.$$

Due to the similarity of the flow over ξ, a phase average can be calculated. The spatial wavenumber is fixed at $\kappa_x^+ = 0.008$ and the two cases are studied with $\omega^+ = 0.01$ and $\omega^+ = 0.03$. The drag reduction achieved in the $\omega^+ = 0.01$ case is actually slightly lower than the standing wave with the same wavenumber, also at 38% (rounded to nearest percent). As the frequency is increased, the DR begins to deteriorate, and can give a drag increase at certain combinations of the forcing parameters. At $\omega^+ = 0.03$ the oscillation in drag reduction over the period, shown in figure 6.36, becomes large and the DR achieved drops to 24%.

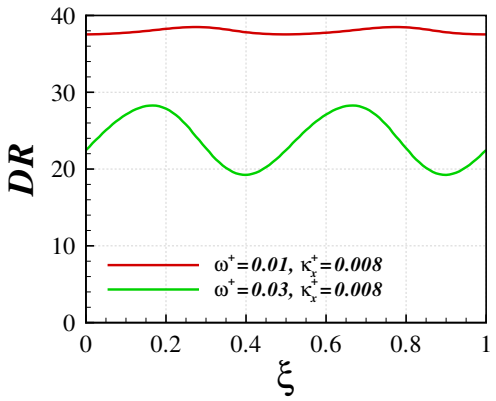

Figure 6.36: Variation of DR over the spatial period for frequencies $\omega^+ = 0.01$ and $\omega^+ = 0.03$ with fixed wavenumber $\kappa_x^+ = 0.008$.

6.3.1 Mean Profiles

The mean streamwise velocity profile for the $\omega^+ = 0.01$ case is shown in figure 6.37. The profile, as in the wall oscillation and standing wave cases, is reduced from the

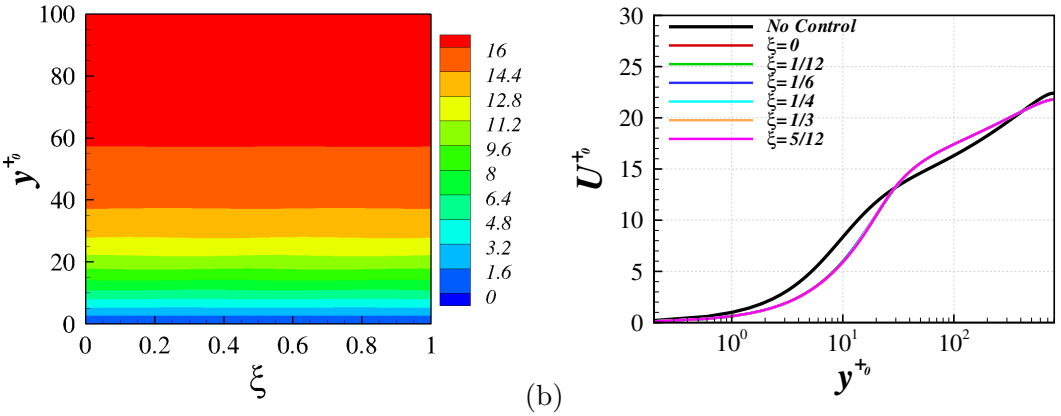

(a) (b)

Figure 6.37: Variation of U^+ over the period for frequency $\omega^+ = 0.01$ and wavenumber $\kappa_x^+ = 0.008$ in 2d format (a) and 1d format (b).

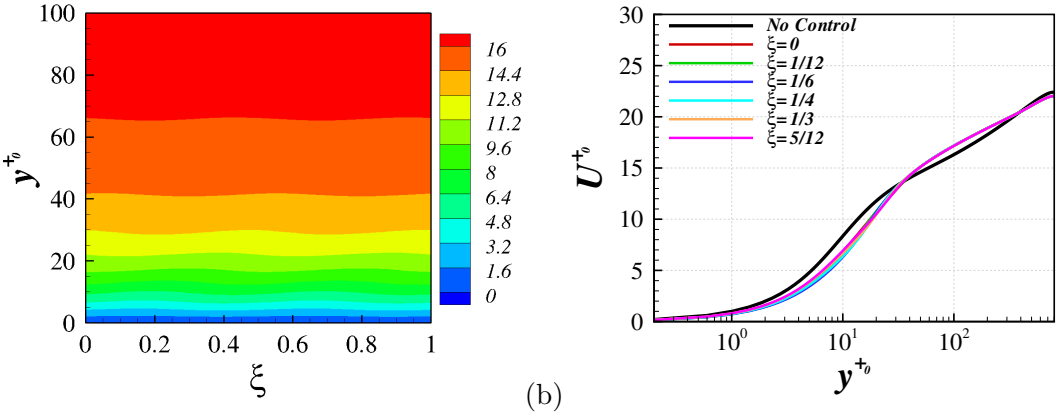

(a) (b)

Figure 6.38: Variation of U^+ over the period for frequency $\omega^+ = 0.03$ and wavenumber $\kappa_x^+ = 0.008$ in 2d format (a) and 1d format (b).

no-control case in the near-wall region in agreement with previous studies [Quadrio et al., 2009]. As the mass flow rate is fixed, the mean velocity is increased in the log-law region, but slightly decreases in the channel centreline. A very similar behaviour occurs to a lesser extent in the $\omega^+ = 0.03$ case, figure 6.38, however some evidence of the oscillation is visible in the near-wall region relating to the oscillation seen in the drag reduction.

Figure 6.39 shows the mean spanwise velocity for the $\omega^+ = 0.01$ case. Due to the forward travelling wave in the streamwise direction the spatial delay of the spanwise wall motion into the flow is reduced. This creates a region of almost

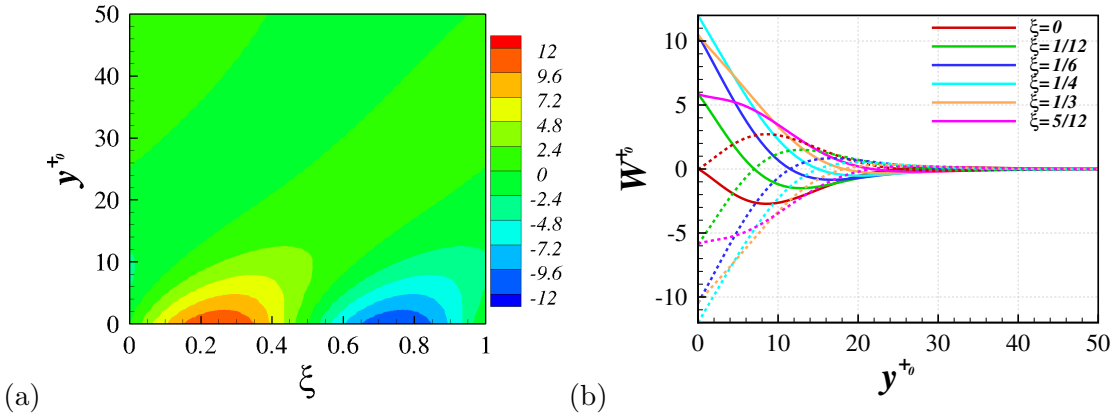

Figure 6.39: Variation of W^+ over the period for frequency $\omega^+ = 0.01$ and wavenumber $\kappa_x^+ = 0.008$ in 2d format (a) and 1d format (b). The solid lines represent the time points over the first half period and the dashed lines are from the second half-period.

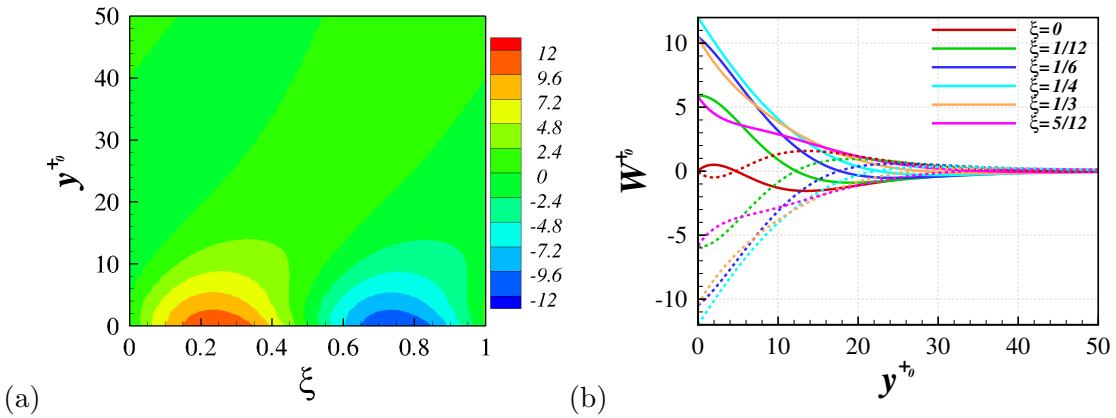

Figure 6.40: Variation of W^+ over the period for frequency $\omega^+ = 0.03$ and wavenumber $\kappa_x^+ = 0.008$ in 2d format (a) and 1d format (b). The solid lines represent the time points over the first half period and the dashed lines are from the second half-period.

constant velocity in the near-wall region at $\xi = \frac{5}{12}$. In the $\omega^+ = 0.03$ case the speed of the wave is faster than the delay of the spanwise velocity into the flow. This means that, when the magnitude of the wall velocity is decreasing, the spanwise velocity within the flow can be less than the wall value, as seen at $\xi = \frac{5}{12}$ in figure 6.40. This means that the wall-normal gradient of this spanwise velocity can by either positive or negative within the near-wall region. This shows good agreement with visualisation of the mean spanwise velocity shown by Quadrio et al. [2009].

As in the wall oscillation and standing wave forcings, sloped contours are seen

in both mean and turbulent statistics for the travelling wave cases. For the case with $\omega^+ = 0.03$ and $\kappa_x^+ = 0.008$ the slope is initially backwards in the parameter ξ and becomes forwards further from the wall. It is important to note that, due to the definition of ξ, the reference frame moves with the spatial wave. As in all the travelling wave cases in the current study, the wave travels forwards in the streamwise direction. As the speed of the wave is faster than the mean flow near the wall, and hence is faster than its propagation into the flow, the wave propagates backwards in ξ. Further from the wall where the velocity is faster, the contours become sloped forwards in ξ.

6.3.2 Velocity Fluctuations

The u rms profile for the $\omega^+ = 0.01$ case is presented in figure 6.41. The profile is reduced from the no-control case and the maximum value is moved away from the wall [Quadrio and Ricco, 2011]. There is a little oscillation in the profile, which is limited to the near-wall region. For the $\omega^+ = 0.03$ case, figure 6.42, the u rms profile is also reduced. The near-wall values oscillate with the ξ value and the peak becomes less prominent.

The wall-normal fluctuation for the $\omega^+ = 0.01$ case is shown in figure 6.43. The profile is reduced universally from the no-control case, with a small level of oscillation in this parameter close to the wall. For the $\omega^+ = 0.03$ case the v rms profile is reduced from the no-control case, figure 6.44. In the near-wall region the v rms values are larger than that of the no-control case for certain ξ values, but also vary below the no-control profile.

Figure 6.45 shows the change in the w rms profile over the period for the $\omega^+ = 0.01$ case. There is visible oscillation in the profile in the near-wall region with a peak emerging and moving away from the wall around $y^+ \approx 10$. For the $\omega^+ = 0.03$ case, figure 6.46, there is a very strong oscillation in the w rms value. The peak appears and becomes large at $y^+ \approx 10$. This peak value then decreases as it moves

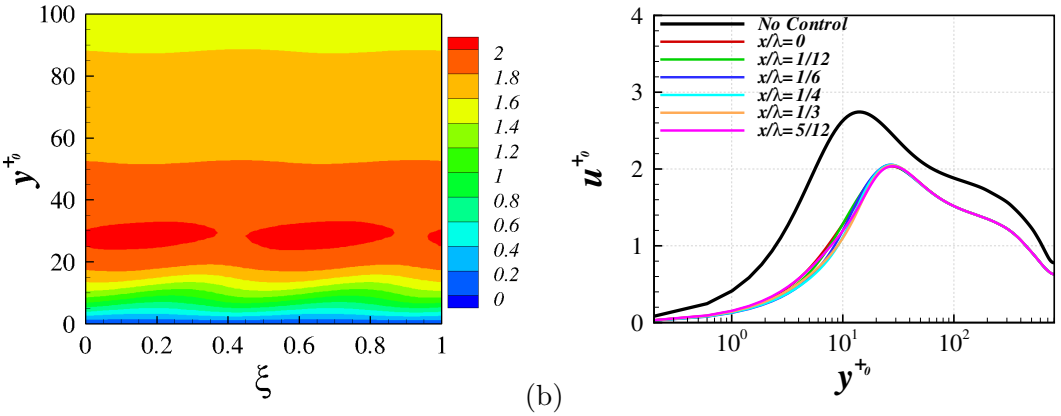

(a) (b)

Figure 6.41: Variation of u^+-rms over the period for frequency $\omega^+ = 0.01$ and wavenumber $\kappa_x^+ = 0.008$ in 2d format (a) and 1d format (b).

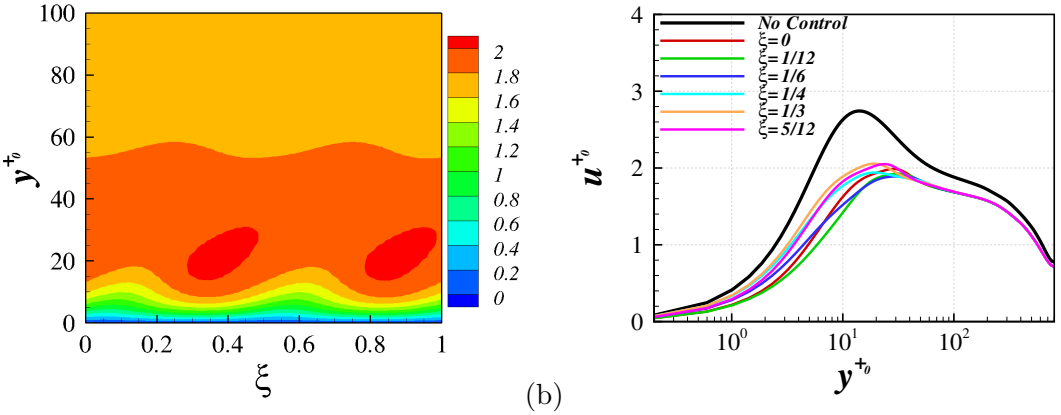

(a) (b)

Figure 6.42: Variation of u^+-rms over the period for frequency $\omega^+ = 0.03$ and wavenumber $\kappa_x^+ = 0.008$ in 2d format (a) and 1d format (b).

away from the wall. Although the profile is reduced from the no-control case in the centre of the channel, in the near-wall region it is increased over the majority of the period. As in the standing wave forcing, the production term for w^{+0} is:

$$P_{33} = -2\overline{uw}\frac{\partial W}{\partial x} - 2\overline{vw}\frac{\partial W}{\partial y}.$$

In the travelling wave forcing it may be possible that the values of $\frac{\partial W}{\partial y}$ and $\frac{\partial W}{\partial x}$ can be further tuned to allow large spanwise shear with small P_{33}. Quadrio et al. [2009] showed that $\overline{uw}$ is non-zero for both the near-optimal case and a drag increase case. There is a clear oscillation in this quantity over the period.

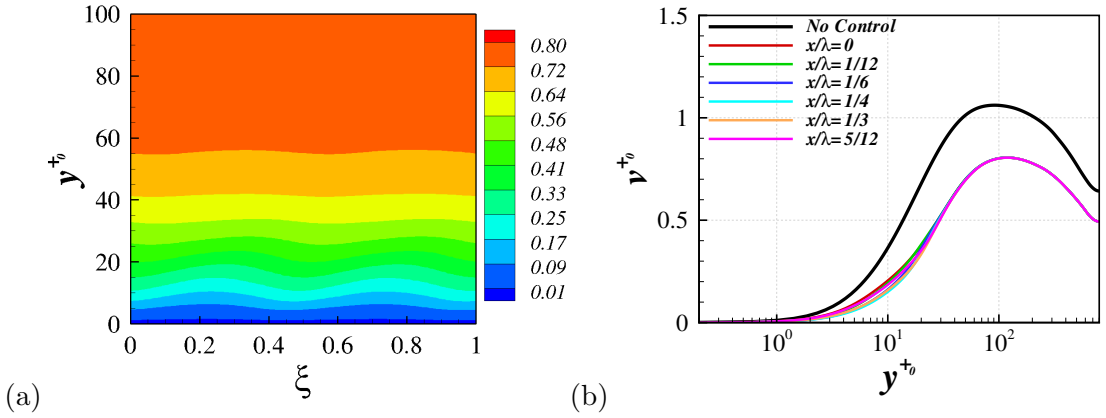

(a) (b)

Figure 6.43: Variation of v^+-rms over the period for frequency $\omega^+ = 0.01$ and wavenumber $\kappa_x^+ = 0.008$ in 2d format (a) and 1d format (b).

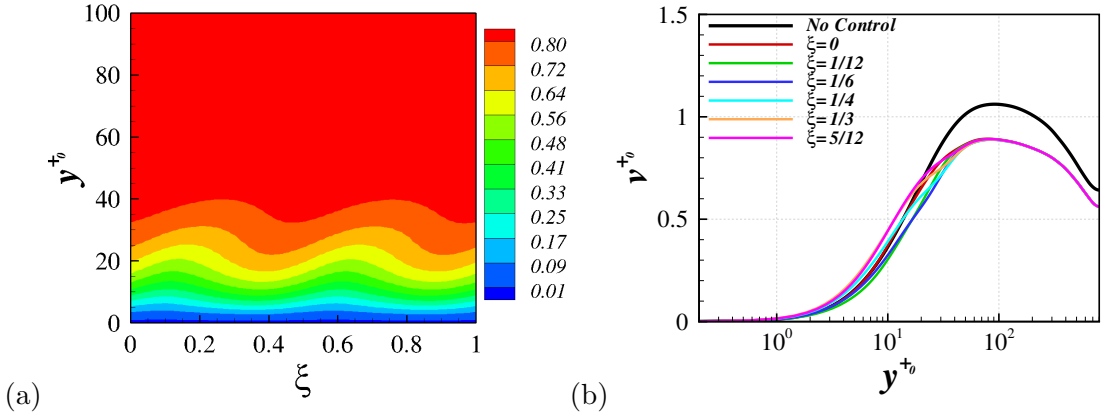

(a) (b)

Figure 6.44: Variation of v^+-rms over the period for frequency $\omega^+ = 0.03$ and wavenumber $\kappa_x^+ = 0.008$ in 2d format (a) and 1d format (b).

In general the plots of the velocity fluctuations over the period show qualitative agreement with the Reynolds stresses shown by Quadrio et al. [2009]. The near-optimal cases show very little oscillation for the streamwise and spanwise stresses, but clear evidence is seen of oscillation in the spanwise fluctuations with a peak strong peak occurring and moving away from the wall over the half-period. For the case with large oscillations in the drag reduction (actually a drag increase case presented Quadrio et al. [2009]), the oscillations in the Reynolds stresses are most notable in the streamwise and spanwise profiles.

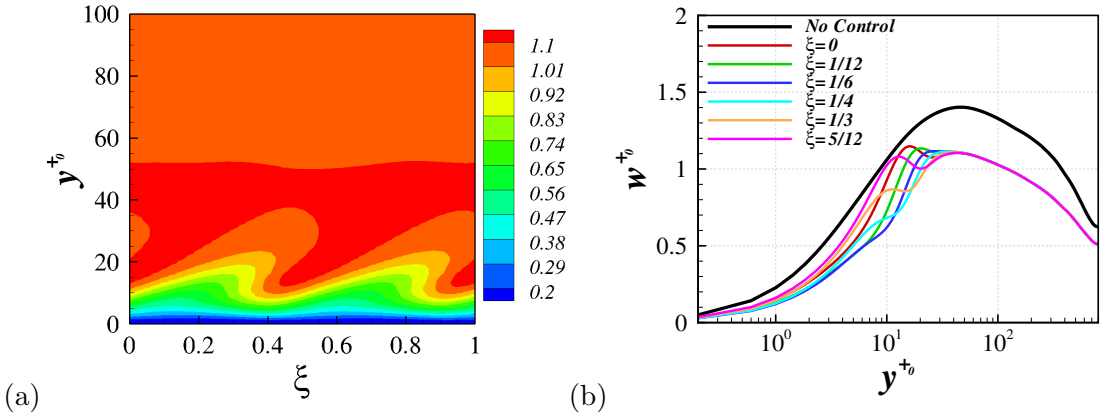

Figure 6.45: Variation of w^+-rms over the period for frequency $\omega^+ = 0.01$ and wavenumber $\kappa_x^+ = 0.008$ in 2d format (a) and 1d format (b).

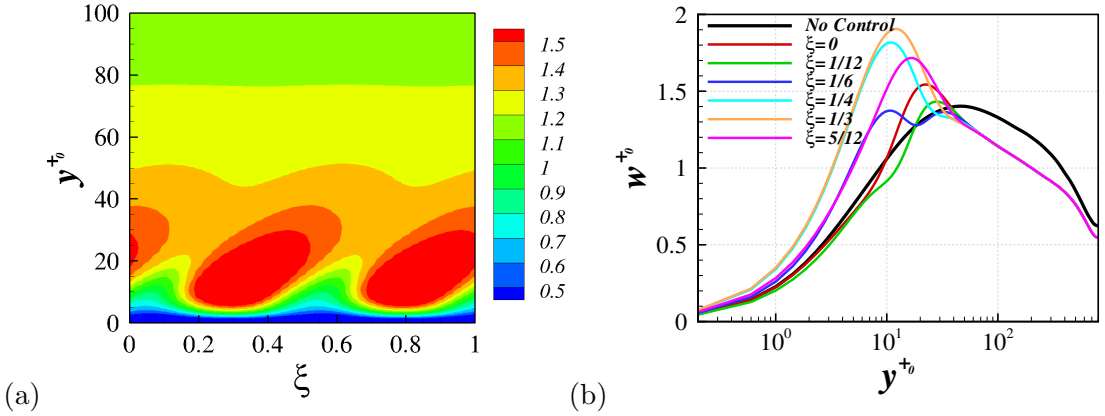

Figure 6.46: Variation of w^+-rms over the period for frequency $\omega^+ = 0.03$ and wavenumber $\kappa_x^+ = 0.008$ in 2d format (a) and 1d format (b).

6.3.3 Vorticity Fluctuations

The streamwise vorticity fluctuations for the $\omega^+ = 0.01$ case are presented in figure 6.47. The wall value is reduced and there is a variation in its magnitude over the period. The peak location changes with ξ, moving away from the wall. For the $\omega^+ = 0.03$ case, the wall value of ω_x^+ rms is increased from the no-control case. The oscillation in the peak value and location is fairly small, with a value larger than the no-control case. Further from the wall there is no evident oscillation in the profile, which is reduced from the no-control case.

The rms of the wall-normal vorticity component in the $\omega^+ = 0.01$ case is

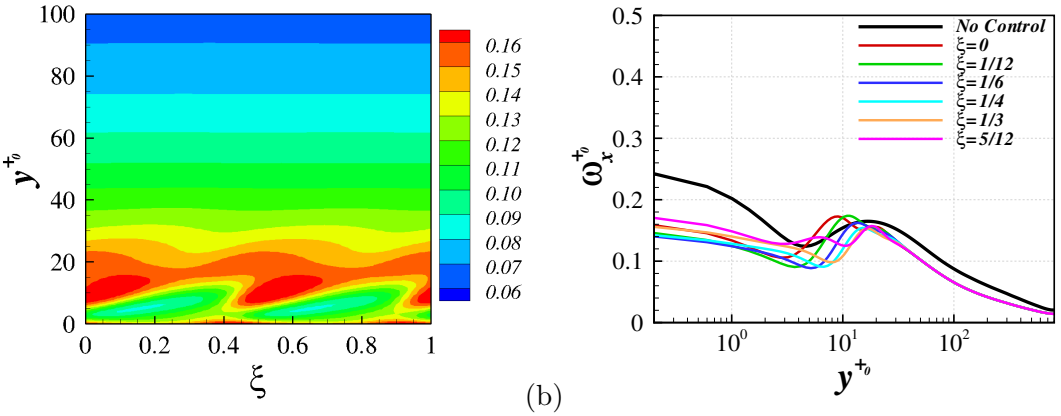

(a) (b)

Figure 6.47: Variation of ω_x^+-rms over the period for frequency $\omega^+ = 0.01$ and wavenumber $\kappa_x^+ = 0.008$ in 2d format (a) and 1d format (b).

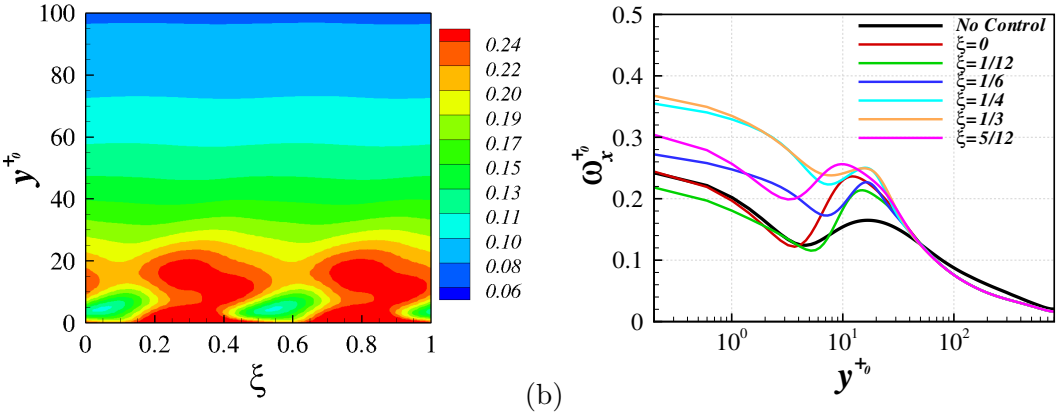

(a) (b)

Figure 6.48: Variation of ω_x^+-rms over the period for frequency $\omega^+ = 0.03$ and wavenumber $\kappa_x^+ = 0.008$ in 2d format (a) and 1d format (b).

shown in figure 6.49. The profile is reduced from the no-control case for all ξ. Although the peak value is fairly constant, the location moves away from the wall, as the profile in the near-wall region oscillates. The oscillation in the peak value is much greater in the $\omega^+ = 0.03$ case, figure 6.50, reaching its maximum when $\xi = \frac{1}{3}$, which is larger than the maximum from the no-control case. The location of the peak is at $y^+ \approx 10$ as the value increases and moves away from the wall as the value decreases. The profile is again reduced in the outer region.

Figure 6.51 shows the profile of the spanwise vorticity with $\omega^+ = 0.01$. The wall value is greatly reduced and there is a small amount of oscillation in the value

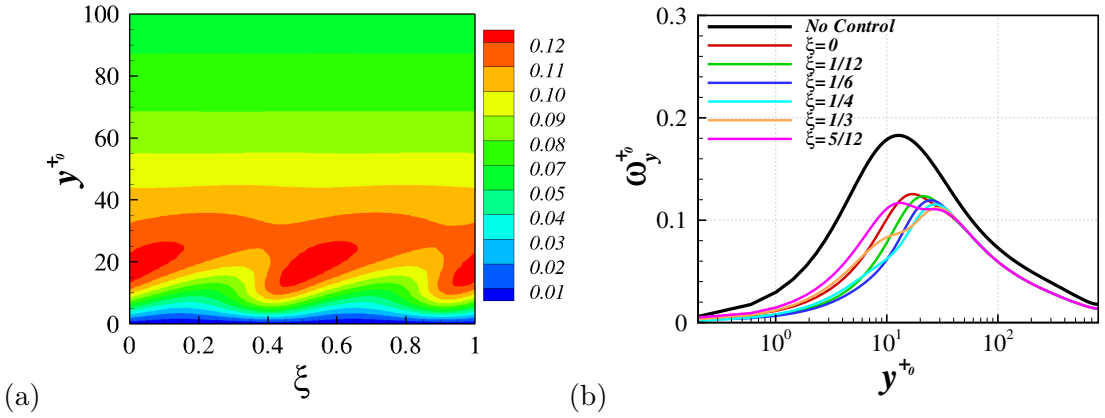

Figure 6.49: Variation of ω_y^+-rms over the period for frequency $\omega^+ = 0.01$ and wavenumber $\kappa_x^+ = 0.008$ in 2d format (a) and 1d format (b).

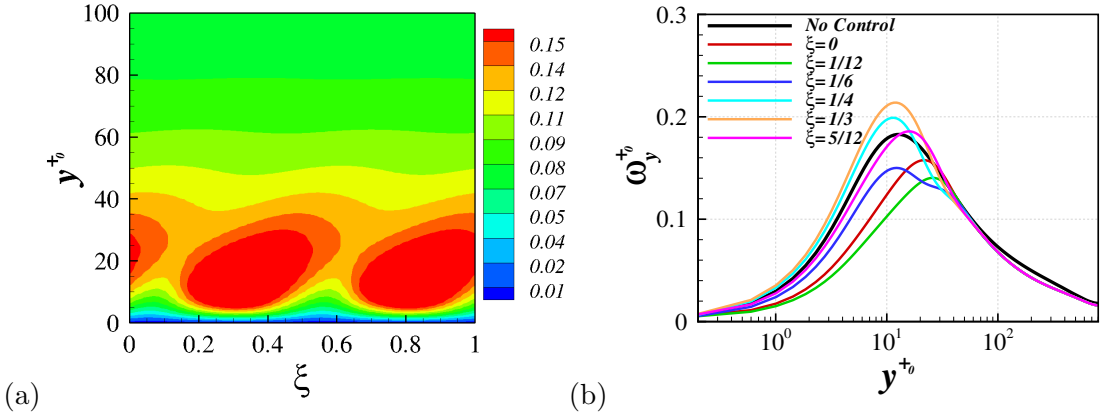

Figure 6.50: Variation of ω_y^+-rms over the period for frequency $\omega^+ = 0.03$ and wavenumber $\kappa_x^+ = 0.008$ in 2d format (a) and 1d format (b).

over the period. A peak emerges in the controlled flow, the location of which varies slightly with ξ. The wall value is also reduced in the $\omega^+ = 0.03$ case, presented in figure 6.52, and there is a large oscillation in the wall value with ξ. The peak value increases such that the profile becomes larger, at that y^{+0} location, than the no-control case. The profile is reduced slightly in the centre of the channel where no oscillation occurs.

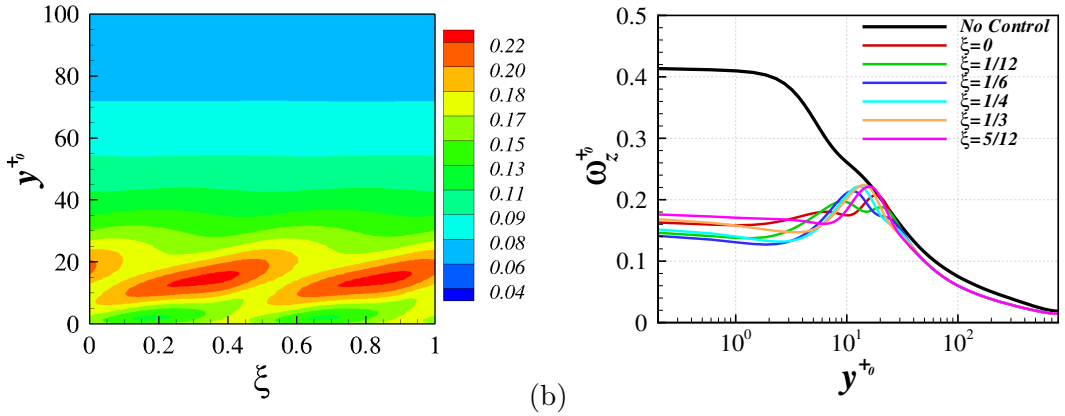

(a) (b)

Figure 6.51: Variation of ω_z^+-rms over the period for frequency $\omega^+ = 0.01$ and wavenumber $\kappa_x^+ = 0.008$ in 2d format (a) and 1d format (b).

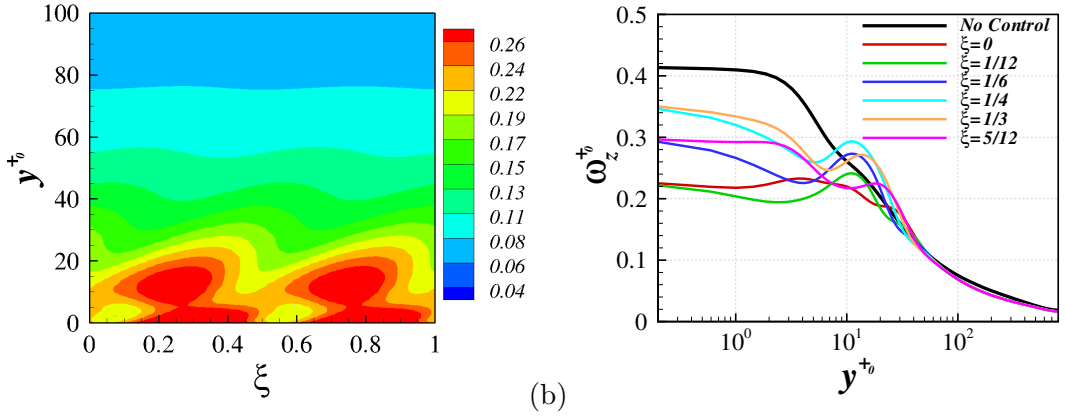

(a) (b)

Figure 6.52: Variation of ω_z^+-rms over the period for frequency $\omega^+ = 0.03$ and wavenumber $\kappa_x^+ = 0.008$ in 2d format (a) and 1d format (b).

6.4 Conclusions

Studying the change in the turbulent statistics over the period for the three different waveforms showed similar behaviour for the different forcing methods. The effective cases, where little oscillation in the drag reduction occurs also experience very small levels of oscillation in their velocity fluctuations. The velocity profiles are strongly reduced from the no-control case. The streamwise vorticity fluctuations reduce from the no-control flow near the wall, but are sometimes slightly increased around the local maximum. There is a larger oscillation (as compared to the velocity) in the vorticity rms profiles with peaks emerging and moving away from the wall over the

half-period. The spanwise vorticity is strongly reduced near the wall causing the emergence of a peak with is not visible in the no-control profile.

The ineffective cases, in which large levels of oscillation is found in the drag reduction [Quadrio et al., 2009], also experience a greater oscillation in the turbulent statistics. Most notably in the w rms profile, where a larger near wall peak exists at certain points in the forcing period. This peak is believed to be related to the production in w' from the spanwise shear and is at a comparable location to the u rms. The streamwise vorticity fluctuations are strongly increased from the no-control case near the wall.

In all of the case shown there is evidence of some oscillation in all of the Reynolds stresses and vorticity fluctuations. In these profiles, the oscillation is restricted to the near wall region (within the Stokes' layer), while the profiles are identical towards the centre of the channel at each point in the forcing period.

Chapter 7

Time- and Plane-Averaged Turbulent Statistics and their Correlations with Drag Reduction

This chapter investigates how the turbulent statistics behave when the forcing parameters are varied. This study is divided into subsections based on the different waveforms of the applied forcing. The results from the wall oscillation cases are presented here, while the results from the other waveforms can be found in Appendix A. To easily compare the results to existing studies the Reynolds number is fixed at $Re_\tau = 200$ and the maximum wall velocity of $W_m^+ = 12$ is set for all control parameters investigated. The statistical profiles are calculated by subtracting the phase-dependent mean from the velocity, vorticity and Reynolds shear stress, giving a result which varies over the period (as studied in the previous chapter). The average is then taken over the period, giving a variety of one dimensional, y dependent graphs for each frequency and wavenumber combination. One major feature of

previous study is that the focus tends to be on optimal forcing. This investigation aims to give an overview of the change in turbulent statistics for both efficient and inefficient forcings.

Although the behaviour of the turbulent statistics of the specific forcing methods is known, a quantitative understanding of the change in the statistics with the forcing parameters has not been studied. The aim of this section is to find measurable parameters which vary with the drag reduction. This would both aid in the understanding of the drag reduction mechanism and also allow the calibration of models which cannot directly measure drag reduction. To achieve this the effect of the control is then compared by correlating the drag reduction to the values and locations of the maxima and minima of the rms and shear profiles. The drag reduction is also correlated with the turbulent statistics at each y value to investigate any relationships which are dependent on a specific wall-normal location.

7.1 1d Averages

The 1d averages are calculated for the whole DR map, shown in section 5.2.1. The presentation of these results are divided into four sections: wall oscillation, standing wave, travelling wave effect in ω^+ and travelling wave effect in κ_x^+ (where the wall oscillation results are shown and the remaining results presented in the appendix). The profiles are shown, scaled in wall units by both the no-control case (using u_{τ_0}) and the local (from the flow with reduced/increased drag) u_τ. This allows the interpretation of the effect of the drag reduction on the statistics, but also an idea of the change in the flow physics independent of the drag reducing effects. It is important to note that, even for the uncontrolled flow, the turbulent statistics do not scale exactly with Reynolds number, as discussed in section 5.1.

7.1.1 Wall Oscillation

The effect of applying the wall oscillation forcing using different ω^+ values is studied, corresponding to the x-axis in the drag reduction map ($\kappa_x^+ = 0$). To aid the comparison with previous studies based on T^+ the results are discussed in decreasing order in ω^+ (as if the $T^+ = \frac{2\pi}{\omega^+}$ value is increasing). The drag reduction increases as the frequency decreases from $\omega^+ = 0.18$ until it reaches a maximum at $\omega^+ = 0.06$. Below this, the drag reduction decreases giving drag increase at $\omega^+ = 0.01$ (shown in figure 5.11a).

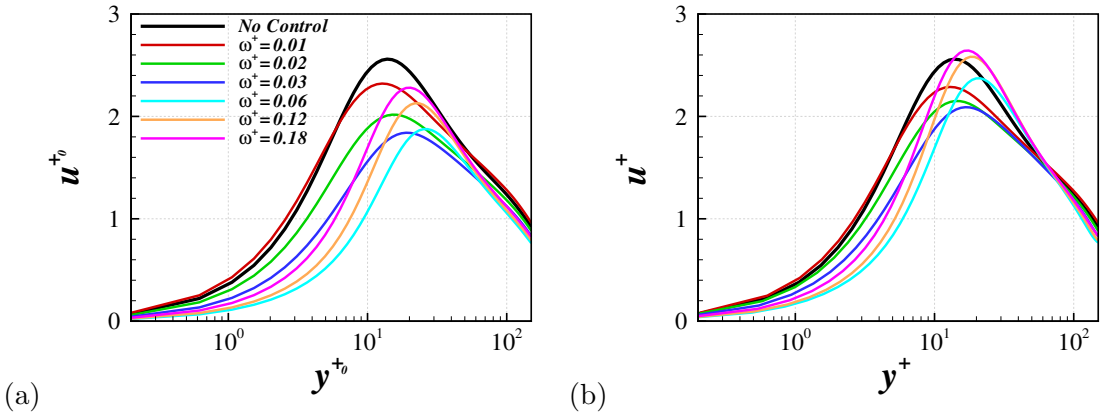

Figure 7.1: Streamwise rms fluctuations scaled by the no-control case (a) and local wall units (b).

The streamwise rms fluctuations, scaled by the no-control case are shown in figure 7.1a. The profile is reduced at high forcing frequency and the peak is moved away from the wall [Jung et al., 1992]. This distance of the maximum from the wall is largest when the drag reduction is greatest. This corresponds to a large reduction in the strength of the near wall streaks, shown by Touber and Leschziner [2012] as a 2d slice, in which the streaks are also seen to be angled by the wall forcing. The streaks play an important role in the regeneration of turbulence as argued by Chernyshenko and Baig [2005]. The streamwise velocity fluctuations correspond to the movement of high speed fluid toward the wall and low speed fluid away from the wall, events which contribute to an increase in skin-friction. As ω^+ is

decreased below $\omega^+ = 0.06$, the maximum moves back towards the wall. The near wall fluctuations increase with decreasing ω^+. This relates to the oscillations seen in the near-wall fluctuations over the oscillation period, presented in section 6.1.

When scaled by the local u_τ value, figure 7.1b, the u rms peak locations behave similarly to when scaled by u_{τ_0}, with less change in the values. Baron and Quadrio [1996] showed that the streamwise fluctuation is relatively unchanged for $T^+ = 100$ ($\omega^+ = 0.06$), when scaled in local wall units. The current results show that there is a clear reduction in the near-wall fluctuation, disagreeing with the prior results, however the W_m^+ value is larger in this study. For the initial DR parameters $0.06 \leq \omega \leq 0.18$. There is an increase in the profile from the no-control case in the approximate region $20 < y^+ < 60$, as seen by Baron and Quadrio [1996]. The profiles from all the cases appear to come together at $y^+ \approx 60$. This corresponds to the approximate location at which the log-law is satisfied (although no certain log-law region is present at this low Reynolds number).

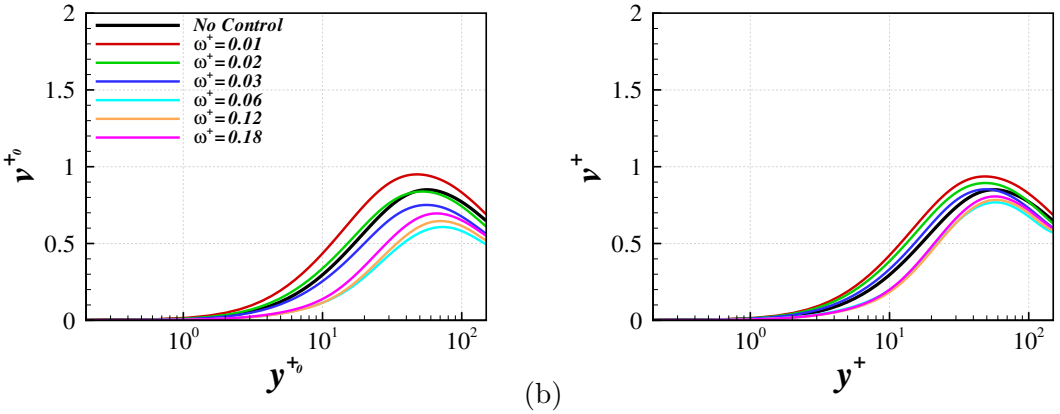

Figure 7.2: Wall normal rms fluctuations scaled by the no-control case (a) and local wall units (b).

The wall-normal velocity fluctuations, scaled by the no-control case, are presented in figure 7.2a. The profile is again reduced and the peak moves away from the wall, reaching a minimum at $\omega^+ = 0.06$. As the frequency is reduced below $\omega^+ = 0.06$, the profile increases again. The peak value at $\omega^+ = 0.02$ is similar to

that of the no-control case, but is closer to the wall. With $\omega^+ = 0.01$, the profile is universally increased from the no-control case profile.

When scaled by local u_τ the variation in the profiles is reduced. The order of the peak values is the same for the control cases, but the $\omega^+ = 0.03$ peak has similar value to the no-control case. For $\omega^+ \geq 0.06$ the near-wall profiles are very similar, with shallow gradient at the wall. It is important to note that even for the no-control case when the Reynolds number is increased the peak in the wall-normal fluctuations flattens and moves away from the wall. When there is a drag reduction there is a corresponding decrease in friction Reynolds number, hence even if the physics of the flow are as in the no-control case, the change in Re_τ would cause a difference in the profiles (an effect which may be occurring in this instance).

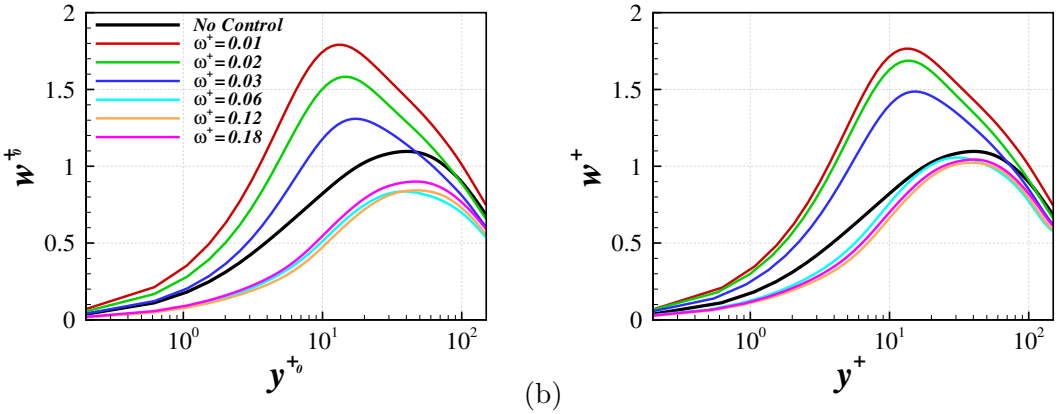

Figure 7.3: Spanwise rms fluctuations scaled by the no-control case (a) and local wall units (b).

Figure 7.3a shows the spanwise rms profiles for the various wall oscillation cases. For $\omega^+ = 0.18$, 0.12 and 0.06, the profiles are reduced. This reduction is relatively large when scaled globally. When the local scaling is applied it becomes clear that the reduction at the peak was predominantly a product of the outer scaling, as claimed by Quadrio and Ricco [2011]. There is, however, still a clear reduction in the near wall fluctuations for these cases.

For $\omega^+ \leq 0.03$, the near-wall fluctuations become large and a peak emerges

at around $y^{+_0} \approx 10$. This peak, as discussed in section 6.1, is a consequence of the increased production in w' due to the spanwise shear $\frac{\partial W}{\partial y}$. Ricco et al. [2012] showed that the spanwise oscillation causes a non-zero $\overline{v'w'}$ at various points over the oscillation period. This, along with the spanwise shear, contribute to a non-zero production of w'. Another way to consider this effect is that it is related to the angling of the flow direction. This three-dimensionality of the flow causes large spanwise fluctuations, as a component of the flow alignment is now in the spanwise direction. This is seen in the mean spanwise velocity profile at high T^+ [Touber and Leschziner, 2012], when the profile differs from that of the laminar Stokes' solution.

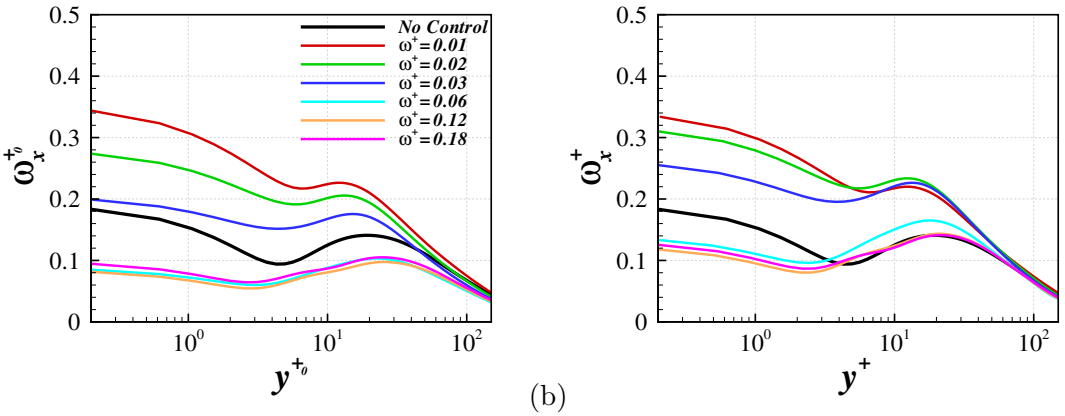

(a) (b)

Figure 7.4: Streamwise vorticity rms fluctuations scaled by the no-control case (a) and local wall units (b).

The streamwise vorticity fluctuations, scaled by u_{τ_0} are shown in figure 7.4a. For $0.06 \leq \omega^+ \leq 0.18$, the profiles are very similar, being universally reduced from the no-control case and the local minima are moved closer to the wall [Baron and Quadrio, 1996]. The profile becomes very flat for these values of the forcing parameter. This flatness is a by-product of the oscillation in the peak location over the forcing period (showed in section 6.1. This oscillation corresponds to the movement of the coherent vortices away from the wall and is discussed later in this thesis. As ω^+ becomes small, with $\omega^+ \leq 0.03$, the profile becomes larger than the no-control case in the near-wall region.

When scaled by local wall units, figure 7.4b, the profiles for $\omega^+ = 0.12$ and 0.18 are almost exactly as in the no-control case for $y^+ > 10$. There is however a strong reduction in ω_x rms near the wall. At $\omega^+ = 0.06$ the near-wall value is still reduced, despite the fact that the profile is increased in the region of the maxima. The profiles are again increased in the near-wall region for $\omega^+ \leq 0.03$. The profiles almost follow the same line as they approach the centre of the channel.

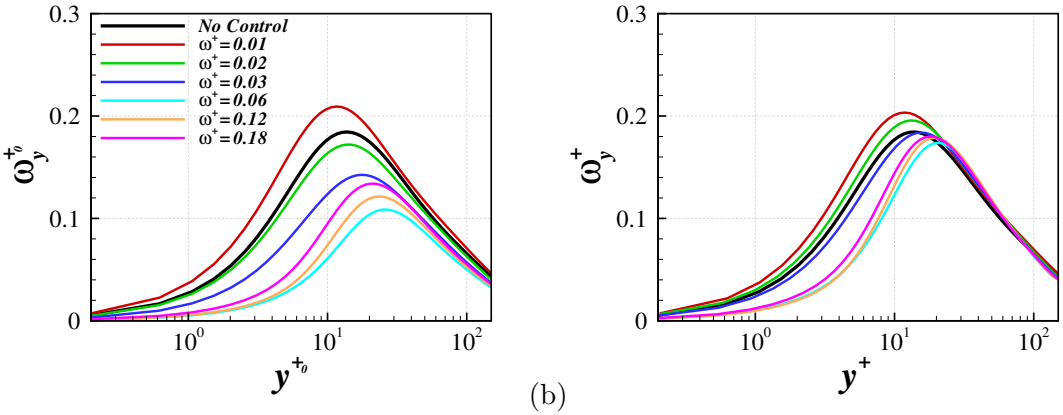

(a) (b)

Figure 7.5: Wall normal vorticity rms fluctuations scaled by the no-control case (a) and local wall units (b).

Figure 7.5a shows the wall-normal vorticity rms profiles. The profile is reduced and the peak moves away from the wall. The minimum peak value is reached when $\omega^+ = 0.06$ and the drag reduction is largest. As the frequency becomes smaller than $\omega^+ = 0.06$, the profile is increased and the peak value moves back towards the wall. The profile becomes larger than the no-control case when $\omega^+ = 0.01$, and a drag increase occurs.

When scaled by local u_τ, figure 7.5b, the change in ω_y rms is reduced, but similar behaviour occurs to the no-control scaling. The order of the control profiles is the same, but the $\omega^+ = 0.02$ profile becomes larger than the no-control case. At $y^{+_0} \approx 60$ the control profiles appear to collapse.

The ω_z rms profile are presented in figure 7.6a, scaled by the no-control case. For $0.06 \leq \omega^+ \leq 0.18$ the wall value is greatly reduced and a peak appears in the

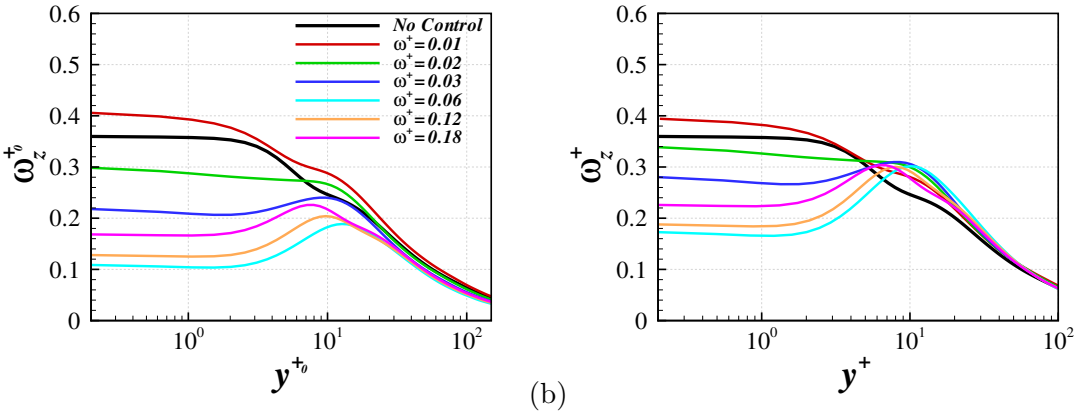

(a) (b)

Figure 7.6: Spanwise vorticity rms fluctuations scaled by the no-control case (a) and local wall units (b).

near-wall region [Baron and Quadrio, 1996]. This peak decreases and moves away from the wall as the drag reduction becomes larger. As $\omega^+ \leq 0.03$ the wall value increases, causing the local maximum to disappear. Touber and Leschziner [2012] attributed the reduction in enstrophy in the optimal wall oscillation case to the large decrease in spanwise vorticity fluctuations.

Figure 7.6b shows the spanwise vorticity scaled by local wall units. The peak values of the profiles are similar, and are in a similar location. In the outer region the profiles are overlapped as they approach channel centreline.

7.2 Correlations with Drag Reduction

Due to the difficulty in measuring the drag in experimental investigation, a relationship between the drag reduction values and measurable flow properties is important in understanding effect of the forcing on the turbulence. With this aim, a study of the correlations between the drag reduction and some simple flow features is undertaken. The maximum (and minimum if applicable) values and locations are calculated from the 1d profiles. The velocity, pressure and vorticity rms, and the Reynolds shear stress maxima from the $Re_\tau = 200$ are initially plotted against $-DR$. The variables which give a reasonable correlation are then studied at $Re_\tau = 400$ and 800, to aid the understanding of the Reynolds number effect. The correlations at fixed y^{+_0} locations are also investigated.

A similar study was performed for flow control using wall-normal blowing and suction by Chung and Talha [2011]. Various parameters were investigated and it was found that the maximum value of wall-normal velocity and vorticity rms showed a good correlation with the drag reduction.

7.2.1 Correlations of Maxima and Minima

To study the oscillation of the maxima and minima of the turbulent statistics over the forcing period, the values and locations of the profiles from the three different forcing methods must be calculated. This is done by first calculating the 1d average profile, and then finding the local maximum or minimum based on the y grid. A cubic spline is then taken around the extrema to find a more accurate value and location in y. The accuracy of the peak value and location measurement is expected to reduce further towards the channel centreline, as the size of the grid spacing increases in this region.

Figure 7.7a is a plot of the drag reduction against the maximum values of the streamwise velocity rms profiles. The no-control case corresponds to the point

at $u^{+_0}_{max} = 2.6$ and $-DR = 0$. Some of the cases appear to follow a curve from the no-control case in which the peak value decreases as the drag reduction increases. The minimum peak value is 1.6, which is found when the drag reduction is greatest. Another correlation appears to occur for some profiles, in which the peak value increases as the DR decreases. This correlation is not particularly strong, especially in the drag increase cases. The reason for these two regimes may be related to the strong oscillation in the u rms profile seen at these forcing parameters (discussed at higher Reynolds number in chapter 6). The lower peak value is an effect of the change of near-wall flow direction and hence the u rms profile begins to look more like the w rms profile (with smaller fluctuations) at these forcing parameters.

Figure 7.7b shows a reasonable correlation between the location of the u rms peak and the drag reduction. The correlation between these two parameters is non linear, so a change at the high DR values correspond to a large change in y^{+_0}, whereas a change in the drag increased forcing correspond to small change in peak location. The problem with this form of correlation is that if used to estimate the drag reduction, any small error in the measurement of the peak location will give a fairly inaccurate result in the drag increase cases. Another clear problem is that there are three points which do not fit into the correlation curve. These points correspond to travelling wave forcings with (ω^+, κ_x^+) of $(0.01, 0.004), (0.03, 0.008)$ and $(0.12, 0.016)$. All of these combinations of the forcing parameters corresponded to large oscillations in the drag reduction over the period. As a large oscillation in the forcing period corresponds to oscillations in the Reynolds stresses and hence movement in the maxima, this could cause the difference in the y location.

Figure 7.8a shows the $-DR$ values plotted against the v rms peak values. The correlation from this parameter is linear and very strong, with a correlation coefficient of 0.996. Interestingly, there is one point that does not appear to sit on the straight line which relates the majority of the maximum in the rms wall-normal velocity and drag reduction. This point is the result from the no-control case.

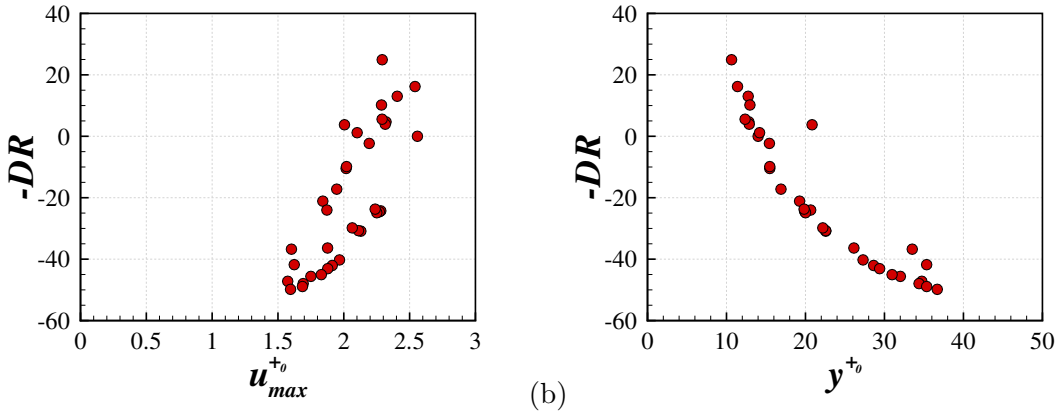

Figure 7.7: Correlation of streamwise velocity rms to the drag reduction for the maximum value (a) and location (b).

Possible reasons for this are discussed later, when the Reynolds effect is studied. The maximum value of the rms of wall-normal velocity has previously been seen to give a good correlation to the drag reduction in the study of flow control by wall blowing and suction [Chung and Talha, 2011]. One key feature of the v rms peak is that it is far from the wall, as compared to the u and w rms maxima. This means that the effect of the near-wall oscillation may not extend into the flow as far as this peak location in the cases studied here. Because of this, the peak could change relative to any change in the wall shear stress and hence is correlated to DR. Also, because of the angling of the near-wall flow direction, the u rms profile reduces while the w rms profile increases, which is not the case with the wall-normal fluctuations. The wall-normal rms is also directly related to the production of Reynolds shear stress $P_{12} = -\overline{v'v'}\frac{\partial U}{\partial y}$.

The correlation between the location of the v rms maxima and the drag reduction is investigated in figure 7.8b. There appears to be a reasonable correlation between some of the values when DR is maximum, which also fits with two of the drag increase cases. The peak is furthest away from the wall when the drag reduction is at the maximum, however many of the cases do not fit into this correlation.

The $-DR$ values are plotted against the maximum w rms values in figure

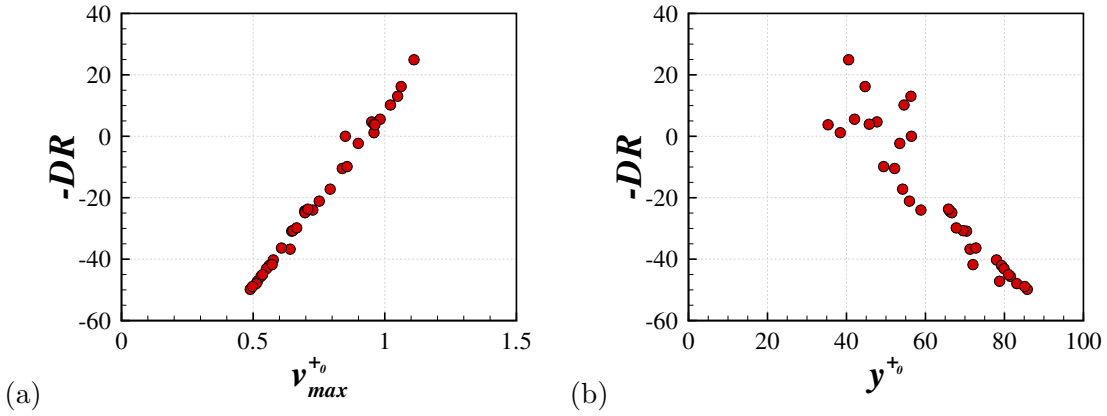

Figure 7.8: Correlation of wall-normal velocity rms to the drag reduction for the maximum value (a) and location (b).

7.9a. There appears to be a correlation, which includes the no-control case, for some of the higher drag reduction cases. The maximum drag reduction is again found when w^{+0}_{max} value is at its minimum. For many of the cases the maximum spanwise velocity rms is too large to fit into the correlation. These correspond to cases where a large near-wall peak occurs. This effect can also be seen in the location of the peak w rms values, figure 7.9b. In this plot the high drag reduction cases have a peak far from the wall ($y^{+0} > 30$), whereas the peak is much closer to the wall for most lower drag reduction cases (including some higher DR values). Although there is no clear correlation for the cases with large y^{+0} values, the near-wall peaks do appear to follow a weak correlation to drag reduction, with the peak moving towards the wall as the drag is increased.

The drag reduction is compared to the value of the peak in the streamwise vorticity profiles in figure 7.10a. Although the general trend is that the maximum value decreases as the drag reduction is increased, there are a number of points with large DR which appear to fit the opposite trend. This can also be seen in the location of the maximum, figure 7.10b. In this plot, at large drag reductions, some of the maxima move away from the wall as the DR increases and some move towards the wall. This may be related to the deformation of the profile around

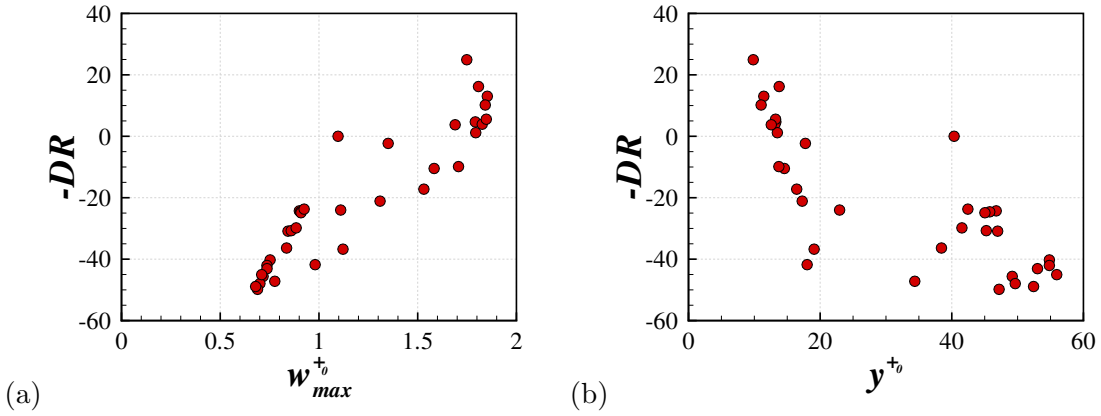

Figure 7.9: Correlation of spanwise velocity rms to the drag reduction for the maximum value (a) and location (b).

this maximum, seen in some of the 1d profiles. In the low drag reduction and drag increases cases there is a reasonable correlation, in which the peak is further from the wall when the drag reduction is largest. This correlation does not include the no-control case.

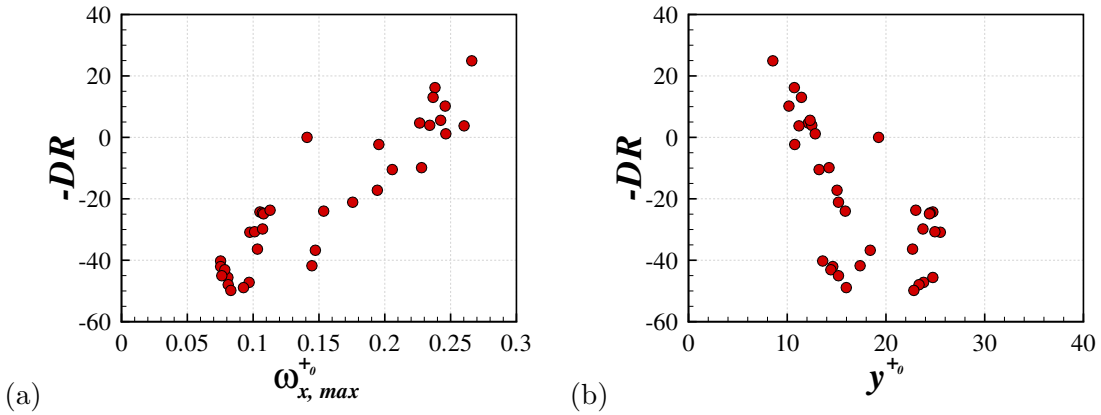

Figure 7.10: Correlation of streamwise vorticity rms to the drag reduction for the maximum value (a) and location (b).

As the streamwise vorticity profile also contains a minimum, this value is also calculated and compared to the drag reduction, figure 7.11a. The minimum ω_x rms value is decreased from the no-control case as the drag reduction increases, reaching a minimum of 0.04. At the points which do no fit this correlation the

streamwise vorticity minima value are higher, corresponding to the large increase in the near-wall fluctuations seen in the 1d profiles. The minima from the ω_x rms profiles are close to the wall and vary around $y^{+_0} \approx 5$, figure 7.11b. There is little correlation seen in these values.

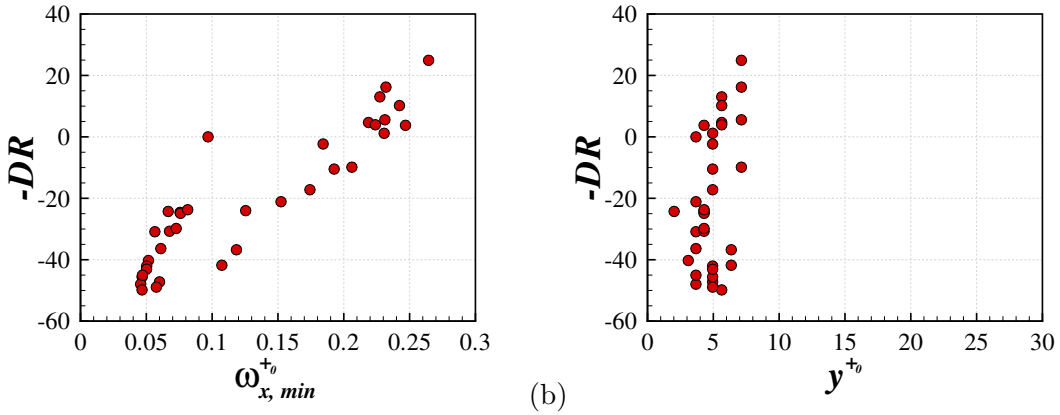

Figure 7.11: Correlation of streamwise vorticity rms to the drag reduction for the minimum value (a) and location (b).

The wall-normal vorticity rms maximum values are compared to the drag reduction in figure 7.12a. This parameter gives a very strong correlation for high drag reduction cases, however this correlation becomes weaker in the negative DR cases. The overall correlation coefficient is 0.946. The location of of the maxima of wall-normal vorticity rms also give a good correlation to the drag reduction, figure 7.12b. This correlation is not linear as a small change in y^{+_0} when near the wall ($10 < y_0^+ < 15$) corresponds to a large change in the drag reduction. There are again a few points, including the no-control case, which do not fit this correlation.

Figure 7.13a shows the drag reduction compared to the maximum value of the spanwise vorticity rms. These local maxima do not exist for all the cases studied. This was seen in the 1d profiles in which some of the near-wall values were decreased, creating a peak, and some were increased leaving no local maximum. For cases where no peak can be calculated, the maximum value is set to zero, as is the location of the maximum in y^{+_0}. For the cases which have maxima the correlation is strong,

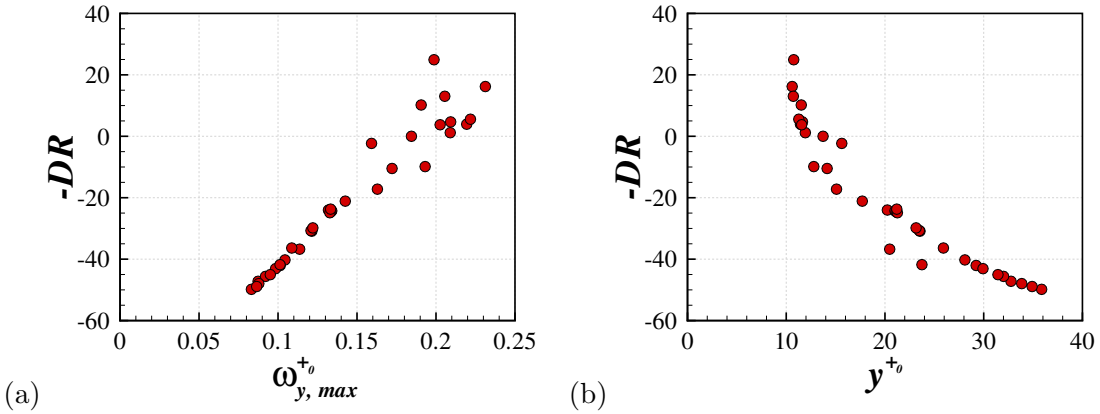

Figure 7.12: Correlation of wall-normal vorticity rms to the drag reduction for the maximum value (a) and location (b).

with one peak slightly too low to fit the correlation. The maximum value decreases as DR increases. The location of these maxima, figure 7.13b, are further from the wall in high drag reduction cases. For the lower (and negative) drag reduction cases the peaks are close to the wall, if they exist.

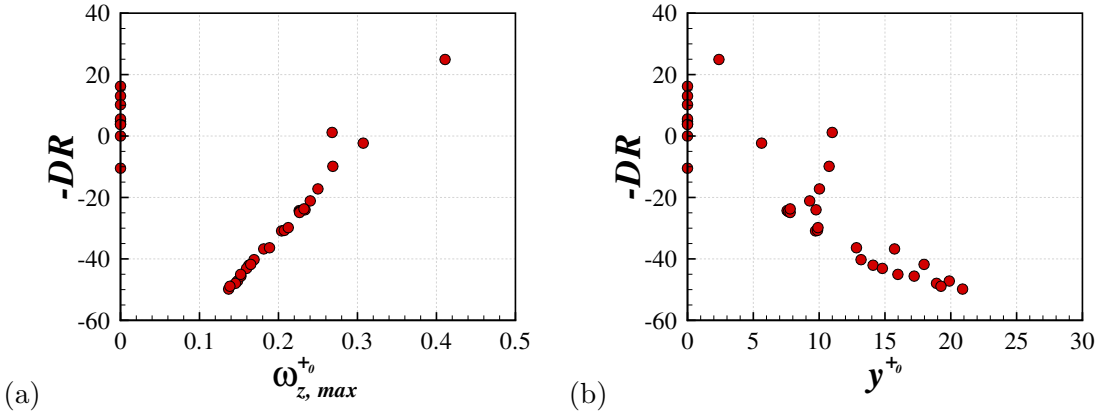

Figure 7.13: Correlation of spanwise vorticity rms to the drag reduction for the maximum value (a) and location (b).

The maximum values of the Reynolds shear stress give very strong correlation to the drag reduction, shown in figure 7.14a. This correlation is expected and may not be useful in the approximation of DR from experimental or numerical modelling data, due to the inherent relationship between Reynolds shear stress and

skin friction. A negative contribution to the Reynolds shear stress occurs when either $v' > 0$ and $u' < 0$ or $v' < 0$ and $u' > 0$. Physically, these events correspond to the movement of high speed fluid towards the wall (sweeps) or the movement of low speed fluid away from the wall (ejections). These fluid motions both work in slowing the flow and hence increasing the skin-friction. Marusic et al. [2007] showed that the skin friction can be calculated from the integral of the Reynolds shear stress, an extension of the previous work by Fukagata et al. [2002].

The location of this maximum is presented in figure 7.14b. This also gives a good correlation, although a few points are slightly further from the wall than expected from the rest of the correlation. This trend is not quite linear, especially in the cases with large drag reductions.

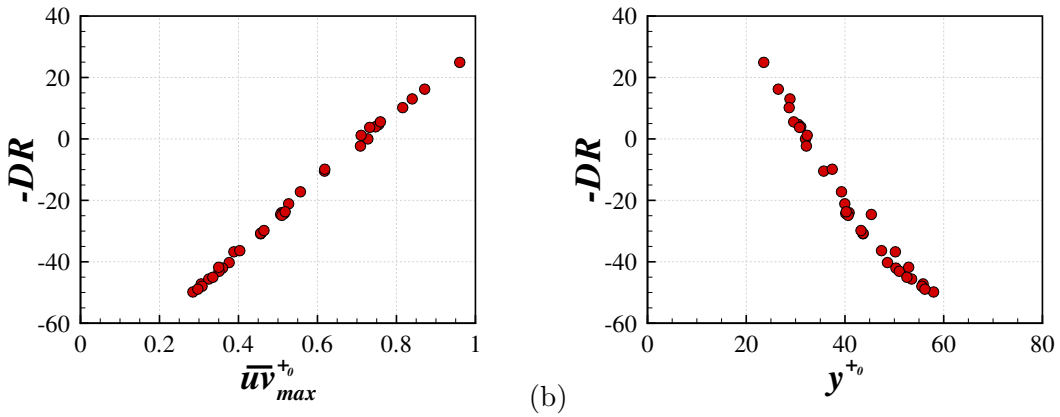

(a) (b)

Figure 7.14: Correlation of Reynolds shear stress fluctuations to the drag reduction for the maximum value (a) and location (b).

7.2.2 Reynolds Number Effect

To discuss the effect of the Reynolds number on the correlations, and hence the extrema, these peak values and locations are also calculated for the $Re_\tau = 400$ and 800 cases. The values which gave reasonable correlations at $Re_\tau = 200$ are presented at the higher Re values.

Figure 7.15a shows the correlation of the location of the maximum of stream-

wise velocity rms to the drag reduction at all three Reynolds numbers. Note that due to the y^{+_0} scaling the location of the maxima in the no-control cases are equal. The correlation appears strong at all three Reynolds numbers and overlap well. There were three points which did not fit the correlation at $Re_\tau = 200$. Two points at $Re_\tau = 400$ and one at $Re_\tau = 800$ also do not follow the correlation.

The Reynolds number effect on the correlation of the location of the maximum wall-normal vorticity rms is shown in figure 7.15b. Due to the scaling, the no-control locations are again the same and hence the correlations roughly overlap. Although there were a few cases which did not fit the correlation at $Re_\tau = 200$, the correlation becomes much weaker at the higher Reynolds numbers.

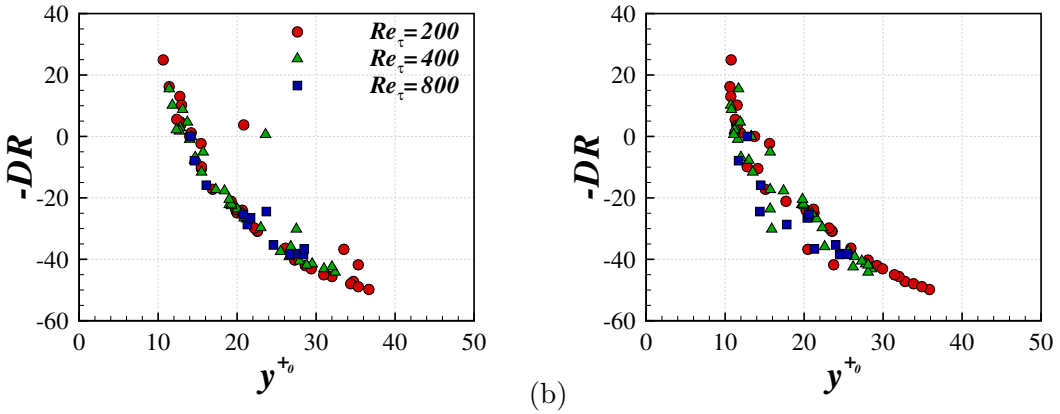

(a) (b)

Figure 7.15: Reynolds number variation of the correlation of maximum locations of streamwise velocity rms (a) and wall-normal vorticity rms (b).

The correlation of the maximum values of the wall-normal vorticity is shown at the three Reynolds numbers, figure 7.16a. As Re is increased the wall-normal vorticity profile from the no-control cases are similar (very slight increase), when scaled by wall units. This means that the correlations overlap for all three Reynolds number. As seen at $Re_\tau = 200$ the correlations at the higher Reynolds numbers also become weaker in the low and negative drag reduction cases.

As the Reynolds number is increased the spanwise vorticity is increased when scaled by wall units. Figure 7.16b show this, and therefore the correlation seen at

$Re_\tau = 200$ does not overlap the higher Re correlations. Although the correlation seems reasonable at $Re_\tau = 400$ and 800 there are still many cases with no local maxima.

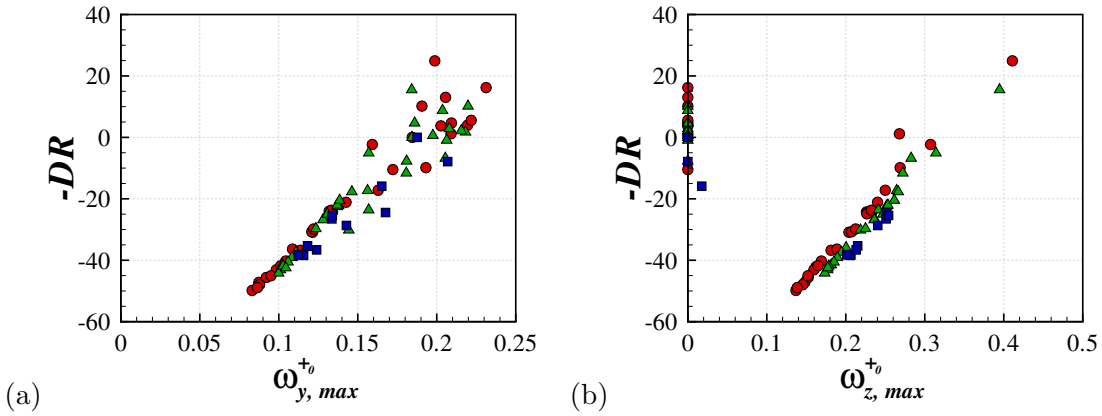

Figure 7.16: Reynolds number variation of the correlation of maximum values of wall-normal vorticity rms (a) and spanwise vorticity rms (b).

Figure 7.17a shows the correlation between the drag reduction and the wall-normal velocity rms maximum values at the three Reynolds numbers. As Re increases the v rms values become larger when scaled by wall units. This means that the correlations from the different Reynolds numbers do not overlap. At $Re_\tau = 200$ the no-control case did not fit into the correlation as the v^{+0}_{max} value was slightly low. The same situation occurs at $Re_\tau = 400$ and 800. The offset of the no-control case from the correlation was measured to be very similar, as a velocity difference of ≈ 0.08 for all three Reynolds numbers. The gradient of the correlation was also noticed to be similar at each of the Reynolds numbers. With these two concepts, the obvious way to equate the correlations was to calculate the difference of the maximum velocity rms from the no-control case (by subtracting the no-control value). Figure 7.17b show the result of using the difference of the v rms maxima from the no-control value. This gives a good correlation, which seem appropriate for all the Reynolds number studied here.

The offset in the no-control case from the v rms correlation is non trivial.

This type of effect has not (to the author's knowledge) been seen in other studies. One possible explanation for this behaviour is that, at certain combinations of the forcing parameters, the Stokes' layer is so thin that there is no drag reduction but the peak value of the v rms is affected slightly. A similar effect is seen in the W_m^+ variation, in which the W_m^+ is initial increased but very small levels of drag reduction are achieved. This concept was used in the S^+ parameter [Choi et al., 2002] where a threshold velocity was used in the logarithmic scaling.

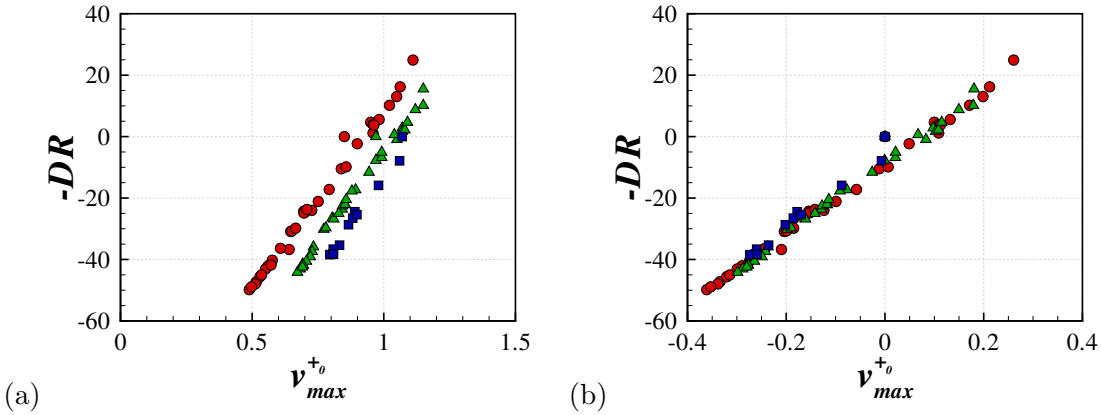

Figure 7.17: Reynolds number variation of the correlation of maximum values of wall-normal velocity rms (a) and wall-normal velocity rms scaled by subtracting the maximum value of the no-control case (b).

7.2.3 Correlations at Wall Normal Locations

To check for linear correlations at specific y^{+0} locations, the correlation coefficient is computed as a function of the wall-normal direction. Figure 7.18a shows the correlation coefficient profiles calculated from the velocity and pressure rms profiles of all the $Re_\tau = 200$ cases. The streamwise velocity has reasonable correlation near the wall. This decreases greatly further from the wall, but become reasonable again when $70 < y^{+0} < 150$. The v rms correlation is low near the wall but becomes strong, reaching a maximum at $y^{+0} \approx 50$. This location is close to the location of the peak value, where a good correlation was seen previously. Both the w and p correlation coefficients are poor near the wall. Although they are slightly increased

in the outer region, there is no good correlation in these parameters.

The vorticity and Reynolds shear stress correlations are shown in figure 7.18b. The correlation of the streamwise and wall-normal vorticity rms profiles are weak in the near-wall region. The spanwise vorticity is reasonably high at a peak near the wall, but does not give very good correlation. All three vorticity rms correlations are strong in to outer region when $80 < y^{+_0} < 150$, especially the wall-normal vorticity. The Reynolds shear stress gives a strong correlation for $y^{+_0} < 20$, this is expected because of the relationship with the wall shear stress.

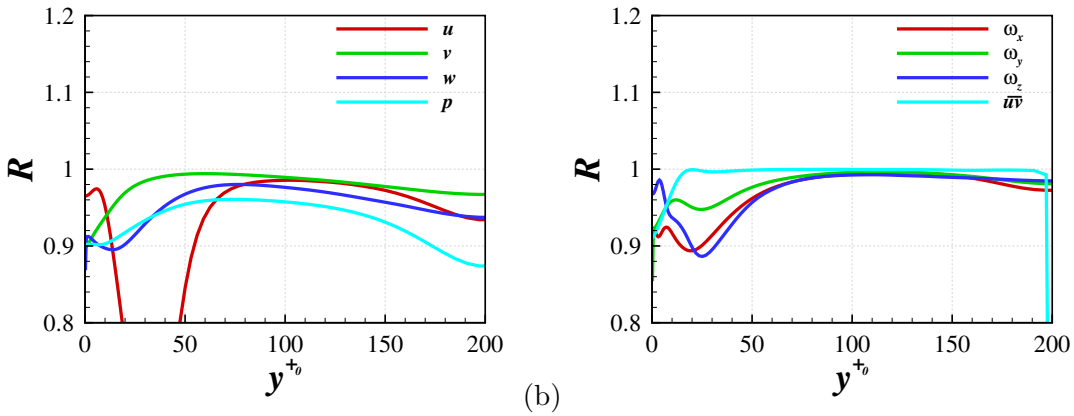

Figure 7.18: Correlation coefficient variation in the wall-normal direction for the (a) rms velocity, pressure, (b) rms vorticity and Reynolds shear stress.

7.3 Conclusions

On initial inspection of the profiles for all three wall forcing methods, when a decrease in drag is observed, a corresponding reduction in the turbulence statistics is noted. To provide a quantitative understanding of how changes in drag affect the turbulence statistics, the maxima (and minima where applicable) values and wall-normal locations of the profiles were compared to the drag reduction.

The maximum value of the streamwise fluctuations were reduced with drag reduction. The way in which the DR and u'_{max} correlate suggest two different flow regimes. One in which the fluctuations are reduced with DR and another in which

the u-fluctuations remain low while the drag reduction drops away (and becomes a drag increase in some cases). This second set of cases corresponded with oscillations in DR over the forcing period.

The wall normal fluctuations showed a strong correlation with drag reduction. The reason for this correlation is believed to be role of the wall normal fluctuation in the production of the Reynolds shear stress. For the current simulations this can be written:

$$P_{12} = -\overline{u'^2}\frac{\partial V}{\partial x} - \overline{u'v'}\frac{\partial V}{\partial y} - \overline{v'u'}\frac{\partial U}{\partial x} - \overline{v'^2}\frac{\partial U}{\partial y}.$$

This reduces to $P_{12} = -\overline{v'^2}\frac{\partial U}{\partial y}$ for the wall oscillation cases (although this term dominates for the spatially dependent cases). The production of v' is zero for the wall oscillation cases but is:

$$P_{22} = -2\overline{u'v'}\frac{\partial V}{\partial x} - \overline{v'^2}\frac{\partial V}{\partial y},$$

for the streamwise varying flow. Again, these terms are small as the values of V are small (section 6.2.1).[Note that this V is oscillates over the period and arises from the changing streamwise mean velocity, $\frac{\partial U}{\partial x}$, and the continuity equation.]

The maximum of w' also correlated reasonably well with DR for some forcing parameters, which tended to give large drag reductions. Chapter 6 showed that oscillations in the drag over the period gave rise to an increase in the w' at certain points in the period. This is seen in the correlations, where the maximum w' value becomes larger for certain forcing parameters. This stems from an increase in the production of w':

$$P_{33} = -2\overline{u'w'}\frac{\partial W}{\partial x} - \overline{v'w'}\frac{\partial W}{\partial y}.$$

This production is caused by the spanwise shear and streamwise change in spanwise velocity from the wall forcing.

The maximum value of wall normal vorticity correlated well with drag re-

duction. Although, the correlation was weaker when a drag increase occurred and the peak value increased.

Chapter 8

The Effect of Wall Forcing on Near-Wall Streaks and λ_2 Structures

This chapter looks at the physics of the flow with control. In doing this, a geometrical approach is undertaken, studying the near-wall streaks and λ_2 structures. To simplify any comparisons, the flow is restricted to the $Re_\tau = 400$ cases (based on the no-control case). The control method is also initially limited to that of the spanwise wall oscillation, although the extension to the other control methods is discussed at the end, with some results presented. The study of the temporal oscillation allows averaging to be performed over the whole domain without the requirement to account for spatial changes. This means that a range of snapshots and averages can be shown at multiple points throughout the period. The presentation of data is actually limited to the half-period due to the symmetry of the oscillation, and therefore a symmetry occurs in any visualisation. The structural dynamics of steady 3D turbulent boundary layers has been previously investigated through coherent structure eduction schemes. This study looks in to the temporal change in the structure

geometry using a similar eduction method. The conditionally averaged λ_2 structure is used to extract the structure angle, which is then compared to a variety of flow angles that are calculated from the statistics.

8.1 Capturing Instantaneous Data

In order to understand the periodic effect of wall oscillation on flow structures instantaneous snapshots of the three-dimensional velocity field were captured at various stages throughout the oscillation cycle. To ensure a reasonable resolution to capture the transient behaviour, 32 snapshots were studied, spaced equally over each period of oscillation. When averaging is performed, the same time point is used from three consecutive forcing cycles, in addition to any spatial averaging. To discuss points throughout the phase of the oscillation the parameter ϕ is defined as $0 \leq \omega t \leq 2\pi$. The results presented are limited to eight equally spaced time points over the half period, as shown in figure 8.1. These correspond to $\phi = 0, \frac{\pi}{8}, \frac{\pi}{4}, \frac{3\pi}{8}, \frac{\pi}{2}, \frac{5\pi}{8}, \frac{3\pi}{4}$ and $\frac{7\pi}{8}$. Note that, in the figure, the wall velocity is initially negative due to its application in the form $w_w = W_m \sin(-\omega t)$, which stems from the definition of the travelling wave forcing.

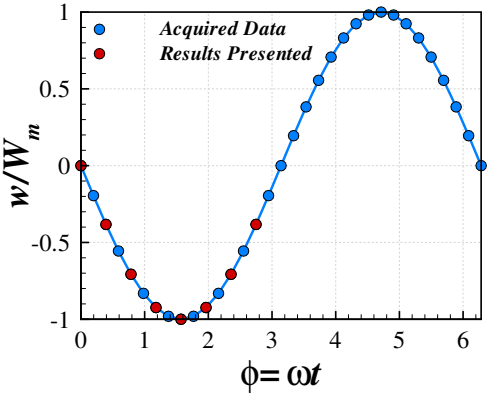

Figure 8.1: Instantaneous data captured at various points over the period of wall oscillation.

8.2 Streak Visualisation

The near-wall fluctuation in u velocity can be visualised to study the distribution of streaks in the xz plane. Although they are universally considered important in understanding the nature of near-wall turbulence, there is still some debate as to their roll in turbulent activity. It has been proposed that they play a vital part in the generation of turbulence [Chernyshenko and Baig, 2005]. Conversely, streaks can be considered as a "footprint" of vortical motion, in which vortex pairs force high speed fluid towards the wall causing the streaky structures.

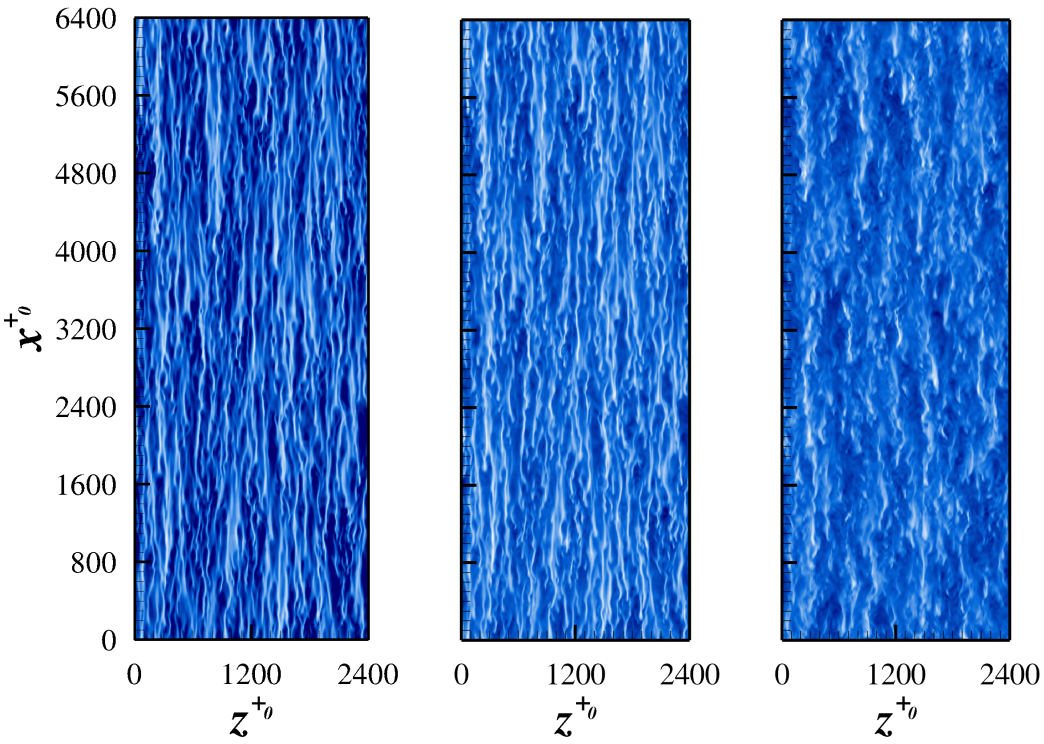

Figure 8.2: Visualisation of the streaks for the no-control case with $Re_\tau = 400$, at wall-normal locations $y^{+_0} = 10, 20$ and 50.

Figure 8.2 shows the streak patterns at $y^{+_0} = 10, 20$ and 50 from the no-control case when $Re_\tau = 400$. At $y^{+_0} = 10$, a field of small scale fluctuations is seen, with streaks strongly aligned in the flow direction. The streak strength is fairly uniform over the whole domain, while the size spacing of the streaks appears

constant. As the reference plane moves away from the wall the strength of the streaks becomes weaker. The spacing between the streaks is also increased, and a greater range in strength is seen along the length of the streaks.

Figure 8.3 shows the streak patterns from the near-optimal wall oscillation case with $\omega^+ = 0.06$. The plots are presented at the 8 points in the first half-period and the first point in the second half of the cycle ($\phi = \pi$). This last point is essentially the inverse (in terms of forcing) of the initial plot. Looking generally at all the snapshots, there are large regions of high-speed and low-speed fluid, within which small scale streaks exist. This is evidence of larger scale structures which affect the wall from the outer region. The reason that these large-scale fluctuations are visible here, and not in the no-control flow is that the near-wall fluctuations are weakened by the control strategy, as seen in the rms profiles. This makes the larger scales more evident in the visualisation, and not necessarily stronger. Although the larger scale fluctuations of streamwise velocity are mostly aligned in the streamwise direction, the near-wall streaks are angled by the spanwise velocity. At $\phi = 0$ the previous wall velocity was positive, hence the small scale streaks are have negative angle to the vertical (x-axis). The reasons for this angling are discussed later. As ϕ increases through the first half period, the angle of the near-wall streaks reduces slightly. When $\phi = \frac{5\pi}{8}$ the angle of the streaks becomes unclear. In some of the regions with negative fluctuations (lighter colour), the streaks could still be angled negatively, but there are small scale fluctuations in the high-speed regions (darker colour) where the streaks have positive angle. By $\phi = \frac{3\pi}{4}$ many more of the near-wall streaks have positive angle which remains true as ϕ increases into the second half-period.

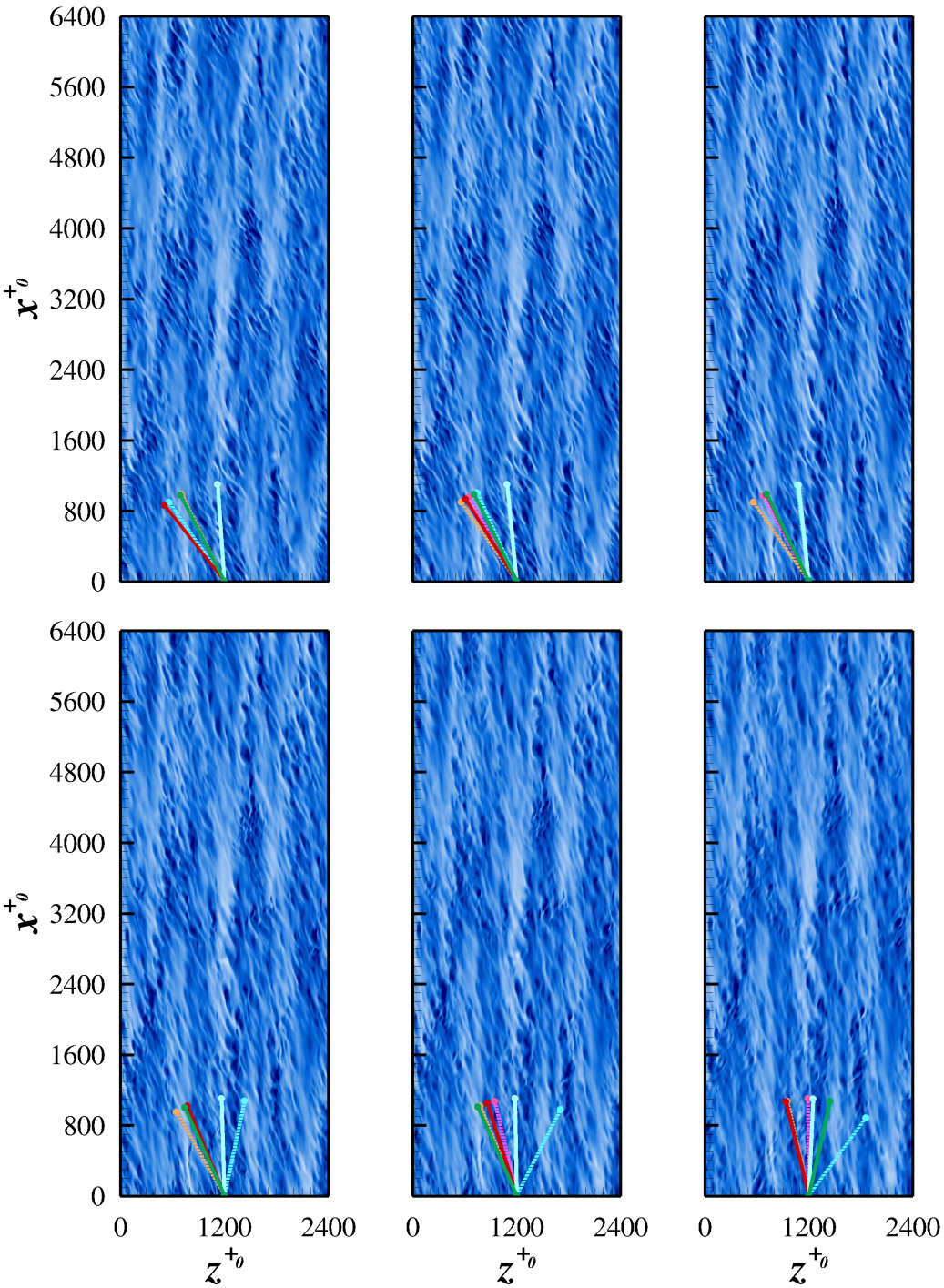

Figure 8.3: Visualisation of the streaks for $\omega^+ = 0.06$ at $y^+ = 10$ for phase points $\phi = 0, \frac{\pi}{8}, \frac{\pi}{4}, \frac{3\pi}{8}, \frac{\pi}{2}$ and $\frac{5\pi}{8}$ (from left to right, top to bottom).

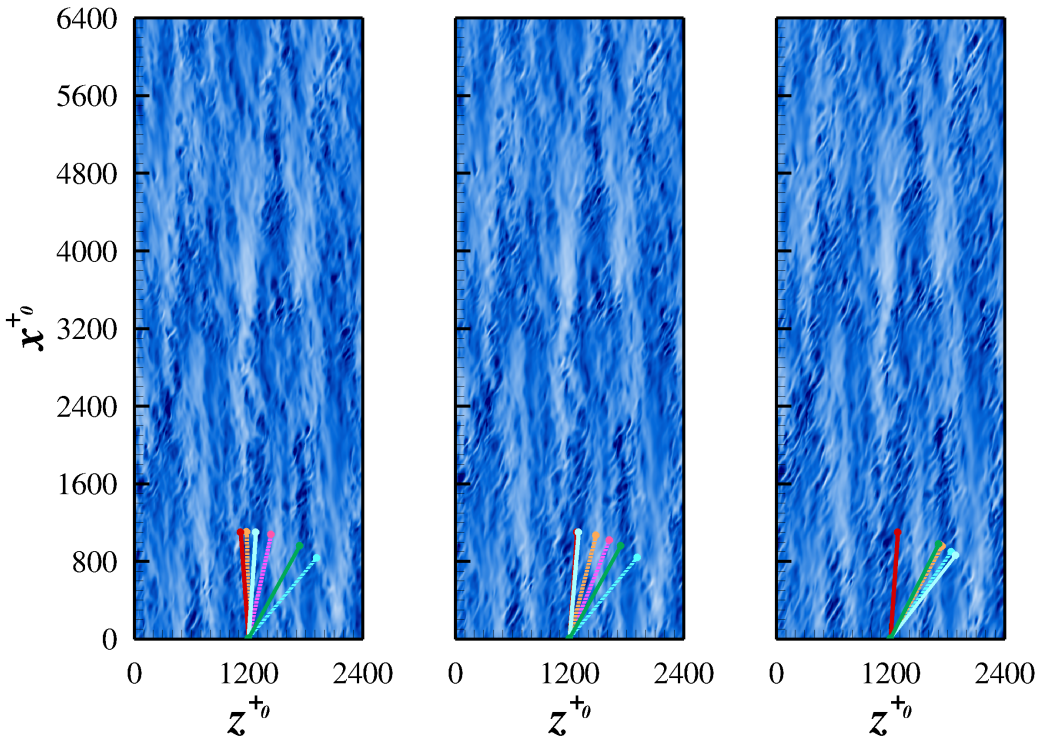

Figure 8.3: (cont.) Visualisation of the streaks for $\omega^+ = 0.06$ at $y^+ = 10$ for phase points $\phi = \frac{3\pi}{4}, \frac{7\pi}{8}$ and π (from left to right). The streak angle is shown in green, and the structure angle for the positive and negative vorticity are shown in red and light blue. The dashed lines represent the flow angles with blue, pink and orange indicating the mean velocity gradient, turbulent shear stress and intensity angles, respectively. This is discussed in more detail in section 8.6.2.

8.3 Quadrant Analysis

Figure 8.4a shows the separation of the Reynolds shear stress divided in to the individual quadrants for the $\omega^+ = 0.06$ case. The colours of the lines distinguish the quadrant, and hence the various lines of the same colour correspond to the different points throughout the half-period. There is a small level of oscillation in the profiles in the near-wall region. The $Q4$ profile has become very slightly flatter around the peak value. The ejections ($Q2$) have decreased more substantially than the sweeps ($Q4$) in the near wall region. This result is in agreement with those of Agostini et al. [2014] who showed the PDFs at $y^+ = 13.5$. Littel and Eaton [1994]

showed that stronger sweeps to ejections occur in a three-dimensional boundary layer when the vorticity opposes the direction of the wall motion.

In the $\omega^+ = 0.03$ case, figure 8.4b, there is a higher level of oscillation in the profiles over the period. Touber and Leschziner [2012] stated that the effect in the $T^+ = 200$ case ($\omega^+ = 0.03$) is less prominent than the lower T^+ case. These is also seen here, due to the small reduction in Reynolds shear stress, but the $Q2$ events do again appear to reduced more strongly.

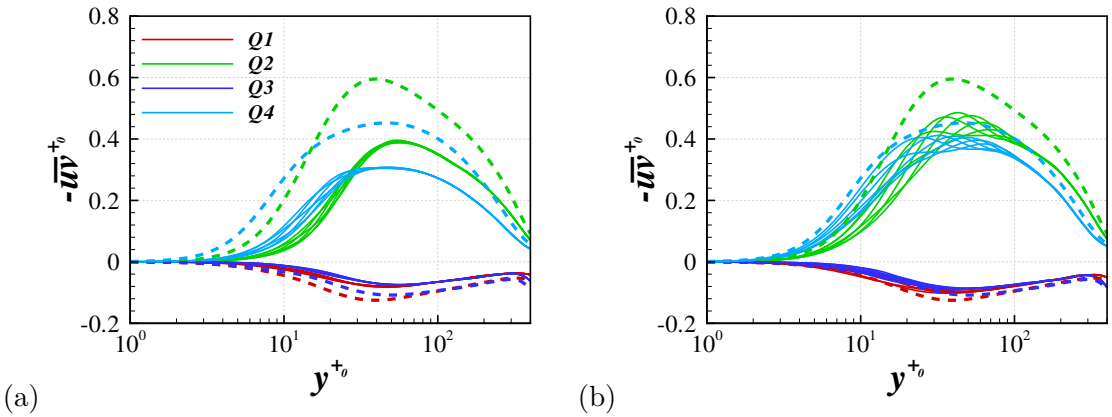

(a) (b)

Figure 8.4: Quadrant analysis for the $\omega^+ = 0.06$ (a) and $\omega^+ = 0.03$ (b) cases. Dashed lines represent the no-control profiles. The dashed lines represent the no-control case, while the solid lines indicate the forced flow.

8.4 λ_2 Structure Visualisation

Figure 8.5 shows the field of the λ_2 structures at the various points throughout the half-period with oscillation frequency $\omega^+ = 0.06$. Structures are coloured red and blue to indicate the positive and negative vorticity, respectively. The λ_2 values are calculated as the second eigenvalue of the matrix $\mathbf{S}^2 + \mathbf{\Omega}^2$ [Jeong and Hussain, 1995]. Given that this is negative, there are at least two negative eigenvalues and therefore the location is inside a vortex core. To show the near-wall coherent structures, a value of $\lambda_2^{+_0} = -0.01$ is chosen to define the structure boundaries.

In the figure, the forcing of the wall reduces the strength of the structures

(hence the reduction in the λ_2 value, as compared to figure 5.1b). Compared to the no-control case, there is also a higher range in the the λ_2 values when the wall oscillation is applied. In all points throughout the period, there are patches where the λ_2 is much stronger, therefore using a particular isosurface value causes points where there are very few coherent structures visible. This behaviour is also seen previously in the streak patterns, and the regions where many λ_2 structures occur are at the locations of the high-speed fluid. At $\phi = 0$, the structures with positive vorticity are angled negatively, whereas the negative vortices are streamwise aligned. As ϕ increases over the period the angle of the positive structures decreases slightly and by $\phi = \frac{7\pi}{8}$ the majority of these structures have become aligned with the flow. The structures with negative vorticity remain aligned in the streamwise direction for the first half-period until $\phi > \frac{5\pi}{8}$, when some evidence of these structures being positively angled is visible.

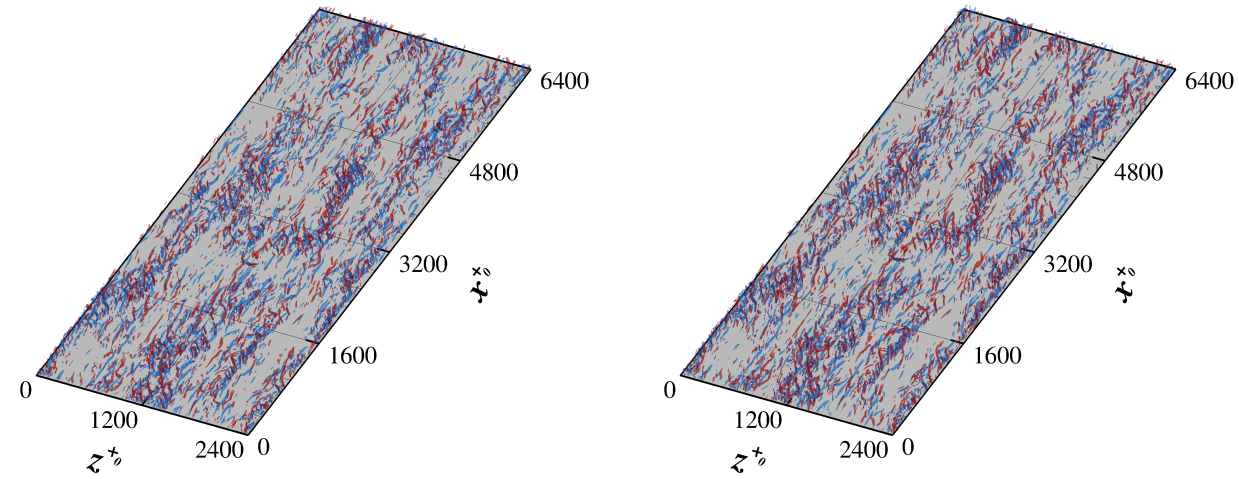

$\phi = 0$ $\phi = \frac{\pi}{8}$

Figure 8.5: Visualisation of the λ_2 structures over a half-period, using $\lambda_2^{+0} = -0.01$

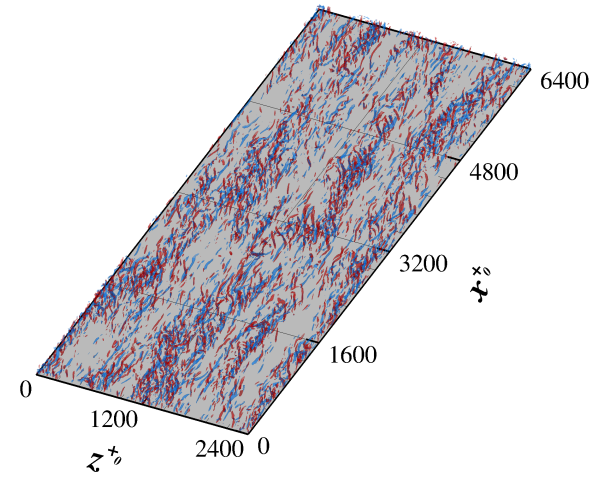

$\phi = \frac{\pi}{4}$

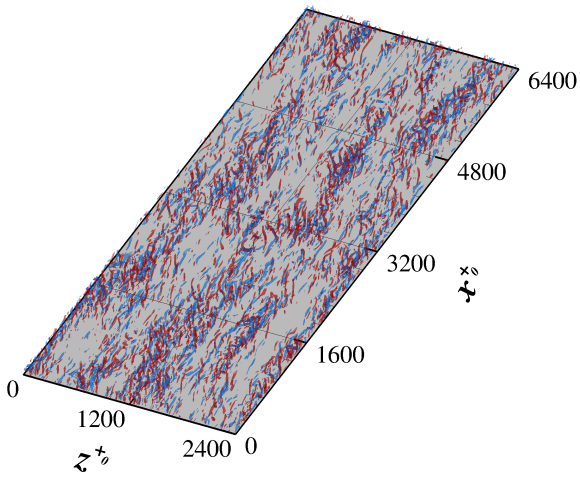

$\phi = \frac{3\pi}{8}$

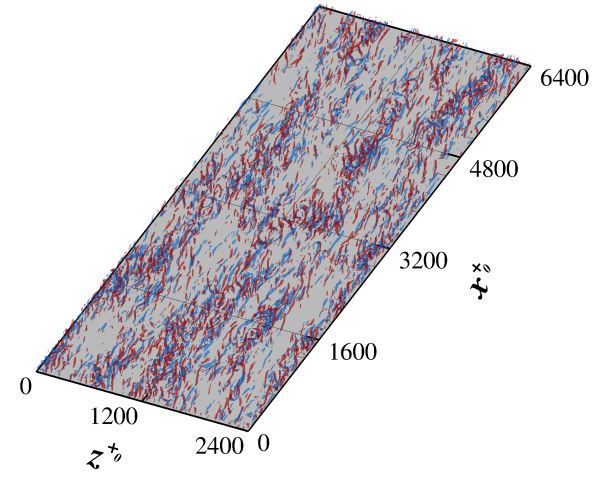

$\phi = \frac{\pi}{2}$

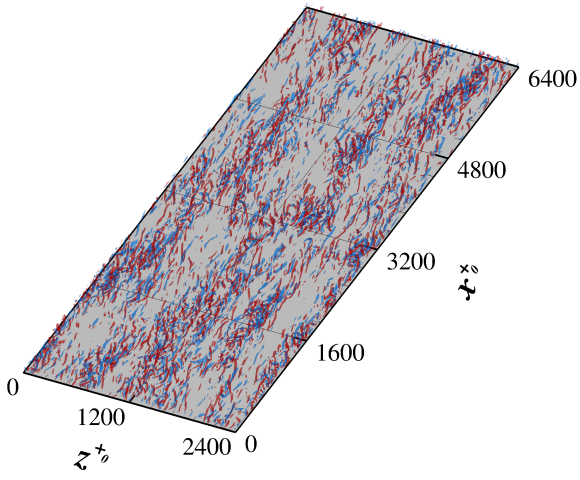

$\phi = \frac{5\pi}{8}$

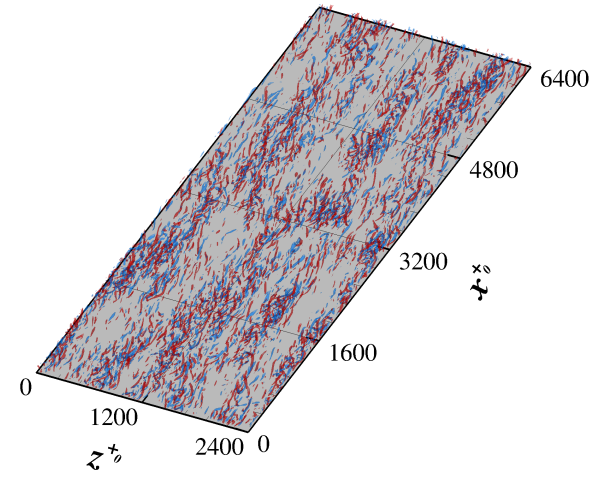

$\phi = \frac{3\pi}{4}$

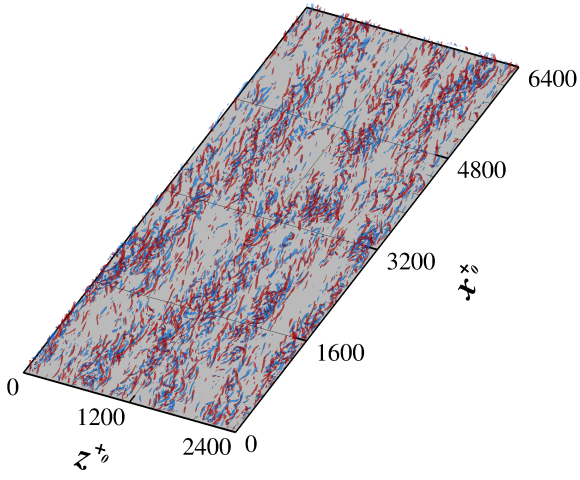

$\phi = \frac{7\pi}{8}$

Figure 8.5: (cont.) Visualisation of the λ_2 structures over a half-period, using $\lambda_2^{+0} = -0.01$

8.5 Average Structure

In order to get a clearer view of the control method on the near-wall flow, a conditionally averaged structure can be found. This can give an interesting insight into the average topology of the structure. One key feature of the turbulent structures is the distance from the wall, as this gives an indication of the structures influence on the wall and hence the skin friction. It is believed that some flow control methods, such as opposition control, can move the vortices away from the wall, causing a drag reduction [Choi et al., 1994]. This technique creates a 'virtual wall' which reduces turbulent activity in the near-wall region. The physics of wall oscillation is different, due to the lateral motion of the wall however some similarities may be drawn. One significant difference is the strong angle incurred in the near-wall streaks [Touber and Leschziner, 2012], when wall oscillation is applied. This is three-dimensional problem and therefore requires a three-dimensional analysis.

8.5.1 Eduction Scheme

The conditionally averaged structure is found following a slightly modified version of the eduction method highlighted in Jeong et al. [1997]. Initially the λ_2 field is calculated from the velocity information and the centres of the structures are found by identifying local minima of λ_2 in the yz-plane. The minima are connected to form structures by searching the domain in the streamwise direction, linking two centres if they are co-located in a streamwise cone at an angle between $\pm 60^\circ$ and have the same streamwise vorticity. This angle is enlarged from that used by Jeong et al. [1997] due to the angling of structures by the control method. The extra check on streamwise vorticity reduces the likelihood of connecting two centres from adjacent flow structures. The structures are accepted if their streamwise length exceeds 100 wall units as to remove any small insignificant structures and anomalies pick up in the procedure. Accepted structures are also confined to the near-wall region, i.e.

they must contain a centre-point within $0 \leq y^+ \leq 60$. Figure 8.6 shows the locations of the centre-points found in accepted structures.

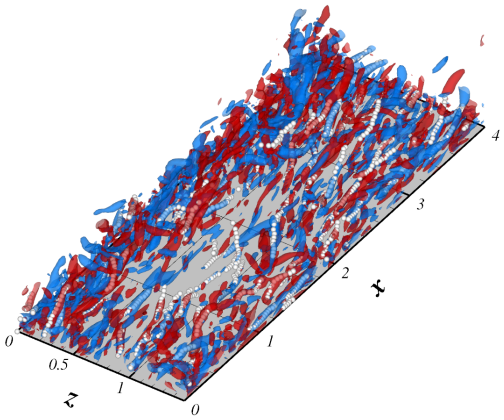

Figure 8.6: Connected structure centres that are found and accepted in the eduction procedure

The structures are then averaged into two crude averages by overlapping the most upstream point and distinguishing the two vorticity directions of the structure. The individual structures are again iterated through, shifting in the xz plane by up to 30 wall units in each direction. The correlation between the current average and the shifted structure is calculated in a window of $150 \times 60 \times 150$ wall units, and the shifted structure is accepted if the maximum correlation greater than 0.3. If accepted the unshifted structure is removed from the current average and the shifted structure is added. The window size is quite wide in the current instance, as a large part of the structure must be used, even when strongly angled. This large window size means that the minimum correlation value must be reduced in order to accept a reasonable number of structures.

8.5.2 No-Control Case

To ascertain the appropriateness of the eduction method, the no-control case is studied and compared to the results obtained by Jeong et al. [1997]. Figure 8.7 shows the result of the averaging of the coherent structures from the current study. The

structure with positive vorticity is seen to be angled negatively to the streamwise direction and the structure with negative vorticity is aligned with positive angle. The tilting angle is measured as 7°, which is higher than the 4° measured by Jeong et al. [1997], however compares well with Jung and Sung [2006]. In the yz-plane it can be seen that both structures sit at the same distance from the wall, although the actual location is dependent on the λ_2 value chosen to visualise the structures. The length and width of the structures is also similar suggesting a similarity in the strength and size. The xy-plane plot shows the inclination angle, measured as 10°, comparing well with the 9° found by Jeong et al. [1997].

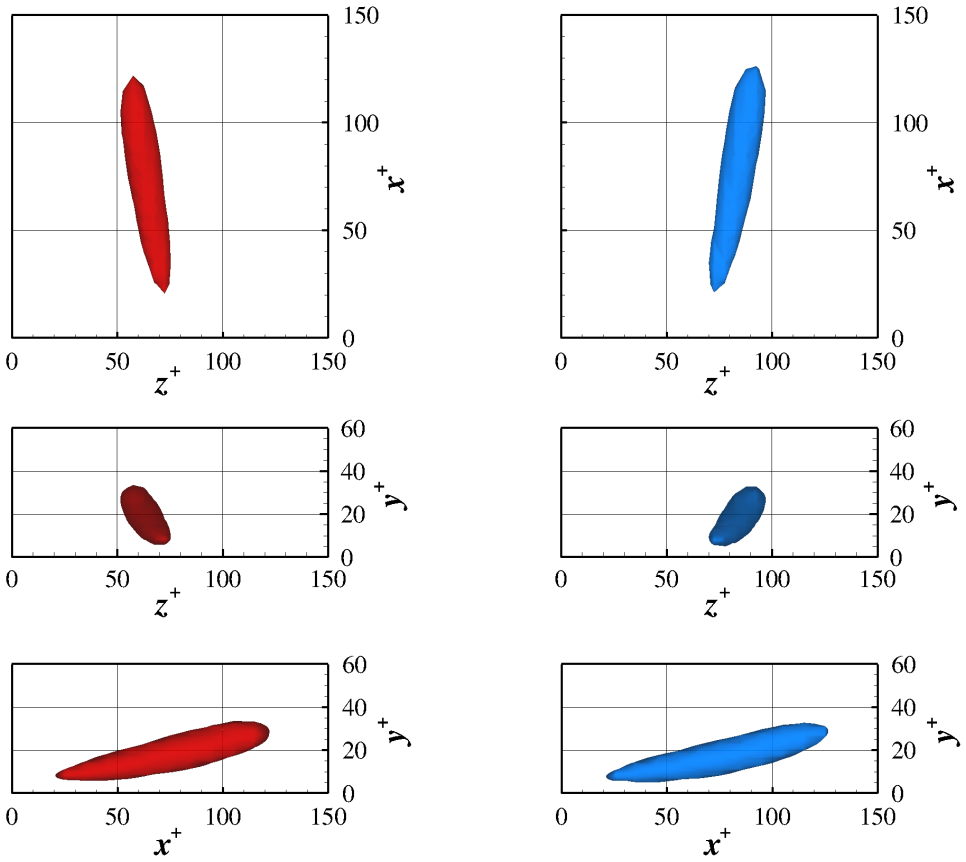

Figure 8.7: Visualisation of the average λ_2 structure for the no-control case at $Re\tau = 400$ in the xz,yz and xy planes (from top to bottom).

8.5.3 Near-optimal Wall Oscillation Case

Figure 8.8 shows the xz view of the averaged coherent structures for the wall oscillation case at the various points over the first half-period. The structures are visualised using $\lambda_2^{+0} = -0.01$, and again the colours represent the direction of the vorticity. At $\phi = 0$ the structure with positive vorticity is very strongly angled with negative angle and is very straight. As ϕ increases through the period the tilting angle of the structure decreases. In the decrease of the angle the downstream end of the structure appears to have a lag in the tilting, hence the structure becomes more curved throughout the period. By $\phi = \frac{3\pi}{4}$ and $\frac{7\pi}{8}$, the upstream end of the structure is slightly positively angled. The structure with negative vorticity has a slight negative angle at the beginning of the period, but is generally aligned in the streamwise direction over the first half-period. At $\pi = \frac{7\pi}{8}$ the structure with negative vorticity has a positive angle. Due to the symmetry of the oscillation, the averaged structures at $\phi = \pi$ is the inverse of the $\phi = 0$ case. The structure with positive vorticity at $\phi = \pi$ has been seen to become the mirror of the negative structure at $\phi = 0$ (although not shown here). Although the same is true for the structure with negative vorticity, there is a rapid change in the angle between these two points.

Looking at the yz plane visualisation, figure 8.9, the distance from the wall can be investigated. These plots also include the mean spanwise velocity profiles, to indicate the significance of the wall distance and structure angling. At $\phi = 0$ the positive structure is close to the wall, sitting within the Stokes' layer, and strongly negatively angled. This structure can exist within the Stokes' layer, due to the agreement of the rotation with the wall motion. As ϕ increases, the spanwise wall velocity becomes negative, entraining the near-wall fluid. As the spanwise velocity is strongest near the wall, the upstream end of the structure is moved at a faster rate than the downstream end. This effect causes the curvature in the structure. The positive structure is seen to move away from the wall slightly over the first

half-period. The structure with negative vorticity is initially positioned away from the wall. It is very slightly within the Stokes' layer, hence the small negative angle of the structure. As ϕ increases through the first half period the structure is moved further from the wall. It is clear why there is very little tilting of this structure, due to the position out of the Stokes' layer, and is therefore not angled by the spanwise velocity. From $\phi = \frac{7\pi}{8}$ to π the averaged structure with negative vorticity goes from being streamwise aligned and far from the wall to being close to the wall and positively angled (as it is the mirror of the positive structure from $\phi = 0$). It is clear that these are not the same structures, and this fact may be an outcome of the averaging process favouring certain structures.

The averaged structures are presented in figure 8.9 in the xy plane view, and is useful in showing the inclination angle. As the structures both move away from the wall, the inclination angle becomes larger as ϕ increases through the period. This inclination angle changes in this way due to the streamwise shearing in the flow which comes from the no-slip boundary condition. The structure with negative vorticity is also seen to reduce greatly in length over the first half of the period. This may suggest a weakening of the structure, which agrees with the idea that the average structure found at π is different.

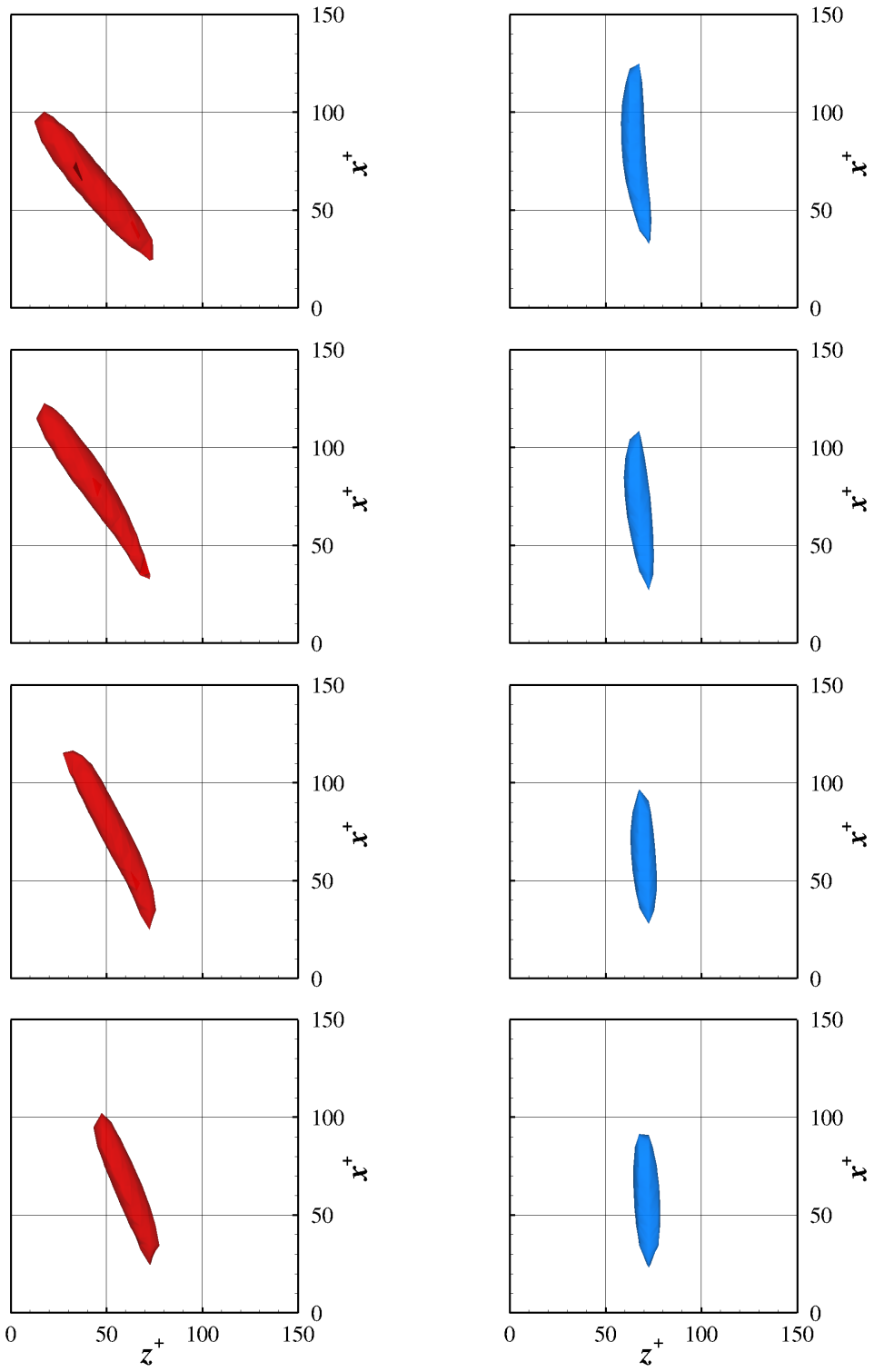

Figure 8.8: Visualisation of the average λ_2 structure in the xz-plane at $\phi = 0, \frac{\pi}{8}, \frac{\pi}{4}$ and $\frac{3\pi}{8}$ (from top to bottom).

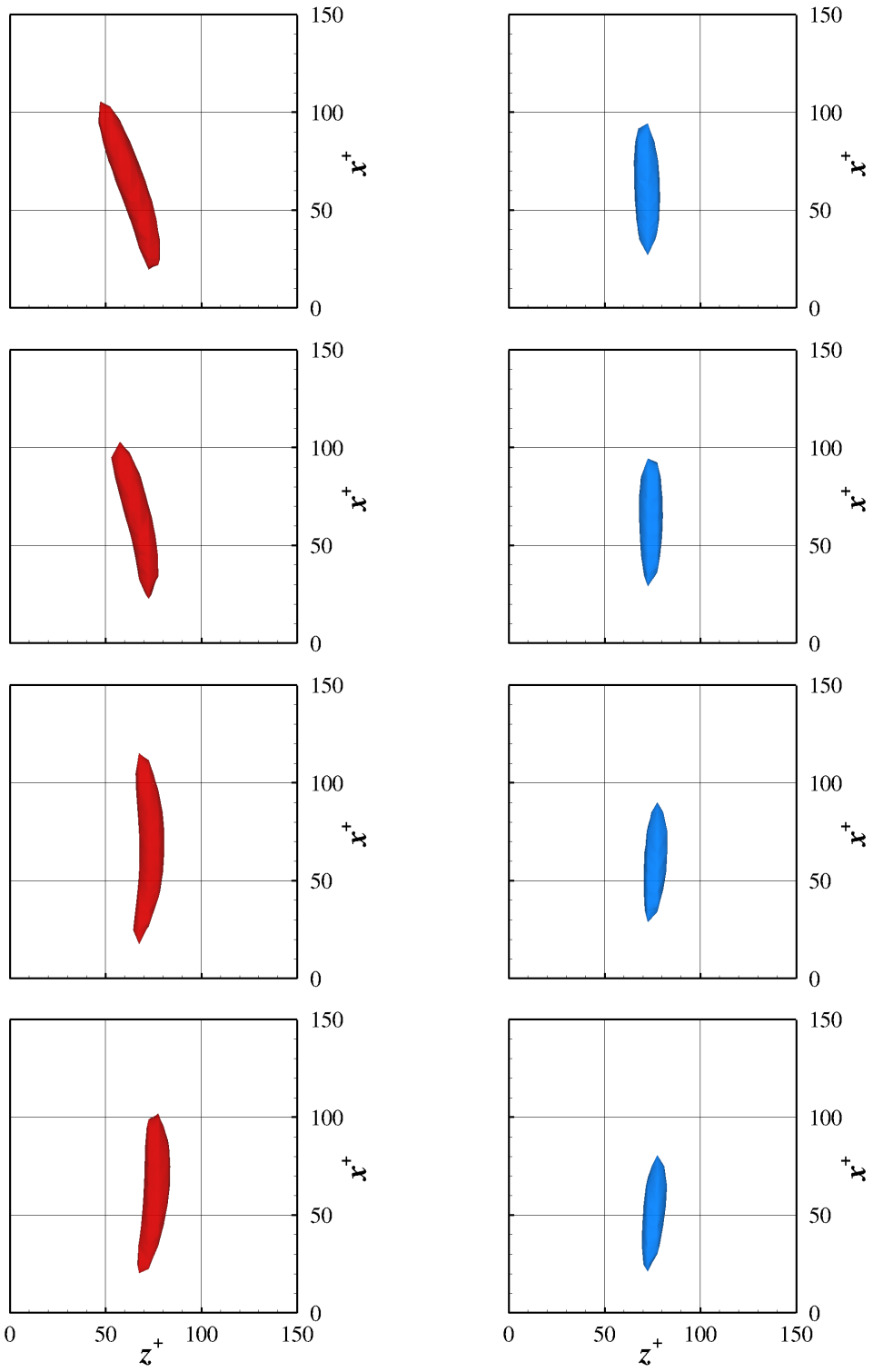

Figure 8.8: (cont.) Visualisation of the average λ_2 structure in the xz-plane at $\phi = \frac{\pi}{2}, \frac{5\pi}{8}, \frac{3\pi}{4}$ and $\frac{7\pi}{8}$ (from top to bottom).

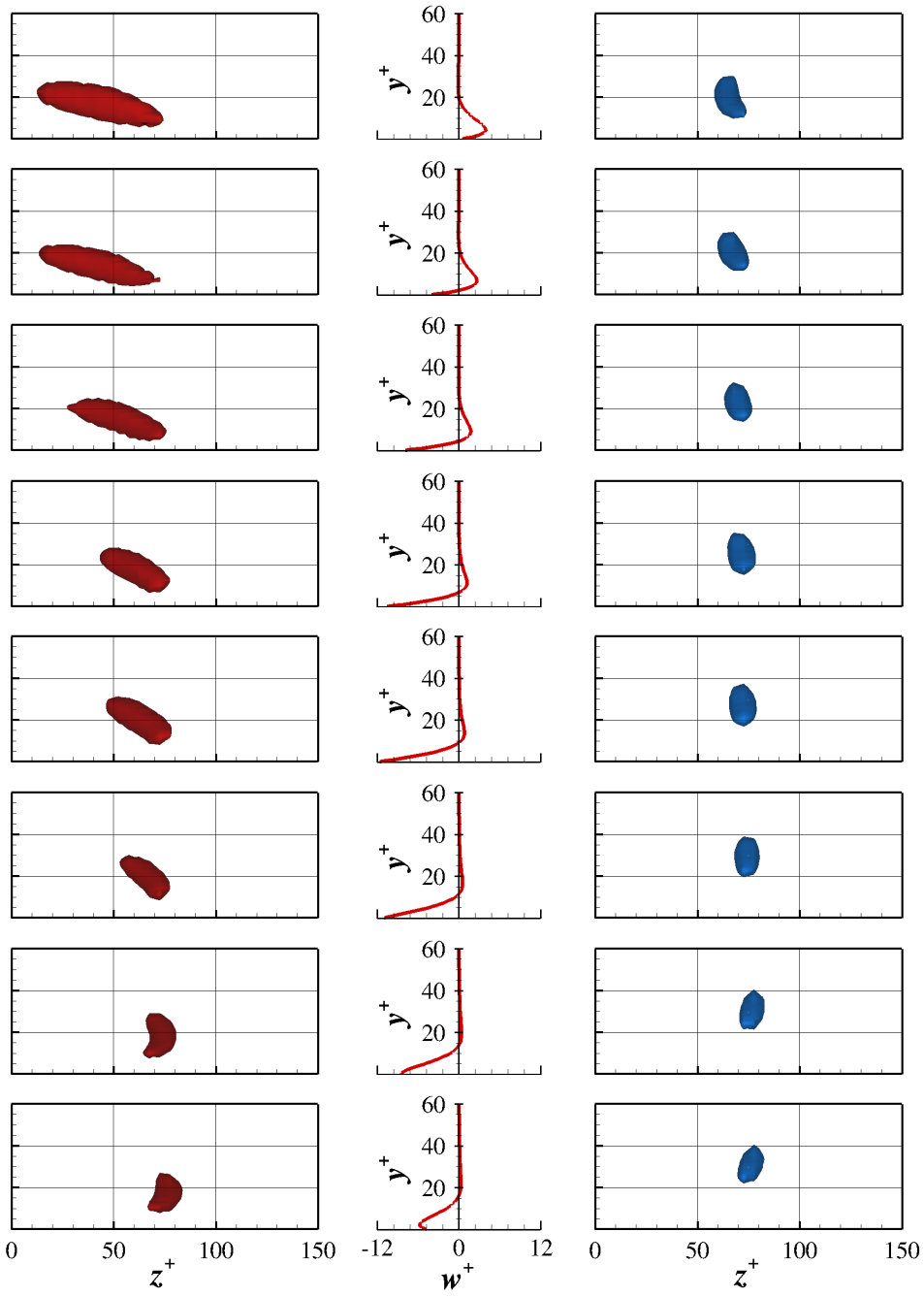

Figure 8.9: Visualisation of the average λ_2 structure in the yz-plane at $\phi = 0, \frac{\pi}{8}, \frac{\pi}{4}, \frac{3\pi}{8}, \frac{\pi}{2}, \frac{5\pi}{8}, \frac{3\pi}{4}$ and $\frac{7\pi}{8}$ (from top to bottom).

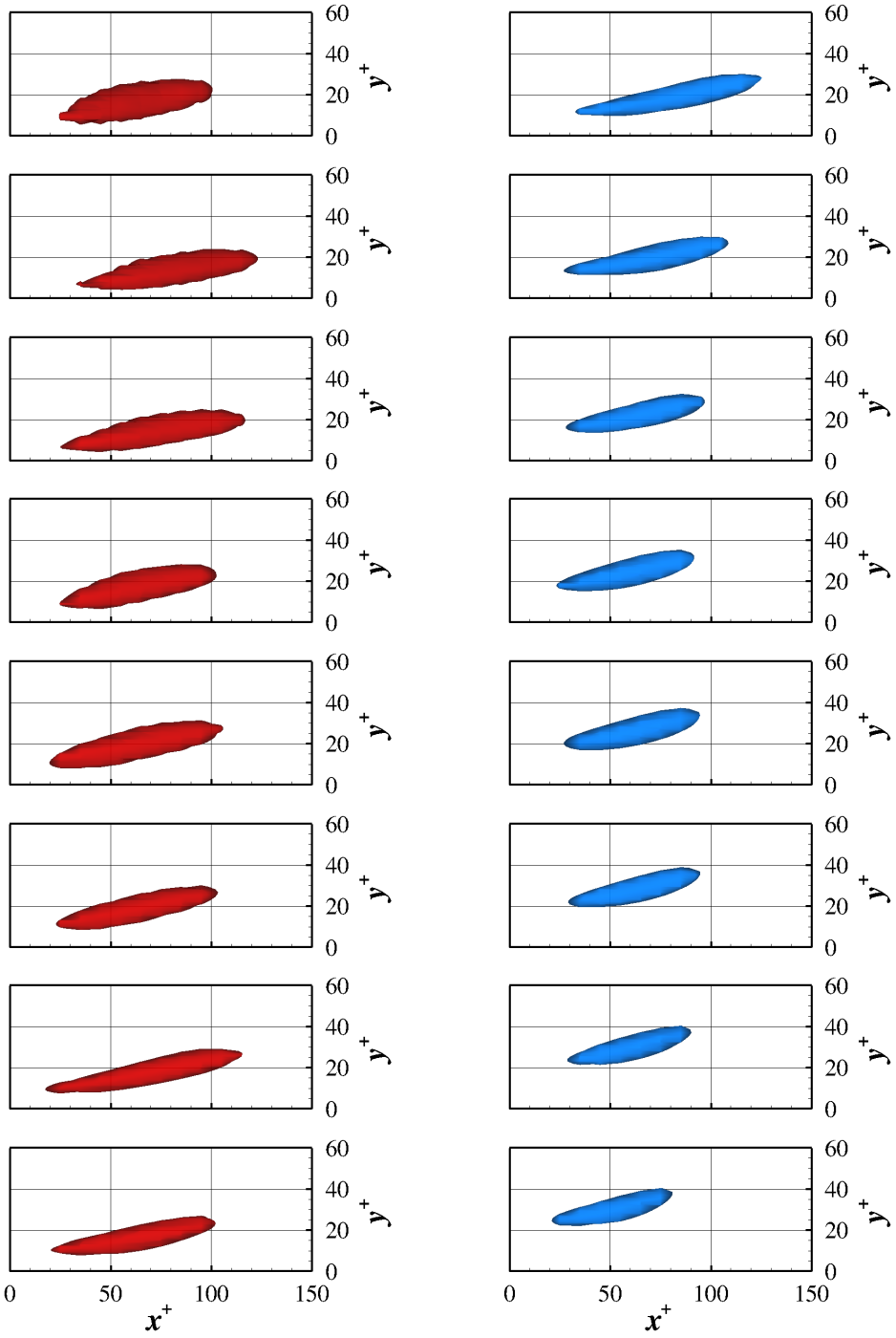

Figure 8.10: Visualisation of the average λ_2 structure in the xy-plane at $\phi = 0, \frac{\pi}{8}, \frac{\pi}{4}, \frac{3\pi}{8}, \frac{\pi}{2}, \frac{5\pi}{8}, \frac{3\pi}{4}$ and $\frac{7\pi}{8}$ (from top to bottom).

8.6 Angles

8.6.1 Flow Angles

In the study of three-dimensional turbulent boundary layer [Holstad et al., 2010] it is common to discuss four flow angles. These are defined as follows:

$$\beta = \arctan\left(\frac{W}{U}\right), \tag{8.1}$$

$$\alpha = \arctan\left(\frac{dW/dy}{dU/dy}\right), \tag{8.2}$$

$$\eta = \arctan\left(\frac{\overline{vw}}{\overline{uv}}\right), \tag{8.3}$$

$$\gamma = \arctan\left(\frac{2\overline{uw}}{\overline{uu} - \overline{ww}}\right), \tag{8.4}$$

where β is the mean flow angle, α is the mean velocity gradient angle, η is the turbulent shear stress angle and γ is the turbulence intensity angle.

The mean flow angle for the $\omega^+ = 0.06$ case is shown in figure 8.11a. The angle at the wall is predominantly $\pm 90°$, because the streamwise velocity near the wall is small compared to the spanwise velocity. This angle decays to zero away from the wall, at the same wall normal position as the Stokes' layer. At certain points in the period the angle within the flow is reasonably strongly opposed to the wall angle. This effect is reduced for the $\omega^+ = 0.03$ case, figure 8.11b, in which the profile becomes flatter. The oscillation also takes place further into the domain than the higher frequency case, and is directly related to the thickening of the Stokes' layer.

Figure 8.12a shows the mean velocity gradient angle calculated at various points over the period for the forcing frequency $\omega^+ = 0.06$. The maximum value reached at the wall is $75°$ in this case. The velocity gradient angle is larger and therefore extends further into the flow than the mean velocity angle. There is regular

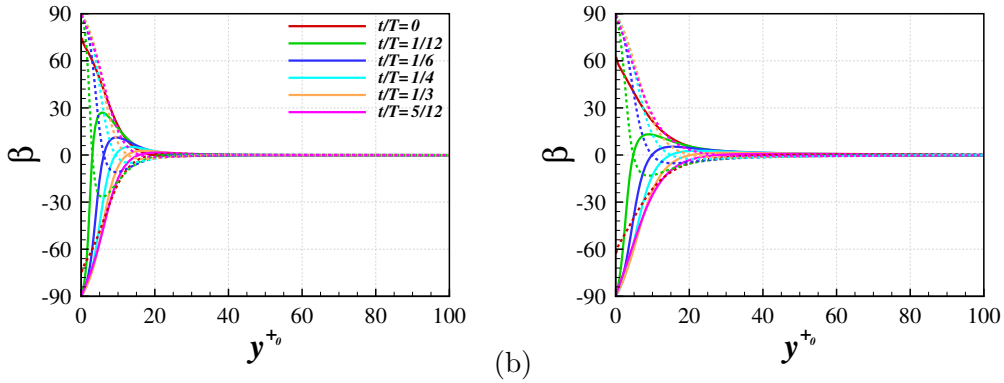

Figure 8.11: The mean velocity angle at various points over the period for the $\omega^+ = 0.06$ (a) and $\omega^+ = 0.03$ (b) cases.

oscillation in this parameter, and the near-wall angle is strongly opposed to the wall angle at some time points in the period. Figure 8.12b shows the oscillation in α for the $\omega^+ = 0.03$ case. The noticeable difference in this case is that, at some time points, the angle is almost constant in the region $40 < y^{+0} < 70$. The angle further from the wall corresponds to the oscillation in the mean streamwise velocity gradient. This behaviour is similar to the steady 3d turbulent boundary layer [Holstad et al., 2010] where the α angle is constant near the wall. The maximum wall angle in this case is actually smaller at 70°.

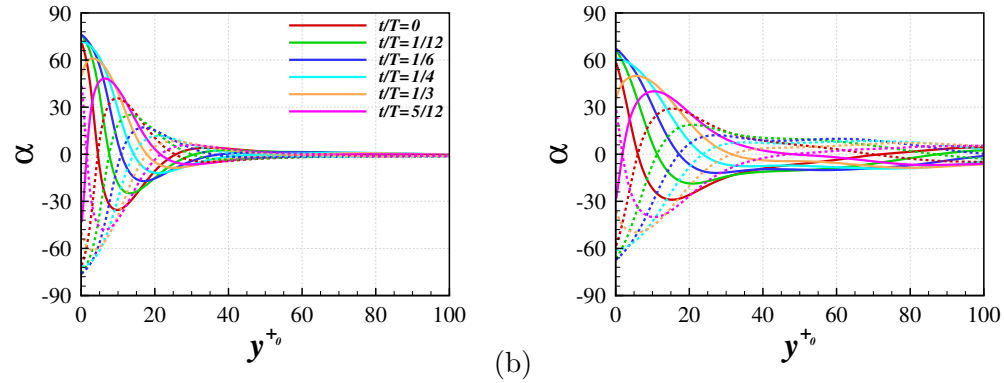

Figure 8.12: The mean velocity gradient angle at various points over the period for the $\omega^+ = 0.06$ (a) and $\omega^+ = 0.03$ (b) cases.

The turbulent shear stress angle is shown for the $\omega^+ = 0.06$ case in figure 8.13a. The angle at the wall is quite small, with a maximum of around 40°. Near

the wall there is a peak in the angle value, which is similar to the occurrence in the steady cross-flow case [Holstad et al., 2010]. The wall values with the lower frequency of oscillation at $\omega^+ = 0.03$ are similar to the $\omega^+ = 0.06$ case, figure 8.13b. The oscillation in the angle again extends much further into the flow.

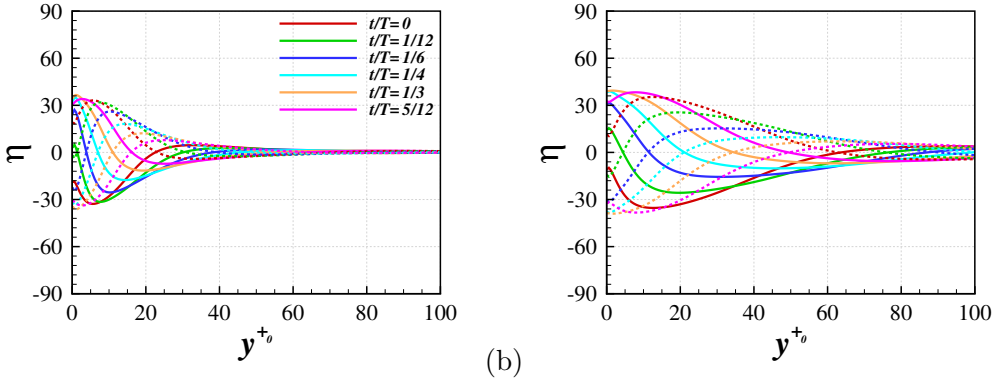

Figure 8.13: The turbulent shear stress angle at various points over the period for the $\omega^+ = 0.06$ (a) and $\omega^+ = 0.03$ (b) cases.

Figure 8.14a presents the intensity angle angles measure from the $\omega^+ = 0.06$ case. This angle has maximum at the wall, a feature also seen in the steady cross-flow, [Holstad et al., 2010]. In the wall oscillation the profile decreases before a local maximum is observed, and the angle decays to zero above this. When $\omega^+ = 0.03$, figure 8.14b, the wall angle is very much stronger, and the angle oscillation extends much further into the domain.

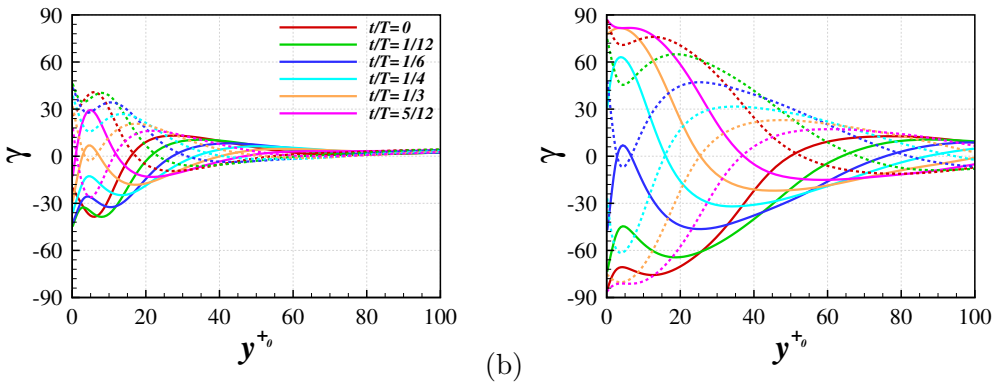

Figure 8.14: The intensity angle at various points over the period for the $\omega^+ = 0.06$ (a) and $\omega^+ = 0.03$ (b) cases.

8.6.2 Streak and Coherent Structure Angles

With the aim of understanding how the streak and structure angles relate to both each other and the flow angles, these properties are calculated using the forcing case with $\omega^+ = 0.06$. The streak angles have been calculated previously by Touber and Leschziner [2012], and the same method is employed here. As seen in the streak patterns, there are strong large-scale variations in the near-wall streak values due to the outer flow motions. In order to measure the angles of the near-wall streaks the large scales must first be removed so that the values are not contaminated by these large scales. A Fourier transform is used to apply a high-pass filter, removing the large-scale fluctuations from the velocity field, the effect of which is shown in figure 8.15.

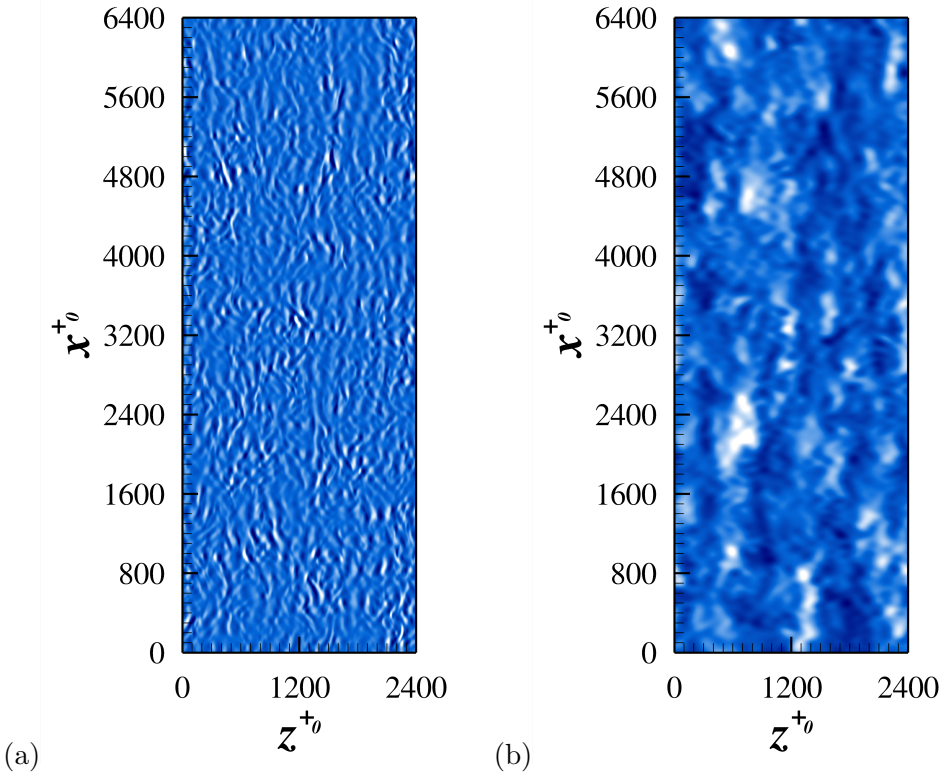

Figure 8.15: Example of filtering of the streaks for $\omega^+ = 0.06$ and $\phi = 0$. (a) shows the smaller scales and (b) shows the larger scales which are removed.

The 1D correlation at $y^{+_0} = 10$, performed in the spanwise direction, is

strongly increased from the no-control case in the small scales, moving the minimum to a larger z distance [Touber and Leschziner, 2012]. The control profile is shown in figure 8.16a after various stages of filtering. The minimum value is seen to appear as the larger scales are removed. A 2D correlation in xz is calculated at all the data points in the period, to calculate the average near-wall streak. This is shown for $\phi = 0$ in figure 8.16b. From this the curve of maximum correlation is found, and a linear regression is used to calculate the angle. A similar method is used to calculate the angle of the conditionally averaged structures. A curve in the three-dimensional domain is found based on the minimum λ_2 locations, and linear regression is employed to find the tilting angle.

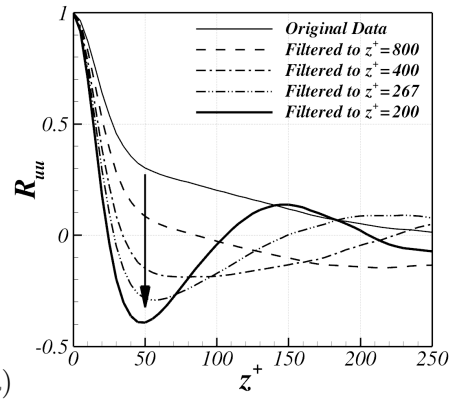

(a)

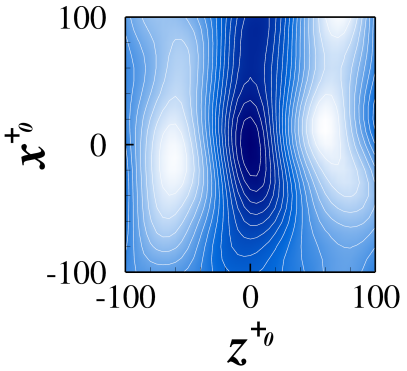

(b)

Figure 8.16: 1D correlation of u to show the effect of filtering (a) and 2D correlation of streamwise velocity after filtering for $\omega^+ = 0.06$ and $\phi = 0$.

The angles of the structures with positive and negative vorticity, and the calculated streak angle at $y^{+_0} = 10$ are plotted over the time period in figure 8.17a. The streak angle is initially negative at around 27°. This remains fairly constant, reducing slightly, and when $0.24 < t/T < 0.26$ it rapidly changes becoming positive. This flipping in the angle was discussed by Touber and Leschziner [2012]. The average λ_2 structure with positive vorticity is initially 39° and negative. This structure angle gradually reduces, becoming slightly positive in the second half of the period. The structure with negative vorticity behaves as the inverse to the

structure with positive vorticity. The angle of the structures also flips, this time from being small to being large. This is because the structures being averaged are different types of structures, seen previously in the wall distance.

Figure 8.17b shows the calculated streak angle in the wall normal direction, at various points in the first half-period. At many time point there is a near-wall region which has an almost constant streak angle. Above this the streak angle changes gradually. Th y location at which at which the streak angle first varies moves away from the wall. This agrees with the idea that the streak angle is determined by the angle of the near-wall coherent structures. This structure has been seen to move away from the wall in the λ_2 averaging and the periodic change in the streamwise vorticity fluctuations.

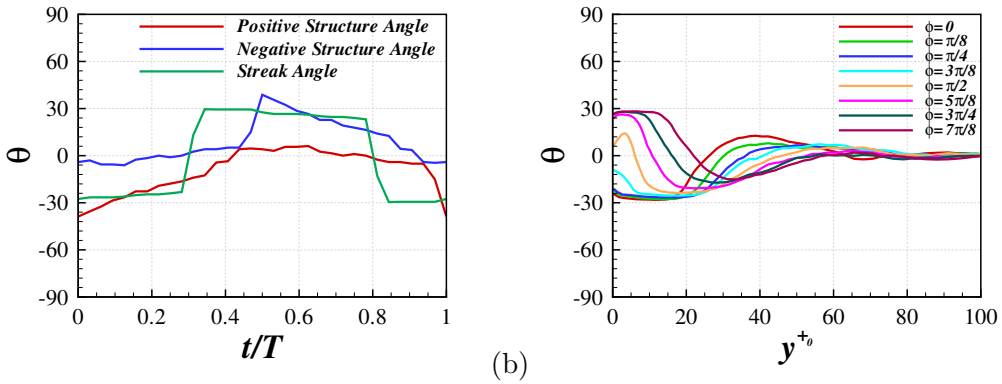

Figure 8.17: The streak angle at $y^{+0} = 10$ and structure angles (a) and the streak angles in y^{+0} over the half-period (b).

To check the streak-angle calculation and also to compare the structure and flow angles to the individual streaks, the angles are included in figure 8.3. The streak angle is shown in green, and the structure angle for the positive and negative vorticity are shown in red and light blue. The dashed lines represent the flow angles with blue, pink and orange indicating the mean velocity gradient, turbulent shear stress and intensity angles, respectively. The streak angle appears to follow the general trend of the streaks, suggesting that the calculation method is correct. It could probably be argued that the streaks follow any of these angles at some point

throughout the period. However, due to the 's' shaped nature of some of the streaks, some streaks could follow both the structures with positive and negative vorticity. This could imply a similar model to that discussed in Jeong et al. [1997], with modification for the spanwise flow.

Figure 8.18a shows the comparison of the structure and the streak angles at $y^{+0} = 10$ to the mean velocity gradient angle at $y^{+0} = 10, 20$ and 30. Although the period is similar to the streak angle, the mean flow angle has opposite sign. Figure 8.18b shows the streak and structure angle compared to the mean velocity gradient angle at various wall normal heights. Although the streak angle does not relate well with the flow angle at $y^{+0} = 10$, the location of the maximum in the velocity gradient angle follows similarly the structure angles (although is a little low).

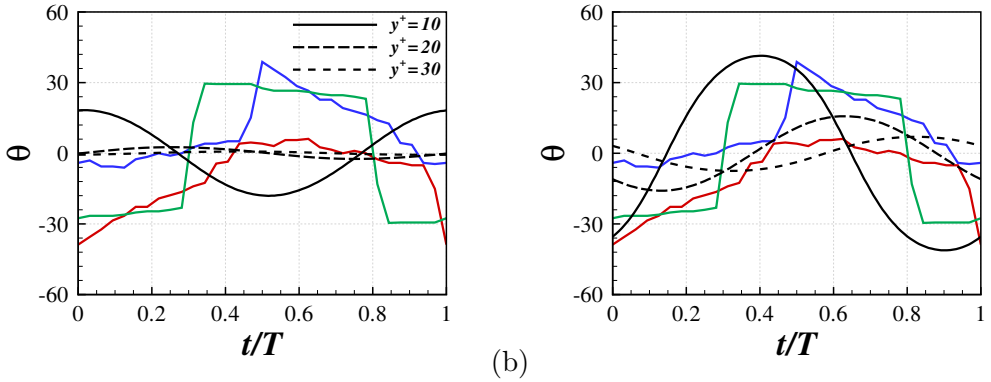

(a) (b)

Figure 8.18: The streak and structure angles compared to the mean velocity angle (a) and mean velocity gradient angle (b) at various y locations.

The period of the shear stress angle at $y^{+0} = 10$ is almost exactly that of the streaks at this wall normal location, figure 8.19a. The shape of the angle variation does differ somewhat. The maximum in this angle could also follow the structure angle. The value of the intensity angle at different y locations is shown in figure 8.19b. The shape of the profile at $y^{+0} = 10$ is similar to the variation in structure angle with slightly different phase (although the structures are not limited to a particular location). The structure angle could follow this angle at varying locations. The similarity to the streak angle is minimum.

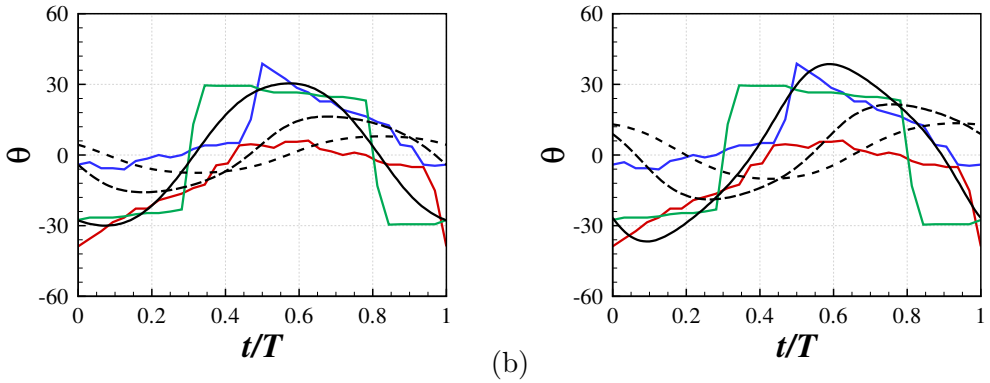

Figure 8.19: The streak and structure angles compared to the turbulent shear stress angle (a) and intensity angle (b) at various y locations.

8.7 Standing Wave

As the visualisation of the standing wave shows the information over the whole period in a single snapshot, this can be used to show the effect of increasing the Reynolds number. Using this concept, the results from the standing wave case with $\kappa_x^+ = 0.008$ are presented.

8.7.1 Streak Visualisation

Figure 8.20 shows the streak patterns from the three lower Reynolds number cases at $y^{+0} = 10$. At all of the Re values the near-wall streaks are angled by the forcing. This can be seen to follow the pattern of the wall forcing in the streamwise direction. As compared to the no-control flow the streaks are much shorter in x. As the Reynolds number increases the structures become smaller, but the waveform of the control also becomes smaller (in global units) due to the wall unit scaling. The larger scales of variation are also more evident in the higher Re flows, with large regions of high and low-speed fluid. This corresponds to a greater difference in scales at the higher Reynolds number.

The streaks from the $Re_\tau = 1600$ case are presented in figure 8.21 at three wall normal heights. The near-wall streaks at $y^{+0} = 10$ are again smaller and

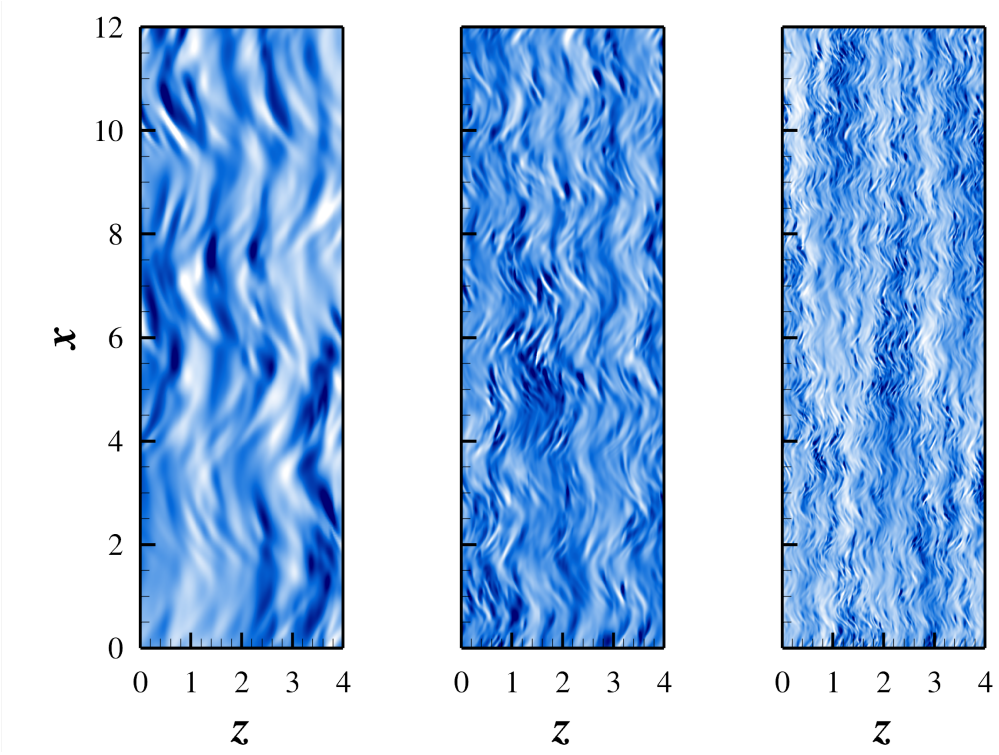

Figure 8.20: Visualisation of the streaks with $\kappa_x^+ = 0.008$ at $y^{+0} = 10$ for $Re_\tau = 200, 400$ and 800.

strongly angled, following the oscillation of the wall velocity in the streamwise direction. There is a much stronger large-scale variation near the wall as compared to the no-control case (figure 5.3), implying the increased influence of the outer structures. At $y^{+0} = 20$ there is still evidence of the angling of the streaks and it appears that two distinct angles can exist at similar x locations at this wall normal distance. Further from the wall, at $y^{+0} = 50$, there is no clear angling of the streaks. This may be because, at this height, there is no spanwise velocity. At this point the streaks are much longer and can be related to the larger scale fluctuations near the wall.

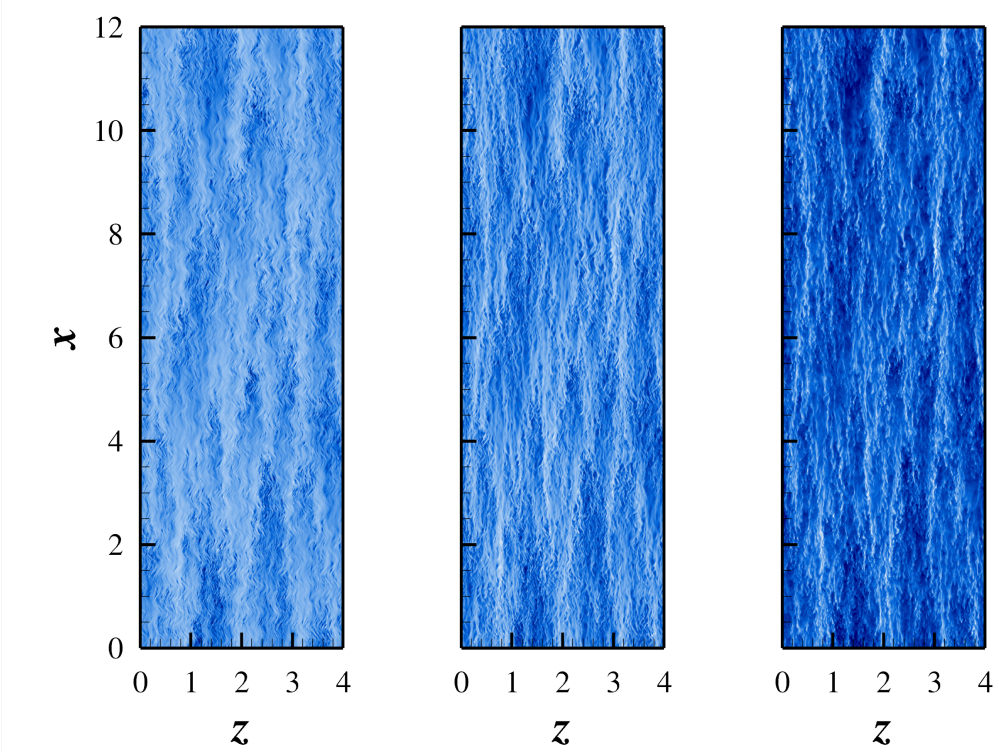

Figure 8.21: Visualisation of the streaks with $\kappa_x^+ = 0.008$ for $Re_\tau = 1600$ at $y^{+0} = 10, 20$ and 50.

8.8 Conclusions

The instantaneous data from 3 periods of the wall oscillation flow with $\omega^+ = 0.06$ was utilised to give an impression of some of the structural characteristics of the turbulent flow. The streaks were presented, showing the changing angles at certain points in the period. Quadrant analysis was used to the effects of the fluid motion on the Reynolds shear stress. The change in the λ_2 structures over the period was shown in an instantaneous form, showing the angling of structures dependent of the sign of the vorticity. To aid in the physical understanding the conditionally averaged structures were found at various ϕ. The structure which rotates in a direction agreeing with the wall motion existed within the Stokes' layer and hence was angled by the spanwise forcing. The structure with opposing vorticity to the wall velocity was more streamwise aligned and was further from the wall. Both

structures moved away from the wall over the oscillation cycle and a new strongly angled structure was found near the wall. The movement of the structures away from the wall caused an increase in the inclination angle.

Various flow angles as well as the streak and structure angles were quantified. The streaks showed almost constant angle in a near-wall region, the size of which varied over the period. This suggests that the streaks are influenced from a particular location which is moving away from the wall over the period, linking with the wall normal motion of the structures. The turbulent shear stress angle at $y^{+_0} = 10$ showed a similar phase, and maximum size to the streak angle found at this location.

A visualisation of the streaks was shown for the standing wave case at all four Reynolds numbers. The streaks were angled by the wall forcing, with an oscillation in the streamwise direction. As the Reynolds number was increased the influence of larger scales was more evident.

Chapter 9

Conclusions and Future Work

9.1 Conclusions

The efficient parallelisation of the in-house DNS code allowed for the performance of computationally expensive simulations. As the Reynolds number effect was known to exist in the wall oscillation flow control method, but was not well understood, this allowed for the investigation into the specifics of the change in drag reduction and power saving with Re.

Simulations were performed to find the DR map of Quadrio et al. [2009], albeit a coarser version, at $Re_\tau = 200, 400$ and 800, where the forcing parameters were scaled in wall units (based on the no control flow). The maximum drag reduction was reduced as the Reynolds number was increased, as was the maximum drag increase. Studying the DR results further, and including a single wall oscillation and standing wave case at $Re_\tau = 1600$, it was seen that the optimal parameters varied with Reynolds number. This corresponded to a non-uniform reduction in the drag, with a stronger scaling occurring when the forcing is close to the optimal parameters. The values of the control parameters which caused maximum drag reduction were seen to increase in ω^+ for the wall oscillation cases, increase in κ_x^+ for the standing wave cases, and decrease in ω^+ and increase in κ_x^+ for the travelling

wave cases.

The mean spanwise wall velocity profiles at various phase points are known to deviate from the laminar solutions when the drag reduction decays. This was linked to large oscillations in the drag reduction. This oscillation was quantified by taking the difference between the maximum and minimum phase-averaged drag reduction, δ_{DR}. This quantity was seen to be large when the drag deteriorated and especially when a drag increase occurred. When the oscillation in DR was large the turbulent statistics showed a high level of variation over the period. This effect was especially apparent in the spanwise velocity fluctuations, in which a large near-wall peak emerged at various points in the oscillation. This relates to the angling of the streaks and coherent structures seen in the λ_2 visualisation.

To understand the effect of the forcing on the near-wall coherent structures the λ_2 field was conditionally averaged. The structure which had vorticity in agreement with the mean vorticity caused by the wall motion could exist in the Stokes' layer, and was therefore strongly angled by the forcing. As the period progressed the structure angle reduced and was moved away from the wall. The structure with vorticity opposing the mean vorticity generated by the wall motion was out of the Stokes' layer, streamwise aligned and moved away from the wall. This was also seen strongly in the vorticity fluctuations, in which the extrema moved away from the wall over the oscillation cycle. There was two different structures of the same vorticity sign identified within a period, where they went from being far from the wall and streamwise aligned to being close to the wall and strongly angled. A similar behaviour is seen in the near-wall streaks which flipped quickly from being negatively angled to having positive angle. The streak angle in the near-wall region was almost constant and had a similar period and maximum value to the turbulent shear-stress angle. As the Reynolds number was increased, larger scale variations were evident in the near-wall streaks.

As the streamwise and spanwise fluctuations were oscillated due to the tilting

of flow direction, the wall-normal statistics gave reasonable results when correlating the maxima with the drag reduction. The wall-normal vorticity fluctuations have a peak closer to the wall so the correlation began to deteriorate as the Stokes' layer extended further into the domain. The wall-normal velocity fluctuations, however, gave a very strong correlation to DR. The no-control case did not fit into the correlation, and as the Reynolds number was increased the v rms maximum also increased in the no-control case. This meant that the correlation at each Reynolds number was different. The various Re correlations were associated by subtracting the no-control case v_{max}, which yielded a strong, Reynolds number independent correlation.

The power saving was also calculated and showed a universal decrease as the Reynolds number increased. This was seen to scale well $Re_\tau^{-0.16}$. The net power saving was also seen to reduce with increased Reynolds number, dropping from 19% to 9% as Re_τ was increased from 200 to 800. Although this is high, the forcing parameters were seen to move, and it is possible that small changes in the forcing parameters could achieve higher power saving. Also, the maximum wall velocity used is quite large to give a good net power saving, and the scaling with Re may vary with W_m^+, however this was not investigated.

9.2 Future Work

9.2.1 High Reynolds Number Simulations

Although the DR calculated at $Re_\tau = 1600$ is believed to be reasonably accurate, the study of the turbulent statistics showed that these simulations were not fully converged. A good starting point has been made here for further research into high Reynolds number simulations with the control strategy applied. As this is the highest Reynolds number DNS of control by streamwise travelling waves of spanwise wall velocity, it could be very useful in both the understanding of both the physics

of the forcing technique and of flows which have larger scale structures.

9.2.2 Scaling Parameter

Although the scaling parameter S^+ gave a good correlation with the drag reduction for some parameter combinations, it fails for both small W_m^+ and large T^+. This is an interesting area of study and may be improved by further knowledge of the flow physics. One useful physical phenomenon may be the angling of the mean flow direction.

If the laminar Stokes' solution is differentiated or integrated, the scaling is still linear with W_m^+. However, if W_m^+ is stronger the flow is angled further, and therefore less of the spanwise forcing is acting perpendicular to the flow. If the angle of the flow is defined by some relationship between the spanwise and streamwise flow, possibly the ratio of the gradient (mean gradient angle), then this ratio can be written as $W_m^+ f(\omega^+, U^+)$. Then the angle can be calculated as:

$$\theta = \arctan\left(W_m^+ f(\omega^+, U^+)\right).$$

Taking the component of this perpendicular to the flow we have:

$$\begin{aligned} w_\theta &= \cos\left(\arctan\left(W_m^+ f(\omega^+, U^+)\right)\right) \\ &= \frac{1}{\sqrt{1 + (W_m^+ f)^2}}. \end{aligned}$$

$1 - \frac{1}{\sqrt{1+(W_m^+ f)^2}}$ appears to give a good scaling to the variation in W_m^+. If ω^+ is fixed then f is constant (and f^2 chosen as 0.266). The parameter is multiplied by 52 to fit the CFD data, as this scaling does not include T^+ variation. Figure 9.1 shows the measured drag reduction compared with the angle scaling and the log scaling $\ln\left(\frac{W_m^+}{W_{th}^+}\right)$ from the S^+ parameter. The threshold velocity is $W_{th}^+ = 1.2$ and the log scaling is multiplied by 15.8 to fit the data.

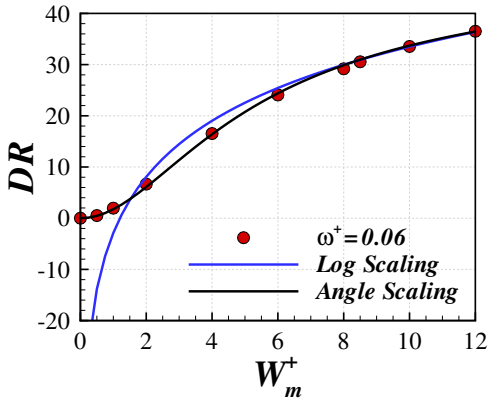

Figure 9.1: Comparison of the variation in DR with W_m^+ against the log scaling and angle scaling.

The log scaling is clearly inaccurate, especially as it tends to $-\infty$ as W_m^+ decreases to zero. However, the angle scaling fits the data extremely well and is definitely an interesting field of research and including the frequency variation would be an important next step.

9.2.3 Boundary Layers

In the present work, although not discussed, a boundary layer DNS code has been implemented. The recycling method of Lund et al. [1998] was employed to allow higher Re boundary layers to be studied without a large transition region. This could be an interesting topic of further investigation as it would allow for better comparison with experimental results. The Reynolds number effect could also be analysed continuously in space.

Appendix A

1d Averages of Turbulent Statisitics - Standing and Travelling Waves

A.0.4 Wall Oscillation Further Profiles

The pressure fluctuations and Reynolds shear stress for the wall oscillation cases are also presented.

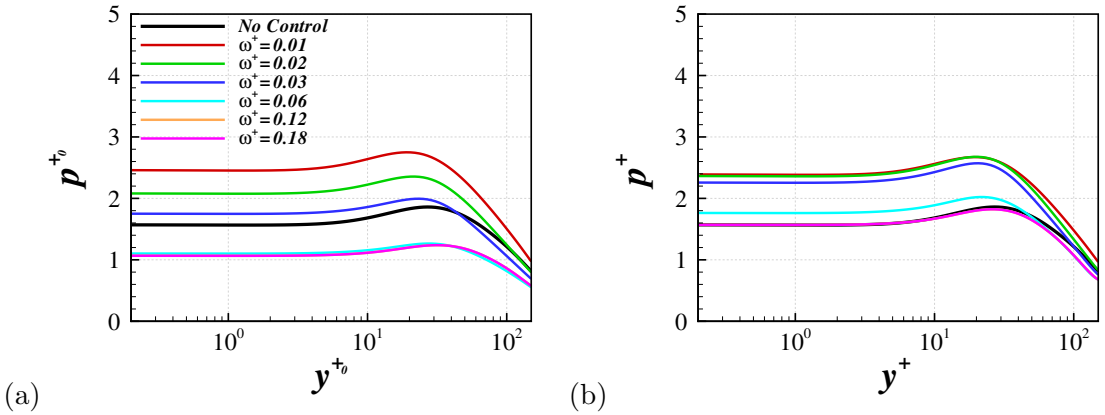

(a) (b)

Figure A.1: Pressure rms fluctuations scaled by the no-control case (a) and local wall units (b).

The pressure fluctuations, scaled by the no-control case, are presented in figure A.1a. The p rms profile is reduced everywhere at forcing frequency $\omega^+ = 0.18$. For $\omega^+ \leq 0.06$, fluctuations become larger, strengthening in the wall region. When scaled by local u_τ, figure A.1b, the wall value remains at a similar level to the no-control case, when $\omega^+ = 0.18$, but the fluctuation is reduced in the outer region. At $\omega^+ = 0.06$ the outer region remains as in $\omega^+ = 0.18$, but the near-wall value is increased. This near-wall p rms value continues to increase as the frequency is reduced.

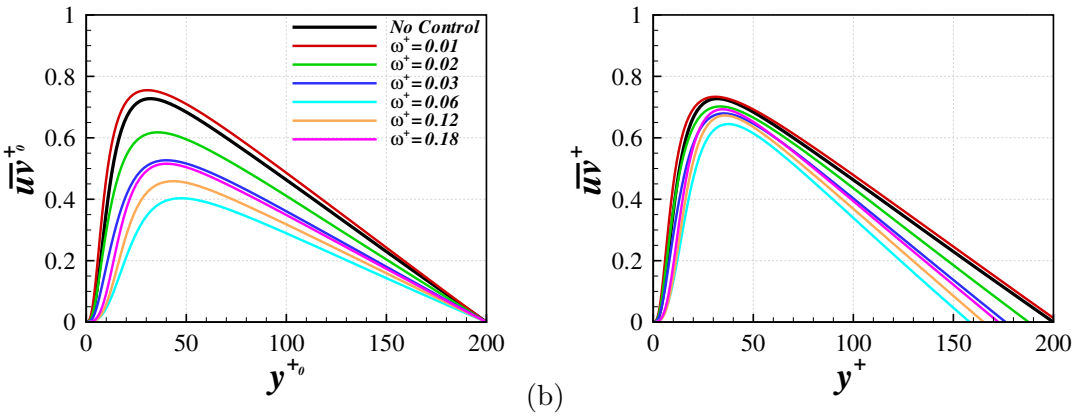

Figure A.2: Reynolds shear stress fluctuations scaled by the no-control case (a) and local wall units (b).

The Reynolds shear stress, scaled by the no-control case is presented in figure A.2a. The profile is reduced when a drag reduction is achieved, reaching its minimum at $\omega^+ = 0.06$. As the ω^+ value becomes lower than 0.06, the profile increases surpassing the no-control case when $\omega^+ = 0.01$ and a drag increase is found. When scaled by local wall units, figure A.2b, there is evendence of a stronger decrease in the profile for the frequencies which achieve a higher level of drag reduction, especially in the near-wall region. Comparing the $\omega^+ = 0.03$ and $\omega^+ = 0.18$ cases, when the drag reduction is similar, the $\omega^+ = 0.03$ case peak is slightly lower but the profile is higher in the near-wall region.

A.0.5 Standing Wave

A comparison of the standing wave cases is performed. The standing wave cases correspond to the y-axis in the drag reduction map, with $\omega^+ = 0$. As with the wall oscillation study and to aid in the comparison, the cases are discussed in order of increasing wavelength (the inverse of wavenumber). The large wavenumber values are initially studied, and the analysis is presented in reducing κ_x^+. For $\kappa_x^+ = 0.016$ a drag reduction of 40% is achieved. This increases when κ_x^+ reduces, reaching a maximum of 47% at $\kappa_x^+ = 0.006$. As κ_x^+ becomes smaller than 0.006, the level of drag reduction decreases, achieving only 18% at $\kappa_x^+ = 0.002$ (shown in figure 5.11b).

The streamwise velocity rms profile is scaled by u_{τ_0} and presented in figure A.3a. For $\kappa_x^+ = 0.016$, the profile is reduced and the peak moves away from the wall. This decreases with κ_x^+ and hence increases with the drag reduction. Although the maximum DR is achieved when $\kappa_x^+ = 0.006$, the minimum peak value is found with $\kappa_x^+ = 0.004$. Comparing these two profiles, the near-wall values are higher in the $\kappa_x^+ = 0.004$ case. At $\kappa_x^+ = 0.002$ the peak is increased and moves back towards the wall. At this wavenumber, the peak location is similar to that of the no-control case, despite the drag reduction achieved. When scaled by local u_τ, figure A.3b, the peak value with $\kappa_x^+ = 0.016$ is similar to the no-control case, but is moved away from the wall. The $\kappa_x^+ = 0.002$ and 0.004 cases, even though there is a large difference in the drag reduction achieved, have similar peak values but the $\kappa_x^+ = 0.002$ maximum is closer to the wall.

The v rms profiles, scaled by the no-control case, are shown in figure A.4a. The $\kappa_x^+ = 0.016$ case profile is reduced from the no-control case and the shape of the profile changes, being more strongly reduced nearer the wall. For $0.004 \leq \kappa_x^+ \leq 0.008$, the profiles are very similar and greatly reduced from the no-control flow. When $\kappa_x^+ = 0.002$ the peak is slightly decreased from the no-control case, but the profile is increased nearer the wall. The profile scaled by local wall units, figure A.4b, is very similar for $\kappa_x^+ \geq 0.004$. The $\kappa_x^+ = 0.016$ case appears slightly more

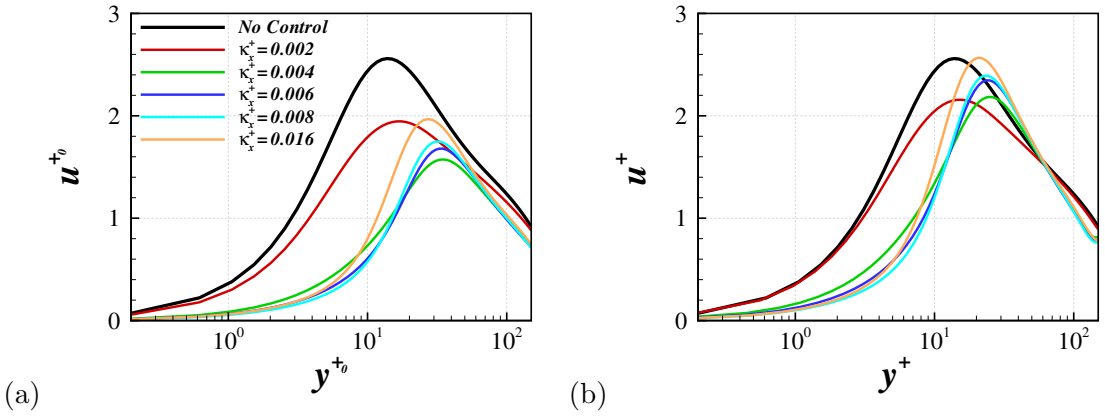

Figure A.3: Streamwise rms fluctuations scaled by the no-control case (a) and local wall units (b). The grey dashed line shows the profile from the no-control case.

reduced in the near-wall region and higher in the outer region. The $\kappa_x^+ = 0.002$ case is actually higher than the no-control case for $y^+ = 60$ and is decreased above this location.

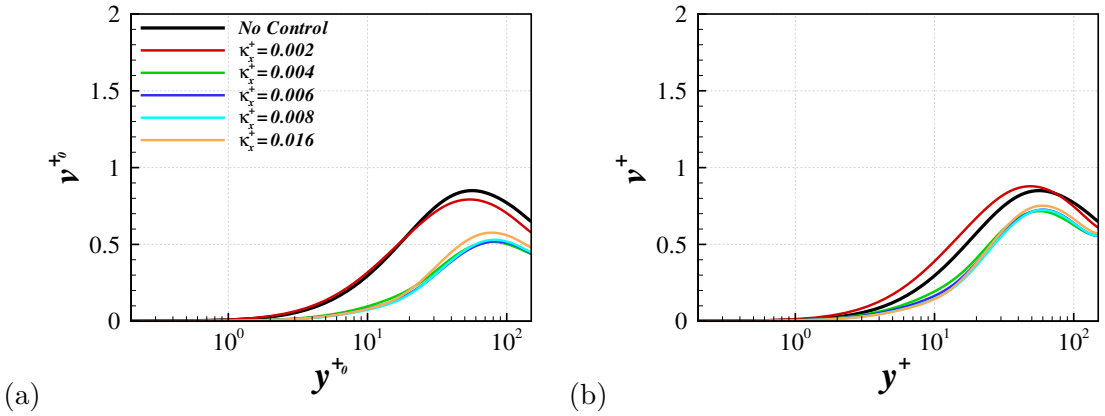

Figure A.4: Wall normal rms fluctuations scaled by the no-control case (a) and local wall units (b). The grey dashed line shows the profile from the no-control case.

Figure A.5a shows the spanwise velocity fluctuations, scaled by the no-control case. The profile is reduced by the forcing, reaching a minimum when $\kappa_x^+ = 0.006$ (but is very similar to the $\kappa_x^+ = 0.008$ case). The near-wall fluctuations become larger when $\kappa_x^+ = 0.004$ and a large peak occurs when $\kappa_x^+ = 0.002$. When scaled by local wall units, figure A.5b, the $\kappa_x^+ = 0.004$ case is higher than the no-control

case near the wall. This suggests that the near-wall spanwise fluctuations become stronger, relative to the skin friction.

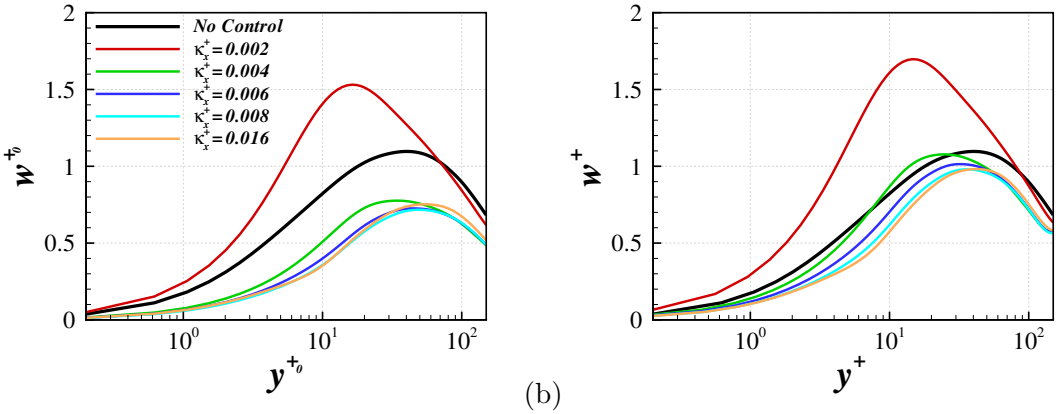

Figure A.5: Spanwise rms fluctuations scaled by the no-control case (a) and local wall units (b). The grey dashed line shows the profile from the no-control case.

The pressure fluctuations are scaled by the no-control shear velocity and presented in figure A.6a. For large κ_x^+ the fluctuations are strongly reduced from, and follow a similar shape to the no-control flow. As κ_x^+ becomes lower than the maximum drag reduction value of $\kappa_x^+ = 0.006$, the fluctuations become stronger in the near-wall region. The near-wall p rms values become larger than the no-control case values when $\kappa_x^+ = 0.002$, even though they are reduced in the outer region. When scaled by local u_{τ_0}, figure A.6b, the wall value does not reduce from the no-control case and simply increases as κ_x^+ is reduced. In the outer region the pressure rms profile initially reduces with large κ_x^+ and increases again as the drag reduction decreases.

Figure A.7a shows the streamwise vorticity fluctuations scaled by the no-control case. The $\kappa_x^+ = 0.016$ case is strongly reduced from the no-control flow, however the shape of the profile has changed somewhat. Although the profile is similar near the wall, a local maximum occurs just above the minimum, which is closer to the wall than the peak from the no-control flow. There is then a decrease in the profile but a second peak occurs further away from the wall. The $\kappa_x^+ = 0.008$

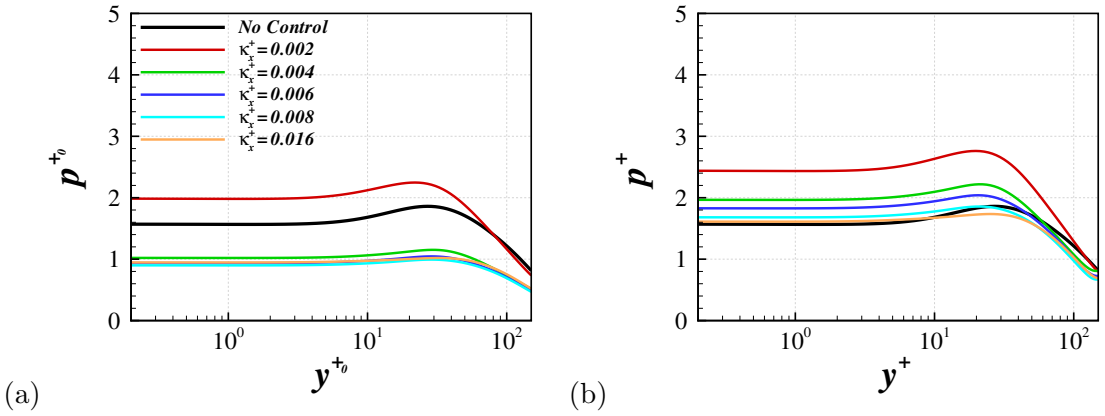

Figure A.6: Pressure rms fluctuations scaled by the no-control case (a) and local wall units (b). The grey dashed line shows the profile from the no-control case.

and 0.006 profiles are again very similar, and are reduced slightly more from the no-control flow than seen in the $\kappa_x^+ = 0.016$ case. At $\kappa_x^+ = 0.004$ the profile, although still reduced from the no-control flow, is larger than the high-wavenumber cases near the wall. The $\kappa_x^+ = 0.002$ profile, although lower than the no-control case in the outer region is greatly increased near the wall, showing a clear modification in the shape of the profile. When scaled by local u_τ, figure A.7b, the $\kappa_x^+ = 0.016$ case is again reduced from the no-control case near the wall. Above the local minimum the profile is slightly increased, but becomes reduced around the no-control peak. The $\kappa_x^+ = 0.008$ and 0.006 cases, although reduced near the wall, the peak is larger than the no-control case value, with the 0.006 case slightly exceeding the 0.008 case peak. For $\kappa_x^+ = 0.004$ the wall value is still slightly reduced from the no-control flow, but the peak becomes larger still. By $\kappa_x^+ = 0.002$ the profile is strongly increased in the near-wall region.

The rms wall-normal vorticity profiles are scaled by the no-control shear velocity and presented in figure A.8a. The $\kappa_x^+ = 0.016$ profile is strongly reduced from the no-control profile, especially near the wall, causing the peak to move away from the wall. The $\kappa_x^+ = 0.008$ and 0.006 cases are reduced further, and the peak moved away from the wall, where the maximum in the $\kappa_x^+ = 0.006$ case is slightly

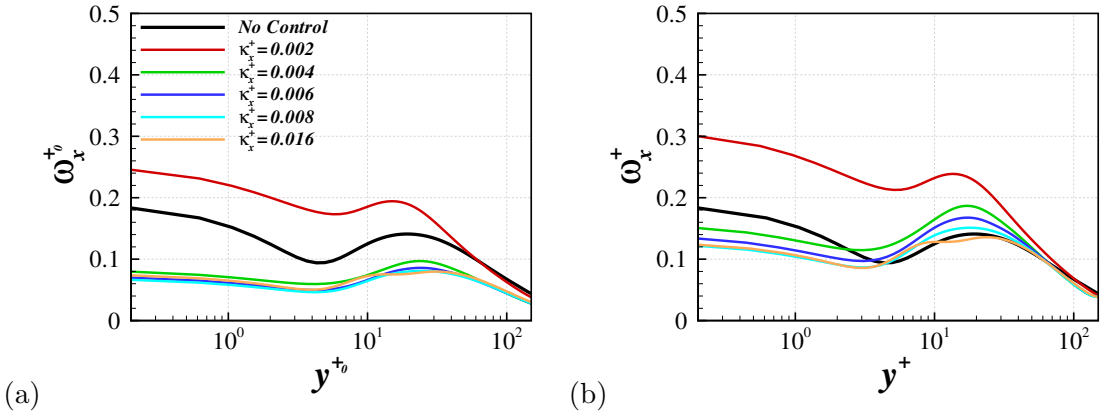

Figure A.7: Streamwise vorticity rms fluctuations scaled by the no-control case (a) and local wall units (b). The grey dashed line shows the profile from the no-control case.

lower. The profile from the $\kappa_x^+ = 0.004$ case is still strongly reduced from the no-control case. The maximum value is similar to that of the $\kappa_x^+ = 0.006$ peak but the near-wall fluctuations are increased, hence the peak is closer to the wall. The $\kappa_x^+ = 0.002$ case profile is reduced by a small amount from the no-control profile. When scaled by local u_τ, figure A.8b, the trend is very similar, except the variation in the profiles is reduced. Also, the $\kappa_x^+ = 0.002$ case has larger fluctuations near the wall than the no-control flow, relative to the increasing drag reduction.

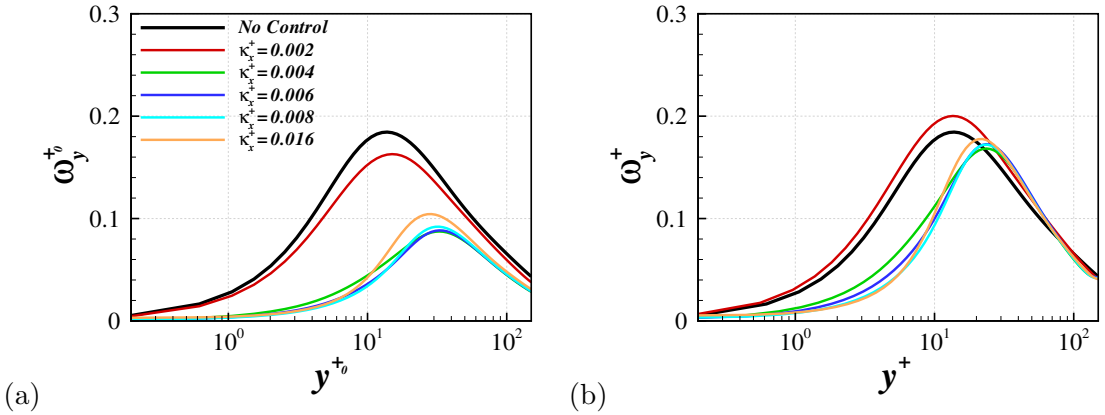

Figure A.8: Wall normal vorticity rms fluctuations scaled by the no-control case (a) and local wall units (b). The grey dashed line shows the profile from the no-control case.

The spanwise vorticity is scaled by the no-control case and is presented in figure A.9a. When $\kappa_x^+ = 0.016$ the profile is strongly reduced from the no-control case in the near-wall region, forming a peak at $y^{+_0} = 15$. As the wavenumber is reduced to $\kappa_x^+ = 0.008$ and 0.006 the wall value decreases slightly but a stronger decrease is observed in the near-wall region and the peak reduces and moves away from the wall. At $\kappa_x^+ = 0.004$, although the peak is at a similar value to the $\kappa_x^+ = 0.008$ case, the wall value is higher. At $\kappa_x^+ = 0.002$ the profile is very similar to the no-control case. The near-wall ω_z values are reduced from the no-control case, but a peak is still evident near the wall. When scaled by the local u_τ values, figure A.9b, the profiles become very similar in the outer region. The peak values also become similar and are at a level which is increased from the no-control case at that y location.

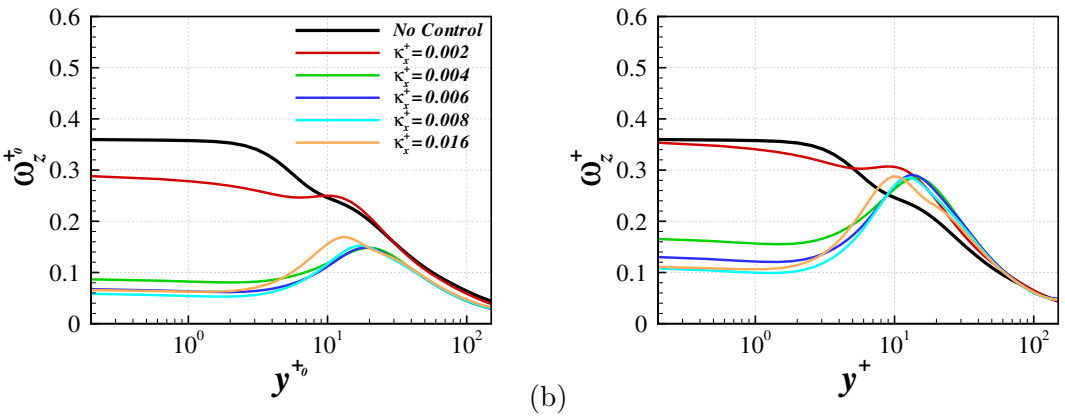

(a) (b)

Figure A.9: Spanwise vorticity rms fluctuations scaled by the no-control case (a) and local wall units (b). The grey dashed line shows the profile from the no-control case.

The Reynolds shear stress for the standing wave cases are shown in figure A.10a, scaled by the no-control case. For $0.004 \leq \kappa_x^+ \leq 0.016$ the profiles are reduced from the no-control flow and moves away from the wall. The near-wall shear at these wavenumbers is strongly reduced, causing a decrease in the gradient of the profile at the wall. The $\kappa_x^+ = 0.002$ is again reduced from the no-control case but the near-wall shear stress attains similar values. When scaled by local wall units, figure A.10b,

the $\kappa_x^+ = 0.002$ case actually becomes slightly higher than the no-control case in the near-wall region. This shows that the Reynolds shear stress also becomes stronger relative to the skin friction. The other standing wave parameters are still reduced, despite the scaling.

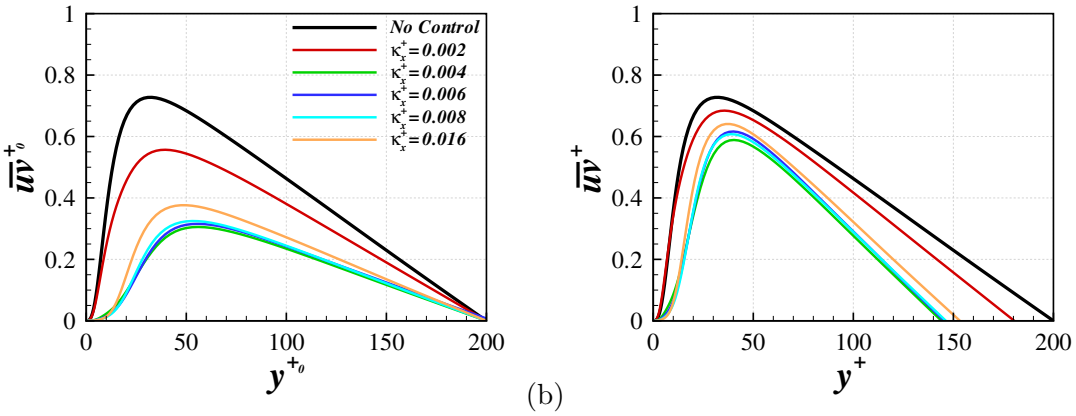

(a) (b)

Figure A.10: Reynolds shear stress fluctuations scaled by the no-control case (a) and local wall units (b). The grey dashed line shows the profile from the no-control case.

A.0.6 Travelling Wave

The effect of the travelling wave is studied by looking at the effect of fixing κ_x^+ while varying ω^+, and fixing ω^+ while varying κ_x^+. In the following figures the black line, which previously represented the no-control case now represents the zero value of the varying parameter, i.e. the standing wave or wall oscillation cases in the fixed κ_x^+ or ω^+ comparisons respectively. The figures also include a dashed grey line to show the no-control case profile to aid the understanding of the drag reduction.

Frequency Variation

The initial study of travelling waves looks into variation of the temporal frequency. The spatial wavenumber is fixed at $\kappa_x^+ = 0.008$. This corresponds to a horizontal line in the drag reduction map which passes through the parameter combination which achieves the maximum drag reduction. The standing wave at this wavenumber

achieves a drag reduction of 47%, this is increased slightly to 50% as ω^+ increases to 0.02. By $\omega^+ = 0.06$ a small drag increase is found and at the highest ω^+ value studied of 0.18, a modest drag reduction has returned (shown in figure 5.12a).

The u rms profiles, scaled by the no-control case, is presented in figure A.12a. The standing wave case is greatly reduced from the no-control case and the peak moves away from the wall. The $\omega^+ = 0.01$ and 0.02 cases are very similar to the standing wave case but are reduced and the peak moves further from the wall. The $\omega^+ = 0.03$ profile is strongly increased from the $\omega^+ = 0.02$ case near the wall. This may be evidence of the oscillation in the profile, seen also at $Re_\tau = 800$ in section 6.3. The $\omega^+ = 0.06$ case profile is increased from the lower ω^+ cases, but is still reduced from the no-control profile. As ω^+ increases from $\omega^+ = 0.06$, the peak value is larger and further from the wall. When scaled in local wall units, figure A.12b, the standing wave peak is reduced from the no-control value and moves away from the wall. Just above the peak, the fluctuations are larger than in no-control flow in the region $0 < y^+ < 50$. A similar behaviour occurs from $\omega^+ = 0.01$ and 0.02 with the peak decreasing and moving away from the wall. At $\omega^+ = 0.03$ the peak is also decreased and moves away from the wall, however the near-wall values are greatly increased. These values increase as ω^+ becomes larger moving the peak back towards the wall. The $\omega^+ = 0.18$ peak is at the same level as the no-control case, but the peak moves away from the wall.

The v rms fluctuations are shown in figure A.12a, scaled by the no-control case. The profiles when $0 \leq \omega^+ \leq 0.02$ are strongly reduced from the no-control case, especially in the near-wall region. At $\omega^+ = 0.03$ the peak is slightly higher than in the lower frequency cases and is moved slightly closer to the wall, and the near-wall fluctuations are stronger. At $\omega^+ = 0.06$, the near-wall fluctuations become very large with the peak becoming stronger and closer to the wall than in the no-control flow. At $\omega^+ = 0.12$, although the drag is reduced, the profile is still higher than the no-control case. When $\omega^+ = 0.18$, the peak is lower than in the no-control

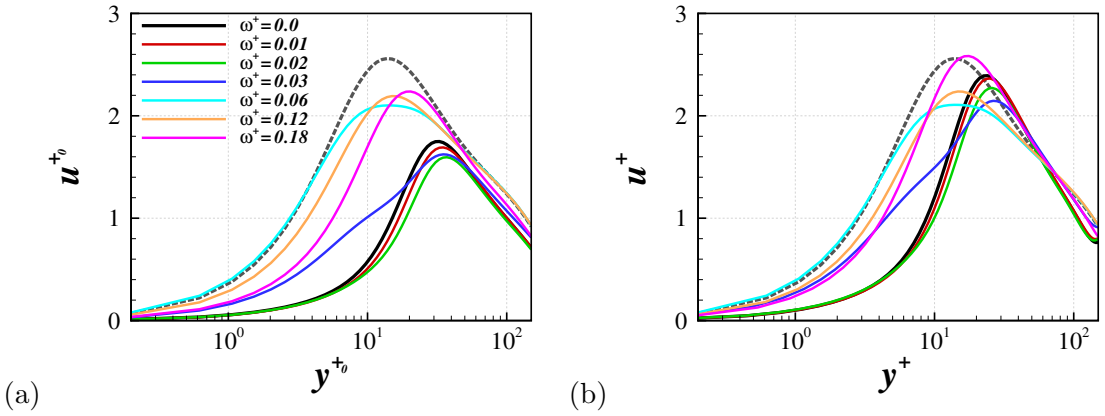

Figure A.11: Streamwise rms fluctuations scaled by the no-control case (a) and local wall units (b). The grey dashed line shows the profile from the no-control case.

case. Figure A.12b, show the profiles scaled by the local u_τ. The profiles become closer together because of the scaling, but the general trend is as before.

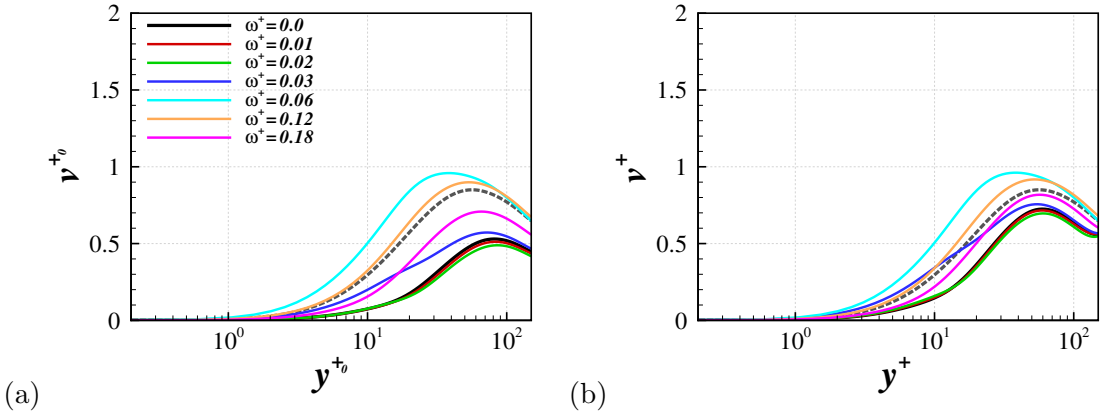

Figure A.12: Wall normal rms fluctuations scaled by the no-control case (a) and local wall units (b). The grey dashed line shows the profile from the no-control case.

Figure A.13a shows the spanwise velocity fluctuations scaled by the no-control case. The profile from the standing wave case is strongly reduced from the no-control case but has a similar shape. For $\omega^+ \leq 0.02$ the profiles are close to the standing wave case, but become slightly less reduced near the wall and more reduced in the outer region. At $\omega^+ = 0.03$ a strong near-wall peak emerges which is higher even at $\omega^+ = 0.06$. With $\omega^+ = 0.12$ peak is lower, and by $\omega^+ = 0.18$ the

profile returns to be a similar shape to the no-control case but is slightly reduced. When scaled by local wall units, figure A.13b, the $0 \leq \omega^+ \leq 0.02$ cases are only slightly reduced from the no-control case. The general trend, as ω^+ becomes large is similar to that previously discussed, except the $\omega^+ = 0.03$ and $\omega^+ = 0.12$ cases show similar near-wall profiles, despite the difference in DR.

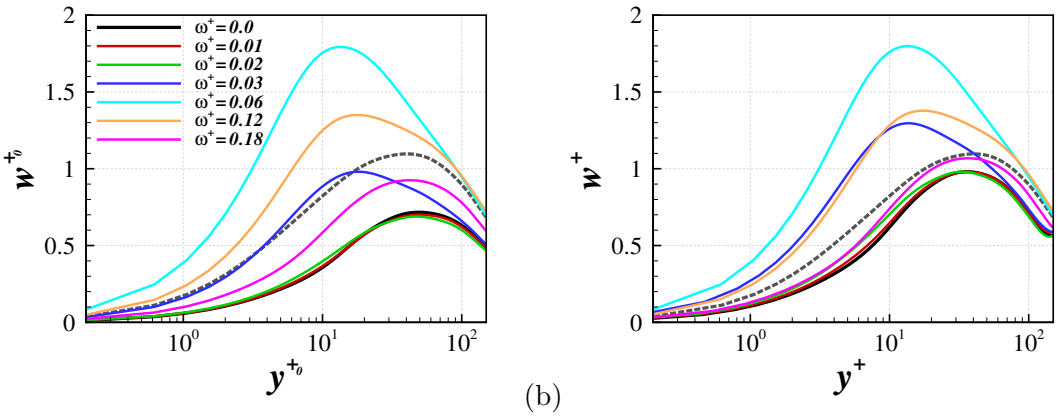

Figure A.13: Spanwise rms fluctuations scaled by the no-control case (a) and local wall units (b). The grey dashed line shows the profile from the no-control case.

The pressure fluctuations, scaled by the no-control case are presented in figure A.14a. The $0 \leq \omega^+ \leq 0.02$ profiles are again very similar, with a fairly uniform reduction from the no-control curve. At $\omega^+ = 0.03$, the near-wall fluctuations are increased from the no-control flow, despite the strong reduction in the outer region. At $\omega^+ = 0.06$ the strongest increase from the no-control case is seen. At this forcing frequency the wall value of p rms has doubled from the no-control case, even though the centreline values are almost the same. By $\omega^+ = 0.12$ the near-wall fluctuations have again reduced, with the outer region remaining at a similar level to the no-control case. When $\omega^+ = 0.18$ the profile shape becomes similar to the no-control case but the intensity is reduced. When scaled by local u_τ, the wall value is never reduced from the no-control value. For small ω^+, the relative fluctuations are increased near the wall and reduced in the outer region. As ω^+ increases the near-wall values become large, reducing back to the level of the no-control case as

ω^+ becomes large.

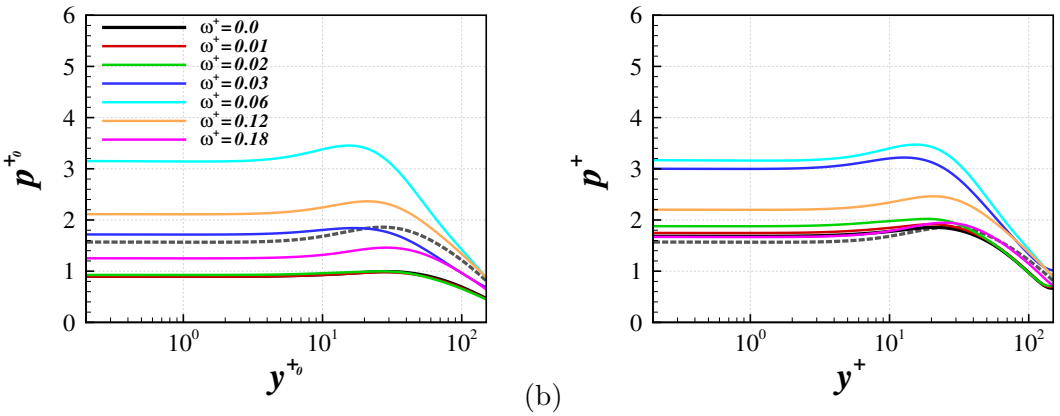

(a) (b)

Figure A.14: Pressure rms fluctuations scaled by the no-control case (a) and local wall units (b). The grey dashed line shows the profile from the no-control case.

The streamwise vorticity profile is presented in figure A.15a, scaled by u_{τ_0}. The $0 \leq \omega^+ \leq 0.02$ profiles are again similar with a strong reduction in the fluctuations. The $\omega^+ = 0.03$ profile follows closely the no-control profile in the near-wall region, with a slightly lower wall value, and slightly higher local minimum. This profile is reduced from the no-control flow in the outer region. At $\omega^+ = 0.06$ the wall value is strongly increased from the no-control case, even though the profiles are very similar in the outer region. At $\omega^+ = 0.12$, the near-wall profile is larger still, but by $\omega^+ = 0.18$ the profile becomes again reduced from the no-control case. Although the profile has a similar shape to the no-control case below the local minimum, above this the profile becomes flatter with the local maximum moved away from the wall. When scaled in local wall units, figure A.15b, the standing wave case is reduced from the no-control case at the wall. The local maximum is, in fact, increased. A similar behaviour occurs with $\omega^+ = 0.01$ and 0.02, where the near-wall profile increases slightly. This kind of near-wall reduction suggests that the decrease in u_τ comes with suppression of streamwise vorticity very close to the wall. At $\omega^+ = 0.03$, the near-wall profile is very similar to the $\omega^+ = 0.12$ case and the minimum location is similar, however the peak at $\omega^+ = 0.03$ is much larger.

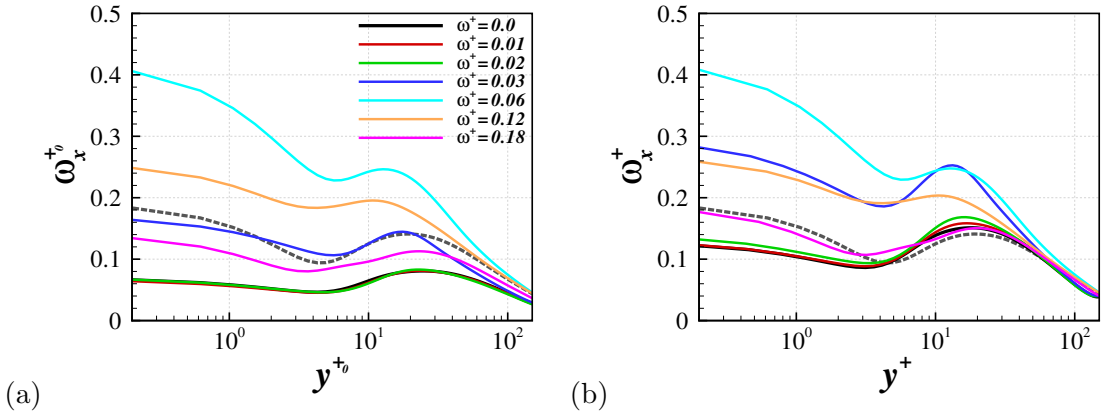

Figure A.15: Streamwise vorticity rms fluctuations scaled by the no-control case (a) and local wall units (b). The grey dashed line shows the profile from the no-control case.

Figure A.16a shows the wall-normal vorticity fluctuations, scaled by u_{τ_0}. For $0 \leq \omega^+ \leq 0.02$ the profiles are strongly reduced and the peaks moved away from the wall. At $\omega^+ = 0.03$ the profile is similar to the lower frequency cases in the outer region, but is strongly increased near the wall causing the peak to move back towards the wall. At $\omega^+ = 0.06$ the profile has increased and become larger than the no-control case. At $\omega^+ = 0.12$ the profile has reduced below the no-control profile, reducing further still by $\omega^+ = 0.18$. When scaled by local wall units, figure A.16b, the $0 \leq \omega^+ \leq 0.02$ case maxima are slightly reduced from the no-control case but are strongly moved away from the wall. This correspond to a weaker influence near the wall and a stronger influence of the fluctuations with $25 < y^+ < 50$. With $\omega^+ = 0.03$ the effect of the fluctuations is similar in the outer region, but become stronger near the wall. By $\omega^+ = 0.06$ the fluctuations are increased which decrease again for the larger frequencies.

The spanwise vorticity fluctuations are presented in figure A.17a, scaled by the no-control case. The standing wave case profile is strongly reduced in the near-wall region, with a peak emerging around $y^{+_0} = 15$. For $\omega^+ = 0.01$ and 0.02 although the wall values are similar to the standing wave case, the peak is decreased and moved from the wall. At $\omega^+ = 0.03$ the wall value has increased from the lower

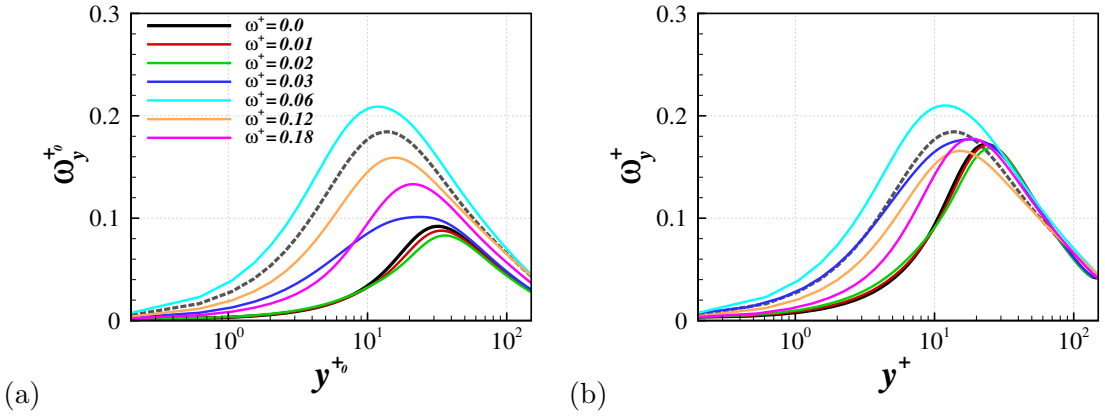

Figure A.16: Wall normal vorticity rms fluctuations scaled by the no-control case (a) and local wall units (b). The grey dashed line shows the profile from the no-control case.

frequency cases and the peak is also increased. By $\omega^+ = 0.06$, the near-wall profile is similar to the no-control case, except for the higher wall value. For $y^{+0} > 10$ there is also a local maximum which causes the fluctuations to be larger than the no-control case in this region. When $\omega^+ \geq 0.12$ the wall value decreases. When scaled by local u_τ, figure A.17b, the peak value and location for $0 \leq \omega^+ \leq 0.03$ is very similar. The wall value at $\omega^+ = 0.03$, however, is much larger. At $\omega^+ = 0.06$ the profile is similar to the u_{τ_0} scaling, due to the similar shear velocity. When $\omega^+ = 0.12$, the near-wall value is slightly reduced and is closer to the wall. By $\omega^+ = 0.18$ the wall value decreases further and the peak moves away from the wall.

The Reynolds shear stress is scaled by the no-control flow and presented in figure A.18a. For $0 \leq \omega^+ \leq 0.02$ the profiles are again similar. The shear stress is strongly suppressed near the wall causing a convex profile with decreased peak value which is moved away from the wall. At $\omega^+ = 0.03$ the near-wall fluctuations are much stronger than with $\omega^+ \leq 0.02$ and the peak is slightly increased. The $\omega^+ = 0.06$ profile is increased from the no-control case near the wall, but the peak is lower. When $\omega^+ = 0.12$ the near-wall shear stress decreases, with the profile becoming very similar to the no-control curve. By $\omega^+ = 0.18$, the profile becomes again reduced from the no-control case with the peak moved away from the wall.

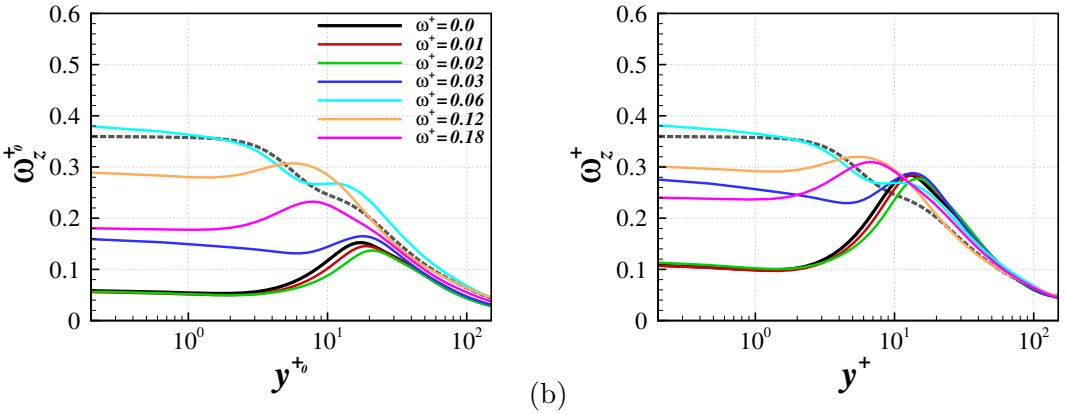

(a) (b)

Figure A.17: Spanwise vorticity rms fluctuations scaled by the no-control case (a) and local wall units (b). The grey dashed line shows the profile from the no-control case.

When scaled by local u_τ, figure A.18b, the variation in the profiles is smaller but the trend is unchanged.

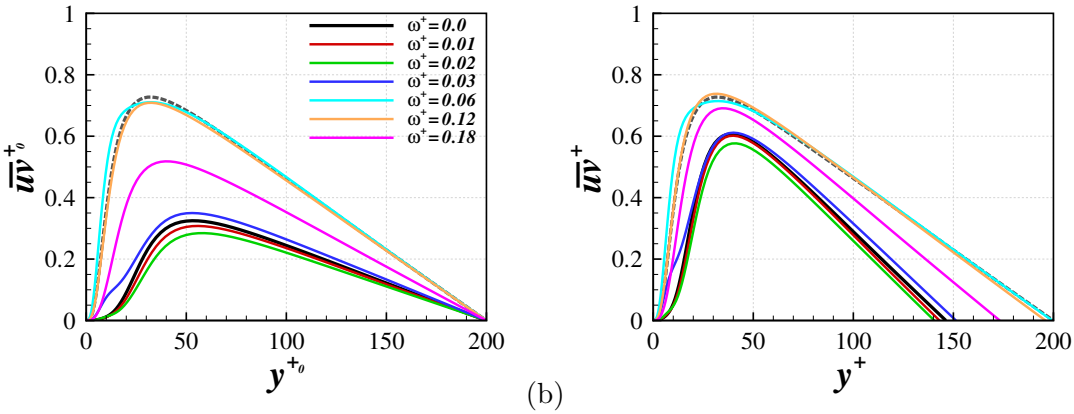

(a) (b)

Figure A.18: Reynolds shear stress fluctuations scaled by the no-control case (a) and local wall units (b). The grey dashed line shows the profile from the no-control case.

Wavenumber Variation

The effect of fixing the temporal frequency and changing the wavenumber is also investigated. The frequency chosen is $\omega^+ = 0.02$, which again passes through the maximum drag reduction case. The wall oscillation case at this frequency gives a

modest drag reduction of 9%. Increasing κ_x^+ to 0.002 gives a drag increase of 16%, but by $\kappa_x^+ = 0.004$ the drag reduction has returned to 9%. The maximum DR of 50% is achieved at $\kappa_x^+ = 0.008$ which then reduces to 44% when $\kappa_x^+ = 0.016$ (shown in figure 5.12b).

The u rms profiles, scaled by u_{τ_0}, are shown in figure A.19a. The wall oscillation case gives a reasonable reduction from the no-control profile with a fairly similar peak location. At $\kappa_x^+ = 0.002$ the profile is larger than the no-control case near the wall with a peak value close to that of the no-control flow, but is closer to the wall. In the outer region this profile is increased from the no-control profile. At $\kappa_x^+ = 0.004$ the profile is very similar to the wall oscillation profile. When $\kappa_x^+ = 0.008$ the profile is most strongly reduced and the peak moved away from the wall. The shape of the profile has changed at this wavenumber, as it is more strongly decreased near the wall. At $\kappa_x^+ = 0.016$ the profile is reduced less than the optimal DR case and the peak is closer to the wall. When scaled by local wall units, figure A.19b, the $\kappa_x^+ = 0$ and 0.004 cases are reduced near the wall, but follow the no-control case in the outer region. When $\kappa_x^+ = 0.002$ the near-wall profile is similar to the no-control case, but is increased in the outer region. At $\kappa_x^+ = 0.008$, the local near-wall fluctuations are reduced from the no-control case, increased for $30 < y^+ < 60$, and decreased above this. The $\kappa_x^+ = 0.016$ case is similar to $\kappa_x^+ = 0.008$, but is slightly higher around the peak location.

Figure A.20a shows the wall-normal velocity fluctuations scaled by the no-control case. The $\kappa_x^+ = 0$ case has a profile which compares well with the no-control case, despite the drag reduction, but is slightly higher near the wall and is decreased in the outer region. At $\kappa_x^+ = 0.002$ the profile is strongly increased from the no-control profile and the maximum is moved towards the wall. At $\kappa_x^+ = 0.004$ the profile is again similar to the no-control case with a slight increase near to the wall and a reduction in the outer region. The profile, when $\kappa_x^+ = 0.008$, has been strongly reduced from the no-control case, with the peak moved away from the wall. At this

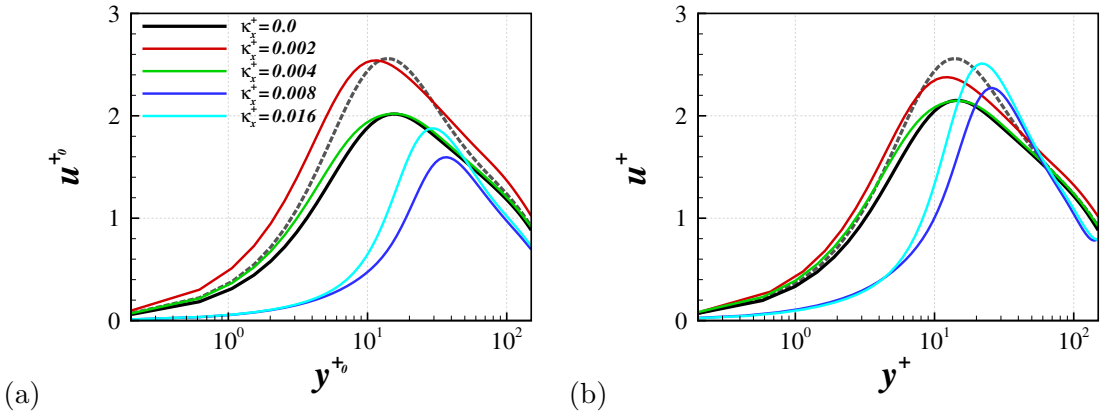

Figure A.19: Streamwise rms fluctuations scaled by the no-control case (a) and local wall units (b). The grey dashed line shows the profile from the no-control case.

wavenumber the profile and the drag reduction is at the minimum achieved. When $\kappa_x^+ = 0.016$ the near-wall profile is similar to the $\kappa_x^+ = 0.008$ case, but the peak is higher and at a lower y^{+_0} value. When scaled by local wall units, figure A.20b, the near-wall fluctuations in the wall oscillation case are much stronger than the no-control case. The $\kappa_x^+ = 0.002$ profile is reduced by the scaling. The $\kappa_x^+ = 0.004$ case fluctuations are very similar to the $\kappa_x^+ = 0.002$ case near the wall, with lower profile for $y^+ > 20$. The $\kappa_x^+ = 0.008$ and $\kappa_x^+ = 0.016$ are similar and still reduced from the no-control flow.

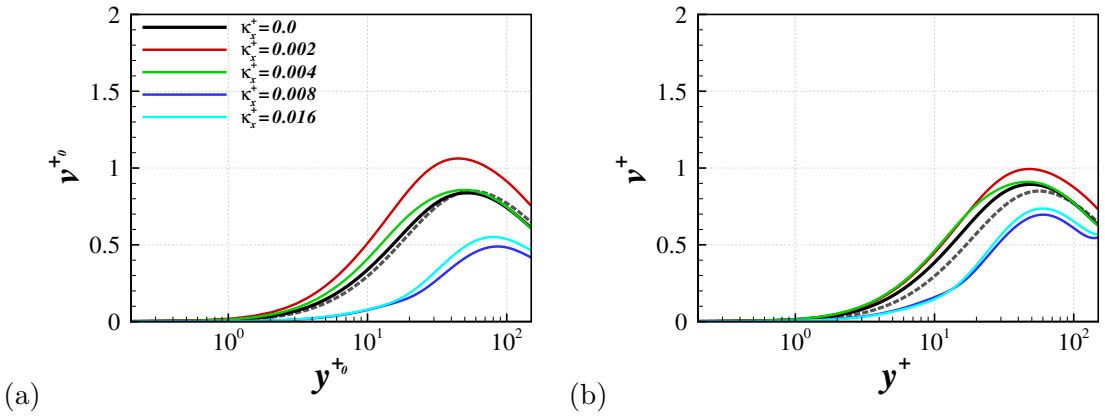

Figure A.20: Wall normal rms fluctuations scaled by the no-control case (a) and local wall units (b). The grey dashed line shows the profile from the no-control case.

The spanwise velocity fluctuation scaled by the no-control flow are shown in figure A.21a. The wall oscillation case is very similar to the no-control flow in the outer region, but is greatly increased for $y^+ < 80$ with a near-wall peak emerging. With $\kappa_x^+ = 0.002$ the profile is increased further and has a peak in a similar location to the wall oscillation case. The shape of the profile changes, and has almost linear profile in the region above the peak. For $\kappa_x^+ = 0.004$ the outer fluctuations are again similar to the no-control flow and has slightly higher than the wall oscillation case. When $\kappa_x^+ = 0.008$ and 0.016 the profiles are decreased from the no-control case and are similar in shape. Although the $\kappa_x^+ = 0.008$ and 0.016 profiles are very similar to each other near the wall, the $\kappa_x^+ = 0.008$ case is slightly lower above $y^{+_0} \approx 20$. The profiles are shown scaled by local u_τ in figure A.21b. The $\kappa_x^+ = 0$ and 0. 002 cases have very similar near-wall profiles but the relative fluctuations of the $\kappa_x^+ = 0.002$ case are larger away from the wall. The $\kappa_x^+ = 0.004$ case has largest peak value but is still lower than the $\kappa_x^+ = 0.002$ case in the outer region. The $\kappa_x^+ = 0.008$ and 0.016 cases are again reduced from the no-control case.

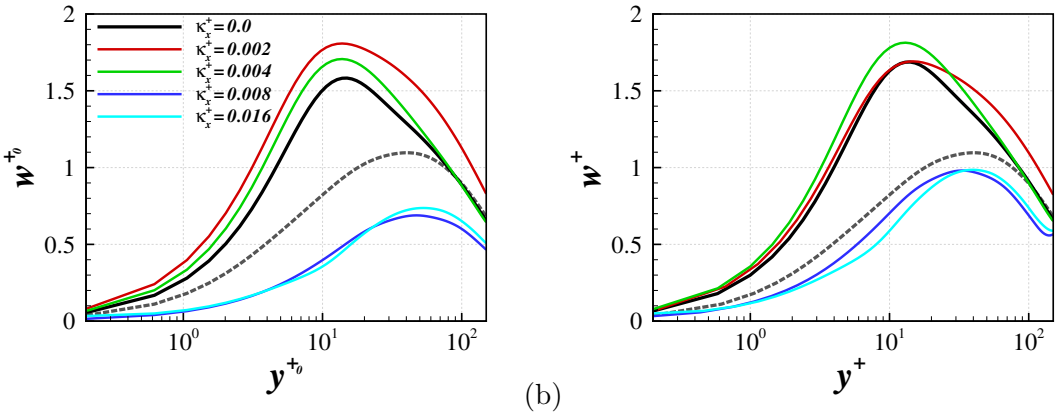

Figure A.21: Spanwise rms fluctuations scaled by the no-control case (a) and local wall units (b). The grey dashed line shows the profile from the no-control case.

Figure A.22a shows the pressure fluctuations scaled by the no-control case. The wall oscillation case is increased from the no-control flow near the wall. At $\kappa_x^+ = 0.002$, the near-wall fluctuations are increased from the wall oscillation case

and by $\kappa_x^+ = 0.004$ the fluctuations increase further. The $\kappa_x^+ = 0.008$ and 0.016 cases are again similar, with the profiles reduced from the no-control flow. When scaled by local u_τ, figure A.22b, the wall value is not decreased from the no-control case for any forcing parameters. The $\kappa_x^+ = 0.004$ case has the highest wall value, however this decreases below the $\kappa_x^+ = 0.002$ profile. The $\kappa_x^+ = 0.008$ and 0.016 profiles, although increased from the no-control case near the wall, are decreased above $y^+ = 50$.

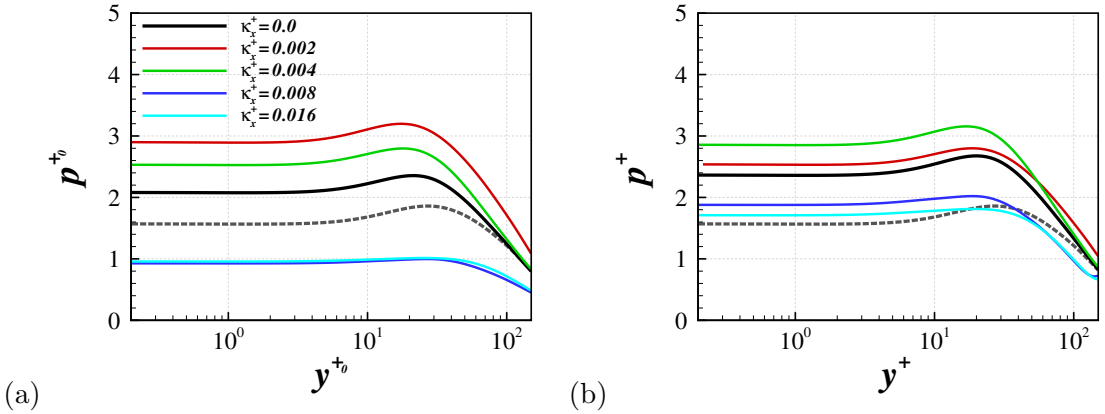

Figure A.22: Pressure rms fluctuations scaled by the no-control case (a) and local wall units (b). The grey dashed line shows the profile from the no-control case.

The streamwise vorticity rms, scaled by u_{τ_0}, is presented in figure A.23a. The wall oscillation case is strongly increased from the no-control flow near the wall. The $\kappa_x^+ = 0.004$ case is slightly higher than the $\kappa_x^+ = 0$ profile and the local maximum is further from the wall. The $\kappa_x^+ = 0.002$ case is higher than the wall oscillation case and the maximum peak value is reached from the profiles presented here. Again, the $\kappa_x^+ = 0.008$ and 0.016 profiles are reduced from the no-control case in a similar fashion. The peak from $\kappa_x^+ = 0.008$ is positioned slightly further from the wall than the $\kappa_x^+ = 0.016$ case. Figure A.23b shows the profiles scaled by the local u_τ values. The wall oscillation is increased from the no-control case near the wall. The $\kappa_x^+ = 0.002$ profile is similar to the profile from the wall oscillation flow near the wall, but the peak value is lower. The $\kappa_x^+ = 0.004$ profile is larger than the

wall oscillation case near the wall. By $\kappa_x^+ = 0.008$ the profile is reduced from the no-control flow near the wall but the local maximum is larger. The $\kappa_x^+ = 0.016$ case follows closely the no-control flow except is also reduced at the wall and the local maximum is moved to a lower y^+ location.

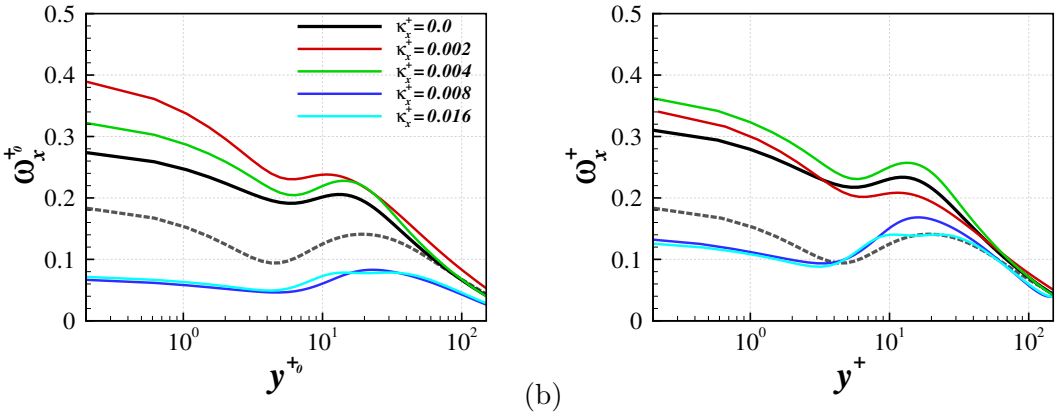

(a) (b)

Figure A.23: Streamwise vorticity rms fluctuations scaled by the no-control case (a) and local wall units (b). The grey dashed line shows the profile from the no-control case.

The wall-normal vorticity fluctuations are shown in figure A.24a scaled by the no-control flow. The profile from the wall oscillation forcing is reduced from the no-control case near the wall. The $\kappa_x^+ = 0.002$ case is strongly increased from the no-control flow, whereas the $\kappa_x^+ = 0.004$ case is only slightly increased. The $\kappa_x^+ = 0.008$ and 0.016 cases have similar near-wall profiles, but the $\kappa_x^+ = 0.016$ peak is slightly higher. Both are strongly reduced from the no-control profile. When scaled by local wall units, figure A.24b, the wall oscillation profile is increased from the no-control flow. The peak for the $\kappa_x^+ = 0.002$ case is slightly higher and closer to the wall than the wall oscillation profile. At $\kappa_x^+ = 0.004$ the peak is higher still and is further from the wall than in the $\kappa_x^+ = 0.002$ profile. By $\kappa_x^+ = 0.008$ the profile is strongly reduced near the wall, causing the peak to be far from the wall. The $\kappa_x^+ = 0.016$ case is slightly reduced near the wall as compared to the $\kappa_x^+ = 0.008$ case, but has a higher peak which is slightly closer to the wall.

Figure A.25a shows the spanwise vorticity, scaled from the no-control case.

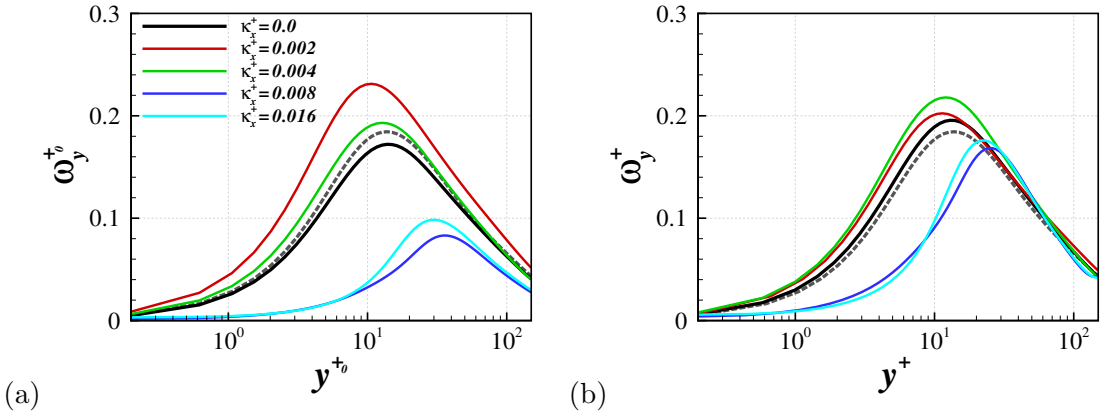

Figure A.24: Wall normal vorticity rms fluctuations scaled by the no-control case (a) and local wall units (b). The grey dashed line shows the profile from the no-control case.

The wall oscillation profile is reduced from the no-control flow near the wall, but is slightly increased for $5 < y^{+_0} < 20$. The $\kappa_x^+ = 0.002$ case is similar in shape to the no-control case but is higher. The $\kappa_x^+ = 0.004$ case is again reduced slightly near the wall but increased for $10 < y^{+_0} < 60$, as a peak emerges in the profile. The $\kappa_x^+ = 0.008$ profile is universally reduced from the no-control profile. This reduction is strongest at the wall with a peak at $y^{+_0} \approx 20$. The $\kappa_x^+ = 0.016$ is similar to the $\kappa_x^+ = 0.008$ case in the outer region, but the peak is higher and closer to the wall. When scaled by local wall units, figure A.25b, the peaks are closer together. The wall oscillation case is similar to the no-control scaling, but has a slightly larger increase from the no-control case at $5 < y^+ < 60$. The $\kappa_x^+ = 0.002$ profile is similar to the no-control case near the wall, except the wall value is slightly higher. The $\kappa_x^+ = 0.004$ case also follows the no-control case near the wall, but is increased strongly at the wall value, and is higher in the $5 < y^+ < 60$ region because of the local maximum. The $\kappa_x^+ = 0.008$ and 0.016 cases are again reduced near the wall but are also increased for $y^+ > 15$.

The Reynolds shear stress profiles are scaled by the no-control flow and presented in figure A.26a. The $\kappa_x^+ = 0$ and 0.004 cases have similar profiles which are reduced and the peaks moved away from the wall when compared to the no-

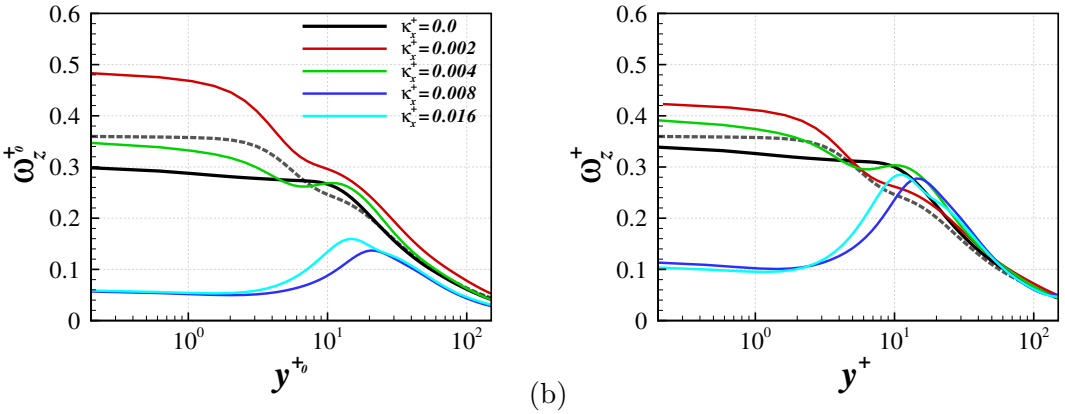

Figure A.25: Spanwise vorticity rms fluctuations scaled by the no-control case (a) and local wall units (b). The grey dashed line shows the profile from the no-control case.

control case. The $\kappa_x^+ = 0.004$ profile is slightly higher than the wall oscillation case near the wall. The $\kappa_x^+ = 0.002$ case is increased from the no-control flow and the peak is moved towards the wall. The profiles of the $\kappa_x^+ = 0.008$ and 0.016 cases are strongly decreased from the no-control flow. The shape of the profile is slightly changed as there is a very strong reduction in Reynolds shear stress close to the wall. Figure A.26b shows the profiles scaled by the local u_τ values. The order and behaviour of the profiles is qualitatively similar to the no-control scaling but with small variation between the profiles.

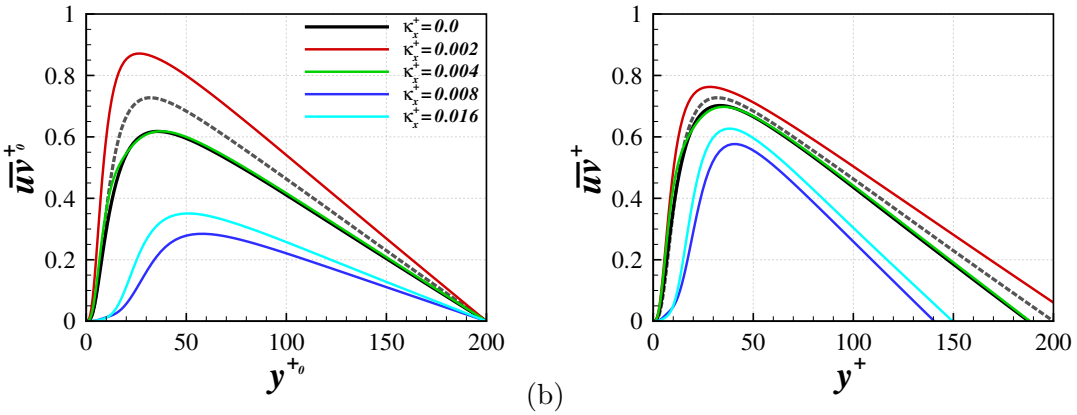

Figure A.26: Reynolds shear stress fluctuations scaled by the no-control case (a) and local wall units (b). The grey dashed line shows the profile from the no-control case.

Bibliography

H. Abe, H. Kawamura, and Y. Matsuo. Surface heat-flux fluctuations in a turbulent channel flow up to $Re_\tau = 1020$ with $Pr = 0.025$ and 0.71. *International Journal of Heat and Fluid Flow*, 25(3):404–419, 2004.

L. Agostini, E. Touber, and M. A. Leschziner. Spanwise oscillatory wall motion in channel flow: drag-reduction mechanisms inferred from dns-predicted phase-wise property variations at $re_\tau = 1000$. *Journal of Fluid Mechanics*, 743:606–635, 2014.

R. Akhavan, W. J. Jung, and N. Mangiavacchi. Turbulence control in wall-bounded flows spanwise oscillations. In F. T. M. Nieuwstadt, editor, *Advances in Turbulence IV*, volume 51 of *Applied Scientific Research*, pages 299–303, 1993.

S. D. Anderson and J. K. Eaton. Reynolds stress development in pressure-driven three-dimensional turbulent boundary layers. *Journal of Fluid Mechanics*, 202: 236–294, 1989.

F. Auteri, A. Baron, M. Belan, G. Campanardi, and M. Quadrio. Experimental assessment of drag reduction by traveling waves in turbulent pipe flow. *Physics of Fluids*, 22:115103, 2010.

P. R. Bandyopadhyay. Stokes mechanism of drag reduction. *Transaction of the ASME, Series E: Journal of Applied Mechanics*, 73:483, 2006.

A. Baron and M. Quadrio. Turbulent drag reduction by spanwise wall oscillation. *Applied Scientific Research*, 55:311–326, 1996.

G. K. Batchelor. *An introduction to fluid dynamics*. Cambridge University Press, 1967.

R. M. Beam and R. F. Warming. An implicit factored scheme for the compressible Navier-Stokes equations. *AIAA Journal*, 16:393–402, 1978.

M. Belan and M. Quadrio. A pertubative model for predicting the high-reynolds-number behaviour of the streamwise travelling waves technique in turbulent drag reduction. 93(12), 2013.

O. Blesbois, S. I. Chernyshenko, E. Touber, and M. A. Leschziner. Pattern preduction by linear analysis of turbulent flow with drag reduction by wall oscillation. *Journal of Fluid Mechanics*, 724:607–641, 2013.

P. Bradshaw and N. Pontikos. Measurements in the turbulent boundary layer of an 'infinite' swept wing. *Journal of Fluid Mechanics*, 159:105–130, 1985.

S. I. Chernyshenko and M. F. Baig. Streaks and vortices in near-wall turbulence. *Philosophical Transaction of the Royal Society A*, 363:1097–1107, 2005.

H. Choi, P. Moin, and J. Kim. Active turbulence control for drag reduction in wall-bounded flows. *Journal of Fluid Mechanics*, 262:75–110, 1994.

J. I. Choi, C. X. Xu, and H. J. Sung. Drag reduction by spanwise wall oscillation in wall-bounded turbulent flows. *AIAA Journal*, 40(5):842–850, 2002.

K. S Choi. Near-wall structure of turbulent boundary layer with spanwise-wall oscillation. *Physics of Fluids*, 14(7):2530–2542, 2002.

K. S. Choi and B. R. Clayton. The mechanism of turbulent drag reduction with wall oscillation. *International Journal of Heat and Fluid Flow*, 22(1):1–9, 2001.

K.-S. Choi, J.-R. DeBisschop, and B. R. Clayton. Turbulent boundary-layer control by means of spanwise wall oscillation. *AIAA Journal*, 36(7):1157–1163, 1998.

M. S. Chong, A. E. Perry, and B. J. Cantwell. A general classification of three-dimensional flow fields. *Physics of Fluids A*, 2(5):765–777, 1990.

A. J. Chorin. A numerical method for solving incompressible viscous flow problems. *Journal of Computational Physics*, 2(1):12–26, 1967.

Y. M. Chung and T. Talha. Effectiveness of active flow control for turbulent skin friction drag reduction. *Physics of Fluids*, 23(2):025102, 2011.

A. Cimarelli, B. Frohnapfel, Y. Hasegawa, E. De Angelis, and M. Quadrio. Prediction of turbulence control for aribrary periodic spanwise wall movement. *Physics of Fluids*, 25(7):075102, 2013.

G. N. Coleman, J. Kim, and A. T. Le. A numerical study of three-dimensional wall-bounded flows. *International Journal of Heat and Fluid Flow*, 17(3):333–342, 1996.

J. C. del Alamo and J. Jiménez. Spectra of the very large anisotropic scales in turbulent channels. *Physics of Fluids*, 15(6):L41–L44, 2003.

J. C. del Alamo, J. Jiménez, P. Zandonade, and R. D. Moser. Scaling of the energy spectra of turbulent channels. *Journal of Fluid Mechanics*, 500:135–144, 2004.

M. R. Dhanak and C. Si. On reduction of turbulent wall friction through spanwise wall oscillations. *Journal of Fluid Mechanics*, 383:175–195, 1999.

Y. Du and G. E. Karniadakis. Supressing wall turbulence by means of a transverse travelling wave. *Journal of Fluid Mechanics*, 288:1230–1234, 2000.

Y. Du, V. Symeonidis, and G. E. Karniadakis. Drag reduction in wall-bounded turbulence via a transverse travelling wave. *Journal of Fluid Mechanics*, 457: 1–34, 2002.

J. K. Dukowicz and A. S. Dvinsky. Approximate factorization as a high order splitting for the implicit incompressible flow equations. *Journal of Computational Physics*, 102(2):336–347, 1992.

C. A. Duque-Daza, M. F. Baig, D. A. Lockerby, S.I. Chernyshenko, and C. Davies. Modelling turbulent skin-friction control using linearized navier stokes equations. *Journal of Fluid Mechanics*, 702:403–414, 2012.

K. Fukagata, K. Iwamoto, and N. Kasagi. Contribution of Reynolds stress distribution to the skin friction in wall-bounded flows. *Physics of Fluids*, 14(11):L73–L76, 2002.

D. Gatti and M. Quadrio. Performance losses of drag-reducing spanwise forcing at moderate values of the reynolds number. *Physics of Fluids*, 25:125109, 2013.

K. Gouder, M. Potter, and J.F. Morrison. Turbulent friction drag reduction using electractive polymer and electromagnetically driven surfaces. *Experiments in Fluids*, 54(1441):1–12, 2013.

F. H. Harlow and J. E. Welch. Numerical calculation of time-dependent viscous incompressible flow of fluid with free surface. *Physics of Fluids*, 8(12):2182–2189, 1965.

A. Holstad, H. I. Andersson, and B. Pettersen. Turbulence in a three-dimensional wall-bounded shear flow. *International Jounal for Numerical Methods in Fluids*, 62:875–905, 2010.

s. Hoyas and J. Jiménez. Scaling of the velocity fluctuations in turbulent channels up to $re_\tau = 2003$. *Physics of Fluids*, 18:011702, 2006.

W. X. Huang and C. X. Xu. Transient response of reynolds stress transport to spanwise wall oscillation in a turbulent channel flow. *Physics of Fluids*, 17:018101, 2004.

J. C. R. Hunt, A. A. Wray, and P. Moin. Eddies, streams, and convergence zones in turbulent flows. Proceedings of the 1988 Summer Program, Center for Turbulence Research, NASA Ames/Stanford University, pages 193–208, 1988.

E. Hurst and Y. M. Chung. The reynolds number effect of turbulent drag reduction. In *UK Turbulence Consortium*, 2012a.

E. Hurst and Y. M. Chung. The reynolds number effect of turbulent drag reduction. In *9th European Fluid Mechanics Conference*, 2012b.

K. Iwamoto, Y. Suzuki, and N. Kasagi. Reynolds number effect on wall turbulence: Toward effective feedback control. *International Journal of Heat and Fluid Flow*, 23(5):678–689, 2002.

K. Iwamoto, K. Fukagata, N. Kasagi, and Y. Suzuki. Friction drag reduction achievable by near-wall turbulence manipulation at high Reynolds numbers. *Physics of Fluids*, 17(1):011702, 2005.

B. L. Jensen, B. M. Sumer, and J. Fredsoe. Turbulent oscillatory boundary layers at high reynolds numbers. *Journal of Fluid Mechanics*, 206:265–297, 1989.

J. Jeong and F. Hussain. On the identification of a vortex. *Journal of Fluid Mechanics*, 285:69–94, 1995.

J. Jeong, F. Hussain, W. Schoppa, and J. Kim. Coherent structures near the wall in a turbulent channel flow. *Journal of Fluid Mechanics*, 332:185–214, 1997.

J. Jiménez. Cascades in wall-bounded turbulence. *Annual Review of Fluid Mechanics*, 44:27–45, 2012.

P. S. Johansson, H Alfredsson, and J.. Kim. Evolution and dynamics of shear-layer structures in near-wall turbulence. *Journal of Fluid Mechanics*, 224:579–599, 1991.

M. R. Jovanović. Turbulence suppression in channel flows by small amplitude transverse wall oscillations. *Physics of Fluids*, 20:1–11, 2008.

S. Y. Jung and H. J. Sung. Characterization of the three-dimensional turbulent boundary layer in a concentric annulus with a rotating inner cylinder. *Physics of Fluids*, 18(11):115102, 2006.

W. J. Jung, N. Mangiavacchi, and R. Akhavan. Suppression of turbulence in wall-bounded flows by high-frequency spanwise oscillations. *Physics of Fluids A*, 4(8): 1605–1607, 1992.

H. S. Kang, H. Choi, and Y. Y. Jung. On the modification of the near wall coherent structure in a three-dimensional turbulent boundary layer on a free rotating disk. *Physics of Fluids*, 10(9):2315–2322, 1998.

J. Kim and P. Moin. Application of a fractional-step method to incompressible Navier-Stokes equations. *Journal of Computational Physics*, 59(2):308–323, 1985.

J. Kim, P. Moin, and R. Moser. Turbulence statistics in fully developed channel flow at low Reynolds number. *Journal of Fluid Mechanics*, 177:133–166, 1987.

K. Kim, S.-J. Baek, and H. J. Sung. An implicit velocity decoupling procedure for the incompressible Navier-Stokes equations. *International Jounal for Numerical Methods in Fluids*, 38(2):125–138, 2002.

S. J. Kline, W. C. Reynolds, F. A. Schraub, and P. W. Runstadler. The structure of turbulent boundary layers. *Journal of Fluid Mechanics*, 30(4):741–773, 1967.

F. Laadhari, L. Skandaji, and R. Morel. Turbulence reduction in a boundary layer by local spanwise oscillating surface. *Physics of Fluids*, 6(10):3218, 1994.

J. Lardeau and M. A. Leschziner. The streamwise drag-reduction response of a boundary layer subjected to a sudden imposition of transverse oscillatory wall motion. *Physics of Fluids*, 25:075109, 2013.

A. T. Le, G. N. Coleman, and J. Kim. Near-wall turbulence structures in three-

dimensional boundary layers. *International Journal of Heat and Fluid Flow*, 21 (5):480–488, 2000.

H. Le and P. Moin. An improvement of fractional step methods for the incompressible Navier-Stokes equations. *Journal of Computational Physics*, 92(2):369–379, 1991.

N. Li and S. Laizet. 2decomp and fft - a highly scalable 2d decomposition library and fft interface. In *Cray User Group 2010 Conference*, 2010.

H. S. Littel and J. K. Eaton. Turbulence characteristics of the boundary layer on a rotating disk. *Journal of Fluid Mechanics*, 266:175–207, 1994.

S. S. Lu and W. W. Willmarth. Measurements of the structure of the reynolds stress in a turbulent boundary layer. *Journal of Fluid Mechanics*, 60:481–511, 1973.

T. S. Lund, X. Wu, and K. D. Squires. Generation of turbulent inflow data for spatially-developing boundary layer simulations. *Journal of Computational Physics*, 140(2):233–258, 1998.

I. Marusic, D. D. Joseph, and K. Mahesh. Laminar and turbulent comparisons for channel flow and flow control. *Journal of Fluid Mechanics*, 507:467–477, 2007.

M. V. Melander and F. Hussain. Cut-and-connect of two antiparallel vortex tubes. *Centre for Turbulence Research Rep.*, CTR-S88:257–286, 1993.

R. Moarref and M. R. Jovanović. Model-based design of transverse wall oscillations for turbulent drag reduction. *Journal of Fluid Mechanics*, 707:205–240, 2012.

J. F. Morrison. The interaction between inner and outer regions of turbulent wall-bounded flow. *Philosophical Transaction of the Royal Society A*, 365(1852):683–698, 2007.

R. Moser, J. Kim, and N. Mansour. Direct numerical simulation of turbulent channel flow up to $Re_\tau = 590$. *Physics of Fluids*, 11(4):943–945, 1999.

N. Nikitin. On the mechanism of turbulence supression by spanwise surface oscillations. *Fluid Dynamics*, 35(2):185, 2000.

P. Orlandi and M. Fatica. Direct simulations of turbulent flow in a pipe rotating about its axis. *Journal of Fluid Mechanics*, 343:43–72, 1997.

A. T. Patera. A spectral element method for fluid dynamics: laminar flow in a channel expansion. *Journal of Computational Physics*, 23:185–208, 1984.

J. B. Perot. An analysis of the fractional step method. *Journal of Computational Physics*, 108(1):51–58, 1993.

M. Quadrio and P. Ricco. Initial response of a turbulent channel flow to spanwise oscillation of the walls. *Journal of Turbulence*, 4, 2003.

M. Quadrio and P. Ricco. Critical assessment of turbulent drag reduction through spanwise wall oscillations. *Journal of Fluid Mechanics*, 521:251–271, 2004.

M. Quadrio and P. Ricco. The laminar generalized stokes layer and turbulent drag reduction. *Journal of Fluid Mechanics*, 667:135–157, 2011.

M. Quadrio, P. Ricco, and C. Viotti. Streamwise-travelling waves of spanwise wall velocity for turbulent drag reduction. *Journal of Fluid Mechanics*, 627:161–178, 2009.

P. Ricco and S. Hahn. Turbulent drag reduction through rotating discs. *Journal of Fluid Mechanics*, 722:267–290, 2013.

P. Ricco and M. Quadrio. Wall-oscillation conditions for drag reduction in turbulent channel flow. *International Journal of Heat and Fluid Flow*, 29(4):891–902, 2008.

P. Ricco and S. Wu. On the effects of lateral wall oscillations on a turbulent boundary layer. *Experimental Thermal and Fluid Science*, 29:41–52, 2004.

P. Ricco, C. Ottonelli, Y. Hasegawa, and M. Quadrio. Changes in turbulent dissipation in a channel flow with oscillating walls. *Journal of Fluid Mechanics*, 700: 77–104, 2012.

S. K. Robinson. Coherent motions in the turbulent boundary layer. *Annual Review of Fluid Mechanics*, 23:601–639, 1991.

T. Sarpkaya. Coherent structures in oscillatory boundary layers. *Journal of Fluid Mechanics*, 253:105–140, 1993.

W. Schoppa and F. Hussain. Genesis of longitudinal vortices in near-wall turblence. *Meccanica*, 33:489–501, 1998.

M. Skote. Turbulent boundary layer flow subject to streamwise oscillation of spanwise wall velocity. *Physics of Fluids*, 23:081703, 2011.

M. Skote. Temporal and spatial transients in turbulent boundary layer flow over an oscillating wall. *International Journal of Heat and Fluid Flow*, 38:1–12, 2012.

M. Skote. Comparison between spatial and temoral wall oscillations in turbulent boundary layer flows. *Journal of Fluid Mechanics*, 730:273–294, 2013.

C. Smith and S. Metzler. The characteristics of low-speed streaks in the near-wall region of a turbulent boundary layer. *Journal of Fluid Mechanics*, 129:27–54, 1983.

A. J. Smits, B. J. McKeon, and I. Marusic. High-reynolds number wall turbulence. *Annual Review of Fluid Mechanics*, 43:353–375, 2011.

J. I. Steger and P. Kutler. Implicit finite-difference procedures for the computation of vortex wakes. *AIAA Journal*, 15(4):581–590, 1977.

T. Talha. *A numerical investigation of three-dimensional unsteady turbulent channel flow subjected to temporal acceleration.* PhD thesis, School of Engineering, University of Warwick, UK, March 2012.

M. Tanahashi, S. J. Kang, T. Miyamoto, S. Shiokawa, and T. Miyauchi. Scaling law of fine scale eddies in turbulent channel flows up to $Re_\tau = 800$. *International Journal of Heat and Fluid Flow*, 25(3):331–340, 2004.

E. Touber and M. A. Leschziner. Near-wall streak modification by spanwise oscillatory wall motion and drag-reduction mechanisms. *Journal of Fluid Mechanics*, 693:150–200, 2012.

A. A. Townsend. Equalibrium layers and wall turbulence. *Journal of Fluid Mechanics*, 11:97–120, 1976.

C. Truesdell. The kinematics of vorticity. *Indiana University*, page 107, 1953.

C. Viotti, M. Quadrio, and P. Luchini. Streamwise oscillation of spanwise velocity at the wall of a channel for turbulent drag reduction. *Physics of Fluids*, 21(11): 115109, 2009.

D. J. Wise and P. Ricco. Turbulent drag reduction through oscillating discs. *Journal of Fluid Mechanics*, 746:536–564, 2014.

I. Yudhistira and M. Skote. Direct numerical simulation of a turbulent boundary layer over an oscillating wall. *Journal of Turbulence*, 12(9):1–17, 2011.

H. Zhao, Wu J.-Z., and J.-S. Luo. Turbulent drag reduction by traveling wave of flexible wall. *Fluid Dynamics Research*, 34:175–198, 2004.